KEELE UNIVERSITY

Catalytic reforming of biogas using nickel based perovskite materials

A thesis submitted to Keele University in partial fulfilment of the requirements for the degree of Doctor of Philosophy

Samuel E. Evans

June 2017

Abstract

The utilisation of biogas as an energy source or as a feed stock for the chemical industry would help to lower the present wasteful and environmentally unfriendly venting of greenhouse gases to the atmosphere. One obstacle to this becoming a reality include finding a catalyst that is active towards carbon dioxide reforming of methane as well as resistance to carbon deposition and sulphur poisoning.

As a potential alternative to supported nickel catalysts, a nickel doped perovskite has been produced *via* a hydrothermal synthesis method for reforming biogas. The selected perovskite, $SrZrO_3$, was doped with 4 mol % nickel into the structure and shown to be phase pure by XRD. This material was rigorously tested catalytically using a range of biogas conditions.

4 mol% Ni doped $SrZrO_3$ was shown to be resistant to carbon deposition under high temperature, methane rich biogas reforming conditions with no observable trend between the amount of carbon formed and the time on stream. This catalyst showed high activity and selective towards the formation of the desired products, an equimolar mixture of hydrogen and carbon monoxide.

As naturally derived biogas is not a pure mixture of methane and carbon dioxide, studies into the effect that two of the other important components of biogas, water and sulphur containing compounds, were carried out. The perovskite material was seen to be stable towards continued dry reforming of methane irrespective of the inclusion of water, and at elevated reaction temperatures was able to convert the water into the required products of hydrogen and carbon monoxide.

The effect of hydrogen sulphide was studied and the perovskite material was seen to be susceptible to sulphur poisoning. However the extent and the recovery from this type of deactivation was an improvement on that seen by Ni/YSZ and 5% ceria doped Ni/YSZ

“Magic rocks…….”

Acknowledgements

The completion of a thesis is a solitary experience, particularly in the final write up stage. However, I would have never completed my thesis without a strong support team around me, consisting of academic and emotional supporters. These people I would like to thank.

Firstly, I would like to thank Professor Mark Ormerod for not only believing that I was capable and deserving of this opportunity, but also for careful and thoughtful guidance throughout the process. Mark's ability to be extremely knowledgeable on a subject with limited information, whilst juggling many other demanding and tiring tasks is second to none. I would also like to thank Dr John Staniforth; without John's daily input and expertise I would have struggled to make a start never mind finished this project. In addition to expertise in both subject matter and equipment, John became a person to drink coffee with, moan about anything and everything with, and most of all became a very firm friend, and for that cannot say thank you enough. The final member of my academic support team was Dr Richard Darton who proved to truly be the engine room of what became a successful group both in terms of publications and general progression in research. Richard's door was always open and his advice invaluable.

In addition to my direct academic support team there are many other members of the staff in the Lennard-Jones building that I would like to thank. In no particular order these people include: Dave Evans, John Clews, Ralph Patterson, Amy Cowles,

I would like to thank my friends and family that have been there for me throughout the process. To all my fellow PhD students who have shared this experience with me, drank

coffee, drank beer, talked science, bitched and moaned, it would not have been the same without you, you all know who you are. I would like to mention two very close friends, Oliver Good and Emma Garrett who I also shared my undergraduate years with. To my parents for always being there for me, believing in me and supporting me through the good times and the bad. You raised me both to have a passion for science and to always achieve the best that I can, and perhaps most importantly just to be the person that I am today. I am sure I will never be able to thank you enough for this. I hope that you are proud of me.

Lastly, I would like to thank Jessica Thompson. Who knew that we would come this far together? You have kept me going and we have shared so much together in that time. I hope that I have supported and encouraged you as much as you have me, and that I will return that favour throughout the rest of your PhD.

Contents

Contents

1 Introduction

1.1 General Context

As the world's need for energy rises year on year, and the realisation that fossil fuels will become progressively more depleted, subject to greater demand and significantly more expensive in the discernible future, alternative power generation systems are assuming greater importance. Furthermore, with strong evidence that the use of carbon based sources of energy damages the ecosystem, the need for more efficient, low carbon methods of power generation becomes more pressing.

The worldwide dependence on coal, oil and natural gas is well documented; almost 90% of global energy production is currently being met by fossil fuels[1]. The combustion of these fuels leads to the emission of large amounts of greenhouse gases, predominantly carbon dioxide, a gas directly linked with rising global temperature. It is also evident that these sources of energy will become depleted in the near future raising major questions as to how future generations will meet the large energy requirements of an ever-increasing global population and developing society. This is one of the major reasons for the high levels of research into alternative methods of generating and storing energy.

Hydrogen is seen by many as the medium of choice for energy storage. This is due to hydrogen possessing a very high energy content compared to its weight, and because it produces only water when combusted. However, despite the ubiquitous nature of hydrogen, it is not naturally available as molecular hydrogen (H_2) and must be chemically produced. Hydrogen can be produced using several methods that each has advantages and

disadvantages. Reforming natural gas, in particular methane, is one of the most common methods for hydrogen formation; however, this relies on a dwindling supply of natural gas.

One solution to the global fall in available fossil fuel reserves available and rise in atmospheric concentrations of carbon dioxide and other greenhouse gases is the use of biofuels as an alternative to fossil based fuels. Biofuels are defined as fuels in solid, liquid or gaseous form derived directly from a biomass source[2]. There are several predominant types of biofuel including, bioethanol, biodiesel, bioethers, wood, charcoal and biogas.

1.2 Biogas

Biogas is a variable gaseous mixture comprised primarily of methane and carbon dioxide. Biogas is generated *via* the anaerobic digestion of biomass such as sewage and other faecal matter, plant waste, animal waste, food waste and industrial effluent[2]. The composition is highly variable; usually comprising of 40-70% methane, 30-60% carbon dioxide and impurities such as hydrogen sulphide and other sulphur containing organic compounds[3]. Biogas is a relatively cheap fuel due to the incidental nature of production, however it is underutilised. In the UK biogas produced at landfill sites is often vented into the atmosphere or burnt off due to the decentralisation of sites and relative low value of biogas. The high concentration of carbon dioxide can prevent it being used directly in traditional engines and can make simple combustion problematic. At high combustion temperatures CO_2 lowers peak engine power and the concentration of methane can become low enough to prevent combustion. At lower combustion temperatures engines can suffer from instability when using biogas as a fuel and as a result of this high concentrations of methane are found in the exhaust[4]. Biogas is utilised more in countries such as India where

it is burnt directly for cooking and lighting purposes particularly in more rural or remote areas[5,6].

As well as incidental production, it is also possible to deliberately manufacture biogas. In order to provide the anaerobic conditions necessary for digestion, the utilised biomass must be placed into specially designed fermentation vessels called anaerobic digesters, which have become sufficiently advanced to provide continuous and reliable supplies of biogas for as long as suitable substrate is provided. Anaerobic digesters promote the decomposition of biomatter to simple organics and biogas[2]. Biomatter is placed within the digester and sealed so that oxygen is quickly consumed by bacteria and not replenished, and then in the absence of oxygen several types of bacteria contribute to digestion to form biogas. The first step is the hydrolysis of carbohydrates, proteins and lipids into the corresponding monomers. In the second acidogenic stage the produced monomers are further degraded to give organic acids, alcohols, carbon dioxide and hydrogen. In the acetoegenic phase the products of acidogenesis become precursors for a variety of reactions that are dependent on each other. Homoacetic bacteria reduce carbon dioxide and hydrogen to form acetic acid, reducing the hydrogen partial pressure as a result; however methanogenic bacteria that form the methane that makes up the bulk of the final biogas can only thrive at high hydrogen partial pressures. As the acetic acid is one of the substrates for methane formation formed in the final methanogenic step, a delicate symbiotic relationship between the different bacteria is formed.

Due to the variable nature of biogas production, there is a considerable and changeable selection of impurities than can be present in biogas, summarised in *Table 1.1* below:

Table 1-1 Biogas Compositions from Various sources[7]

Components	Sewage Gas	Agricultural Gas	Landfill Gas
CH_4 % vol	65-75	45-75	45-55
CO_2 % vol	20-35	25-55	25-30
CO % vol	<0.2	<0.2	<0.2
N_2 % vol	3.4	0.01-5.0	10-25.0
O_2 % vol	0.5	0.01-2	1-5
H_2 % vol	trace	0.5	0
H_2S mg/m^3	<8000	10-30000	<8000

Biogas is a resource that can be utilised in a solid oxide fuel cell (SOFC) in principle as lower levels of methane can be tolerated[8,9]. This is especially useful as methane and carbon dioxide are both greenhouse gases[10], methane in fact being far more polluting than carbon dioxide[11]. For this reason biogas is a resource that needs to be utilised, not only because it is a cheap, 'clean' source of energy, but by not using it, the already high levels of greenhouse gases that we emit yearly are significantly added to.

The variability in the ratio of methane to carbon dioxide that can be seen in Table 1-1 is part of the reason for the underutilisation of biogas in many more developed countries. It is possible to upgrade biogas to biomethane by removing the carbon dioxide and many of the other components. However, this lowers the efficiency of biogas use, and ultimately still leads to venting carbon dioxide into the atmosphere. This high concentration of CO_2 in biogas is in fact potentially beneficial if biogas was to be used to power a SOFC and this has been reported by a number of reserchers[11–14].

1.3 Fuel Cells

Fuel cells are electrochemical devices for the conversion of chemical energy to direct current (DC) electrical power. The first fuel cell was invented by William Grove in 1839[15], a time when the need for high efficiency, low carbon forms of energy generation was of much lower interest than now. In more recent times the requirement for alternative energy sources has progressed and fuel cells have received a much higher level of interest.

There are several types of fuel cell which all follow the same basic structure and operating principles. Fuel cells are comprised of an anode and cathode, separated by an electrically insulating, ionically conducting electrolyte. The basis of a simple fuel cell is that at the anode, oxidation of hydrogen occurs, and at the cathode, reduction of oxygen. One of these ions (depending on the type of fuel cell) then passes through the electrolyte to meet the other forming water. Upon formation of water the liberated electrons must pass around an external circuit due to the insulating nature of the electrolyte[16], this generates an electrical current. A schematic of a simple hydrogen fuel cell is shown in Figure 1-1.

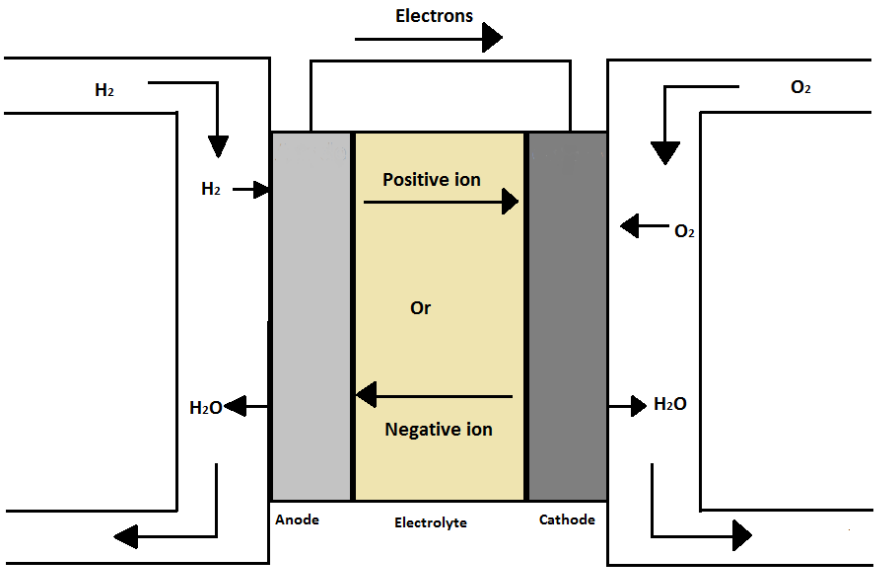

Figure 1-1 Schematic of a simple Hydrogen Fuel Cell

1.3.1 Fuel Cell Types

There are five primary types of fuel cell which are characterised by the electrolyte used. These are Molten Carbonate Fuel Cells (MCFC), Alkaline Fuel Cells (AFC), Polymer Electrolyte Membrane Fuel Cells (PEMFC), Phosphoric Acid Fuel Cells (PAFC) and Solid Oxide Fuel Cells (SOFC). The key characteristics of these cells are summarised in *Table* 1-2: Summary of fuel cell types and characteristics adapted from16,17

:

	MCFC	AFC	PEMFC	PAFC	SOFC
Electrolyte	Molten Carbonate	Potassium Hydroxide$_{(aq)}$	Polymer Membrane	Phosphoric Acid$_{(aq)}$	Ceramic inorganic oxide
Charge Carrier	CO_3^{2-}	OH^-	H^+	H^+	O^{2-}
Operating Temperature / °C	650	60-220	80	200	600-1000
Catalyst	Electrode Material	Platinum	Platinum	Platinum	Electrode Material or separate nickel catalyst
Electrodes	Nickel and Nickel Oxide	Transition Metal	Carbon	Carbon	Perovskite and Metal Cermet/ Perovskite

Table 1-**2**: Summary of fuel cell types and characteristics adapted from[16,17]

1.3.1.1 Molten Carbonate Fuel Cell

Molten carbonate fuel cells (MCFCs) employ an electrolyte of molten carbonate suspended in an alumina based-matrix. The anode and cathode in MCFCs are similar, comprising of nickel and nickel oxide respectively. MCFCs operate at relatively high temperatures (600-700 °C) which enables the internal reformation of higher carbon based fuels and the use of nickel based catalysts as opposed to more precious metals[18]. At the cathode oxygen combines with carbon dioxide to form a carbonate ion:

$$O_2 + 2CO_2 + 4e^- \rightleftharpoons 2CO_3^{2-} \qquad \text{(Equation 1.1)}$$

The carbonate ions then migrate through the electrolyte to the anode and react with hydrogen to give water and carbon dioxide, the carbon dioxide is often then redistributed back to the cathode. The reaction liberates the electrons that were initially consumed allowing a current to be generated:

$$2H_2 + 2CO_3^{2-} \rightleftharpoons 2H_2O + 2CO_2 + 4e^- \quad \text{(Equation 1.2)}$$

1.3.1.2 Alkaline Fuel Cell

Alkaline fuel cells (AFCs) are distinguished by the use of an aqueous alkaline solution electrolyte, usually potassium hydroxide. The anode and cathode employ a bilayer system, one layer for catalytic reduction or oxidation, the other is hydrophobic to contain the electrolyte[19]. The anode is usually platinum with a transition metal cathode, often nickel. Hydroxide ions are the charge carries in AFCs and are produced at the cathode by combining air and water:

$$H_2O + \frac{1}{2}O_2 + 2e^- \rightleftharpoons 2OH^- \quad \text{(Equation 1.3)}$$

The hydroxide ions then diffuse through the electrolyte and combine with hydrogen at the anode to form water and liberate electrons (Equation 1.4):

$$2OH^- + H_2 \rightleftharpoons 2H_2O + 2e^- \quad \text{(Equation 1.4)}$$

1.3.1.3 Polymer Electrolyte Membrane Fuel Cell

Polymer Electrolyte Membrane Fuel Cells (PEMFCs) are proton conducting cells. PEMFC consist of a polymer electrolyte membrane sandwiched between two electrode layers comprised of supported platinum catalyst that catalyse fuel oxidation and oxygen reduction. These layers are coated with a thin carbon layer that acts as a current collector

and also as a support. At the anode side hydrogen is oxidised and the electrons released pass round the external circuit to the cathode generating a current[20]:

$H_2 \rightleftharpoons 2H^+ + 2e^-$ (Equation 1.5)

The protons pass through the polymer electrolyte where they combine with oxygen, consuming the electrons from the anode to form water (Equation 1.6):

$\frac{1}{2}O_2 + 2H^+ + 2e^- \rightleftharpoons H_2O$ (Equation 1.6)

1.3.1.4 Phosphoric Acid Fuel Cell

Like PEMFC, Phosphoric acid fuel cells (PAFCs) work with a proton conducting electrolyte, in this case, aqueous phosphoric (or in some cases sulphuric) acid. PAFC employ noble metals for catalysts at the electrodes, usually platinum based backed with a hydrophobic medium to contain the liquid electrolyte[21]. At the anode hydrogen is oxidised (Equation 1.7) to form protons that migrate from the anode to the cathode:

$H_2 \rightleftharpoons 2H^+ + 2e^-$ (Equation 1.7)

Upon migration the protons react with oxygen ions that are reduced at the cathode forming water and liberating electrons[22]:

$2H^+ + O^{2-} \rightleftharpoons H_2O + 2e^-$ (Equation 1.8)

1.3.1.5 Solid Oxide Fuel Cell

One of the most promising and intensively researched fuel cells is the solid oxide fuel cell (SOFC). Generating electricity electrochemically by use of a SOFC has many advantages over traditional methods, not least efficiency gains. SOFCs operate at high temperatures giving rise to the capability of reforming a wide range of fuels from methane, to heavier carbonaceous sources such as butane[23,24], ethanol[25,26], propane[27,28] and biogas[9,29].

Solid oxide fuel cells have a solid ceramic electrolyte, traditionally composed of yttria stabilised zirconia (YSZ), a perovskite based cathode, often lanthanum strontium manganite, La_1-$xSrxMnO_3$, (LSM) and a supported nickel anode. At the cathode oxygen is reduced (Equation 1.9) and passes through the electrolyte *via* oxygen vacancies[30]:

$$O_2 + 4e^- \rightleftharpoons 2O^{2-} \qquad \text{(Equation 1.9)}$$

At the anode oxygen ions and hydrogen ions combine to form water (Equation 1.10) and electrons travel around an external circuit back to the cathode

$$H_2 + O^{2-} \rightleftharpoons H_2O + 2e^- \qquad \text{(Equation 1.10)}$$

The electrolyte of a SOFC must possess good oxygen ion conductivity, negligible electrical conductivity, as well as being easy to engineer and compatible with other cell components. Zirconia stabilised with yttria (YSZ) is the most common electrolyte used for SOFCs. This is as a result of several attractive properties that are yet to be fully matched or surpassed. YSZ is very stable both thermally and chemically, it is an electrical insulator

under SOFC operating temperatures, as well as being an oxygen ion conductor over a wide range of oxygen partial pressures[31]. Further to this YSZ is an attractive material due to its relatively low cost.

SOFC cathodes, like any electrode material, must be electrically conducting. In addition to this the material used has to be stable in an oxidising atmosphere. Lanthanum strontium manganite adopts a perovskite crystal structure and has the general formula $La_{1-x}Sr_xMnO_3$. LSM is a common choice for the cathode of SOFCs due to its high electrical conductivity at elevated temperatures and activity towards oxygen reduction. A further advantage to the use of LSM, in traditional SOFC systems at least, is the thermal compatibility to YSZ. This ensures that no separation of materials occurs when the temperature of the cell is cycled due to expansion or contraction.

The third major components of a SOFC is the anode. The anode is responsible for either direct catalytic oxidation of the fuel source or reformed fuel (H_2 and CO). The anode must be electronically conducting and stable in a strongly reducing atmosphere. Nickel is a cheap and suitable metal that is very commonly used. This is then supported on YSZ to maintain porosity by preventing sintering of the nickel particles. Addition of YSZ also helps to make the nickel based anode material more thermally compatible with the YSZ electrolyte.

1.4 Direct Internal Reforming Solid Oxide Fuel Cells (DIR-SOFC)

SOFCs tend to have the highest operating temperature of any fuel cells which offers several advantages. The excess heat generated can be recovered and used in combination

systems to turn a turbine[32], or to heat water in stationary systems[33]. This significantly increases the overall efficiency of the system and lowers energy waste. Several consumer level products have been proposed in which good quality excess heat is used to provide hot water to the consumer for the extent of cell operation. Approaches such as these bring down the overall cost of running SOFC systems by improving energy efficiency, and bring wide scale production and integration into national grids closer to feasible reality.

Several SOFC designs have made it to market with mixed success; these designs vary from stationary large scale applications, transportation solutions, and military systems. One of the original market leaders is Siemens Westinghouse who are utilising a tubular stack design with reports of high efficiency and small percentage losses in performance, this includes hybridisation with a gas turbine to further increase efficiency[32].

Ceramic Fuel Cells, an Australian company, has developed a product called "BlueGen" which is used for small scale electrical generation for domestic applications with efficiencies reported at 60 % when waste heat is reclaimed to provide hot water to the household. This system can produce up to 36 Kilowatt-hours per day when utilising a direct supply of natural gas.

Another advantage of arguably higher benefit is the ability to catalytically reform carbon based fuels into synthesis gas. Synthesis gas is a mix of carbon monoxide and hydrogen, as SOFCs are oxygen ion conducting, both components of this gas can be oxidised and thus used as fuel for the electrochemical anodic reaction:

$H_2 + O^{2-} \rightleftharpoons H_2O + 2e^-$ (Equation 1.11)

$CO + O^{2-} \rightleftharpoons CO_2 + 2e^-$ (Equation. 1.12)

For this internal reformation to be possible directly inside the cell the anode material must possess sufficient catalytic activity to reform the fuel fed to the cell. The material also has to meet the mechanical requirements of the cell including a good electronic conductivity and thermal compatibility with the electrolyte to avoid formation of cracks during cell operation.

1.5 Heterogeneous Catalysis

Heterogeneous catalysis involves the use of a catalyst and substrate that are in different phases, usually a solid catalyst and gaseous or liquid substrate. For the purpose of this work the catalyst will be considered as solid and the reactants gaseous.

The two primary mechanisms that are used to satisfy heterogeneously catalysed reactions, either wholly or in combination are the Langmuir-Hinshelwood mechanism and the Rideal-Eley mechanism. The Langmuir-Hinshelwood mechanism is the one most commonly used to describe heterogeneous catalysis[34].

The Langmuir-Hinshelwood mechanism involves the separate adsorption of two reactant species onto the active site of the catalyst material. If the correct species are chemisorbed on neighbouring active sites, they can then react together and desorb as a product species. This can be described using the following reaction steps:

$A_{(g)}$ + Surface ⇌ $A_{(ads)}$

$B_{(g)}$ + Surface ⇌ $B_{(ads)}$

$A_{(ads)}$ + $B_{(ads)}$ ⇌ $AB_{(ads)}$

$AB_{(ads)}$ ⇌ $AB_{(g)}$ + Surface

The Rideal-Eley mechanism differs in that only one reactant species is chemisorbed onto the catalyst surface. Whilst one species is chemisorbed onto the surface, a second reactant species still in the gas phase can react with this species to form a product. This product then desorbs from the surface. This can be described using the following reactions:

$A_{(g)}$ + Surface ⇌ $A_{(ads)}$

$A_{(ads)}$ + $B_{(g)}$ ⇌ $AB_{(ads)}$

$AB_{(ads)}$ ⇌ $AB_{(g)}$ + Surface

1.5.1 Methane Reforming

It is likely that methane (natural gas) will remain the major feedstock for the catalytic production of hydrogen for the foreseeable future due to the financial benefit of natural gas production plants over coal based plants[35]. There are three primary heterogeneously catalysed processes to reform methane into synthesis gas. These reactions are the partial oxidation of methane (POx), steam reforming of methane and dry reforming of methane (DRM) each reaction will be covered in the following sections.

Within these reactions there are many other reactions that can occur simultaneously. These reactions then each influence the overall reforming reaction profile. Figure 1-2 shows how

the Gibbs free energy changes with the temperature of the side reactions. As an example, for reactions such as the Boudouard reaction, the likelihood of the reaction taking place increases with decreasing temperature, as shown by the decrease in the Gibbs free energy at lower temperature.

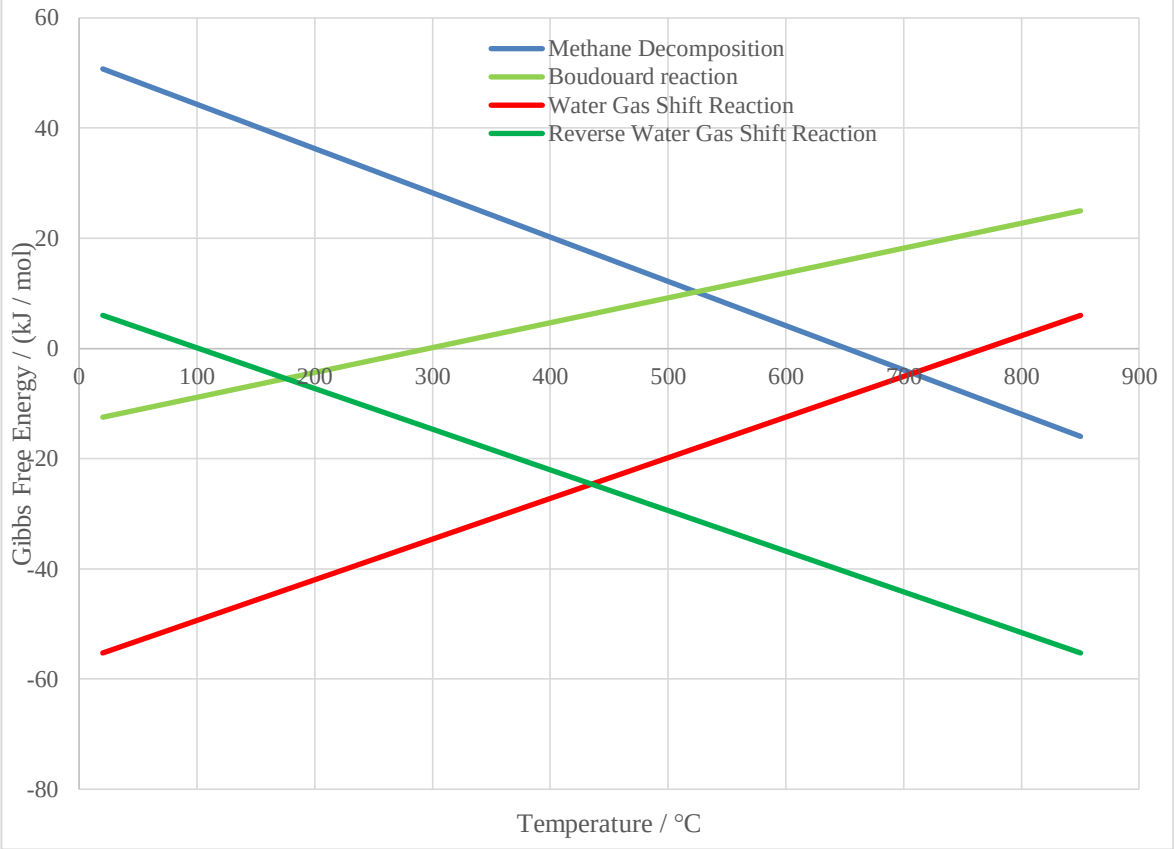

Figure 1-2 Varying ΔG with temperature of several reactions that occur within methane reforming reactions

1.5.1.1 Steam Reforming of Methane

Steam reforming of methane (SRM) has been an industrially important reaction for the production of synthesis gas since the 1960s, and as a result has become a well described and optimised process[36]. The reforming of steam with methane gives the highest hydrogen

to carbon monoxide ratio of the three primary methane reforming reactions (Equation 1.13) and this is one of the main reasons that it is industrially significant, as well as controllability and steam being an easily available reactant.

Due to the endothermic nature of the SRM reaction industrial steam reforming plants operate in excess of 800 °C, which can cause the decomposition of methane, with undesirable deleterious formation of carbon as a result. In order to inhibit the formation of carbonaceous species on the catalyst, steam is often added in excess to shift the reaction away from carbon formation[37]. If steam is added in excess then carbon dioxide can be produced in addition to hydrogen (Equation 1.14), this also ensures that the water gas shift reaction (Equation 1.15) favours the right-hand side of the equation.

$CH_4 + H_2O \rightleftharpoons CO + 3H_2$ $\Delta H^{\ominus}$ 298 K = +206 kJ mol^{-1} (Equation 1.13)

$CH_4 + 2H_2O \rightleftharpoons CO_2 + 4H_2$ $\Delta H^{\ominus}$ 298 K = +165 kJ mol^{-1} (Equation 1.14)

$CO + H_2O \rightleftharpoons H_2 + CO_2$ $\Delta H^{\ominus}$ 298 K = -41 kJ mol^{-1} (Equation 1.15)

1.5.1.2 Partial Oxidation of Methane

If the oxygen to methane ratio is less than stoichiometric for combustion, partial oxidation (POx) can occur. POx results in the formation of hydrogen rich synthesis gas (Equation. 1.17), and is exothermic and thus favoured at lower temperatures than endothermic steam reforming or dry reforming reactions which can result in lower formation of carbon due to pyrolysis of methane. However, at lower reaction temperatures the total oxidation combustion reaction becomes progressively more favoured over partial oxidation.

$CH_4 + 2O_2 \rightleftharpoons CO_2 + 2H_2O$ $\Delta H^{\ominus}$ 298K= −890 kJ mol^{-1} (Equation 1.16)

$CH_4 + \frac{1}{2}O_2 \rightleftharpoons 2H_2 + CO$ $\Delta H^{\ominus}$ 298K= −36 kJ mol^{-1} (Equation 1.17)

The 2:1 ratio of hydrogen to carbon monoxide is ideal for the formation of methanol, and catalytic partial oxidation of methane is an important reaction industrially. POx of methane can be achieved without the use of a catalyst at high pressure and temperature. The use of a catalyst can bring down the reaction temperature and pressure required, as a result s lowering costs[38].

1.5.1.3 Dry Reforming of Methane

$CH_4 + CO_2 \rightleftharpoons 2CO + 2H_2$ $\Delta H^{\ominus}$ 298 K = +247 kJ mol^{-1} (Equation. 1.18)

Dry reforming of methane is potentially an attractive process for several reasons. Environmentally the most significant reason to utilise the DRM reaction is that it simultaneously consumes two greenhouse gases in methane and carbon dioxide. A second advantage to DRM is that the synthesis gas produced is equimolar in hydrogen and carbon monoxide, making it more suitable for Fischer–Tropsch catalysis to produce higher hydrocarbon fuels and for dimethyl ether production[39]. A third advantage is that biogas contains both methane and carbon dioxide, and thus theoretically can be directly reformed to form synthesis gas with little or no requirement for additional oxidant.

The dry reforming of methane reaction is an endothermic process and as a result is favoured at higher temperatures. Consequently, this means the reaction takes place in a

temperature range where the formation of carbon is thermodynamically favourable, which will be covered in section 1.5.3 in greater detail including the reactions that cause this. In addition to carbon forming reactions there is potential for the reverse water-gas shift reaction to occur (Equation. 1.19), particularly when the concentration of CO_2 is high, resulting in the formation of steam and carbon monoxide and a reduction in the hydrogen yield.

$CO_2 + H_2 \rightleftharpoons H_2O + CO$ $\Delta H^{\ominus}$ 298 K = 41 kJ mol^{-1} (Equation. 1.19)

The reaction mechanism of carbon dioxide and methane reforming to synthesis gas is not a universally agreed one however, it can be assumed that the reaction could occur by stepwise methane dehydrogenation, dissociative adsorption of carbon dioxide and hydrogen and reduction of carbon dioxide on the catalyst surface in a Langmuir-Hinshelwood type reaction [40]:

$CH_{4(g)} \rightleftharpoons C_{(ads)} + 4H_{(ads)}$

$CO_{2(g)} \rightleftharpoons CO_{(ads)} + O_{(ads)}$

$C_{(ads)} + O_{(ads)} \rightleftharpoons CO_{(ads)}$

$CO_{(ads)} \rightleftharpoons CO_{(g)}$

$2H_{(ads)} \rightleftharpoons H_{2(g)}$

An Eley-Rideal type mechanism is also a possible mechanism[41,42]. This involves initial thermal decomposition of methane which would be the rate determining step, followed by the reverse Boudouard reaction:

$CH_{4(g)} \rightleftharpoons C_{(ads)} + 2H_{2(g)}$

$C_{(ads)} + CO_{2(ads)} \rightleftharpoons 2CO_{(g)}$

1.5.2 Nickel supported with Yttria Stabilised Zirconia

The anode material of a solid oxide fuel cell must meet several key criteria. Failure to meet one will result in a non-functioning cell. As with any type of cell the anode material must be able to transfer charge to the external circuit, so under operating conditions electrical conductivity is a key feature of any SOFC anode material. The anode must be thermally and chemically compatible with any components that it comes into contact with, primarily the electrolyte and any interconnect materials used. Any anode material selected must be porous in nature to allow gas diffusion through the material to the electrolyte, where dissociated oxygen can meet the fuel, and electrons can pass towards the external circuit, this area is called the triple phase boundary as is shown in Figure 1.3.

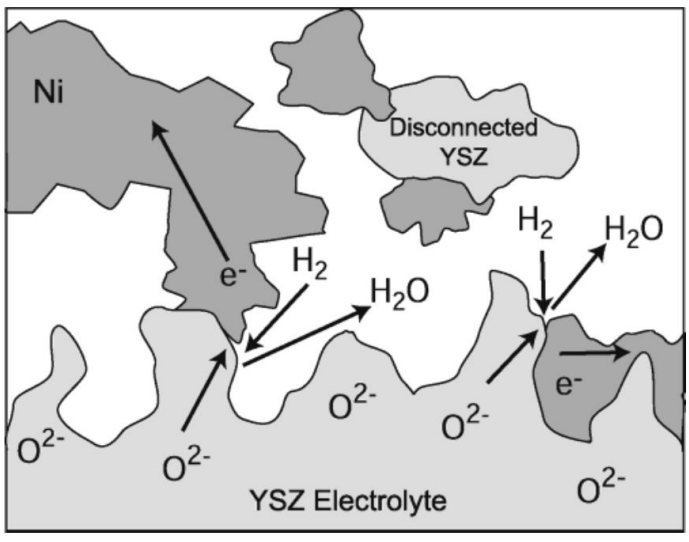

Figure 1-3 Diagram showing triple phase diagram at microscopic level [43]

Due to the reducing nature of the fuel gas used for SOFCs, metals such as nickel are appropriate electrocatalysts as they remain in the reduced state during operation and have good conductivity and catalytic properties. Nickel has high activity towards the catalytic oxidation of hydrogen, and due to being relatively cheap, as well as possessing a relatively low melting point and thus propensity to sinter, a nickel anode stabilised with yttria stabilised zirconia (YSZ) has become the most commonly used anode for SOFCs[44]. This Ni/YSZ cermet offers the required catalytic and electronic properties, whilst being compatible thermally with a YSZ based electrolyte and being porous in nature. Ni/YSZ suffers from loss of reforming activity due to possessing low redox stability, propensity to form deposits of solid carbon and affinity for sulphur containing compounds for binding to active sites.

1.5.3 Carbon Deposition on Nickel Based SOFC Cermet Materials

When reforming methane based fuels over Ni/YSZ there are two primary carbon forming reactions, the Boudouard reaction (Equation. 1.20) and methane pyrolysis (Equation 1.21). The occurrence of these reactions is partially controlled by thermodynamics, with the Boudouard prevalent at lower temperatures, and methane pyrolysis becoming more predominant with increasing temperature.

$2CO \rightleftharpoons C + CO_2$ $\Delta H^{\ominus}$ 298 K = -172 kJ mol^{-1} (Equation. 1.20)

$CH_4 \rightleftharpoons C + 2H_2$ $\Delta H^{\ominus}$ 298 K = 75 kJ mol^{-1} (Equation. 1.21)

When carbon deposits are found on the surface of the anode material the carbon can occupy the active sites lowering the catalytic and electrocatalytic activity of the material[45].

Carbon can also cause physical damage to the anode material by breaking up pore structures and disrupting the flow of reactant gases. In some cases however carbon deposits can be useful, connecting isolated components of the anode structure with conductive 'fingers'[46].

Carbon formation created during methane reforming is not limited to one single form of carbon. Methane pyrolysis is the fastest of the carbon forming processes and forms graphitic or amorphous carbon often known as 'coke'[38,47,48]. The Boudouard reaction forms primarily filament, whisker or nanotube carbon which possesses more ordered structures. These forms of carbon can cause splitting of metal crystals from the support on supported metal catalysts by growing in between the two components[49]. It is important to note that although some minor distinction can be made between 'coke' and 'carbon', the terms are often used interchangeably to refer to any form of carbon formed on a catalyst surface.

In order to minimise the quantity of carbon deposited there are two major approaches. The first approach is to increase the amount of oxidant in the inlet stream making the formation of carbon thermodynamically unfavourable[36,50]. In steam reforming this is usually achieved by increasing the steam to carbon ratio. However, elevating the steam content of the fuel intake has repercussions for the lifetime of nickel based anodes as it promotes sintering of the anode material. This sintering effect leads to a reduction in the area available for catalysis. Increasing the steam content also lowers the efficiency of the cell by lowering the Nernst potential, ultimately cancelling out much of the efficiency gains acquired by directly internally reforming fuels[51]. The second approach used to minimise the levels of solid carbon deposited is to alter the anode formulation, either by

doping a nickel based material, altering the fabrication method or by creating a new material. The synthesis and use of different perovskite materials has become a progressive area of research in this area as will be covered in section 1.8.

1.6 Sulphur Poisoning of Nickel Based SOFC Materials

Contamination by sulphur containing compounds has been shown to have an extremely negative effect on the reforming activity of nickel based anode materials[52–55] . This is particularly prevalent when reforming biogas as sulphur containing compounds are inherently present in relatively high levels as a natural side product of the anaerobic digestion process. These compounds are all converted into hydrogen sulphide under the reducing conditions of a SOFC reactor[36], and for this reason any reference to sulphur containing compounds made in this work will be in respect to hydrogen sulphide.

1.6.1.1 Sulphur Poisoning Mechanism

Hydrogen sulphide poisons the anode material of SOFCs by adsorbing on the active nickel sites, reducing the available sites for reformation and hydrogen oxidation. Studies have suggested that there is an inverse linear relationship between the surface coverage of adsorbed sulphur species and adsorbed hydrogen[56]. The mechanism by which this happens is complex and dependant on various conditions. Theoretical studies have predicted that H_2S dissociatively adsorbs to the surface above 300 K[57]. This would suggest a rather simplistic equation with a stoichiometric ratio of nickel to sulphur as proposed by reaction:

$$Ni_{(s)} + H_2S_{(g)} \rightleftharpoons NiS_{(ads)} + H_{2(g)} \qquad \text{(Equation. 1.22)}$$

However, this simple view on the degradation mechanism fails to account for the severe degradation observed when only a few ppm of H_2S are present in the reactant feed. Gong *et al.* suggested that the degradation mechanism caused by sulphur poisoning can follow several different pathways including chemisorption of atomic sulphur to three nickel sites on the surface in a hexagonal-close packed or cubic-closed packed arrangement of atoms. However, if there are any deviations away from these packing systems, atomic sulphur has the potential to chemisorb to less than three sites. Equation 1.23 gives this general reaction [58]. This provides a potential explanation to the high sensitivity of nickel to H_2S as each sulphur atom that dissociates can block three nickel sites. Sasaki *et al.* also found that at the triple phase boundary there was low level formation of liquid Ni_3S_2. This would cause the irreversible loss of the pore structure of the anode[59].

$$Ni(s) + xH_2S(g) \rightleftharpoons Ni_3S_{x(ads)} + xH_{2(g)} \qquad \text{(Equation. 1.23)}$$

It is possible to postulate that several degradation mechanisms exist for sulphur poisoning using past results. Sasaki *et al.* identified an initial drop in performance resulting in a metastable state; this was then followed by a larger, steadier drop in performance. This suggests that as the reaction progresses the predominant reaction for the loss of performance switches.

Reaction temperature has been found to play a key role in the rate and also the extent of performance loss due to sulphur poisoning. At lower SOFC operating temperatures the severity of the performance loss and also the irreversibility of the poisoning are reported to

increase[60,61]. As the temperature is increased the sulphur is much more likely to desorb from the surface and as a result the surface sulphur coverage decreases.

Increasing the concentration of sulphur in the reactant feed increases the formation of nickel sulphide species, as can be seen by a shift to the right hand side of (Equation. 1.23). This in turn increases the performance loss attributed to sulphur poisoning[59,60,62]. At high partial pressures it is possible to form stable, covalently bonded sulphide compounds rather than chemisorbed species. This results in irreversible changes to the morphology and makeup of the anode[63].

1.6.1.2 Recovery of Ni Based Catalysts from Sulphur Poisoning

As with the poisoning of nickel based anodes with sulphur, the recovery of these catalysts when the sulphur is removed from the feed is complex and dependant on the conditions of the reaction. Birss *et al.* observed that at lower SOFC operating temperatures recovery was minimal or non-existent, suggesting that the sulphur had formed a strong chemical bond with the nickel and was not desorbing when removed from the reactant stream[52]. At higher SOFC operating temperatures recovery has been seen to be almost complete with Rasmussen *et al.* remarking that based on their results that the effect of H_2S on the electrochemical conversion can be regarded as reversible[64]. However this statement perhaps does not take into account all reaction conditions. Rasmussen *et al.* also noted that the concentration of hydrogen sulphide used plays a role in the reversibility of the poisoning reaction, as increasing the concentration increases the formation of stable nickel sulphide species, and thus decreases the likelihood of the catalyst being recoverable[64].

Lussier *et al.* noted that that the recovery of nickel based catalysts from sulphur poisoning is not always as simplistic as the reverse of the poisoning mechanism as might be expected. They suggest that water generation plays a key role in oxidising stable sulphur species to form SO_2, and that if this reaction were not present then recovery would not occur due to the stability of sulphur on nickel up to 1500 K[65].

Matsuzaki *et al.* found that the overriding factor in sulphur poisoning, and the recovery from sulphur poisoning, was the equilibrium partial pressure of sulphur species. However it was seen that the time for saturation with sulphur species was seemingly independent of concentration, with this factor being controlled by the reaction temperature[66].

1.6.1.3 Improving Tolerance to Sulphur Poisoning

Without altering the anodic material there are several methods that can used to mitigate the effects of sulphur in the reactant stream, usually involving introducing or increasing the amount of oxidant present. It is relatively difficult to desulphurise nickel due to the strong overlap between the sulphur p-orbital and nickel d-orbital[67,68]. It is possible by introducing a small amount of oxygen or steam into the reactant stream to remove some sulphur species, oxidising adsorbed sulphur to form SO_2[69,70]. This method can be problematic if the oxidant partial pressure is too high, as NiO can then be formed and the losses due to this can displace the benefit of sulphur removal.

Alternatively, hydrogen can be used to remove sulphur from the surface of the anode, which is the reverse of the sulphurisation process. However this reaction is less efficient than the use of an oxidant, particularly as SO_2 is more stable than H_2S so limits the chance

of repoisoning[67,71]. It is possible to increase the resistance of the anode to sulphur poisoning electrochemically by increasing the current drawn from the cell. By doing this the amount of O^{2-} ions passing through the electrolyte to the anode increases, and as a result some ions can react with sulphur species to form SO_2[72].

1.6.1.4 SPARG Process

Although generally considered a deleterious contaminant for the reasons highlighted above, small controlled amounts of sulphur in the reactant stream have been used to inhibit the formation of carbon. This is used industrially and is known as the SPARG (Sulphur PAssivated ReforminG) process. Sulphur passivation has been shown to lower carbon formation by competitively inhibiting both the Boudouard reaction and decomposition of methane reaction as the chemisorption of sulphur is thermodynamically favoured over the formation of carbon-carbon bonds on the catalyst surface[73]. The use of SPARG is a delicate process as it aims to occupy carbon nucleation sites so that reforming may continue, but carbon formation inhibited[74]. However temperature or flow fluctuations could result in the loss of additional active sites leading to loss of reforming activity.

1.7 Doping Ni/YSZ to Improve Tolerance to Carbon Deposition and Sulphur Poisoning

In order to improve the lifetime of Ni/YSZ anodes without making significant sacrifice to reforming activity, conductivity and thermal compatibility with YSZ, doping other metal or metal oxides into the Ni/YSZ structure is potentially an attractive option. There have

been many studies into the advantages and disadvantages of this approach and in this section some of the more popular dopants will be discussed.

1.7.1.1 Cerium(IV) Oxide

Cerium(IV) oxide, otherwise known as ceria, is a rare earth metal oxide with the formula CeO_2. Ceria has a cubic calcium fluorite structure across the temperature range from room temperature to melting point and is a reasonable conductor[75]. Ceria has been used for catalytic applications since its integration into the exhaust systems of cars as part of a three way catalyst system in the early 1980s. It is originally used to accompany the platinum or rhodium that were used to convert excess hydrocarbons, carbon monoxide and nitrogen oxides into water, carbon dioxide and atomic nitrogen. Ceria is used in these systems as it has the capacity to store and release oxygen depending on the conditions[76,77]. The conversion of the pollutants in the exhaust is at its most efficient when the air to pollutant ratio is close to stoichiometric. Ceria is used for when the conditions in the exhaust became reducing in nature, under reducing conditions oxygen can be released due to the Ce^{4+}/Ce^{3+} redox couple[76]. The reduced form of cerium oxide (Ce_2O_3) takes up oxygen when in an oxidative environment, shifting the reaction equilibrium to the right hand side (Equation. 1.24):

$$Ce_2O_3 + [O_2] \rightleftharpoons CeO_2 \qquad \text{(Equation. 1.24)}$$

Ceria maintains a cubic structure with only a minimal lattice volume change when it changes between the 3+ and 4+ state[77]. However O'Hayre *et al.* have suggested that ceria can cause mechanical issues within the fuel cell structure as when it reduces from Ce^{4+} to

Ce^{3+} lattice expansion occurs which can be enough to cause cracks to form in the cermet material[17], The low % of ceria when used as a dopant prevents this from being an issue usually. Ceria is both an n-type semi-conductor and an oxide ion conductor making it a very useful material for both anodes and electrolytes in SOFCs. Ceria is also a significantly better oxygen ion conductor than YSZ, so incorporating ceria into the anode improves the oxygen ion conductivity of the cell[78]. Although a good catalyst for oxidation of hydrogen, it is not a good enough electrical conductor to be used as standalone anode material[79]. For this reason when utilised for the anode component of an SOFC ceria is used as a dopant, and generally not as the bulk material.

Ceria is one of the most researched dopants for use in Ni/YSZ based anode systems and this is mainly because of its oxygen storage capacity (OSC). It has been shown previously that addition of ceria in low amounts results in lowered deposition of carbon when anodes operate with a methane based fuel[15,80–83]. When used for reforming biogas ceria can also dissociate carbon dioxide when in the reduced form, liberating carbon monoxide and resulting in the oxidised Ce^{4+} (Equation. 1.25) [84]. When in the oxidised form, the ceria is then able to release oxygen and remove solid carbon (Equation. 1.26).

$$Ce_2O_3 + CO_2 \rightleftarrows 2CeO_2 + CO \qquad \text{(Equation. 1.25)}$$

$$CeO_2 + C \rightleftarrows Ce_2O_3 + CO \qquad \text{(Equation. 1.26)}$$

The OSC of ceria also means that ceria can prolong the lifetime of SOFC anodes when operating with fuels contaminated with H_2S. By releasing oxygen into the gaseous phase sulphur species adsorbed onto the surface can be oxidised and removed, and as a result ceria has been found to extend the lifetime of Ni/YSZ based anodes significantly[85].

It would appear that ceria should prolong the lifetime of Ni/YSZ anode indefinitely, as long as an oxidative source is present. However this is not found in practise. This may primarily be attributed to the effect of high temperature sintering of the ceria particles over time. Due to the harsh conditions experienced when in a reforming atmosphere it is found that ceria particles join together to form larger particles over time, this reduces the useful surface area of the ceria and as a result less oxygen can be absorbed and thus released[79]. Further to this if the concentration of H_2S is higher than can be oxidised by ceria, the cell will still eventually fail. The ceria will extend the lifetime but not prolonged it infinitely.

1.7.1.2 Copper

Copper has been investigated by many research groups as an alternative for nickel in the anode layer of SOFCs. This is because copper is a poor catalyst for the formation of C-C bonds, and thus the formation of solid carbon is inhibited compared to using a nickel based catalyst. However copper is also a poor catalyst for C-C and C-H bond scission compared to nickel, the crucial reaction for reforming hydrocarbon based fuels[86]. A further issue with copper in SOFC anodes is that copper melts at a much lower temperature than nickel, 1083°C. This promotes a challenge for the manufacture as anodes are often sintered at above 1100°C. As a result copper based anodes must be sintered for longer at lower temperatures to avoid formation of copper agglomerates and loss of reactive area. However lowering the sintering temperature can result in a less connected YSZ substructure increasing the mobility of the copper under reaction conditions[87].

For these reasons copper shows more promise when mixed with nickel as a dopant to form an alloy, as this raises the overall melting point with increased nickel content, and improves catalytic activity towards C-C and C-H scission[46]. Copper is also useful due to it being a very good electronic conductor which is an additional benefit[25].

1.7.1.3 Gold

One of the major advantages of solid oxide fuel cells compared to other types of fuel cell is the use of noble metal free materials resulting in relatively low cost. However doping the anode with small amounts of gold is scientifically interesting due to the reported carbon suppression properties when added to nickel[88]. Thus doping nickel with small amounts of gold may offer significant benefits if the lifetime of the anode is suitably extended. Gold doping has also been seen as a potentially attractive material in nickel based anodes as gold possesses good CO oxidation capabilities even at relatively low temperatures, an important characteristic for an SOFC anode.

When doping with gold at the anode a nickel-gold surface alloy is formed with the gold particles mostly isolated in the bulk nickel[89]. A slight lowering of the catalytic activity of the anode material has been observed by Proctor *et al.*[90], due to the surface having a proportion of less active gold sites lowering the overall nickel surface coverage[91].

One issue with gold as a dopant is its relatively low melting point. SOFCs are often sintered up to as high as1500°C[92–94]. However gold melts at 1064°C, so using a typical firing procedure results in agglomeration of gold rather than a nickel-gold alloy.

1.8 Perovskites and the potential use as catalysts and alternative anode materials for Solid Oxide Fuel Cells

The word 'perovskite' actually refers to a specific mineral but has come to describe materials with the formula ABO_3. In a perovskite the A and B sites are both cations, with the A cation being 12 coordinated and the B cation 6 coordinated. In a perovskite structure the B cation is the smaller of the two cations. In order to balance out the -6 charge of the 3 oxygen ions per unit cell, the A and B cation must theoretically have a combined charge of +6[95]. Perovskite materials have been very extensively researched due to having a wide range of uses including electro-optic modulators, high temperature superconductors, pyro-electric detectors, fuel cell electrodes, photovoltaics, capacitors and optical memories[96–100]. This is due to the perovskite structure being able to accept cations of different sizes and oxidation states which allow the catalytic and electrical properties to be tuned or tailored to purpose[101]. The structure of an ideal perovskite is that of $SrTiO_3$ which has a cubic structure with titanium atoms on the corners, strontium atoms at the centre of the cube and oxygen ions occupying the centres of the cube edges[102].

Perovskites have attracted interest both as catalysts and as anode materials due to possessing many desirable anode characteristics. One of the primary attributes that make perovskites potentially attractive as SOFC anodes is their ability to oxidise hydrocarbons. Perovskites have been shown to possess this characteristic since the early 1970s when Libby *et al.* reported that $Sr_{0.2}La_{0.8}CoO_3$ rivalled platinum for gas phase reactions at a far lower cost and showed potential as a catalyst for use in car exhausts[103]. Since then certain perovskites, such as transition metal substituted $LaBO_3$ (where B = transition metal), have been shown to possess these qualities, but also high temperature and redox stability[104]. Due

to the sheer number of atomic combinations within a perovskite structure, and the evidence that certain combinations possess some, or even to a certain degree all, of the desirable SOFC anode characteristics, perovskites must be considered as a serious contender for SOFC anode materials of the future.

Standard perovskite preparation methods generally involve heating together the oxides or carbonates of the required product ions at temperatures in excess of 1000°C. However, in more recent times alternative methods have been shown to be more controllable, greener and give purer products[96,105,106].

1.8.1 Synthesis of Perovskite Materials

Perovskites form naturally in the earth's mantle in alkaline regions under the intense heat and pressure that this environment provides. In the laboratory the method of synthesis is different. There are several methods for synthesising perovskites including solid state, sol-gel, hydrothermal, combustion and co-precipitation.

1.8.1.1 Solid State Synthesis

Solid state perovskite synthesis is achieved by thoroughly combining the appropriate metal oxide or carbonate precursors and calcining at elevated temperatures. A solid state synthesis method has several unavoidable drawbacks including a wide range of particle sizes, lack of phase homogeneity, fairly low surface area and relatively low purity[104,107]. This usually results in perovskites which do not possess the required catalytic activity for

hydrocarbon oxidation. The required calcination temperature can be in excess of 1200 °C, and multiple cycles of these are also costly requiring a large input of energy.

1.8.1.2 Sol-Gel Synthesis

Sol-gel synthesis is advantageous over traditional solid state synthesis methods as it can provide a homogenous metastable product at lower reaction temperatures[108,109]. Sol-gel synthesis builds up a macro structure by first forming polymers from precursor reagents such as metal salts or alkoxides. The precursors are first formed into a stable solution whereby the metal alkoxide or salt are solvated. Condensation then occurs increasing the viscosity forming a characteristic metal oxide polymer gel [108]. This gel is amorphous in nature and as a result must then be calcined in order to start crystallisation and to expel water and solvents. As with many materials high temperature calcination has drawbacks including sintering which lowers the useful surface area, but can also induce phase changes dependant on the thermal stability of the product in question and can lead to phase separation

.

1.8.1.3 Combustion Synthesis

Combustion synthesis uses a combination of metal salts and organic fuel to create a quick self-sustaining reaction which yields high surface area, small crystal homogenous products. Unlike sol-gel synthesis this reaction is one-step in that no further calcination step is required post-synthesis[110,111]. This means that post reaction crystal growth or agglomeration is limited so a useful surface area for catalysis is maintained. Often hydrated nitrate compounds are the precursors of choice as they contain ample oxidant in

the form of NO_3^-. These nitrates are usually combined with urea and with the application of moderate heat ignition occurs and a self-maintaining reaction results from this[110]. The fuel can be altered from urea in these reactions and Specchia *et al.* found that glycine, alanine and glycerol as fuels yielded higher surface area products than urea[111]. Combustion synthesis is problematic however, particularly in reference to industrial scale reactions. This is due to the formation of NO_x compounds, a family of compounds responsible for the acid rain and smog and heavily regulated by government legislation in the UK and around the globe.

1.8.1.4 Co-Precipitation Synthesis

Co-precipitation synthesis involves the reactant species first being dissolved in a suitable aqueous solution, the reactants are then encouraged *via* an appropriate mechanism to precipitate out of solution as an insoluble product, as opposed to one or more reactant species[112,113]. This immediate formation of an insoluble product means that nucleation, growth and coarsening are happening simultaneously. Co-precipitation is advantageous in its simplicity, speed, and ease of control of particle sizes[113]. However it has been reported that co-precipitation can result in severe, uncontrollable agglomeration of particles that results in an a product that is difficult to sinter[114]. Co-precipitation synthesis has been shown to be an appropriate method for the production of catalysts for oxidation when compared to several other commonly used synthesis routes including sol-gel and solid state synthesis[115].

1.8.1.5 Hydrothermal Synthesis

Hydrothermal synthesis utilises a sealed vessel such as an autoclave or to bring solvents to higher temperatures than their respective boiling points by increasing the autogenous pressure. This is achieved by placing the vessel in an oven at relatively mild temperatures (90-200°C) compared to the temperature used in traditional solid state preparation methods[105,116–118]. Reactions performed under the outlined conditions benefit from the increased solubility of the precursor materials, lowered cost due to the mild temperatures, and also the formation of highly crystalline products unlike sol-gel methods for example[119]. A further advantage to hydrothermal synthesis is the formation of small particle size products, leading to a large surface area and that alterations in pH, pressure and temperature can be used to control morphology[120]. One of the major disadvantages to the use of a hydrothermal method arises from the use of a sealed autoclave; this means that it is impossible to observe the crystal growth *in-situ*.

1.8.2 Catalytic Activity

In section 1.5.2 the requirements of an anode were outlined. Then in subsequent sections the problems that occur when utilising nickel as the catalyst in these systems were discussed. As a result of the drawbacks in using Ni/YSZ and related materials many groups have investigated perovskites as alternative anodes or as a reforming component on an anode, particularly for the reforming of methane reactions, whether that be partial oxidation, steam reforming or dry reforming[121–124]. Whilst some success has been achieved by this approach so far a viable alternative has yet to be found. Some examples of recent studies are briefly discussed below:

Sauvet *et al.*[125] investigated the use of strontium and nickel doped lanthanum chromites for methane steam reforming. The perovskite materials were prepared by solid state reaction with sintering temperatures between 1100 and 1400 °C. The materials produced were shown to possess some catalytic activity towards steam reforming with low levels of solid carbon formation; however the highest methane conversion achieved was less than 30 %.

A series of $LaNi_xFe_{1-x}O_3$ ($0 \leq x \leq 1$) perovskite catalysts were synthesised by Arandiyan *et al.*[123] for partial oxidation and dry reforming of methane. The catalyst was prepared *via* a sol-gel synthesis route with XRD analysis confirming the formation of a single phase perovskites product. However it was noted that as iron doping increased, so did the formation of a solid solution consisting of $LaFeO_3$ and $LaNiO_3$. When tested for catalytic activity, $LaNi_{0.4}Fe_{0.6}O_3$ was found to have the highest activity for both partial oxidation and dry reforming exhibiting a fluctuating methane conversion between 65 and 80 %. These results were however only shown for a time on stream of three hours, and over that three hours the H_2/CO ratio was well below the predicted value of two, and was seen to fall over the course of the reaction. This suggests that there was formation of unwanted total oxidation products that increased over the course of the reaction.

In 2010 Zhan *et al.*[124] published work on a $La_4Sr_8Ti_{12}O_{38-\delta}$ perovskite catalyst synthesised using a sol-gel route. This method yielded a product surface area of 8.2 m^2g^{-1} determined by N_2 adsorption-desorption, and a cubic perovskite type structure. The catalyst was tested for partial oxidation at 950 °C and compared to a nickel based catalyst, and also quartz as the catalyst was contained within quartz wool. It was found that under the tested conditions a nickel based catalyst gave 84.1 % methane conversion with 100 % and 99.8 % hydrogen and carbon monoxide selectivity respectively. The synthesised perovskite had a

substantially lower conversion of methane at 30.1 % despite the elevated reaction temperatures. The perovskite was also less selective for hydrogen and carbon monoxide production, giving a selectivity of 87.8 % and 88.0 % respectively. This was reduced due a slight production of carbon dioxide, once again showing the propensity for perovskites to form total oxidation products.

Lima *et al.* synthesised a range of substituted $La_{1-x}Ce_xNiO_3$ catalysts (x=0, 0.05, 0.1, 0.4, 0.7, 1.0) using an amorphous citrate decomposition method that yielded a citrate precursor, these were then calcined to give perovskite products with BET surface areas ranging from 0.2-2.4 m^2g^{-1} [126]. The XRD profiles for the samples showed that a wide range of different phases were present including dispersed nickel oxide, particularly at higher levels of Ce doping. The samples were then tested for activity for the oxidative steam reforming of ethanol reaction. Many of the materials yielded some level of coupling, with acetaldehyde identified as a prevalent product. The samples did yield a reasonable amount of hydrogen; however there were still large amounts of ethanol remaining in the exhaust stream. It was also found that carbon deposition occurred on all but one of the samples and that increasing the amount of Ce^{3+} cations present decreased the amount of carbon formed.

1.9 Project Aims and Objectives

The aim of this project was to test new perovskite materials for use as, or a catalyst for, the anode layer of SOFCs for directly internally reforming biogas. The performance of the perovskite material will be directly compared with a conventional Ni/YSZ based cermet anode and also ceria doped Ni/YSZ anodes. This can be broken down into several key objectives:

1: Identify new perovskite based materials potentially suitable for reforming biogas.

2: Characterise the perovskite materials using a range of characterisation methods.

3: Evaluate the reforming characteristics in relation to biogas of the perovskite materials over a range of relevant temperatures and reaction conditions.

4: Determine carbon deposition properties of the perovskite material with standard Ni/YSZ anodes and ceria doped Ni/YSZ anodes over a range of operating temperatures and conditions.

5: Determine tolerance to sulphur poisoning of the perovskite materials with standard Ni/YSZ and ceria doped Ni/YSZ anodes

6: Evaluate suitability of the perovskite for use as a solid oxide fuel cell anode for directly internally reforming biogas.

1.10 References

1 P. Weiland, *Appl. Microbiol. Biotechnol.*, 2010, **85**, 849–60.

2 A. Demirbas, *Energy Convers. Manag.*, 2008, **49**, 2106–2116.

3 Y. Li, S. Y. Park and J. Zhu, *Renew. Sustain. Energy Rev.*, 2011, **15**, 821–826.

4 C. S. Lau, A. Tsolakis and M. L. Wyszynski, *Int. J. Hydrogen Energy*, 2010, **36**, 397–404.

5 J. Singh and S. Gu, *Renew. Sustain. Energy Rev.*, 2010, **14**, 1367–1378.

6 S. S. Kapdi, V. K. Vijay, S. K. Rajesh and R. Prasad, *Renew. Energy*, 2005, **30**, 1195–1202.

7 D. Deublein and A. Steinhauser, *Biogas from Waste and Renewable Resources An Introduction*, Wiley-VCH, Weinheim, 2008.

8 J. Z. Staniforth and K. Kendall, *J. Power Sources*, 2000, **86**, 401–403.

9 C. J. Laycock, J. Z. Staniforth and R. M. Ormerod, *Dalt. Trans.*, 2011, **40**, 5494.

10 A. S. A. Al-Fatesh and A. H. Fakeeha, *J. Saudi Chem. Soc.*, 2012, **16**, 55–61.

11 J. Z. Staniforth and R. M. Ormerod, *Catal. Letters*, 2002, **81**, 19–23.

12 Y. Shiratori, T. Ijichi, T. Oshima and K. Sasaki, *Int. J. Hydrogen Energy*, 2010, **35**, 7905–7912.

13 C. J. Laycock, PhD Thesis, Keele University, 2010.

14 A. Lanzini and P. Leone, *Int. J. Hydrogen Energy*, 2010, **35**, 2463–2476.

15 R. M. Ormerod, *Chem. Soc. Rev.*, 2003, **32**, 17–28.

16 EG&G Technical Services, *Fuel Cell Handbook*, U.S. Department of Energy, Morgantown, West Virginia, Seventh Ed., 2004.

17 R. O'Hayre, S.-W. Cha, W. Coella and F. B. Prinz, in *Fuel Cell Fundamentals*, John Wiley & Sons, 2nd edn., 2009.

18 L. Carrette, K. A. Friedrich and U. Stimming, *Fuel Cells*, 2001, **1**, 5–39.

19 G. F. Mclean, T. Niet and N. Djilali, *Int. J. Hydrogen Energy*, 2002, **27**, 507–526.

20 S. Litster and G. McLean, *J. Power Sources*, 2004, **130**, 61–76.

21 M. Farooque and H. C. Maru, *IEEE Xplore*, 2001, **89**, 1819–1829.

22 N. P. Brandon and D. Thompsett, Eds., *Fuel Cells Compendium*, Elsevier, First Edit., 2005.

23 N. E. Kiratzis, P. Connor and J. T. S. Irvine, *J. Electroceramics*, 2009, **24**, 270–287.

24 J. Fergus, *Solid State Ionics*, 2006, **177**, 1529–1541.

25 E. N. Armstrong, J.-W. Park and N. Q. Minh, *Electrochem. Solid-State Lett.*, 2012, **15**, B75–B77.

26 P. K. Cheekatamarla, C. M. Finnerty, Y. Du, J. Jiang, J. Dong, P. G. Dewald and C. R. Robinson, *J. Power Sources*, 2009, **188**, 521–526.

27 T.-J. Huang, C.-Y. Wu and C.-H. Wang, *Fuel Process. Technol.*, 2011, **92**, 1611–1616.

28 M. Lo Faro, V. Antonucci, P. L. Antonucci and A. S. Arico, *Fuel*, 2012, **102**, 554–559.

29 C. J. Laycock, J. Z. Staniforth and R. M. Ormerod, *Electrochem. Soc. Trans.*, 2009, **16**, 177–188.

30 S. C. Singhal and K. Kendall, *High Temperature Solid Oxide Fuel Cells: Fundamentals, Design and Applications*, Elsevier B.V., 2003.

31 Y. Gong, W. Ji, B. Xie and H. Wang, *Solid State Ionics*, 2011, **192**, 505–509.

32 K. Hassmann, *Fuel Cells*, 2001, **1**, 78–84.

33 K. Joon, *J. Power Sources*, 1998, **71**, 12–18.

34 K. V. Kumar, K. Porkodi and F. Rocha, *Catal. Commun.*, 2008, **9**, 82–84.

35 M. A. Pefia, *Appl. Catal. A Gen.*, 1996, **144**, 7–57.

36 J. Sehested, *Catal. Today*, 2006, **111**, 103–110.

37 J. N. Armor, *Appl. Catal. A Gen.*, 2005, **176**, 159–176.

38 K. Takehira, *J. Catal.*, 2002, **207**, 307–316.

39 P. Gangadharan, K. C. Kanchi and H. H. Lou, *Chem. Eng. Res. Des.*, 2012, **90**, 1956–1968.

40 S. Wang, G. Q. M. Lu and G. J. Millar, *Energy Environ. Sci.*, 1996, **10**, 896–904.

41 A. Erdohelyi, *J. Catal.*, 1993, **141**, 287–299.

42 A. Erdohelyi, *J. Catal.*, 1983, **84**, 446–460.

43 S. Mcintosh and R. J. Gorte, *Chem. Rev.*, 2004, **104**, 4845–4865.

44 S. P. Jiang and S. H. Chan, *J. Mater. Sci.*, 2004, **39**, 4405–4439.

45 K. Girona, J. Laurencin, J. Fouletier and F. Lefebvre-Joud, *J. Power Sources*, 2012, **210**, 381–391.

46 H. Kim, C. Lu, W. L. Worrell, J. M. Vohs and R. J. Gorte, *J. Electrochem. Soc.*, 2002, **149**, A247–A250.

47 H. Takahashi, T. Takeguchi, N. Yamamoto, M. Matsuda, E. Kobayashi and W. Ueda, *J. Mol. Catal. A Chem.*, 2011, **350**, 69–74.

48 K. O. Christensen, D. Chen, R. Lødeng and A. Holmen, *Appl. Catal. A Gen.*, 2006, **314**, 9–22.

49 J. A. Moulijn, a. E. Van Diepen and F. Kapteijn, *Appl. Catal. A Gen.*, 2001, **212**, 3–16.

50 X. Ye, S. R. Wang, J. Zhou, F. R. Zeng, H. W. Nie and T. L. Wen, *J. Power Sources*, 2011, **196**, 5499–5502.

51 I. Gavrielatos, V. Drakopoulos and S. Neophytides, *J. Catal.*, 2008, **259**, 75–84.

52 V. Birss, L. Deleebeeck, S. Paulson and T. Smith, *Electrochem. Soc. Trans.*, 2011, **35**, 1445–1454.

53 T. Yoshizumi, S. Taniguchi, Y. Shiratori and K. Sasaki, *J. Electrochem. Soc.*, 2012, **159**, F693–F701.

54 Z. Cheng, S. Zha and M. Liu, *J. Electrochem. Soc.*, 2006, **153**, A1302.

55 J. H. Hirschenhofer, *IEEE Aerosp. Electron. Syst. Mag.*, 1997, **12**, 23–28.

56 L. Deleebeeck, M. Shishkin, P. Addo, S. Paulson, H. Molero, T. Ziegler and V. Birss, *Phys. Chem. Chem. Phys.*, 2014, **16**, 9383–9393.

57 Y. Zhang, Z. Lu, Z. Yang and T. Woo, *J. Power Sources*, 2013, **237**, 128–131.

58 M. Gong, X. Liu, J. Trembly and C. Johnson, *J. Power Sources*, 2007, **168**, 289–298.

59 K. Sasaki, K. Susuki, A. Iyoshi, M. Uchimura, N. Imamura, H. Kusaba, Y. Teraoka, H. Fuchino, K. Tsujimoto, Y. Uchida and N. Jingo, *J. Electrochem. Soc.*, 2006, **153**, A2023–A2029.

60 G. J. Offer, J. Mermelstein, E. Brightman and N. P. Brandon, *J. Am. Ceram. Soc.*, 2009, **92**, 763–780.

61 T. R. Smith, A. Wood and V. I. Birss, *Appl. Catal. A Gen.*, 2009, **354**, 1–7.

62 S. Zha, Z. Cheng and M. Liu, *J. Electrochem. Soc.*, 2007, **154**, B201–B206.

63 T. S. Li, W. G. Wang, T. Chen, H. Miao and C. Xu, *J. Power Sources*, 2010, **195**, 7025–7032.

64 J. F. B. Rasmussen and A. Hagen, *J. Power Sources*, 2009, **191**, 534–541.

65 A. Lussier, S. Sofie, J. Dvorak and Y. U. Idzerda, *Int. J. Hydrogen Energy*, 2008, **33**, 3945–3951.

66 Y. Matsuzaki, *Solid State Ionics*, 2000, **132**, 261–269.

67 J.-H. Wang and M. Liu, *J. Power Sources*, 2008, **176**, 23–30.

68 D. R. Alfonso, A. V. Cugini and D. C. Sorescu, *Catal. Today*, 2005, **99**, 315–322.

69 P. Lohsoontorn, D. J. L. Brett and N. P. Brandon, *J. Power Sources*, 2008, **183**, 232–239.

70 J. Hepola and P. Simell, *Appl. Catal. B Environ.*, 1997, **14**, 305–321.

71 C. H. Bartholomew, G. D. Weatherbee and G. A. Jarvi, *J. Catal.*, 1979, **60**, 257–269.

72 E. Brightman, D. G. Ivey, D. J. L. Brett and N. P. Brandon, *J. Power Sources*, 2011, **196**, 7182–7187.

73 J. Rostrup-Nielsen and L. J. Christiansen, *Concepts of Syngas Manufacture*, Imperial College Press, 2011.

74 T. L. Roussière, PhD Thesis, Karlsruhe Institute of Technology, 2013.

75 M. Mogensen, N. M. Sammes and G. A. Tompsett, *Solid State Ionics*, 2000, **129**, 63–94.

76 P. Fornasiero, M. Graziani and J. Kas, *Catal. Today*, 1999, **50**, 285–298.

77 M. Sugiura, *Catal. Surv. from Asia*, 2003, **7**, 77–87.

78 P. E. Murray, T. Tsai and S. A. Barnett, *Nature*, 1999, **400**, 649–651.

79 A. Trovarelli, Ed., in *Catalysis by Ceria and Related Materials*, Imperial College Press, 1st edn., p. 471.

80 T. Iida, M. Kawano, T. Matsui, R. Kikuchi and K. Eguchi, *J. Electrochem. Soc.*, 2007, **154**, B234–B241.

81 M. Kawano, H. Yoshida, D. Ueno, S. Hashigami and T. Inagaki, *Electrochem. Soc. Trans.*, 2012, **42**, 305–311.

82 C. Sun and U. Stimming, *J. Power Sources*, 2007, **171**, 247–260.

83 W. Z. Zhu and S. C. Deevi, *Mater. Sci. Eng. A*, 2003, **362**, 228–239.

84 C. Xu, J. W. Zondlo, M. Gong, F. Elizalde-Blancas, X. Liu and I. B. Celik, *J. Power Sources*, 2010, **195**, 4583–4592.

85 H. Kurokawa, T. Z. Sholklapper, C. P. Jacobson, L. C. De Jonghe and S. J. Visco, *Electrochem. Solid-State Lett.*, 2007, **10**, B135–B138.

86 S. Islam and J. M. Hill, *J. Power Sources*, 2011, **196**, 5091–5094.

87 A. Atkinson, S. Barnett, R. J. Gorte, J. T. S. Irvine, a J. McEvoy, M. Mogensen, S. C. Singhal and J. Vohs, *Nat. Mater.*, 2004, **3**, 17–27.

88 D. K. Niakolas, J. P. Ouweltjes, G. Rietveld, V. Dracopoulos and S. G. Neophytides, *Int. J. Hydrogen Energy*, 2010, **35**, 7898–7904.

89 S. Zafeiratos and S. Kennou, *Surf. Sci.*, 1999, **443**, 238–244.

90 I. A. Proctor, A. L. Hopkin and R. M. Ormerod, *Ionics (Kiel).*, 2003, **9**, 242–247.

91 N. Triantafyllopoulos and S. Neophytides, *J. Catal.*, 2006, **239**, 187–199.

92 R. D. la T. Garcia, PhD Thesis, University of Trento, 2011.

93 A. Torabi, T. H. Etsell and P. Sarkar, *Solid State Ionics*, 2011, **192**, 372–375.

94 D. M. Bastidas, S. Tao and J. T. S. Irvine, *J. Mater. Chem.*, 2006, **16**, 1603.

95 C. D. Chandler, C. Roger and M. J. Hampden-Smith, *Chem. Rev.*, 1993, **93**, 1205–1241.

96 M. Niederberger, N. Pinna, J. Polleux and M. Antonietti, *Angew. Chemie Int. Ed.*, 2004, **43**, 2270–2273.

97 G. Brunaccini, M. Lofaro, D. Larosa, V. Antonucci and a Arico, *Int. J. Hydrogen Energy*, 2008, **33**, 3150–3152.

98 M. Johnsson and P. Lemmens, *J. Phys. Condens. Matter*, 2008, **20**, 264001.

99 M. Panneerselvam and K. J. Rao, *J. Mater. Chem.*, 2003, **13**, 596–601.

100 K. R. Kendall, C. Navas and J. K. Thomas, 1995, **2738**.

101 S. Suthirakun, S. C. Ammal, G. Xiao, F. Chen, K. Huang, H.-C. zur Loye and A. Heyden, *Solid State Ionics*, 2012, **228**, 37–45.

102 A. S. B. Ruyan and G. Rustum, *Mater. Res. Innov.*, 2000, **4**, 3–26.

103 W. F. Libby, *Science*, 1971, **171**, 499–500.

104 M. A. Peña and J. L. Fierro, *Chem. Rev.*, 2001, **101**, 1981–2017.

105 W. Zheng, W. Pang and G. Meng, *Solid State Ionics*, 1998, **108**, 37–41.

106 D. R. Modeshia, R. J. Darton, S. E. Ashbrook and R. I. Walton, *Chem. Commun. (Camb).*, 2009, **3430**, 68–70.

107 F. Li, X. Yu, L. Chen, H. Pan and X. Xin, *J. Am. Ceram. Soc.*, 2002, **85**, 2177–2180.

108 C. Wang and J. Y. Ying, *Chem. Mater.*, 1999, 3113–3120.

109 A. . Norman and M. . Morris, *J. Mater. Process. Technol.*, 1999, **92-93**, 91–96.

110 A. Civera, M. Pavese, G. Saracco and V. Specchia, *Catal. Today*, 2003, **83**, 199–211.

111 S. Specchia, A. Civera and G. Saracco, *Chem. Eng. Sci.*, 2004, **59**, 5091–5098.

112 S. Tomiyama, R. Takahashi, S. Sato, T. Sodesawa and S. Yoshida, *Appl. Catal. A Gen.*, 2003, **241**, 349–361.

113 B. J. Prakash and S. Buddhudu, *Indian J. Pure Appl. Phys.*, 2012, **50**, 320–324.

114 J. Li, T. Ikegami, J. Lee, T. Mori and Y. Yajima, *J. Eur. Ceram. Soc.*, 2000, **20**, 2395–2405.

115 R. J. Bell, G. J. Millar and J. Drennan, *Solid State Ionics*, 2000, **131**, 211–220.

116 T. Adschiri, Y. Hakuta and K. Arai, *Ind. Eng. Chem. Res.*, 2000, **39**, 4901–4907.

117 M. M. Lencka, E. Nielsen, A. Anderko and R. E. Riman, *Chem. Mater.*, 1997, **9**, 1116–1125.

118 R. J. Darton, S. S. Turner, J. Sloan, M. R. Lees and R. I. Walton, *Cryst. Growth Des.*, 2010, **10**, 3819–3823.

119 B. L. Cushing, V. L. Kolesnichenko and C. J. O'Connor, *Chem. Rev.*, 2004, **104**, 3893–946.

120 T. Adschiri, Y. Hakuta and K. Arai, *Ind. Eng. Chem. Res.*, 2000, **39**, 4901–4907.

121 H. Iwahara, *J. Electrochem. Soc.*, 1990, **137**, 462.

122 T. Hayakawa, S. Suzuki, J. Nakamura, T. Uchijima and S. Hamakawa, *Appl. Catal. A Gen.*, 1999, **183**.

123 H. Arandiyan, J. Li, L. Ma, S. M. Hashemnejad, M. Z. Mirzaei, J. Chen, H. Chang, C. Liu, C. Wang and L. Chen, *J. Ind. Eng. Chem.*, 2012, **18**, 2103–2114.

124 M.-C. Zhan, W.-D. Wang, T.-F. Tian and C.-S. Chen, *Energy & Fuels*, 2010, **24**, 764–771.

125 A. Sauvet, *Solid State Ionics*, 2004, **167**, 1–8.

126 S. M. de Lima, A. M. da Silva, L. O. O. da Costa, J. M. Assaf, L. V. Mattos, R. Sarkari, a. Venugopal and F. B. Noronha, *Appl. Catal. B Environ.*, 2012, **121-122**, 1–9.

2 Experimental

2.1 Catalyst Synthesis

2.1.1 Nickel/yttria stabilised zirconia cermets

The two Ni/YSZ cermet catalyst materials were prepared using a physical mixing method adapted from previous studies within the Ormerod research group[1–4]. This formulation has been empirically derived and optimised for application to tubular SOFCs[3,5]. The undoped catalyst was a 90:10 Ni/YSZ material representing the outer layer component of a dual layer anode SOFC. For the doped cermet a 5 mol% loading relative to the metal content was added.

For the undoped sample 9.50g of NiO (Alfa Aeser, 99.9%), 0.90g of 8 mol% yttria stabilised zirconia (YSZ) (Tosoh, $(ZrO_2)_{0.92}(Y_2O_3)_{0.08}$), 2.90 g 1,1,1 Trichloethene (Sigma Aldrich), 2.20 g of methanol (Lancaster) and 0.20 g of glyceroltrioleate (BDH Chemicals Ltd) were combined, and the resulting slurry was placed into milling containers with 10 10.0 mm x 9.5 mm zirconia milling beads and milled for 3 hours on a ball mill. This resulted in the formation of a homogenous slurry to which 0.15 g of polyvinyl butyral (BDH Chemicals Ltd) was then added as a binding agent and then milled again for 10 minutes. The mixture was then placed into ceramic combustion boats (Fisher Scientific) and fired on a temperature programme of 1 °C min^{-1} up to 500 °C, 5 °C min^{-1} up to 1300 °C with a dwell of 60 minutes in a furnace (Carbolite furnace RHF 1600). The solid anode material formed was then ground up to form a fine powder using a mortar and pestle and placed in an oven set to 60 °C. For the ceria doped sample ceria was added to give 5 mol % relative to nickel in the reduced catalyst.

2.1.2 Perovskites materials

The appropriate quantity of zirconyl chloride ($ZrOCl_2.8H_2O$) (Alfa Aesar, 99.9%), strontium nitrate ($Sr(NO_3)_2$) (Alfa Aesar, 99.97%), nickel nitrate ($Ni(NO_3)_2.6H_2O$) (Sigma Aldrich, 99.99%), sodium hydroxide (NaOH) (Sigma Aldrich, 97.0%) and ultra-pure water (shown in Table) were all measured out into the Teflon liner of a 23ml stainless steel autoclave (Parr).

Table 2.1: Quantity of reagents in perovskite samples

	Mass of Reagent (g)				
	$ZrOCl_2 \cdot 8H_2O$	**$Sr(NO_3)_2$**	**$Ni(NO_3)_2 \cdot 6H_2O$**	**H_2O**	**NaOH**
$SrZrO_3$	2.0000	1.3121	0.0000	8.0000	2.0000
1 mol% Nickel Doped $SrZrO_3$	2.0000	1.2474	0.0903	8.0000	2.0000
2 mol% Nickel Doped $SrZrO_3$	2.0000	1.1828	0.1806	8.0000	2.0000
4 mol% Nickel Doped $SrZrO_3$	2.0000	1.0562	0.3618	8.0000	2.0000
8 mol% Nickel Doped $SrZrO_3$	2.0000	0.7878	0.7224	8.0000	2.0000

The solution was stirred until a homogeneous gel was formed. The Teflon liner was then sealed within the autoclave and the autoclave was placed within furnace set to 180 °C for 72 Hours. The autoclave was then cooled to room temperature. The resulting mixture was removed from the autoclave and placed into a centrifuge tube and topped up to 40cm^3 with ultra-pure water. This was then centrifuged at 3000 rpm for 15 minutes. The supernatant solution was poured away and the tube refilled with ultra-pure water. This was repeated three times. The sample was placed in an over set to 60 °C overnight and then ground up to form a nickel doped strontium zirconate powder. The perovskite materials were then

calcined in ceramic combustion boats (Fisher Scientific) on a temperature programme of 2 °C min^{-1} up to 600 °C to drive off any water or hydroxide ligands that were bound into the structure.

2.2 Characterisation

The nickel based cermets and the perovskite materials were characterised using powder x-ray diffraction (XRD), scanning electron microscopy (SEM), Brunauer-Emmett-Teller (BET) surface area analysis. More detailed discussion of the nickel perovskite catalysts has been previously reported elsewhere[6].

2.2.1 Powder x-ray diffraction

In order to perform powder X-ray diffraction (pXRD) analysis, ground samples were placed into a sample holder with diameter 25 mm and depth of 1 mm. The samples were packed into the holder and a smooth surface achieved by pressing a glass slide against the sample. The sample holder was then placed into the powder x-ray diffractometer (Bruker D8) which used Cu $K\alpha_2$ radiation with a wavelength of 1.5406 Å at 40 KV and 40 mA tube voltage and current respectively. The 2-theta scan range was from 10-70 °, with a step size of 0.07 ° with a dwell of 4 seconds.

The patterns were extracted as raw .EVA files, which were then converted to Excel files for analysis. Peak identification was achieved using the international centre for diffraction data PDF-2 database by referencing peaks to existing powder XRD patterns.

2.2.2 Scanning electron microscopy

In order to prepare samples for imaging *via* scanning electron microscopy (SEM) samples were scattered onto a conductive carbon tab that was mounted onto a 15 mm stainless steel stub (Hitachi). The stub was then mounted to a pedestal within the SEM (Hitachi TM3000) and the imaging chamber was evacuated. Upon evacuation the SEM was focused onto an appropriate area of material under a magnification of 4000x and an image collected.

2.2.3 BET surface area analysis

BET calculations of surface area were performed using an Autosorb-1 series analyser. Firstly an appropriate mass of sample was measured and recorded, typically around 200 mg. This sample was then placed into a 12 mm sample cell and attached to the Autosorb with a Swagelock fitting. The sample was then outgassed to remove contaminants such as water and other volatiles while the temperature of the sample cell was increased on a temperature programme of 1 °C min^{-1} up to 350 °C and held for 2 hours.

The cell was then cooled to -196 °C by submersion in liquid nitrogen. Nitrogen (BOC high purity) was used as the adsorbate gas to determine desorption and adsorption isotherms. The surface area of samples was then determined by the use of AUTOSORB software and BET theory.

2.3 Catalytic testing apparatus

All catalyst testing measurements were on custom built catalyst testing apparatus. The testing equipment consists of inlet feeds for gases (hydrogen, carbon dioxide (in helium),

methane and oxygen, BOC high purity). Each gas was then channelled through stainless steel piping into mass flow controllers (MFCs, Bronkhorst High-Tech EL-Flow Base). The flow rate of each gas was controlled by the mass flow controllers which were pre-calibrated. Each gas can be independently turned on or off. The gases were then directed to a stainless-steel manifold *via* molecular sieve traps which were used to remove any water, where they were combined to achieve the required gas composition and then fed to a quartz reactor tube within a ceramic furnace. The furnace was constructed from two hollowed-out insulating bricks. Each hollow contained resistive wire (nichrome, total resistance 11 Ω/m) wrapped around 6 ceramic tubes (7.0 cm length, 0.6 cm diameter) which formed a heating filament. The temperature was monitored by a K-type thermocouple placed within the furnace and regulated by a Eurotherm 818 temperature controller. The quartz micro-reactor tube (240 mm in length, inner diameter of 5 mm and thickness of 1 mm) holding the anode material (20 mg ± 0.5 mg) between two plugs of quartz wool was secured into the system with Cajon Swagelock fittings to ensure a gas tight seal. Figure 2.1 shows a photograph of the furnace holding the quartz reactor tube.

Figure 2-1 Image of furnace showing thermocouple, heating wire and quartz reactor tube

The product gases were then passed into a heated four-way valve and can then be passed to a vent or to quadrupolar mass spectrometer (MKS Minilab) *via* a heated capillary line (180°C) to ensure gas mobility. Individual mass fragments are then analysed in effectively real time and stored. The test system was constructed in a way that allowed two flows of different gases in parallel. One flow is the reactant line as discussed above and contained a premeasured mix of gases. The second line contained pure helium which could be directed over the furnace when necessary in order to provide an inert atmosphere for the catalyst

pre-reaction. Flow in this line was controlled using a needle valve. A schematic diagram of the test system is shown in Figure 2.2.

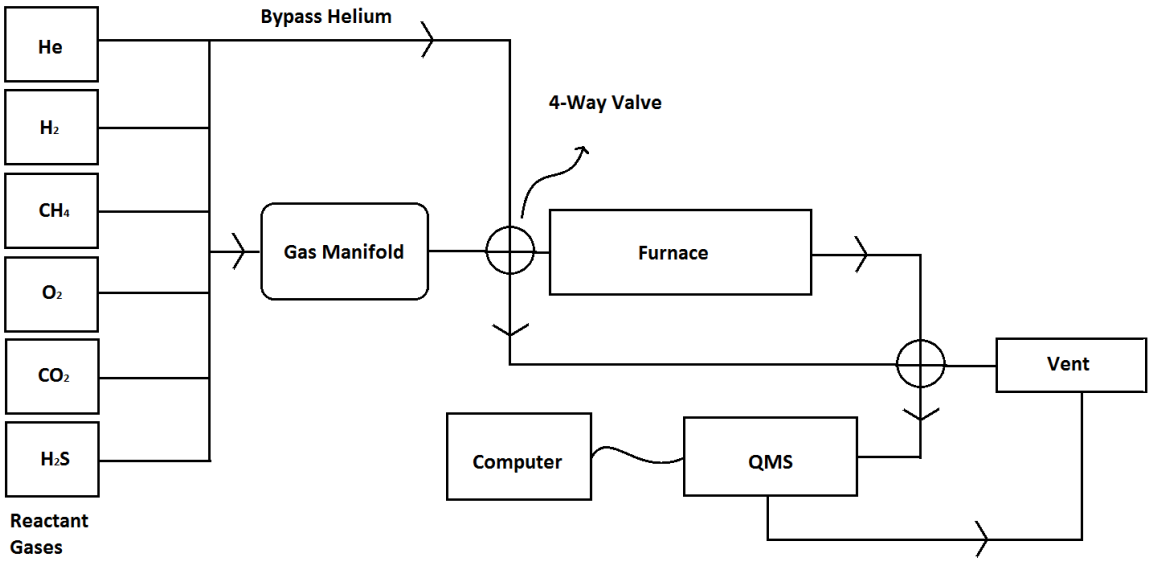

Figure 2.2 Schematic diagram of catalyst test system

2.4 Catalyst Reduction

To activate the nickel cermet and perovskite materials for reaction they were first reduced. Reduction was performed using 10% hydrogen in a helium carrier with a total flow of 20 ml min^{-1}. The temperature programmed reduction (TPR) was performed using a ramp of 10 °C min^{-1} up to 850°C. Upon reaching 850 °C the materials were cooled under hydrogen to prevent reoxidation occurring. Exhaust gases were passed to the QMS and analysed for hydrogen consumption and water production.

TPR profiles were also used as a mechanism for scrutinising catalyst mass and purity from reaction to reaction by intergrsting the peaks for hydrogen consumption and water evolution. TPR is a widely used technique for catalyst characterisation[7–12] with the temperature of the peak maxima/minima being characteristic of the material that is being used and peak area also being used to indicate the amount of reducible material present, or in the case of perovskite materials the number of oxygen vacancies that can be introduced.

2.5 Reforming Reactions

2.5.1 Temperature Programmed Reactions

Preliminary reactions were carried out using a temperature programme (temperature programmed reaction spectroscopy (TPRS)) to elucidate a reaction profile. This TPRS provides a very useful means of comparing and screening different catalysts for different reactions under different reaction conditions. Prior to reaction a TPR (see Section 2.4) was carried out in order to reduce the samples. Upon cooling to room temperature the appropriate reactant gases were measured out through the bypass line, before switching flow to the catalyst material. When the mixture had stabilised, the experiment was performed by applying a temperature programme of 5 °C min^{-1} ramp up to 1000°C. The sample was then cooled under a flow of helium and a temperature programed oxidation (TPO) measurement carried out (see Section 2.6).

2.5.2 Catalyst measurements

After evaluation by TPRS measurements were carried out at different temperatures of interest to evaluate stability and also quantify carbon deposition. These reactions were all carried out after a catalyst reduction (see Section 2.4). After the catalyst had cooled a flow

of pure helium was passed through the quartz reactor tube whilst the appropriate flow rate of reactant gases was established. Once the reactant gases had been set the Eurotherm was programmed to the selected temperature and initial reading of reactant gases was recorded for 5 minutes by the QMS. After the initial readings were recorded the reactant gases were passed over the catalyst and product gases recorded by QMS. At the end of the designated reaction period the product gases are diverted away from the furnace and a flow of pure helium is re-established. The furnace was allowed to cool to room temperature in preparation for temperature programmed oxidation (TPO) (see Section 2.6).

2.6 Temperature Programmed Oxidation

In order to quantify the mass of carbon deposited on the catalyst a temperature programmed oxidation is performed after each reforming reaction. This was achieved using 10% oxygen in a helium carrier with a total flow rate of 20 ml min^{-1} and a temperature programme of 10 °C min^{-1} up to 900 °C from room temperature, carbon deposited on the catalyst is removed in the form of carbon dioxide and carbon monoxide. Product gases are passed to the QMS for analysis. This provides a profile for both carbon monoxide and carbon dioxide, where the integrated area under the curves is proportional to the amount of solid carbon deposited on the surface. A series of calibrations using know masses of carbon were used to create a standard curve which can then be used to quantify a mass of carbon deposited during reactions.

2.7 Sulphur Tolerance Experiments

Reforming experiments were carried out in the presence of H_2S in the same way as the original experiments (see Sections 2.4, 2.5 and 2.6); sulphur was added from a cylinder containing 10 ppm of H_2S in a helium carrier prior to experiment with the other reactant gases. Sulphur concentration was calculated as relative to methane. Each reaction was carried out for 20 hours, in the first set of experiments the concentration of sulphur in the reactant stream was changed; 0 ppm, 5 ppm, 10 ppm or 15 ppm was used and the furnace temperature maintained at 850 °C. In the second set of sulphur tolerance experiments the concentration of sulphur was maintained at 10 ppm and the temperature of the furnace was increased in 50 °C increments from 700 °C to 1000 °C for each experiment. Due to the use of such low concentrations of H_2S any sulphur fragments were undetectable by QMS.

2.7.1 Sulphur Poisoning Recovery

Sulphur recovery experiments were conducted in three different ways and monitored and analysed as in Sections 2.4, 2.5 and 2.6 .

The first experiment type was used to investigate the effect of the concentration of hydrogen sulphide used to poison the catalyst. In this experiment a concentration of 10 ppm, 15 ppm or 20 ppm was used to poison the catalysts at 800 °C for 24 hours. After 24 hours the sulphur feed was removed and the helium flow increased to maintain total flow. The reaction was then allowed to continue for a further 24 hours. For all subsequent recovery reactions poisoning and recovery times were decreased to 22 hours due to logistical difficulties.

The second recovery experiment was designed to show how the temperature of recovery affects the reforming characteristics. In this recovery work the catalyst was poisoned at 800 °C for 22 hours with 10 ppm of hydrogen sulphide. After 22 hours the sulphur was removed from the feed, and balanced with an increase in helium flow rate, the temperature was adjusted to 700°C, 800°C, 850 °C or 900 °C and the reaction continued for a further 24 hours.

The final recovery experiment involved changing the poisoning temperature for the initial 22 hours; 700 °C, 800 °C, 850 °C or 900 °C. This was performed with 10 ppm of sulphur in the reactive line. After 22 hours, the sulphur was removed and the reactive line maintained at 20 ml min^{-1} by a balanced addition of helium and the temperature adjusted to 800°C. The recovery was then monitored for 24 hours before cooling under inert helium flow ready for TPO as in Section 2.6.

2.8 Humidified reactions

To more closely mimic natural sources of biogas, the 2:1 CH_4:CO_2 mixture was humidified with water. To achieve this, after being combined in the manifold, the CH_4:CO_2 mixture was bubbled through water in a saturator (maintained at 0 °C). The flow rate of the gaseous water was 0.13 ml min^{-1} when the total flow rate of the CH_4:CO_2 mixture was 20 ml min^{-1}. The flow rate corresponding to the gaseous water was calculated by plotting $\ln(p/p_0)$ against 1/T, where p and p_0 are the partial pressure of the gas with and without water vapour, respectively, and T is temperature. The values of the standard partial pressure were collected from tables given in the literature and confirmed using the corrected data acquired.

2.9 Powder X-ray diffraction (XRD)

Powder X-ray diffraction, is an important analytical tool for determining the structure of crystalline materials. X-rays are first generated by bombardment of a metallic surface with electrons from a heated filament causing ionisation of K-shell electrons of the metallic atoms, and X-rays are emitted as electrons fall to fill the vacancies[13]. X-rays generated become monochromatic by reflecting the generated beam on to a crystal monchromator. Incoming X-rays are then scattered by the electrons of atoms within the crystal structure and the scattered X-rays are detected depending on the 2θ angle.

Powder XRD can be used to determine several things, firstly determination of crystallinity is clear from the generated pattern. Crystalline materials give a series of sharps peaks due to the structure containing periodically arranged atoms within 3-D space, whereas amorphous materials generate patterns with broad, noisy backgrounds due to the random nature of the arrangement of atoms[14]. Powder X-ray diffraction is primarily used to give information about the crystalline phases or compounds that exist in a sample and this is indicated by the peak position in the powder pattern[15]. It is extremely rare that two different materials present identical patterns.

XRD is used for several purposes when characterising methane reforming catalysts. Firstly, XRD is used to identify the purity of the material that has been produced. Using known XRD patterns it is possible to identify if reactants are still present in the material

that has been manufactured, and if the material has been manufactured and characterised in the past, it is possible to match the produced pattern with historical data. XRD is also used to identify material changes due to the gas phase reaction that has taken place. Deactivation can be caused by changes to the catalyst structure and this can be seen using XRD.

2.10 Scanning Electron Microscopy

Scanning electron microscopy (SEM) is an analytical technique used for analysing the topography and composition of a sample. SEM gives an extremely high magnification image with excellent resolution and a good depth of field.

SEM works by utilising an electron gun, operating in a vacuum, to scan the surface of a sample with a beam of electrons accelerated to an energy between 1 KeV and 40 KeV. These electrons are generated by passing a current through a tungsten filament and are focused towards the sample using electromagnetic lenses. An objective lens is then used to focus the electrons onto the target point of the sample[16]. Without focussing the beam the diameter would be too large to produce an image at high resolution that was sharp enough. Charged plates are used in order to deflect the generated beam onto different parts of the sample so an area can be 'scanned'. As the beam reaches the sample the electrons can either pass through entirely, collide with electrons in the sample causing the release of secondary electrons, or collision can occur between the nucleus of an atom and an electron creating a backscattered electron. Weak secondary electrons are attracted towards a positively charged plate and can be detected to form the SEM image if they are emitted from the surface of the sample.

2.11 Brunauer, Emmett and Teller Theory

By calculating the monomolecular volume of gas that is adsorbed to the surface of a solid at sample at equilibrium it is possible to use Brunauer, Emmett and Teller (BET) theory to calculate the surface area of the sample. This is based upon the theory that on a certain surface, at a set temperature and pressure, a surface will adsorb a set quantity of gas. Thus, by maintaining a set temperature, and altering the pressure it is possible to plot an adsorption/desorption isotherm. Using the isotherm and the BET equation (Equation. 2.1) it is then possible to calculate the surface area of the sample per gram of product measured. By knowing the mass of sample used, it is then possible to calculate the surface area for the material tested.

$$\frac{1}{W\left(\left(\frac{P_0}{P}\right)-1\right)} = \frac{1}{W_m C} + \frac{C-1}{W_m C}\left(\frac{P}{P_0}\right) \qquad \text{(Equation. 2.1)}$$

W = volume of adsorbed gas

W_m = volume of adsorbate gas forming monolayer coverage of sample

P = equilibrium pressure at temperature of adsorption

P_0 = saturation pressure at temperature of adsorption

C = BET constant

2.12 Mass Spectrometry

2.12.1 Background

Mass spectrometry is an analytical technique with many diverse applications, ranging from biochemical analysis to forensic science to monitoring pollution. One of the reasons for this is the very high sensitivity and thus extremely low detection limits that mass spectrometry provides.

Gas analysis *via* mass spectrometry involves several steps; formation of gaseous ions, separation of these ions using a magnetic or electric field and then detection and quantification of ions and ion fragments.

On first entering the mass spectrometer compounds are subjected to bombardment by electrons produced by a heated filament. Some of the electrons collide with the compounds causing electron ionisation as shown by the following reaction:

$$M + e^- \rightleftharpoons M^{\bullet +} + 2e^-$$

If the molecular ion produced has sufficient energy then it can undergo fragmentation resulting in either an ion and a radical, or an ion and another molecule:

$$M^{\bullet +} \rightarrow \text{Even ion}^+ + \text{Radical}^\bullet$$

or

$$M^{\bullet +} \rightarrow \text{Odd ion}^+ + \text{molecule}$$

The ions produced can then be further fragmented. The ions are then separated depending on their mass. In a quadrupolar mass spectrometer, the ions pass through a quadrupole,

which is comprised of four electrically conducting rods which are held in a strict parallel alignment. These rods produce both electric and magnetic fields (two rods for each field type). Each pair of opposing rods are connected to two different generators; a radio frequency (RF) generator and a direct current (dc) generator. The combination of a RF and dc fields in contact with the ions produce a mass filter.

$$a = \frac{8zU}{mr^2\omega^2}$$

$$q = \frac{4zV}{mr^2\omega^2}$$

U = zero to peak voltage of the applied radio frequency

V = applied dc voltage

r = radius of the circle tangent to the inner surface of the quadrupole rods

ω = applied radio frequency

m/z = mass to charge ratio of ion

The rods have an oscillating charge, whereby rods of the same charge are directly opposite each other. The positive ion passing through the quadrupoles will then either be attracted

to the negative pole and discharge upon it, or if this has not happened before the charge of the rod changes, it will then change direction. If the ion continues to pass through the poles without discharging upon them it reaches the detector and is detected on a channeltron detector. Increasing the magnitude of the charge of the poles causes different ion masses to reach the detector[17]. This is an effect based on the mass to charge ratio, with varying mass the ability of the fragment to continue on a stable trajectory varies. Because of this, changing the strength of the field within the quadrupoles changes which ions are able to pass through and hence detected.

2.13 Quadrupolar Mass Spectrometry Data Processing

The quadrupolar mass spectrometer used was an MKS Spectra Mini Lab, which provides signal strength for mass/charge of ion fragments based on partial pressure. To account for non-uniformity in ionisation of different ion fragments a 'sensitivity' value must be determined. Oxygen was chosen to compare the other mass fragments against due to its ionisation ability and limited mass fragmentation pattern. As oxygen was used as a reference gas it was given a sensitivity value of 1. All sensitivity values used are then relative to this value and thus each other. To calculate the relative sensitivity of the instrument to a fragment an applicable fragment is chosen for each gas of interest, the flow rate is then accurately metered using pre-calibrated mass flow meters, as well as a flow of oxygen. The signal intensity is then measured for the chosen fragment and oxygen fragment after the gases signal intensities have settled. This was done for several flow rates. The following formula is used to gain a sensitivity value by recording several values and the average value used:

$$\frac{Flow\ rate\ of\ Oxygen}{Flow\ Rate\ of\ Gas} \times \frac{Reading\ for\ Gas\ Fragment}{Reading\ for\ Oxygen\ Molecular\ ion}$$

$$= Sensitivity\ Relative\ to\ Oxygen$$

In order to convert the raw signal strength data to a meaningful value representing moles of gases, several processing steps were carried out. Firstly the initial helium value was divided by each subsequent value giving an intensity correction factor to account for variances in gas ionisation caused by redox behaviour at the filament. Helium is used to calculate this due to being chemically inert and thus unaffected by the reaction conditions under all circumstances. The next step uses the following formula:

$$\left(\frac{Signal\ Intensity}{Sensitivity}\right) \times\ Intenstiy\ Correction\ Factor$$

$$= Product\ Gases\ Corrected\ Signal\ Strength$$

This formula produces corrected product gases signal strength, which although a value without units, it fundamentally gives the amount of each gas present. To convert this value to moles the ideal gas law is exploited, which states that any gases at the same temperature, pressure and volume have the same number of moles. An average value for methane was taken prior to the gases being passed over the catalyst and all corrected values were then divided by this value. This gives a number of moles for each gas relative to moles of methane. Finally this is plotted against time or temperature to give a reaction profile.

2.14 References

1 C. J. Laycock, J. Z. Staniforth and R. M. Ormerod, *Dalt. Trans.*, 2011, **40**, 5494.

2 C. J. Laycock, J. Z. Staniforth and R. M. Ormerod, *Electrochem. Soc. Trans.*, 2009, **16**, 177–188.

3 C. M. Finnerty, N. J. Coe, R. H. Cunningham and R. M. Ormerod, *Catal. Today*, 1998, **46**, 137–145.

4 C. M. Finnerty and R. M. Ormerod, *J. Power Sources*, 2000, **86**, 390–394.

5 J. Z. Staniforth, PhD Thesis, Keele University, 2000.

6 S. E. Evans, O. J. Good, J. Z. Staniforth, R. M. Ormerod and R. J. Darton, *RSC Adv.*, 2014, **4**, 30816.

7 J. Sfeir, *J. Power Sources*, 2003, **118**, 276–285.

8 T. Désaunay, G. Bonura, V. Chiodo, S. Freni, J.-P. Couzinié, J. Bourgon, a. Ringuedé, F. Labat, C. Adamo and M. Cassir, *J. Catal.*, 2013, **297**, 193–201.

9 C. Guerra, A. Lanzini, P. Leone, M. Santarelli and N. P. Brandon, *J. Power Sources*, 2014, **245**, 154–163.

10 M. Flytzani-Stephanopoulos, T. Zhu and Y. Li, *Catal. Today*, 2000, **62**, 145–158.

11 S. M. de Lima, A. M. da Silva, L. O. O. da Costa, J. M. Assaf, L. V. Mattos, R. Sarkari, A. Venugopal and F. B. Noronha, *Appl. Catal. B Environ.*, 2012, **121-122**, 1–9.

12 J. Sfeir, *J. Catal.*, 2001, **202**, 229–244.

13 A. K. Cheetham and P. Day, Eds., *Solid State Chemistry*, Oxford Science Publications, Oxford, 1987.

14 H. Lipson, *Contemp. Phys.*, 1979, **20**, 87–88.

15 A. R. West, *Basic Solid State Chemistry*, Wiley-VCH, 2nd edn., 1988.

16 J. I. Goldstein, D. E. Newbury, P. Echlin, D. C. Joy, C. E. Lyman, E. Lifshin, L. Sawyer and J. R. Michael, *Scanning Electron Microscopy and X-ray Microanalysis*, Springer US, Boston, MA, 2003.

17 E. de Hoffman and V. Stroobant, *Mass Spectrometry Principles and Applications*, 2008.

3. Sample Characterisation

Supported nickel has been shown to be one of the best catalysts for reforming methane, particularly when cost considerations are taken into place, however supported nickel is highly susceptible to poisoning mechanisms involving carbon formation, nickel agglomeration and sulphur deactivation[1,2]. In chapter 1 perovskites were shown to have potential as anode materials for DIR-SOFC, as they potentially possess a wide range of desirable properties such as increased resistance to carbon formation[3–5] , sulphur resistance[6], redox stability[5] as well as been able to accept a wide range of elements into the structure *via* partial substitution at either the A or B site[7–11]. Nickel doped perovskite material could potentially possess both the activity of a supported nickel catalyst and the stability and resistance of a perovskite catalyst.

Hydrothermal synthesis was the chosen synthesis route as it generally yields very small particle sizes[12–14] and it has been shown in previous research that perovskites with the smallest particle size have the greatest catalytic activity towards the reforming of methane[15]. Hydrothermal synthesis is also seen as a more environmentally friendly technique due to the low temperatures required for reaction. As the theorised material has not been previously reported in the literature the use of hydrothermal synthesis gave the greatest chance of successfully synthesising a single phase material. Hydrothermal synthesis has been previously shown to produce materials or phases that cannot be synthesised by other techniques[16].

Doped strontium titanates ($SrTiO_3$) have been thoroughly researched as alternative anodes for SOFCs in the literature[17–20] with varying levels of success. However, to maintain the

maximum chance of thermal compatibility with the yttria stabilised zirconia (YSZ) electrolyte component, titanium was replaced with zirconium as the B-site cation. Zirconium was also chosen as it was believed a higher nickel loading could be achieved than was reported for the equivalent titanates due to the size increase from the titanium ion to zirconium ion. A range of nickel doping from 1 mol% to 8 mol% was used to evaluate the optimum nickel doping level for catalytic activity whilst maintaining phase purity. Ni/YSZ and ceria doped Ni/YSZ were chosen as catalysts for comparison due to their ubiquitous nature as catalysts for SOFCs and their use as conventional anode materials.

3.1 Powder X-Ray Diffraction

Powder X-ray diffraction was carried out on the nickel cermet materials, and also the cermet precursors, as a way of evaluating that no impurities were introduced into the samples and to show that no new phases were formed. Figure 3-1 shows a comparison between untreated NiO/YSZ prepared as discussed in chapter 2, and the nickel oxide and yttria stabilised zirconia reagents that were used to synthesise it. The XRD pattern shows that the product was more crystalline than the precursors that were used in the synthesis, indicated by the intensity. This is a result of the high temperature calcination used in the synthesis. There was no formation of any undesired impurities indicated by all peaks present corresponding to one of the precursor reagents.

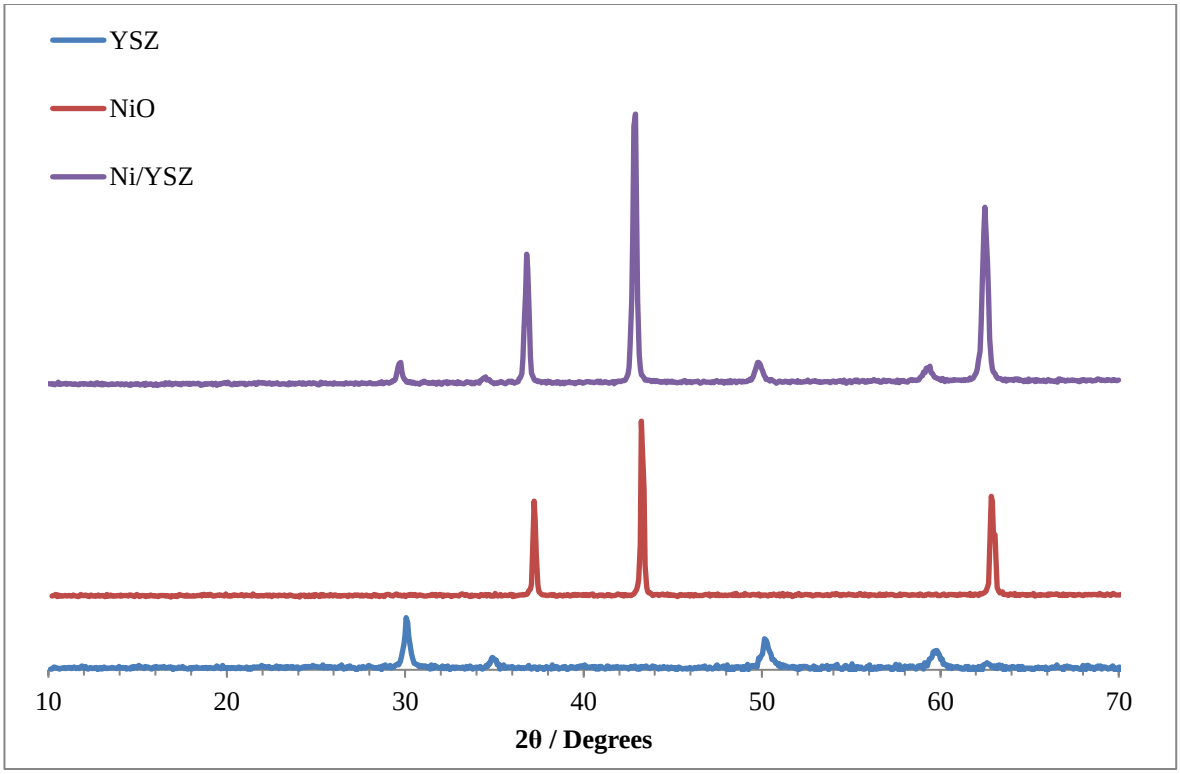

Figure 3-1 Comparison of the XRD patterns for Ni/YSZ (unreduced) and the nickel oxide and yttria stabilised zirconia precursors that were used to synthesise it.

Figure 3-2 shows a comparison between 5% ceria doped Ni/YSZ, prepared *via* the method discussed in chapter 2, and the major precursors that were used to synthesise it. As with Figure 3-1 the increased crystallinity caused by the high temperature calcination can be seen by the decrease in peak width, this is particularly apparent in the peaks that correspond to NiO (37°, 43°and 63° 2θ).

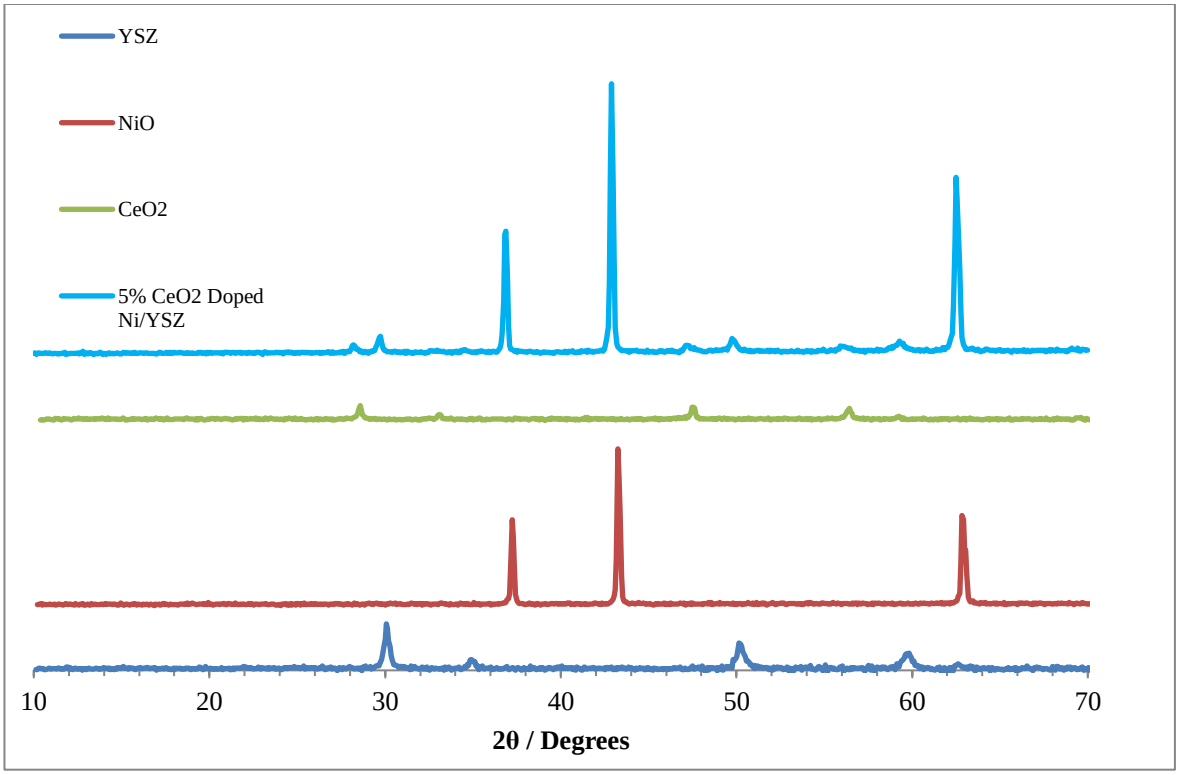

Figure 3-2 Comparison of the XRD patterns for 5% Ceria doped Ni/YSZ (unreduced) and the nickel oxide, yttria stabilised zirconia and ceria precursors that were used to synthesise it

XRD analysis was also used to characterise the perovskite materials to establish phase purity, crystallinity and as a way of identifying any precursor impurities. Figure 3-3 shows powder XRD patterns for a $SrZrO_3$ sample, and then with varying mole percentages of nickel doped into the structure. In all of the XRD patterns, shown in Figure 3-3, there are no discernible impurity peaks that can be observed, either from precursors or possible side products. Although it is possible that impurities still reside in these samples, the level could be very small to be detected using in-house XRD instruments or are amorphous rather than crystalline.

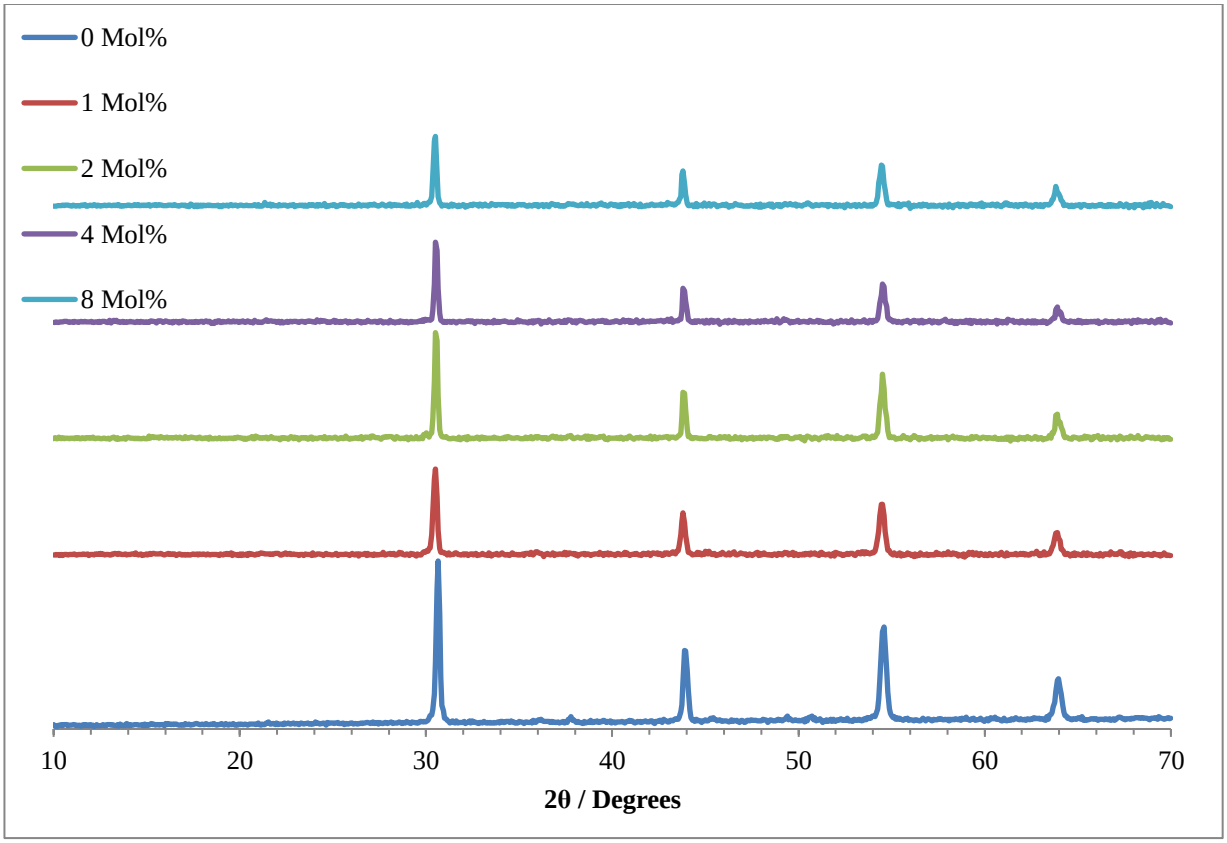

Figure 3-3 XRD patterns of $SrZrO_3$ doped with varying mole percentages of nickel from 1-8%

The XRD pattern for the as-prepared sample of $SrZrO_3$ shows very good agreement with the pattern found in the literature (a = 5.7862 Å b = 5.8151 Å c = 8.1960 Å) Analysis of the powder XRD pattern for the 4 mol% doped sample (Figure 3-4) shows the material to be orthorhombic (Pbnm) with unit cell parameters of a = 5.7948(7) Å, b = 5.8014(2) Å and c = 8.1985 Å(3). This pattern shows no indication of zirconium oxide impurities which would be expected if the nickel had doped onto the B-site rather than the A-site as planned by the synthesis, this was also confirmed by elemental analysis which agreed with the expected formula of $Ni_{0.2}Sr_{0.8}ZrO_3$. Each subsequent nickel doped sample shows the same pattern, suggesting that there is no significant change in the material.

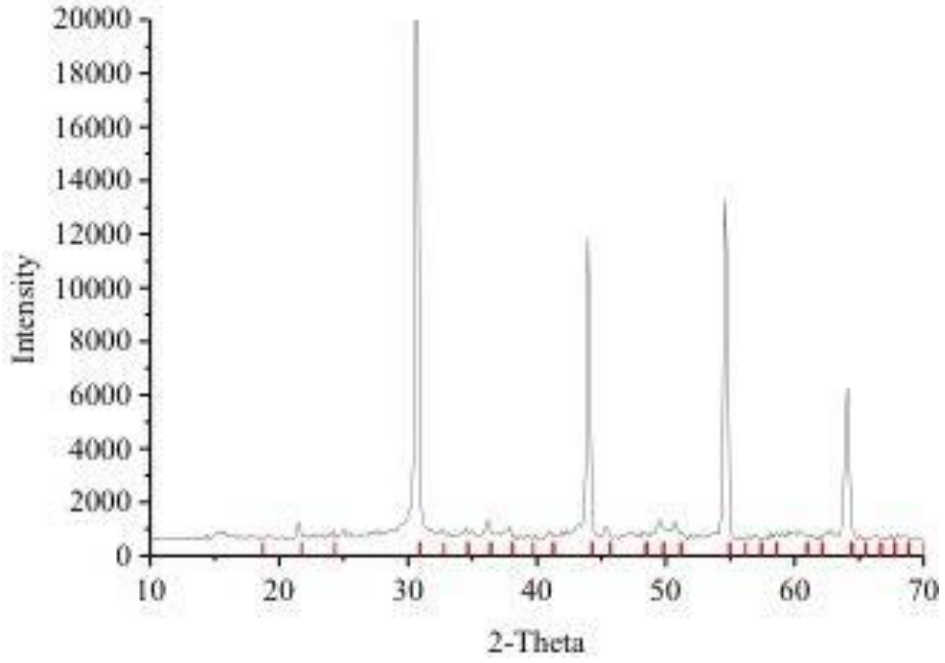

Figure 3-4 XRD pattern of 4 mol% $SrZrO_3$ and corresponding tick marks for orthorhombic $SrZrO_3$

3.2 Scanning Electron Microscopy

Scanning electron microscope images were obtained by first mounting a small amount of sample onto carbon tabs that were fixed to Hitachi metallic stubs, all images were collected on a Hitachi TM3000 electron microscope using a magnification of x4000.

The SEM images obtained, as shown in Figure 3-5 to Figure 3-8 exhibit a trend between crystallite size, and the amount of nickel that was doped into the structure, with the largest crystals formed in the undoped $SrZrO_3$ sample (Figure 3-5). The morphology appears to be mainly assemblies of spherical or icosahedron particles with each sphere being composed of smaller spheres. Some of the 'spheres' appear to be in the process of still being formed and this may give some insight into the growth mechanism. The images show what appears to be one crystal type with the main difference between individual crystals being

the size. Unfortunately, it was not possible to quantify the size of the smallest 'spheres' using this technique and as a result, however analysis of the powder XRD peak widths indicate nanoscale particles.

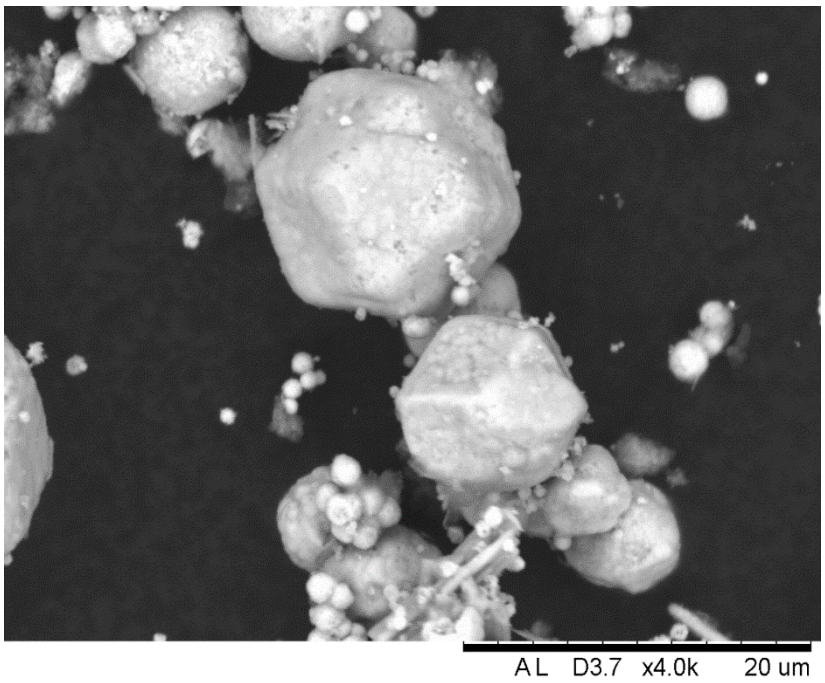

Figure 3-5 SEM image of $SrZrO_3$ at 4000x magnification

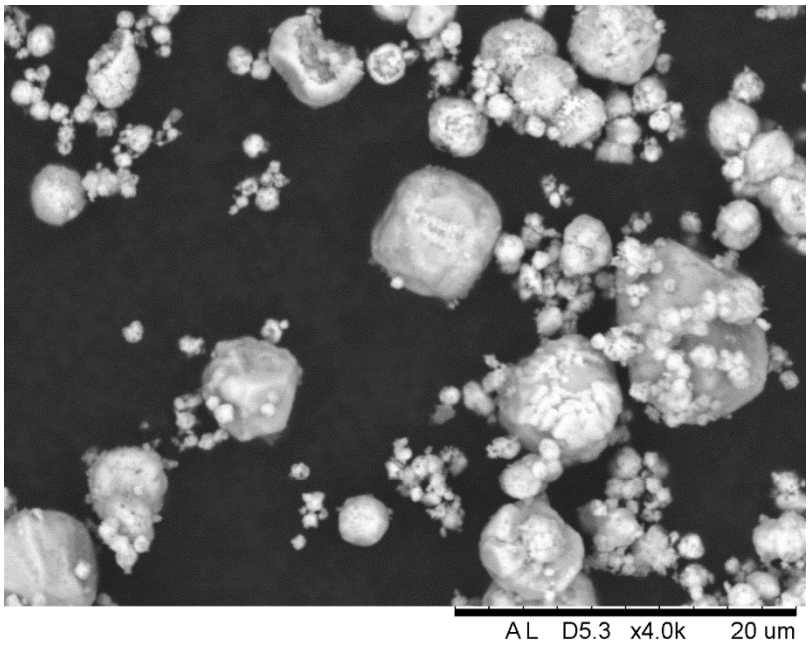

Figure 3-4 SEM image of 1% Ni doped $SrZrO_3$ at 4000x magnification

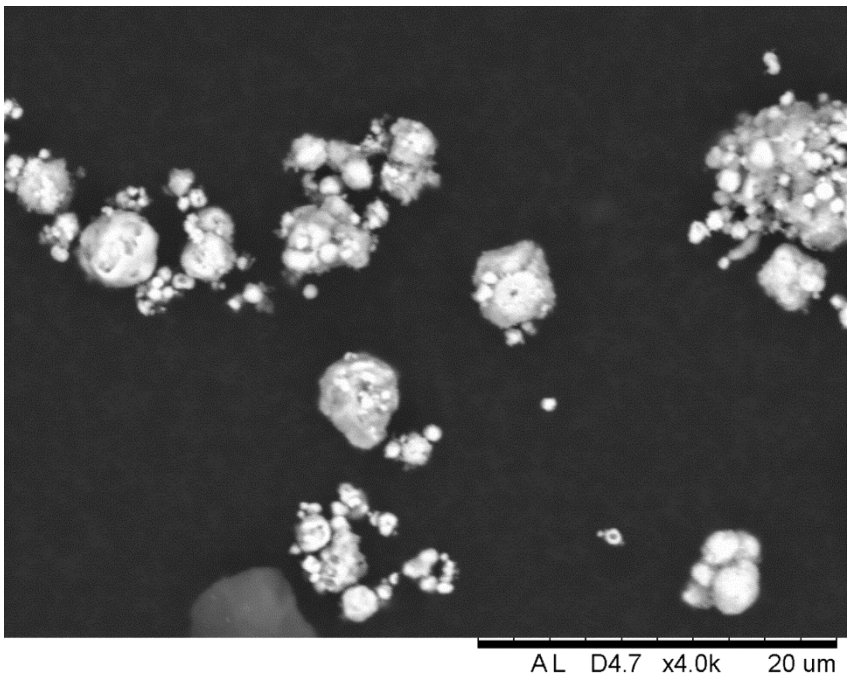

Figure 3-6 SEM image of 2 mol% Ni doped $SrZrO_3$ at 4000x magnification

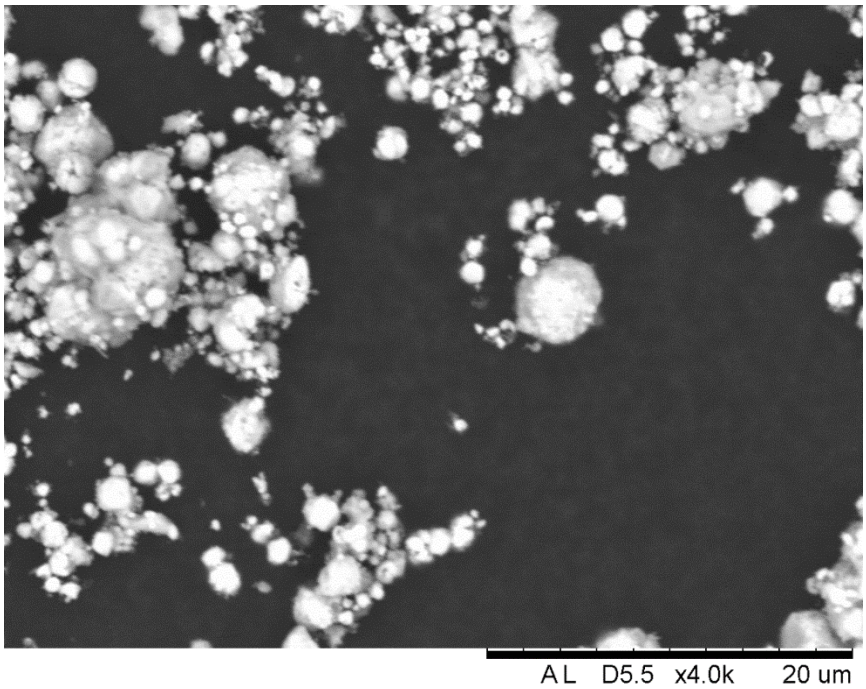

Figure 3-7 SEM image of 4 mol% Ni doped $SrZrO_3$ at 4000x magnification

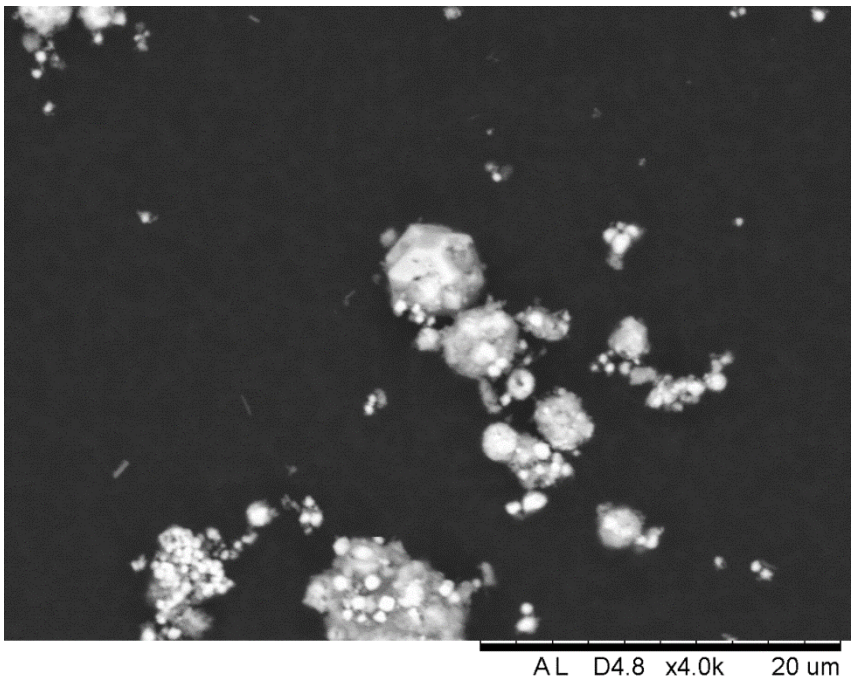

Figure 3-8 SEM image of 8 mol% Ni Doped $SrZrO_3$ at 4000x magnification

3.3 Brunauer–Emmett–Teller (BET) Analysis

After calcination at 600 °C for one hour, samples were outgassed at 350 °C to remove any volatile contaminants and then an adsorption and desorption isotherm collected as described in the experimental section. BET calculations were then carried out using AUTOSORB software in order to define the sample surface area. The results are presented in *Table 1*.

Table 3.1 Surface area of perovskite materials

Sample	**Surface area / m^2g^{-1}**
0 mol% Ni doped $SrZrO_3$	2
1 mol% Ni doped $SrZrO_3$	3
2 mol% Ni doped $SrZrO_3$	19
4 mol% Ni doped $SrZrO_3$	48
8 mol% Ni doped $SrZrO_3$	52
Ni/YSZ	1
5% Ceria doped Ni/YSZ	2

BET analysis showed a trend between the amount of nickel that was doped into the $SrZrO_3$ structure and the surface area calculated by BET, with the largest surface area being observed as the 8 mol% Ni doped $SrZrO_3$ ($Ni_{0.4}Sr_{0.6}ZrO_3$). This was in agreement with SEM analysis, which indicated that the largest particles were in the $SrZrO_3$ undoped sample and the smallest in the 8 mol% Ni doped $SrZrO_3$. The Ni doped perovskites all showed a far higher surface area to that of the cermet materials prepared by a physical mixing method as was predicted.

3.4 Temperature Programmed Reduction.

Temperature programmed reduction measurements were performed prior to all catalytic testing in order to prepare both the cermet samples and the perovskite samples for reaction as described in the experimental section. In the case of the cermets, the NiO in the sample needed to be reduced to form nickel. For the perovskites it is expected that reduction would introduce oxygen vacancies into the structure in the areas where nickel atoms have

been doped in. As well as activating the samples catalytically, TPR can also be used as a form of semi-quantitative characterisation, giving information about the temperature that reduction occurs, and the peak area giving direct indication of the amount of reduction occurring. Figure 3-9 shows the reduction profiles for the five perovskite samples; $SrZrO_3$, 1 mol%, 2 mol%, 4 mol% and 8 mol% Ni doped $SrZrO_3$. The water evolution observed shows that doping nickel into the structure gives rise to a reducible product. The figure shows how increasing the nickel doping increases the area of the reduction peak, with the T_{max} of reduction occurring at ~ 400 °C for all four of the nickel doped samples. The 0 mol% sample does show an apparent reduction peak. However upon closer inspection this can be attributed to the formation of water on the surface of the catalyst, utilising the little oxygen that is in the reactor from unavoidable leaks.

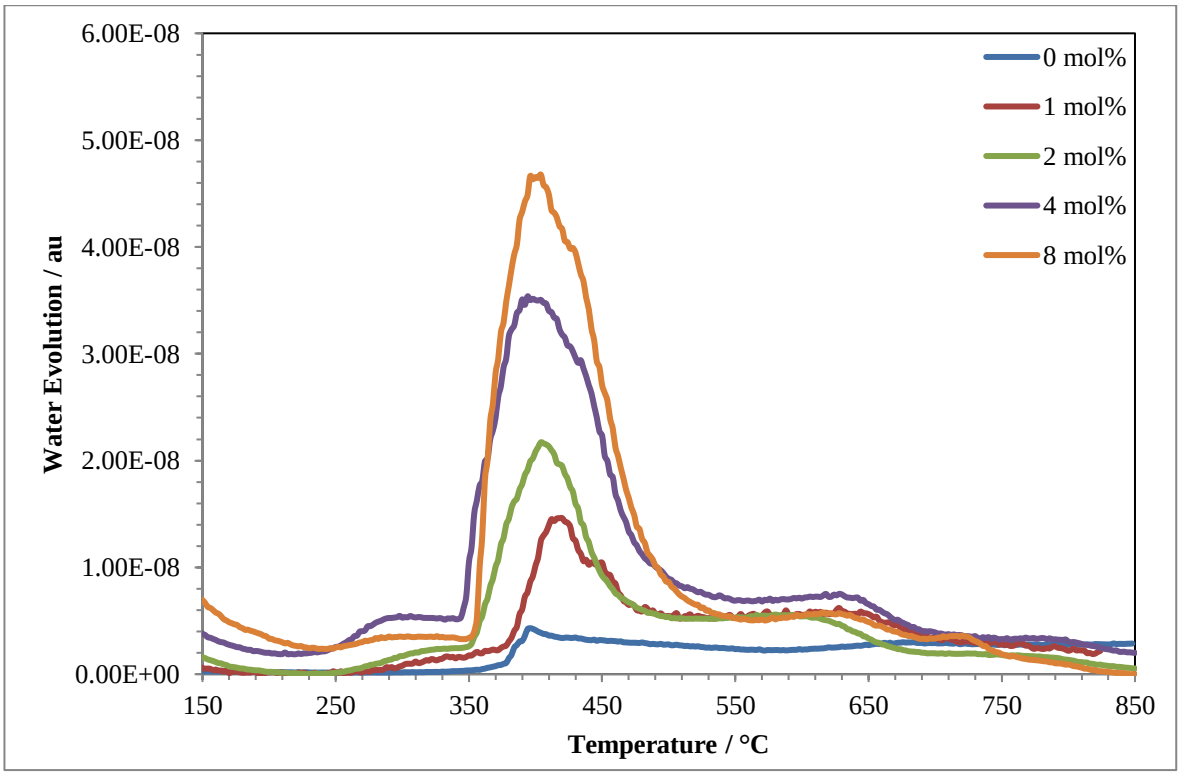

Figure 3-9 Water evolution resulting from temperature controlled reduction of $SrZrO_3$ and various nickel doped $SrZrO_3$ samples

3.5 Discussion

Powder XRD showed that the high temperature calcination of the cermet formulation yielded a crystalline product that was free of impurities that were detectable by XRD analysis. In reference to the perovskite materials, XRD analysis was used to prove that a crystalline perovskite product was formed for all of the nickel doped samples, and that all of these samples were free from detectable impurities. Increasing the nickel doping did not display an increase in peak area for any of the peaks, and thus was not a useful tool for interpreting the level of nickel that had been doped into the structure.

SEM analysis showed that the perovskite samples were comprised primarily of spherical or icosahedron particles that in some cases appeared to still be in the formation stages when the reaction was ceased indicating that particle formation was not complete. In agreement with BET analysis it was shown that there is a relationship between the size of the particles formed and the nickel doping levels. SEM and BET showed that smaller particles were formed at the higher nickel doping levels.

TPR analysis was used to indicate that the formed perovskite product was reducible, seen by the formation of water, and that as the nickel loading increased, the amount of water liberated during TPR increased, as was indicated by the size of the TPR peak.

3.6 References

1 P. Gangadharan, K. C. Kanchi and H. H. Lou, *Chem. Eng. Res. Des.*, 2012, **90**, 1956–1968.

2 C. Sun and U. Stimming, *J. Power Sources*, 2007, **171**, 247–260.

3 H. Li, Y. Tian, Z. Wang, F. Qie and Y. Li, *RSC Adv.*, 2012, **2**, 3857.

4 T. Hayakawa, S. Suzuki, J. Nakamura, T. Uchijima and S. Hamakawa, *Appl. Catal. A Gen.*, 1999, **183**.

5 G. Valderrama, C. Urbina de Navarro and M. R. Goldwasser, *J. Power Sources*, 2013, **234**, 31–37.

6 X. Zhu, Q. Zhong, D. Xu, H. Yan and W. Tan, *J. Alloys Compd.*, 2013, **555**, 169–175.

7 A. S. B. Ruyan and G. Rustum, *Mater. Res. Innov.*, 2000, **4**, 3–26.

8 H. Iwahara, *J. Electrochem. Soc.*, 1990, **137**, 462.

9 M. Johnsson and P. Lemmens, *J. Phys. Condens. Matter*, 2008, **20**, 264001.

10 X. Yan, Q. Huang, B. Li, X. Xu, Y. Chen, S. Zhu and S. Shen, *J. Ind. Eng. Chem.*, 2013, **19**, 561–565.

11 X. Li, H. Zhao, N. Xu, X. Zhou, C. Zhang and N. Chen, *Int. J. Hydrogen Energy*, 2009, **34**, 6407–6414.

12 T. Adschiri, Y. Hakuta and K. Arai, *Ind. Eng. Chem. Res.*, 2000, **39**, 4901–4907.

13 B. Liu and H. C. Zeng, *J. Am. Chem. Soc.*, 2003, **125**, 4430–1.

14 R. J. Darton, S. S. Turner, J. Sloan, M. R. Lees and R. I. Walton, *Cryst. Growth Des.*, 2010, **10**, 3819–3823.

15 H.-C. Yu, K.-Z. Fung, T.-C. Guo and W.-L. Chang, *Electrochim. Acta*, 2004, **50**, 811–816.

16 D. R. Modeshia, R. J. Darton, S. E. Ashbrook and R. I. Walton, *Chem. Commun. (Camb).*, 2009, **3430**, 68–70.

17 F. Gao, H. Zhao, X. Li, Y. Cheng, X. Zhou and F. Cui, *J. Power Sources*, 2008, **185**, 26–31.

18 O. A. Marina, N. L. Canfield and J. W. Stevenson, *Solid State Ionics*, 2002, **149**, 21–28.

19 D. P. Fagg, V. V Kharton, J. R. Frade and A. A. L. Ferreira, *Solid State Ionics*, 2003, **156**, 45–57.

20 M.-C. Zhan, W.-D. Wang, T.-F. Tian and C.-S. Chen, *Energy & Fuels*, 2010, **24**, 764–771.

4 Catalyst Selection

4.1 Catalyst Selection Introduction

In Chapter 3 it was shown by XRD and SEM that nickel can be doped into the $SrZrO_3$ structure by up to 8 mol% without impurities being observed[1]. However, to gain a detailed insight into the reforming characteristics of the nickel doped perovskite, a single composition was selected and studied over a range of reforming conditions. This composition was compared with Ni/YSZ and ceria doped Ni/YSZ cermets over a wide range of reforming conditions to gain an understanding as to the performance of the material in reference to existing catalysts. This sample was chosen based on the characteristics of the methane rich dry reforming reaction and on the carbon deposition. A 2:1 ratio of methane to carbon dioxide was used as it represents the harshest conditions for carbon formation within the range for naturally produced biogas. This is because methane is in excess meaning that the formation of solid a carbon on the catalyst surface is likely due to the elevated reaction temperature. Once a catalyst has been selected using these conditions, the effect that changing this ratio has will be investigated in Section 5.5. The dry reforming reaction conditions used were methane rich as described in Section 2.5.

4.2 Temperature Programmed Biogas Reaction

Temperature programmed reaction (TPRx) of biogas was carried out over Ni/YSZ, 5% ceria doped Ni/YSZ, $SrZrO_3$, 1% Ni doped $SrZrO_3$, 2% Ni doped $SrZrO_3$, 4% Ni doped $SrZrO_3$ and 8% Ni doped $SrZrO_3$. Reactions were followed by QMS and converted to mole equivalent of methane.

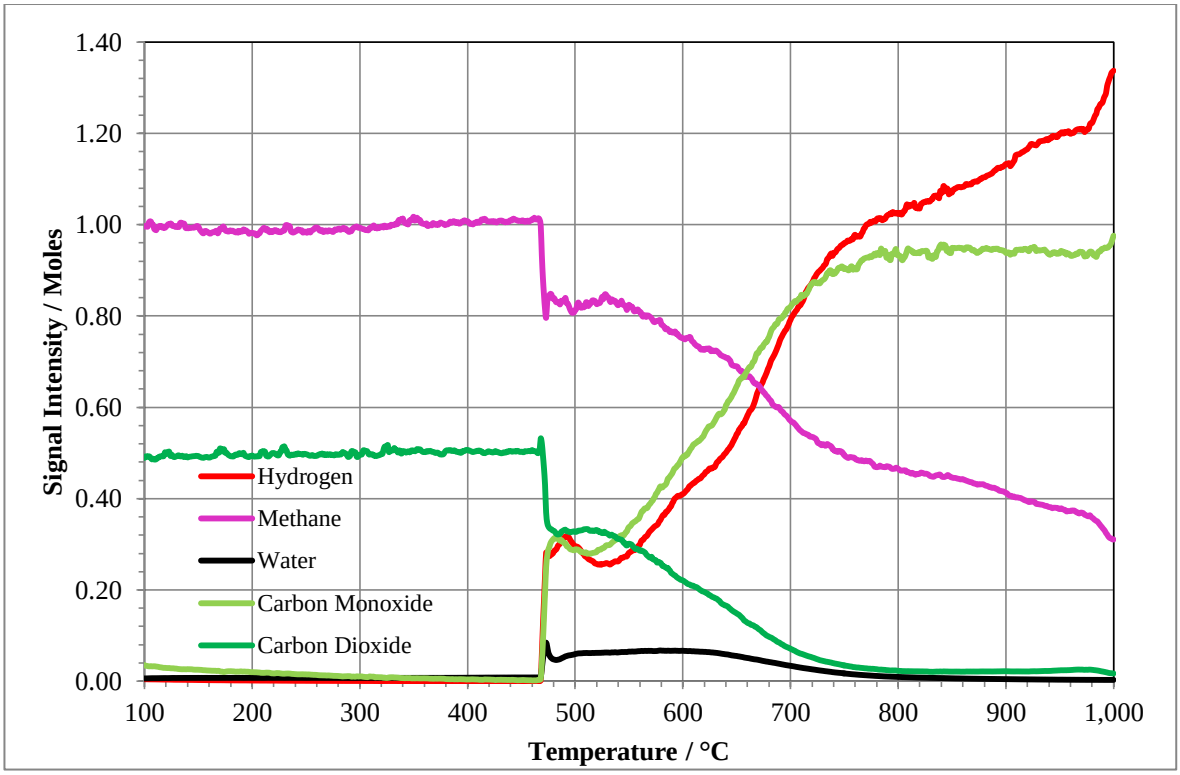

Figure 4-1 Reaction profile for temperature programmed reaction of a 2:1CH_4/CO_2 mixture passed over Ni/YSZ

Figure 4-1 shows the reaction profile for a 2:1 mixture of methane and carbon dioxide passed over the standard Ni/YSZ anode material. Reaction starts abruptly at ~470 °C, with a sharp drop in methane and carbon dioxide matched by production of carbon monoxide and hydrogen. Up to ~800 °C there is also a low level production of water, caused by the reaction between hydrogen and unreacted carbon dioxide *via* the reverse water gas shift reaction (Equation. 1.19). After the carbon dioxide level becomes depleted, the composition of the synthesis gas formed changes and became more hydrogen rich. This is caused by the catalytic decomposition of methane reaction (Equation. 1.21), which continues to increase with increasing reaction temperature.

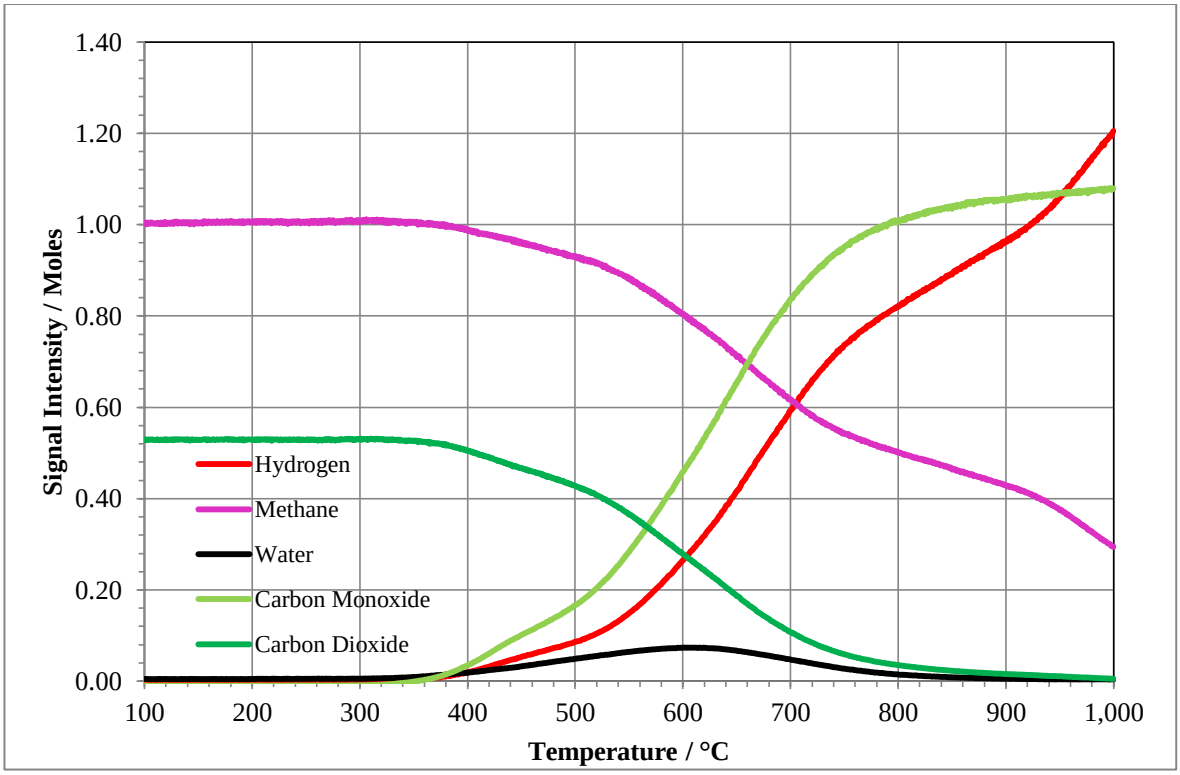

Figure 4-2 Reaction profile for temperature programmed reaction of a 2:1CH_4/CO_2 mixture passed over 5% ceria doped Ni/YSZ

The addition of 5% ceria to the Ni/YSZ (Figure 4-2) lowers the temperature that reforming begins at by around 100 °C compared to undoped Ni/YSZ, with a steadier initial increase in activity. As with Ni/YSZ, when carbon dioxide is available, the reverse water gas shift reaction occurs, resulting in water formation[2,3]. Above 850 °C thermal decomposition of methane occurs resulting in the formation of hydrogen rich synthesis gas. As a result the formation of solid carbon on the catalyst surface is likely which will be discussed in more detail in Section 5.4.1 [4].

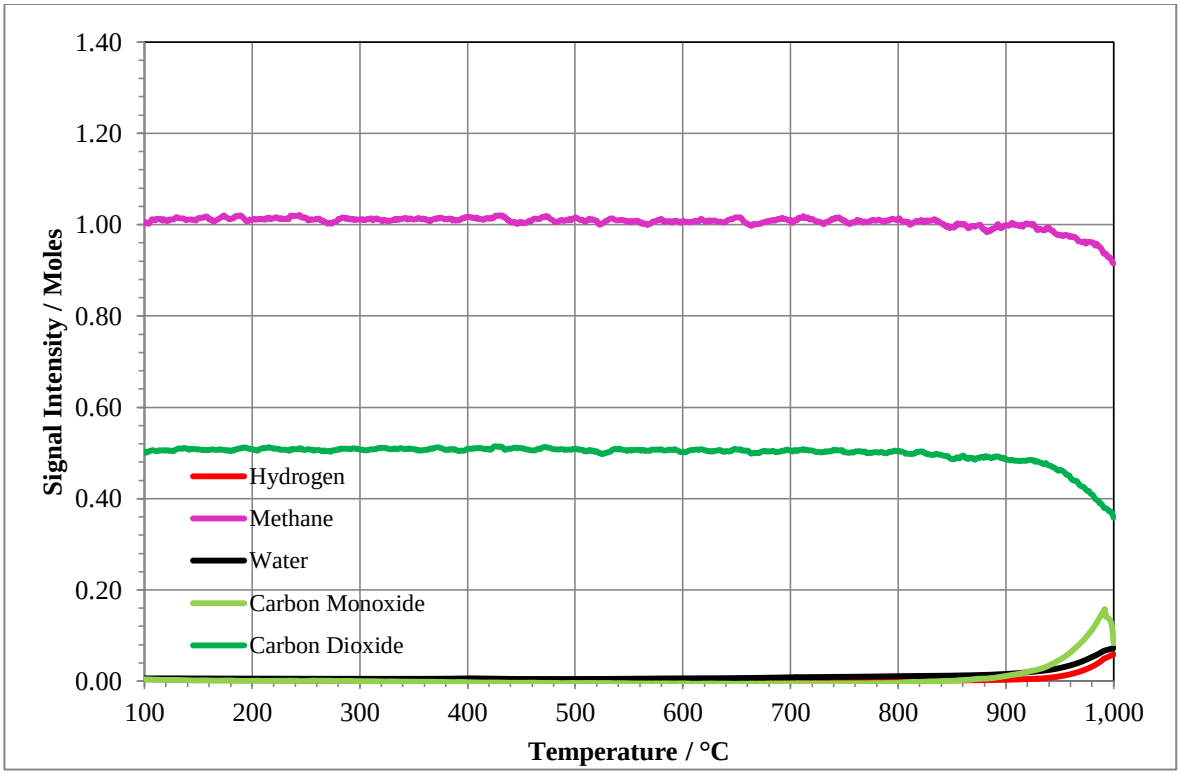

Figure 4-3 Reaction profile for temperature programmed reaction of a 2:1CH_4/CO_2 mixture passed over $SrZrO_3$

The temperature programmed reaction (TPRx) of a 2:1 CH_4/CO_2 simulated biogas mixture over $SrZrO_3$ is shown in Figure 4-3. The profile shows that no reaction occurs until ~690 °C, at which point water starts to form. This is the only product seen until ~820 °C. Above ~820 °C some carbon monoxide and hydrogen are formed, however, this formation is negligible even at 1000 °C.

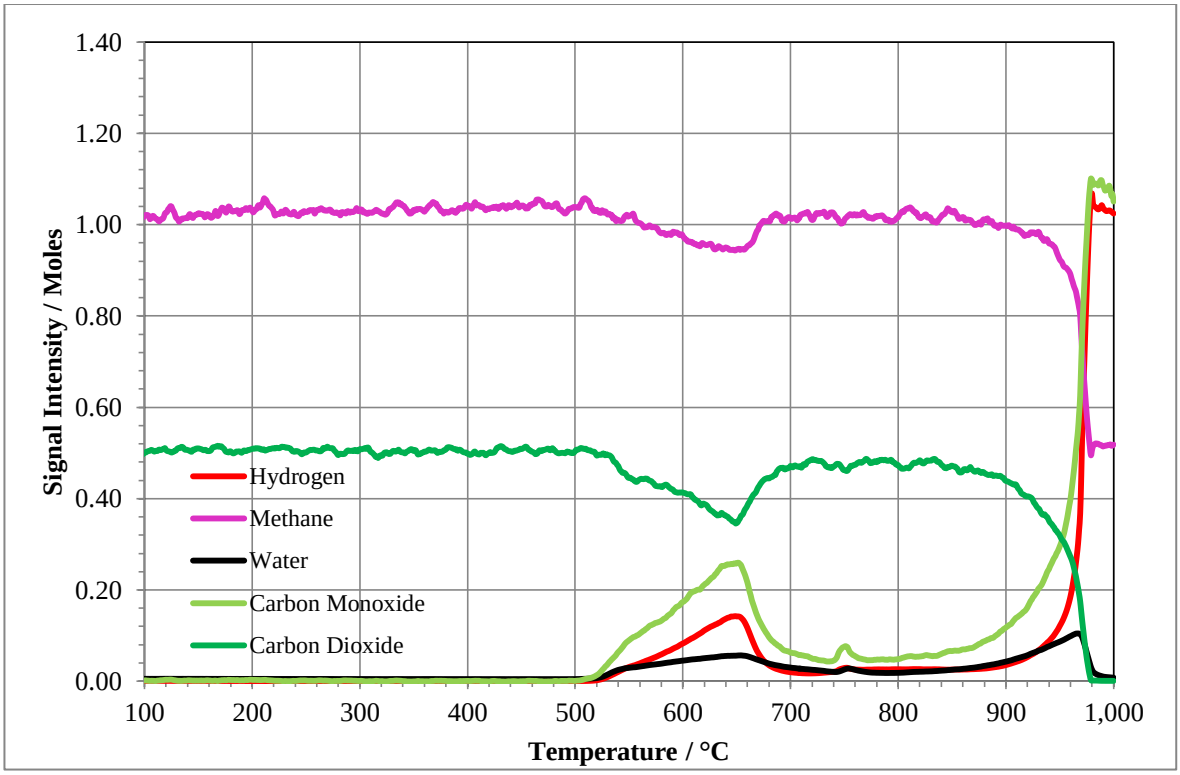

Figure 4-4 Reaction profile for temperature programmed reaction of a 2:1 CH_4/CO_2 mixture passed over 1 mol% Ni Doped $SrZrO_3$

Figure 4-4 Reaction profile for temperature programmed reaction of a 2:1 CH4/CO2 mixture passed over 1 mol% Ni Doped SrZrO3 shows a stark contrast to the profile for the undoped $SrZrO_3$. At ~510 °C carbon monoxide and hydrogen start to form and this is matched by a stoichiometric fall in methane and carbon dioxide, resulting in a peak for syn-gas production at ~610 °C. The dry reforming products then sharply falls and the methane and carbon dioxide consumption decline in parallel. This may be as a result of saturation of active sites with adsorbed gas phase species. After 800 °C syn-gas formation begins to steadily increase again, and then more sharply increase after 900 °C, this is likely to be due to surface species being adsorbed and desorbed much faster due to the increased temperature. At ~985 °C, stoichiometric dry reforming reaction is occurring, with a H_2:CO ratio of 1 and methane conversion of 50% (the maximum level of methane conversion

where there can be theoretically no carbon deposition), as the reaction becomes more thermodynamically favourable, and site saturation is limited due to the decrease in desorption time.

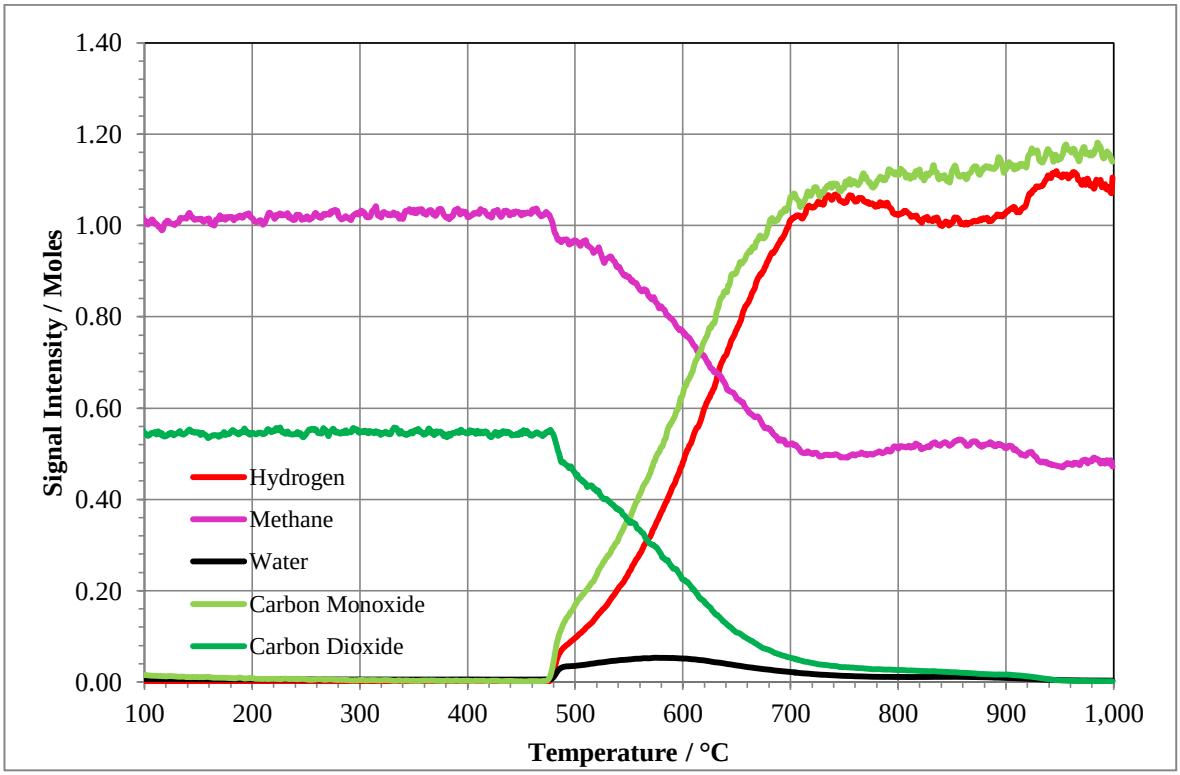

Figure 4-5 Reaction profile for temperature programmed reaction of a 2:1CH_4/CO_2 mixture passed over 2 mol% Ni Doped $SrZrO_3$

As the amount of nickel incorporated into the structure was increased from 1 mol% to 2 mol%, the quenching of the dry reforming reaction due to surface site saturation was not seen and was likely to be caused by increasing the number of active sites available (Figure 4-5). Over the 2 mol% Ni doped $SrZrO_3$ sample the reforming reaction begins at ~475 °C and from this temperature syngas production increases linearly, and with an almost 1:1 ratio of H_2:CO until 722°C, when the consumption of methane begins to plateau and the carbon dioxide that is available for reaction becomes relatively insignificant. In this temperature regime there is a small amount of water production due to the occurrence of

the reverse water gas shift reaction occurring between some of the unreacted carbon dioxide and hydrogen. In the final stages of reaction thermal decomposition of excess methane becomes favourable as the temperature increases above 700 °C. However this is not observed at 1000 °C where the conversion of methane remains at ~50% [5]. This reaction profile shows some similarity to that of the cermet materials, but without the decomposition of excess methane at elevated temperatures.

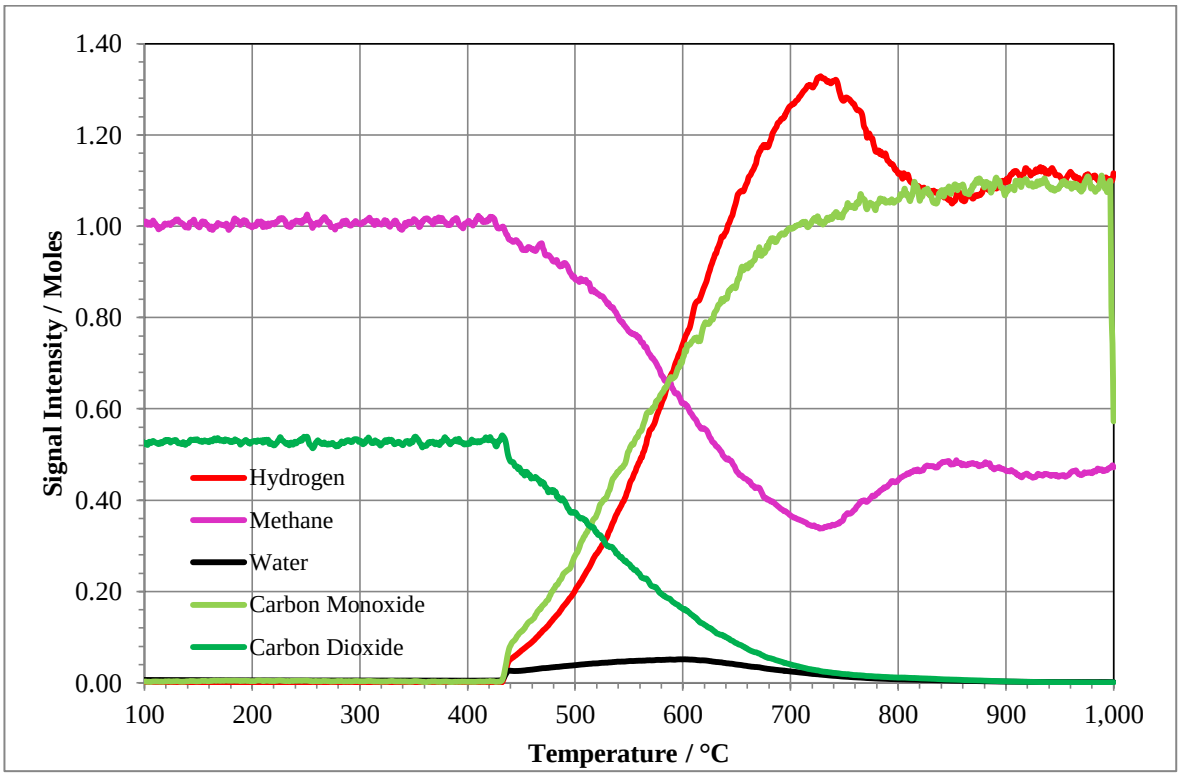

Figure 4-6 Reaction profile for temperature programmed reaction of a 2:1CH_4/CO_2 mixture passed over 4 mol% Ni Doped $SrZrO_3$

Figure 4-6 shows the TPRx profile for biogas over 4 mol% Ni doped $SrZrO_3$. Syngas production occurs at marginally lower temperature than for the 2 mol% doped sample and similarly increases linearly at the lower temperatures. By 600 °C the H_2:CO ratio starts to exceed 1. The increased consumption of methane suggests that the Boudouard reaction is

favouring the recombination of carbon monoxide to form carbon dioxide, this is in turn being reformed with methane resulting in a greater methane consumption and hydrogen formation. As the temperature increases the Boudouard reaction becomes less thermodynamically favourable and this effect falls off, with the H_2:CO ratio stabilising at ~1 by 1000 °C.

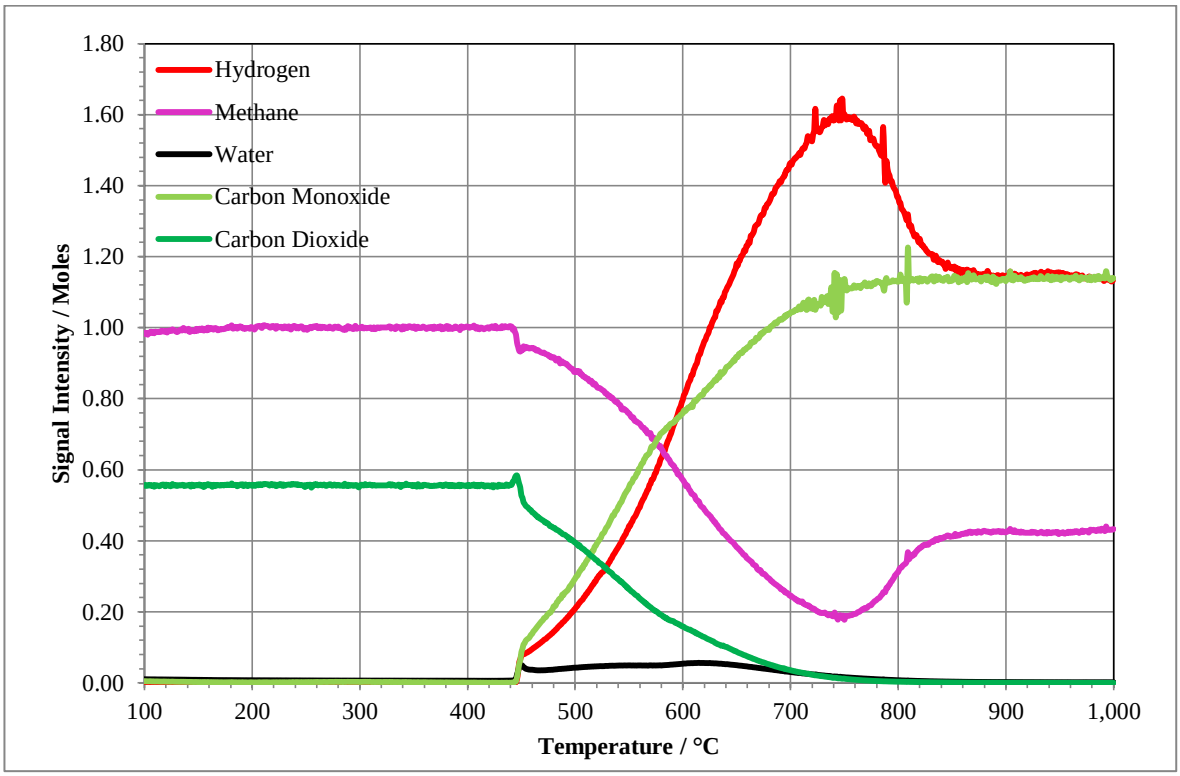

Figure 4-7 Reaction profile for temperature programmed reaction of a 2:1CH_4/CO_2 mixture passed over 8 mol% Ni Doped $SrZrO_3$

Doubling the mol% of Ni from 4 mol% to 8 mol% overall (Figure 4-7) has little effect on the temperature that reforming begins, and up until 600 °C yields an almost identical reaction profile compared to 4 mol% Ni doped $SrZrO_3$. Above 600 °C the level of Boudouard reaction occurring increases sharply with over half of the excess methane being

consumed by 750 °C. However, similarly to the 4 mol% Ni doped sample (Figure 4-6) at the highest temperatures, when the Boudouard reaction became thermodynamically unfavourable, the methane levels rise and the hydrogen production drops to stoichiometric DRM levels.

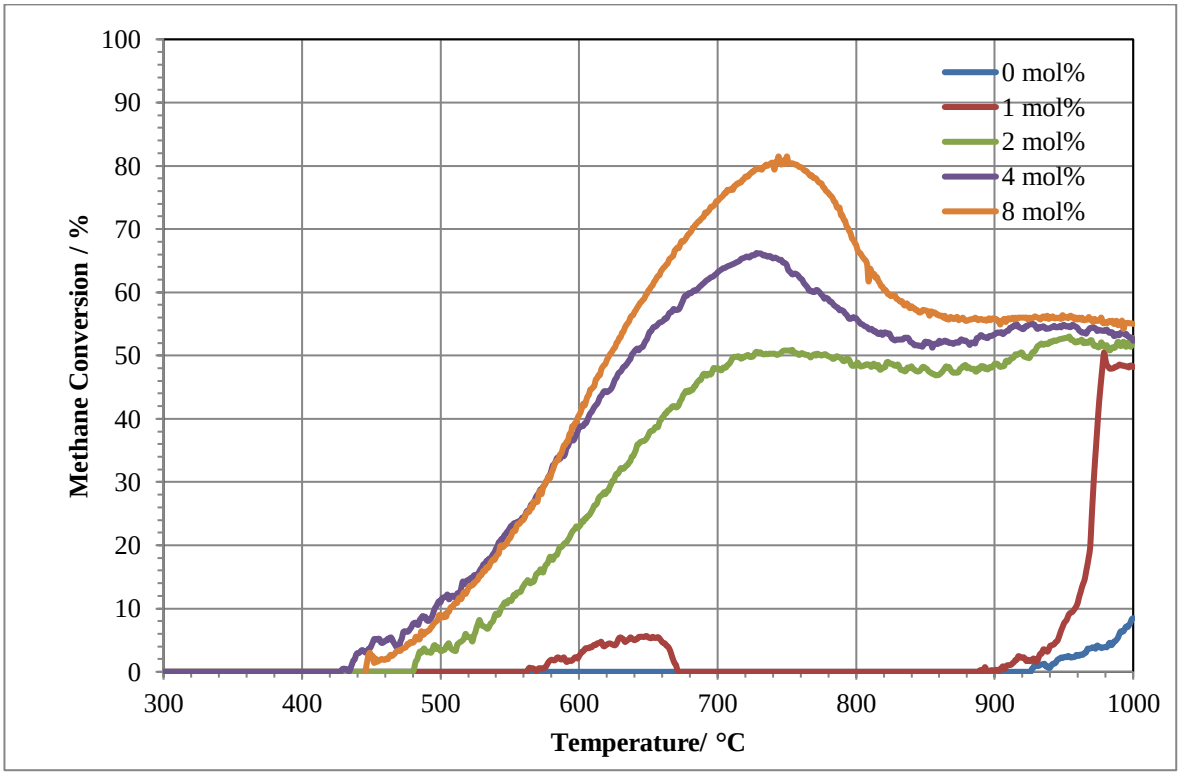

Figure 4-8 Methane conversion during temperature programmed reaction of a 2:1 CH_4/CO_2 mixture passed over $SrZrO_3$ and various nickel doped $SrZrO_3$ samples.

Figure 4-8 shows the methane conversion for the five TPRx reactions for the $SrZrO_3$ and the four nickel doped samples (Figure 4-3-Figure 4-7). The onset temperature for methane conversion lowers as the nickel doping is increased from 0 mol% to 4 mol%, from ~550 °C down to ~450 °C, with little difference in onset temperatures seen between the 4 and 8 mol% doped samples. Once reaction began the methane conversion increases at approximately the same rate for the 8 mol%, 4 mol% and 2 mol% doped samples. However the rate of increase for the 1 mol% sample is much lower, and is quenched until

the temperature reaches approximately 900°C. In the middle phase of reaction the level of Boudouard reaction that occurs increases with increasing nickel doping. However, for all the samples, methane conversions returns to approximately 50% methane conversion by 1000 °C, with a marginal upward trend in conversion as the nickel doping was increased.

4.3 Biogas reforming over nickel doped $SrZrO_3$

The biogas reforming characteristics of the perovskite catalysts were investigated further by carrying out reactions at 850 °C for 20 hours using a 2:1 methane to carbon dioxide mixture (1 ml min^{-1} of methane, 18.5 ml min^{-1} of helium and 0.5 ml min^{-1} of carbon dioxide). 850 °C was chosen as the initial reaction temperature of interest as it represents the lowest temperature where a full reforming reaction for both the perovskite and the cermet catalysts occurs. Post reaction temperature programmed oxidation was then used to compare the carbon deposited on each catalyst.

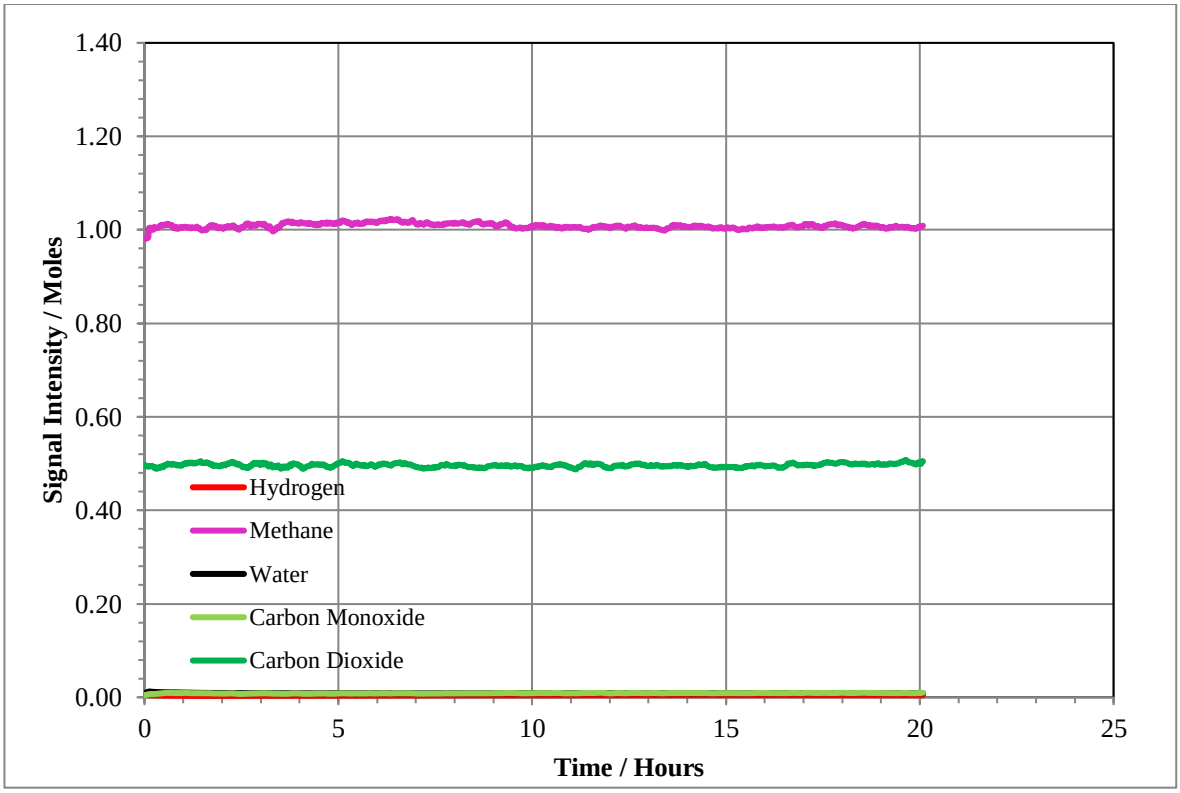

Figure 4-9 Reaction profile of a 2:1 CH_4/CO_2 mixture over $SrZrO_3$ at 850 °C for 20 hours

As was predicted by the temperature programmed reaction carried out over $SrZrO_3$ (Figure 4-3), Figure 4-9 shows that no reaction occurs over $SrZrO_3$ at 850 °C for the extent of the 20 hour reaction.

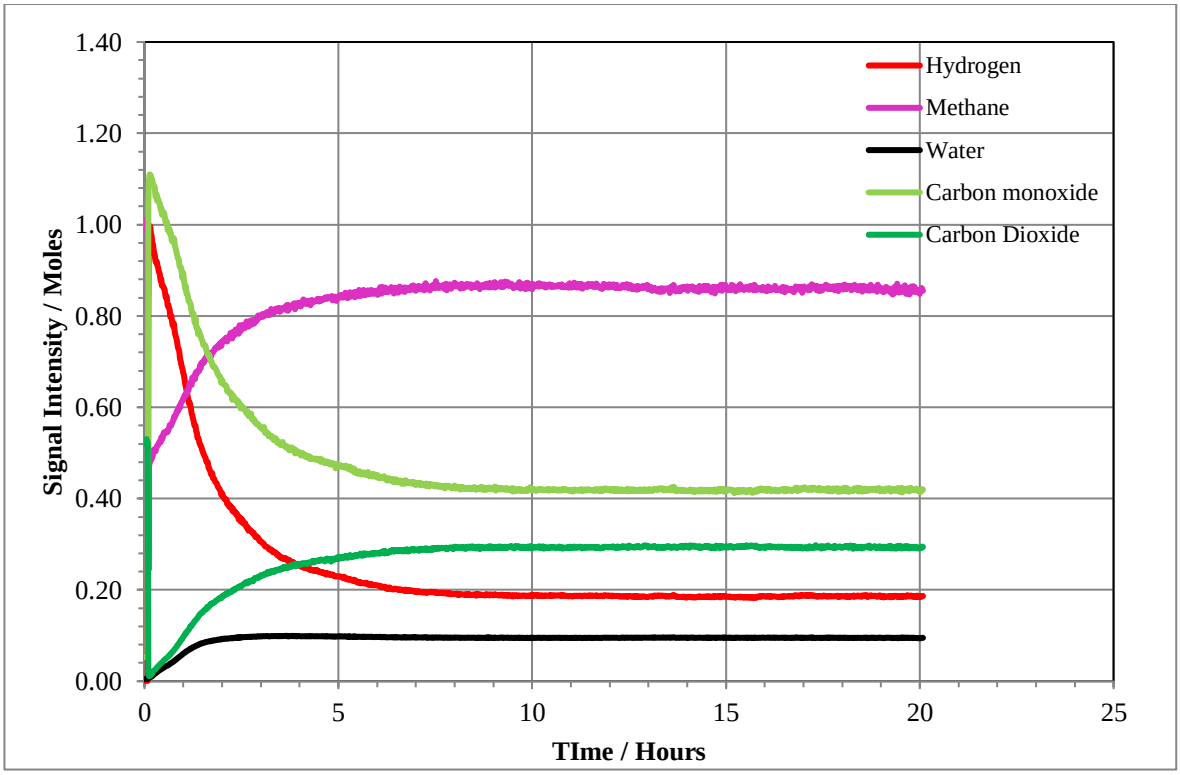

Figure 4-10 Reaction profile of a 2:1 CH_4/CO_2 mixture over 1% Ni Doped $SrZrO_3$ at 850 °C for 20 hours

In agreement with the temperature programmed reaction the introduction of 1 mol% nickel into the perovskite structure resulted in some dry reforming activity, particularly in the first 5 hours of reaction (Figure 4-10*)*. The methane and carbon dioxide conversion falls with time and by 7 hours on stream the methane conversion has fallen to ~15%. The high concentration of carbon dioxide available results in the consumption of hydrogen and formation of carbon monoxide and water *via* the reverse water gas shift reaction.

Increasing the mol% of nickel in the $SrZrO_3$ perovskite structure from 1 mol% to 2 mol% improves the stability of the reforming reaction. Using a 2 mol% Ni doped $SrZrO_3$ catalyst as opposed to a 1 mol% doping level yields a steady production of synthesis gas with a

H_2:CO ratio of ~1 for the extent of the reaction. All of the carbon dioxide is consumed and as a result is unavailable for the reverse water gas shift reaction to occur.

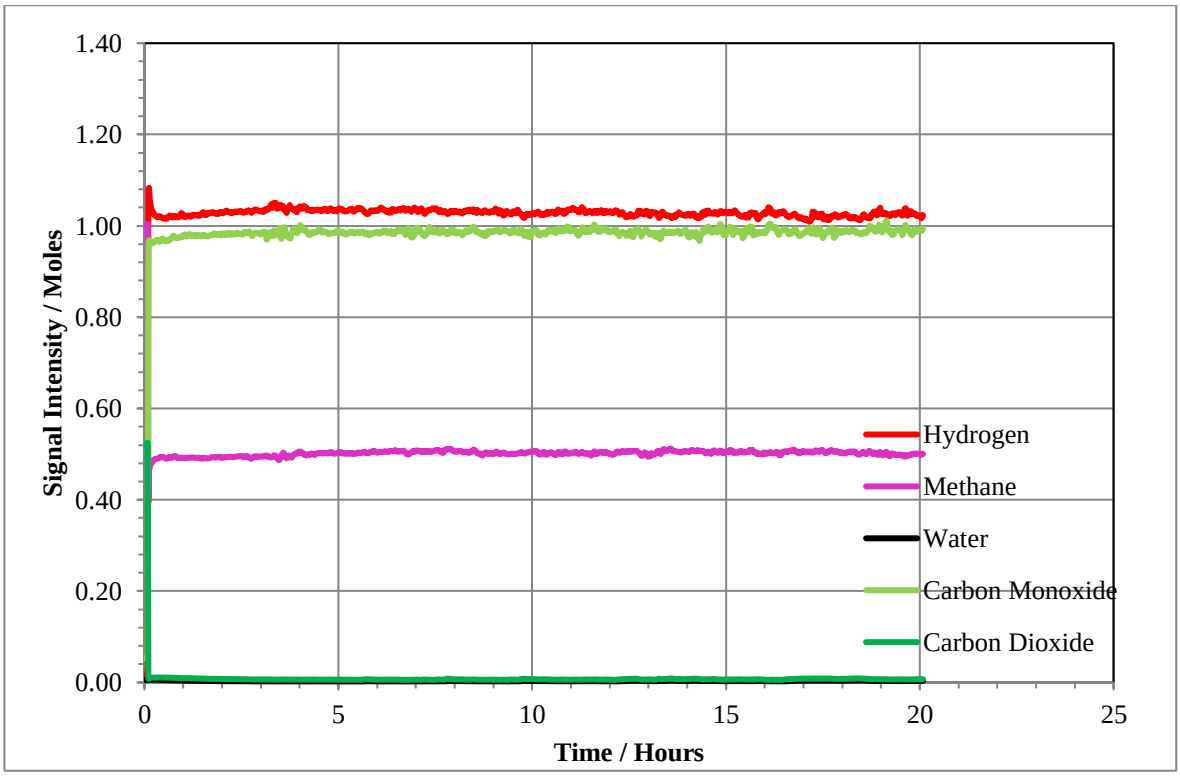

Figure 4-11 Reaction profile of a 2:1 CH_4/CO_2 mixture over 2 mol% Ni Doped $SrZrO_3$ at 850 °C for 20 hours

Further increasing the nickel doping has very little overall effect on the reforming characteristics displayed (Figure 4-12 and

Figure 4-13). In each case the carbon dioxide is fully consumed and the H_2:CO ratio is ~1. However, the amount of methane consumed increases marginally with increasing nickel doping resulting in formation of additional hydrogen. This suggests that the number of nickel sites increases, by increasing the nickel content in the structure, then thermal decomposition of methane occurs at these sites.

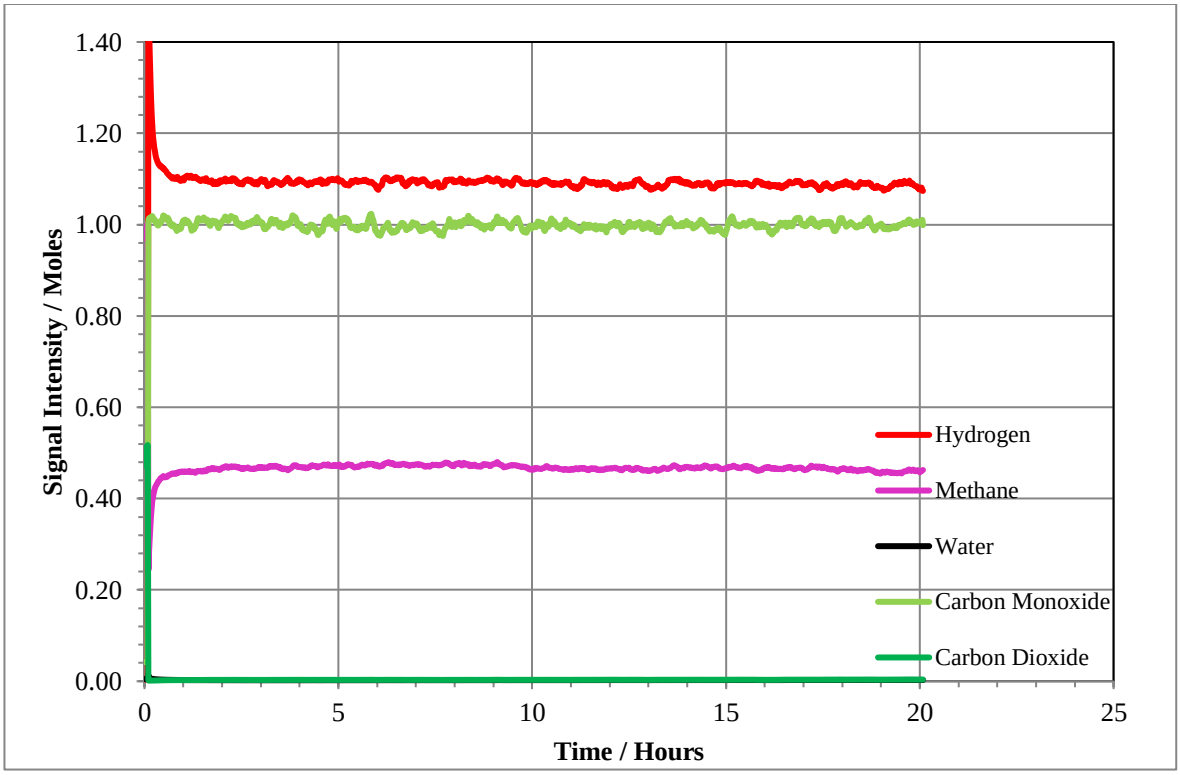

Figure 4-12 Reaction profile of a 2:1 CH_4/CO_2 mixture over 4 mol% Ni Doped $SrZrO_3$ at 850 °C for 20 hours

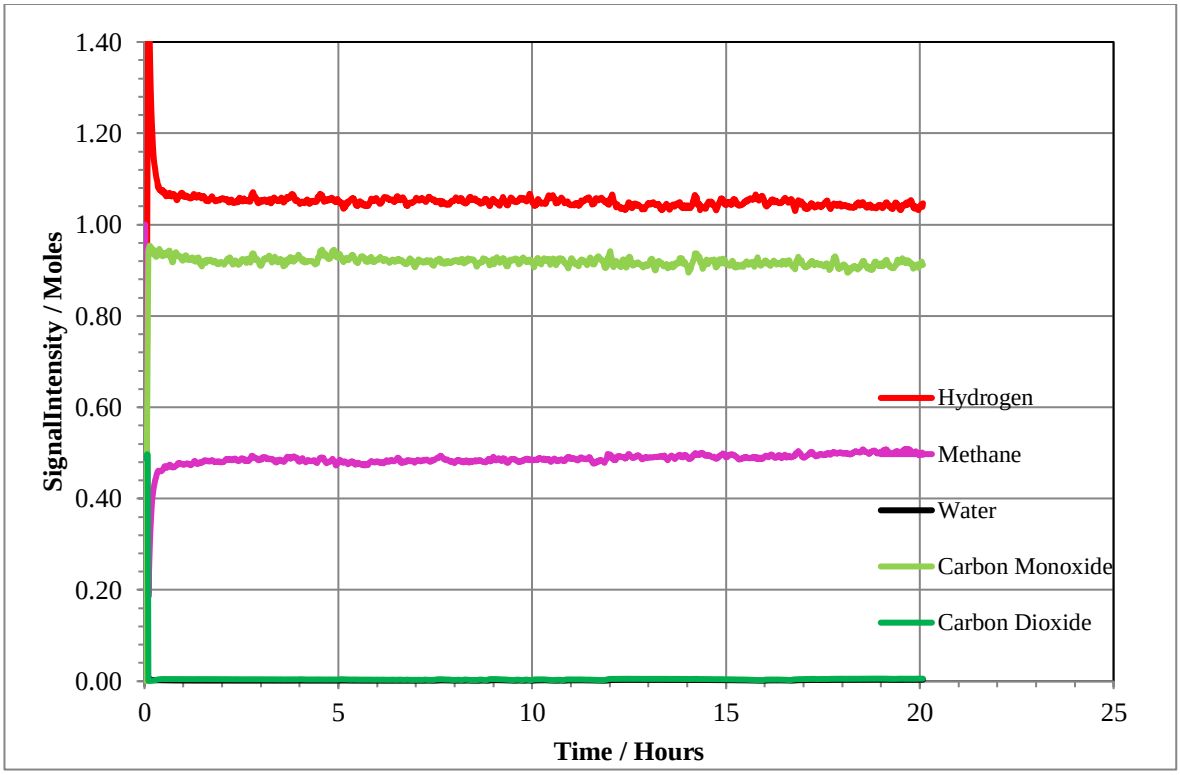

Figure 4-13 Reaction profile of a 2:1 CH_4/CO_2 mixture over 8 mol% Ni Doped $SrZrO_3$ at 850 °C for 20 hours

6.3.1 Carbon Deposition

Figure **4-14** shows post reaction TPO analysis following passing a 2:1 CH_4/CO_2 mixture over $SrZrO_3$ catalysts at 850 °C for 20 hours. The traces shown are the result of passing oxygen over the catalyst and monitoring the carbon dioxide signals this produces as the temperature of the furnace increases. The figure shows that altering the nickel doping did not alter the type of carbon formed during reaction as all profiles contain one distinct peak. As there is no significant evidence for the occurrence of the Boudouard reaction, due to the reaction temperature (850 °C), it is likely that the carbon formed is from the pyrolysis of excess methane and is likely to be graphitic in nature[6–10]. Based on the stability of the reaction profiles for the 2 mol% nickel doped $SrZrO_3$ and above it is unlikely that the

carbon formed is deactivating in nature or some loss of reforming activity would have been evident. This form of carbon could become physically deleterious if the quantity deposited became more significant as the flow of gases could become disrupted. As the nickel loading increases the area of the peak increases and the temperature in which the carbon begins to be removed as CO_2 is lower. This lowering in temperature is due to the amount of carbon present and the arrangement of this carbon. As the amount increases the carbon is not as compact on the catalyst surface and microstructure, and as a result becomes easier to remove, thus requiring a lower temperature.

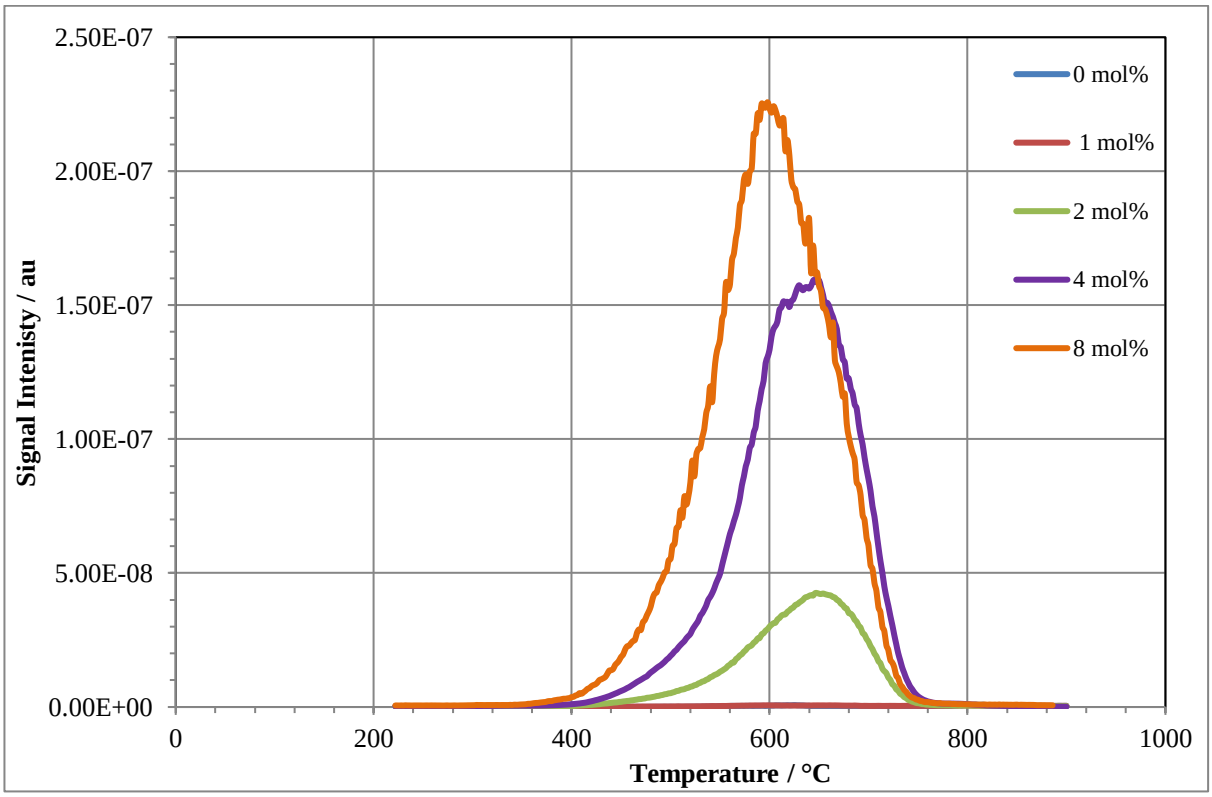

Figure 4-14 Post reaction TPO profiles of isothermal dry reforming reactions for 2:1 CH_4/CO_2 mixture over various nickel doped $SrZrO_3$ catalysts.

The post reaction quantification of deposited carbon shows a trend of increasing carbon deposition with the amount of nickel in the perovskite structure. This trend was attributed to the slight increase in the methane decomposition reaction occurring on free nickel sites within the structure, as more sites are available for reaction more carbon was formed. This would also be true for the Boudouard reaction in terms of more sites being available for reaction, however in these profiles at least there was no significant evidence of the Boudouard reaction occurring.

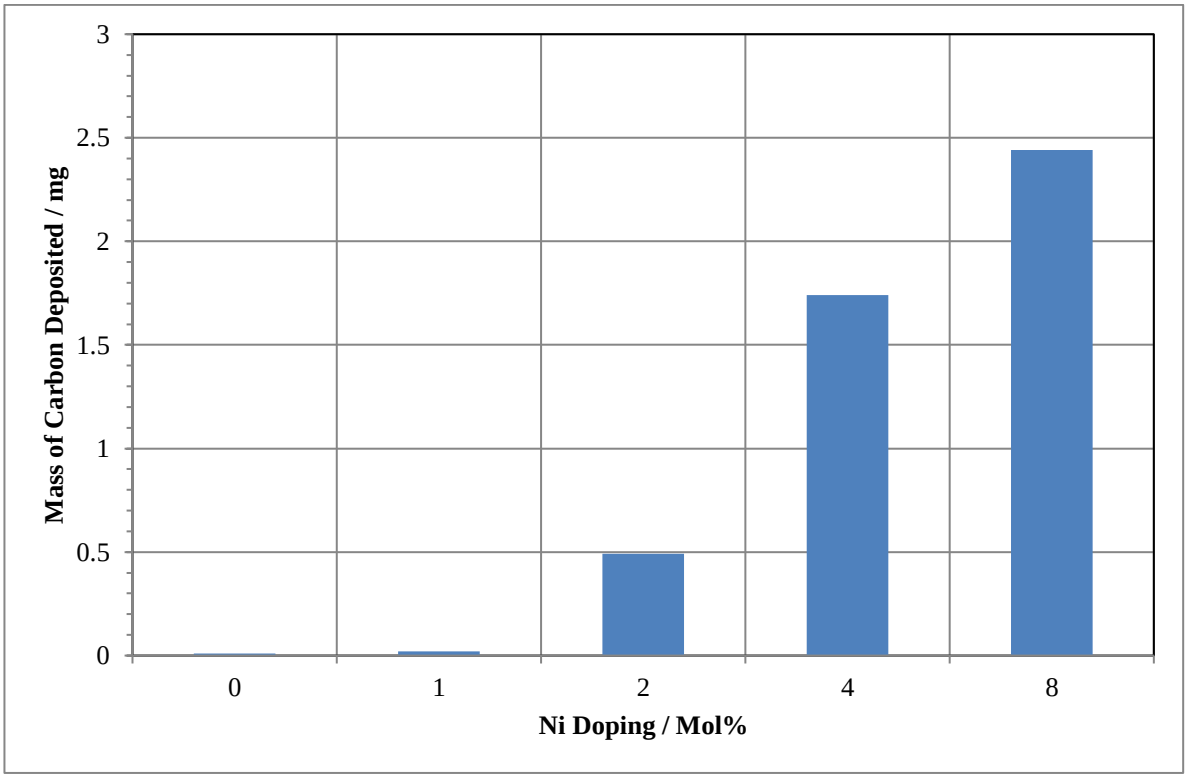

Figure 4-15 Amount of carbon formed during dry reforming reactions for 2:1 CH_4/CO_2 mixture over various nickel doped $SrZrO_3$ catalysts.

4.4 Conclusions

In this chapter the 4 mol% Ni doped $SrZrO_3$ catalyst was selected as the most suitable catalyst for further testing and comparison with conventional nickel cermet materials. This was done on the basis of purity, nickel content, catalytic activity and low propensity to

form solid carbon depositions. The profile for temperature programmed reaction of methane and carbon dioxide (DRM) was shown to be similar to that of Ni/YSZ and 5% ceria doped Ni/YSZ, but with lowered consumption of excess methane at the higher temperatures. The profile showed the DRM reaction begins at ~400 °C and that the carbon dioxide was fully consumed by ~ 850 °C and after an initial burst of hydrogen production, a H_2:CO ratio of 1 was observed.

Reactions at 850 °C showed that of the samples tested 2 mol% Ni doping was the minimum amount of nickel that gave a viable reaction. Isothermal studies were used to show that the 4 mol% Ni doped $SrZrO_3$ was stable towards the formation of synthesis gas *via* the DRM reaction over a period of three hours, with no visible loss of performance, or evidence of formation of unwanted products *via* side reactions. Temperature programmed oxidation (TPO) analysis of the various doped materials post reaction showed that as the amount of nickel incorporated into the structure increased, so did the quantity of solid carbon being deposited onto the catalyst surface over the same time period.

It was shown in Figure 4-9 and Figure 4-10 that 0 mol% and 1 mol% nickel doped strontium zirconate are unsuitable for use as dry reforming catalysts, as neither material gave the required catalytic activity to produce a sustained reaction. 2, 4 and 8 mol% Ni doped $SrZrO_3$ all gave a sustained dry reforming reaction, with evidence of increased decomposition of methane with increased nickel doping. Despite 2 mol% Ni doped $SrZrO_3$ giving the lowest formation of carbon, it also represented the catalyst that was most likely to show some degradation with time owing to the fewer amount of potential active sites. Although, this observation has not been confirmed, it does represent an interesting route for further exploration. The potential degradation of the sample at lower mol% Ni

could be caused either by loss of surface area or reactive sites caused by either sintering or poisoning mechanisms[11–13].

The 4 mol% nickel doped $SrZrO_3$ sample was selected as the catalyst of choice for further investigation in this work as it was more likely to be resistant to some loss of surface area or poisoning effects but showed less evidence of methane decomposition when compared to 8 mol% nickel doped $SrZrO_3$.

4.5 References

1 S. E. Evans, J. Z. Staniforth, R. J. Darton and R. M. Ormerod, *Green Chem.*, 2014, **16**, 4587–4594.

2 C. J. Laycock, J. Z. Staniforth and R. M. Ormerod, *Dalt. Trans.*, 2011, **40**, 5494.

3 G. J. Offer, J. Mermelstein, E. Brightman and N. P. Brandon, *J. Am. Ceram. Soc.*, 2009, **92**, 763–780.

4 Y. Li, B. Zhang, X. Tang, Y. Xu and W. Shen, *Catal. Commun.*, 2006, **7**, 380–386.

5 A. S. A. Al-Fatesh and A. H. Fakeeha, *J. Saudi Chem. Soc.*, 2012, **16**, 55–61.

6 N. Triantafyllopoulos and S. Neophytides, *J. Catal.*, 2006, **239**, 187–199.

7 I. V. Yentekakis, *J. Power Sources*, 2006, **160**, 422–425.

8 T. Kim, G. Liu, M. Boaro, S.-I. Lee, J. M. Vohs, R. J. Gorte, O. H. Al-Madhi and B. O. Dabbousi, *J. Power Sources*, 2006, **155**, 231–238.

9 C. M. Finnerty, N. J. Coe, R. H. Cunningham and R. M. Ormerod, *Catal. Today*, 1998, **46**, 137–145.

10 EG&G Technical Services, *Fuel Cell Handbook*, U.S. Department of Energy, Morgantown, West Virginia, Seventh Ed., 2004.

11 J. Sehested, *J. Catal.*, 2004, **223**, 432–443.

12 J. Sehested, *Catal. Today*, 2006, **111**, 103–110.

13 P. Forzatti and L. Lietti, *Catal. Today*, 1999, **52**, 165–181.

5 Simulated Biogas Reforming over Nickel Doped $SrZrO_3$, Ni/YSZ and Ceria Doped Ni/YSZ Cermet Materials

5.1 Introduction

In this chapter the dry reforming characteristics of 4 mol% Ni doped $SrZrO_3$ is compared to Ni/YSZ and 5% ceria doped Ni/YSZ in order to study the methane rich (methane:carbon dioxide = 2:1) dry reforming characteristics in greater detail. The reforming conditions used were as described in Sections 2.51 and 2.52, initial analysis was achieved using methane rich conditions; 1 ml min^{-1} of methane, 0.5 ml min^{-1} of carbon dioxide in a 18.5 ml min^{-1} flow of helium carrier. Further analysis was then undertaken in which the flow of methane remained the same and the flow of carbon dioxide and helium were adjusted so that total flow was maintained at 20 ml min^{-1}, and the flow of carbon dioxide varied from 0.1 ml min^{-1} to 1.1 ml min^{-1} so that the methane to carbon dioxide ration varied from 1:0.1 up to 1:1. The samples were pre-reduced as described previously using a temperature programme of 10 °C min^{-1} up to 850 °C under 10 % hydrogen. Each sample was tested isothermally at temperatures varying from 600 °C to 900 °C and the deposited carbon analysed using post reaction TPO. The relationship between time on stream and carbon deposited was then evaluated for all three materials under methane rich conditions.

5.2 Evaluation of Dry Reforming Reaction Characteristics

As 4 mol% Ni doped $SrZrO_3$ was selected as a suitable catalyst for DRM reaction, it was then possible to thoroughly compare the chosen 4 mol% Ni doped $SrZrO_3$ catalyst to the two standard SOFC cermet materials using several data analysis techniques. Figure 5-1

shows the reaction profile for the temperature programmed DRM reaction over the three catalysts.

5.2.1 Temperature Programmed Simulated Biogas Reformation

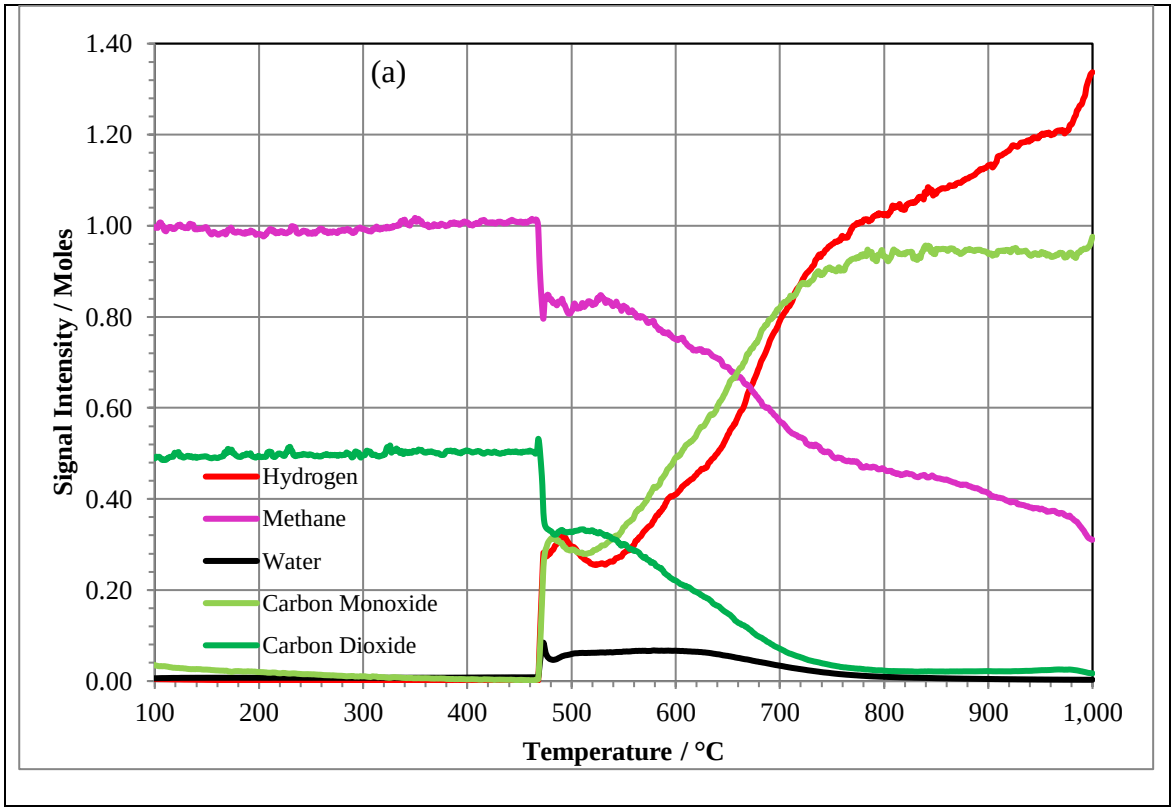

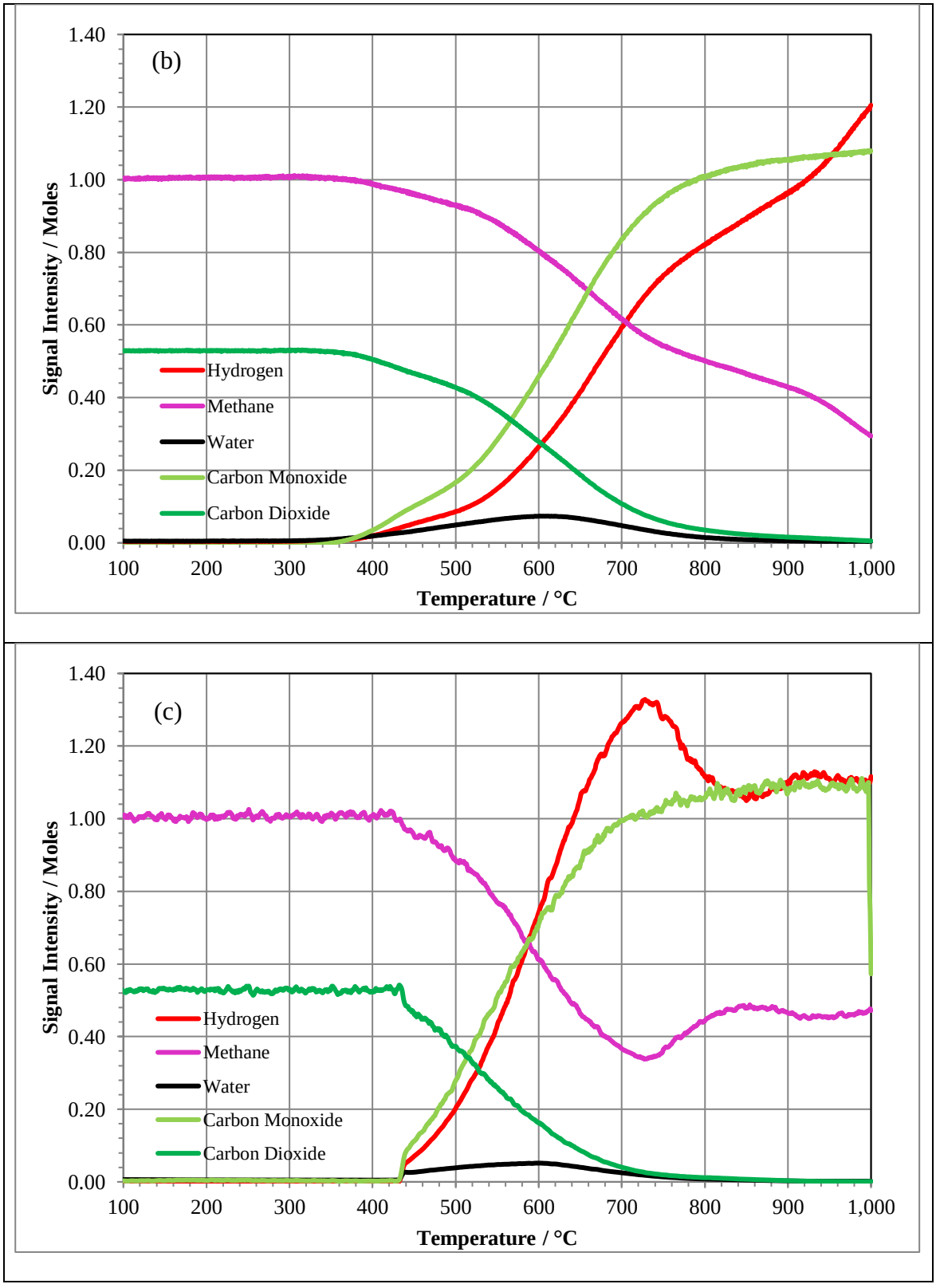

Figure 5-1 Temperature programmed reaction of a 2:1 CH_4/CO_2 mixture passed over (a) Ni/YSZ (b) 5% Ceria Doped Ni/YSZ and (c) 4 mol% Ni Doped $SrZrO_3$.

5.2.1.1 H_2:CO Ratio

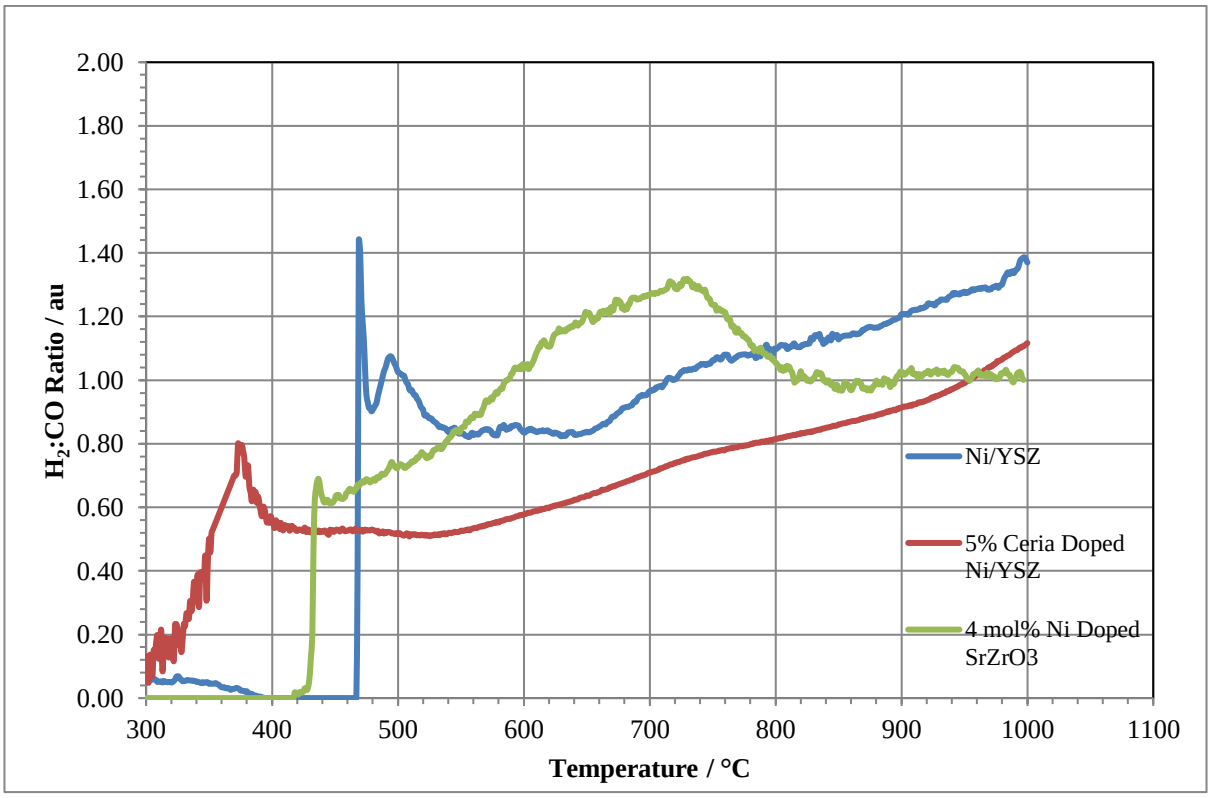

Figure 5-2 H_2:CO ratio for temperature programmed dry reforming of methane with a 2:1 CH_4/CO_2 ratio passed over different catalysts.

The temperature programmed reaction profiles for Ni/YSZ, 5% ceria doped Ni/YSZ and 4 mol% Ni doped $SrZrO_3$ were shown in Section 4.1 (Figure 4-1, Figure 4-2 and Figure 4-6) and the data then used to plot the change in the H_2:CO ratio with reaction temperature (Figure 5-2). The data shown starts at a temperature slightly below at which synthesis gas production begins in order to exclude data that would be meaningless in this case i.e. pre-reaction.

The reaction for Ni/YSZ starts at ~450 °C leading to an abrupt, transient spike in the H_2:CO ratio which quickly subsides. As this spike exceeds the predicted ratio of 1 it shows that as the reaction begins some methane is thermally decomposed on the nickel

surface. This decomposition is then suppressed at the cooler temperatures, attributed to adsorbed species occupying active sites. After the initial spike in the H_2:CO ratio drops, the ratio falls below 1. This is attributed to the consumption of some hydrogen *via* the reverse water gas shift reaction due to the availability of unreformed carbon dioxide, which is reflected by the production of water observed in the reaction profile. Once the carbon dioxide level drops, the H_2:CO ratio reaches the theoretical value of 1 for dry reforming of methane, and then continues to increase with reaction temperature. Once again this was attributed thermal decomposition of excess methane which becomes more thermodynamically favourable at higher reaction temperature, to the extent that by 1000 °C the ratio has risen to 1.40, 0.4 above the value for a pure dry reforming reaction.

The addition of 5% ceria to the Ni/YSZ cermet lowers the H_2:CO ratio for the extent of the reaction. Ceria is known to suppress the decomposition of methane reaction and also promote the reverse Boudouard reaction[1,2]. Both of these effects contribute to a lower H_2:CO ratio by increasing carbon monoxide production and lowering hydrogen levels. The suppression of methane decomposition was seen more predominantly at temperatures above 800 °C where Ni/YSZ already gives a H_2:CO ratio of greater than 1. However ceria doped Ni/YSZ maintained the theoretical maximum for DRM until 925 °C.

The profile for the H_2:CO ratio of the nickel doped perovskite was significantly different to that of the two cermet materials which show similarities to each other, particularly in that after an initial transient phase the H_2:CO ratio steadily increased with reaction temperature. The DRM reaction over the perovskite begins without the large transient spike in the H_2:CO ratio which was seen for Ni/YSZ. However the ratio quickly exceeds 1. In contrast to the nickel cermet materials the H_2:CO ratio over the perovskite post ~700 °C fell sharply

to the theoretical maximum of 1 and remained in proximity of this value up until 1000 °C. The rise and fall in H_2:CO ratio is attributed to promotion of the Boudouard reaction[1,3–5]. Between 600 °C and 800 °C there is a crossover in the exchange between thermodynamics and kinetics of this reaction. Carbon monoxide is consumed to make carbon dioxide, which then reacts with methane to make hydrogen and carbon monoxide, causing a significant increase in the H_2:CO ratio. As the temperature increases, despite the reaction rate being faster, it is not thermodynamically favoured and so this effect heavily supressed[6].

5.2.1.2 Methane and Carbon Dioxide Conversion

Figure 5-3 and Figure 5-4 show the methane and carbon dioxide conversion for the three catalysts. Ni/YSZ and ceria doped Ni/YSZ gave similar profiles in that methane conversion rises quickly up to 700 °C, and then after a small plateau it continues to rise again. The cause of this small plateau becomes evident on examining Figure 5-4 as the carbon dioxide is almost fully consumed at this temperature, and this coincides with 50% methane conversion. The secondary increase in methane conversion is then attributed to an increase in the rate of thermal decomposition of excess methane, due to this reaction becoming more favourable at higher temperatures[7–9].

The perovskite catalyst shows a different methane conversion profile in that methane conversion increases more than the cermet materials initially, which results in a methane conversion of ~70 % by 725 °C. This also corresponds to almost complete carbon dioxide conversion (see Figure 5-4). However despite the thermal decomposition of methane becoming more thermodynamically favourable, this reaction was seen to decrease with the

methane conversion dropping to 50% and the carbon dioxide remaining fully consumed. This suggests that that thermal decomposition of excess methane is much less favoured in the case of the perovskite catalyst, which is potentially very significant in terms of developing a suitable catalyst for biogas reforming.

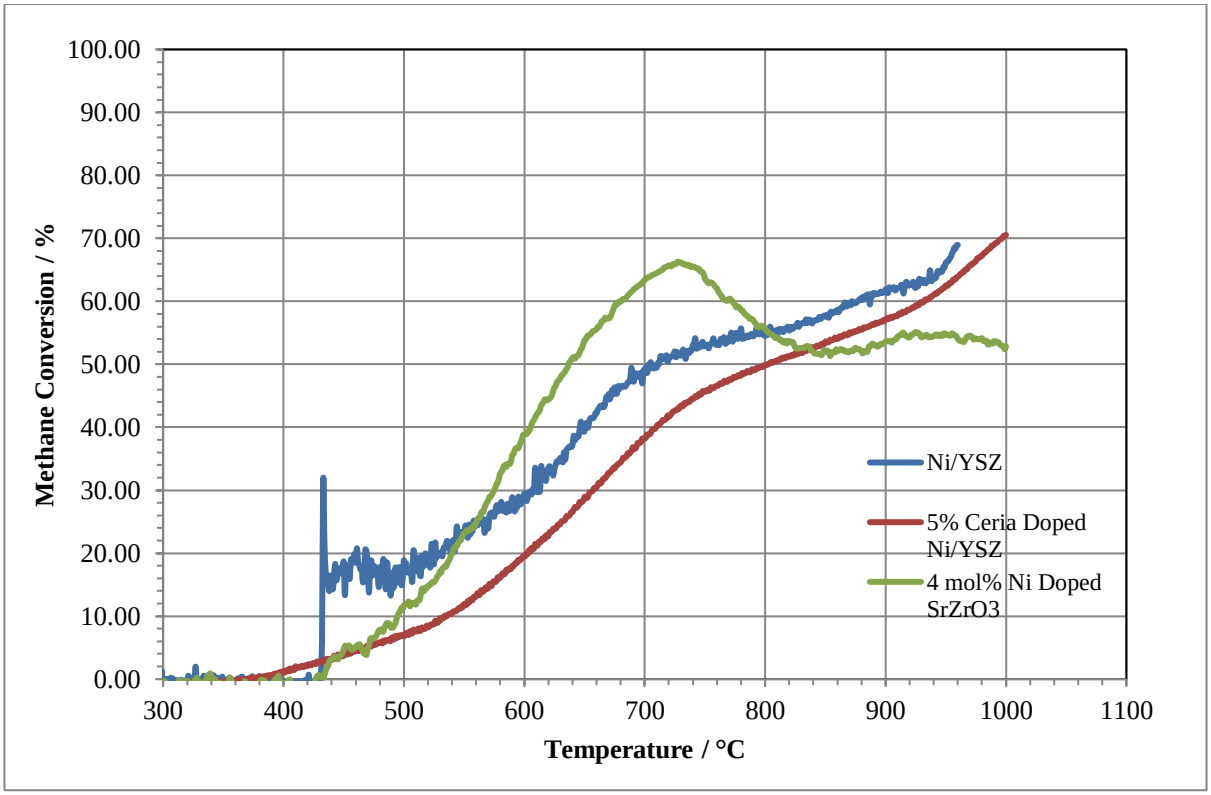

Figure 5-3 Methane conversion for temperature programmed reaction of a 2:1 CH_4/CO_2 over Ni/YSZ, 5% ceria doped Ni/YSZ ad 4 mol% Ni doped $SrZrO_3$

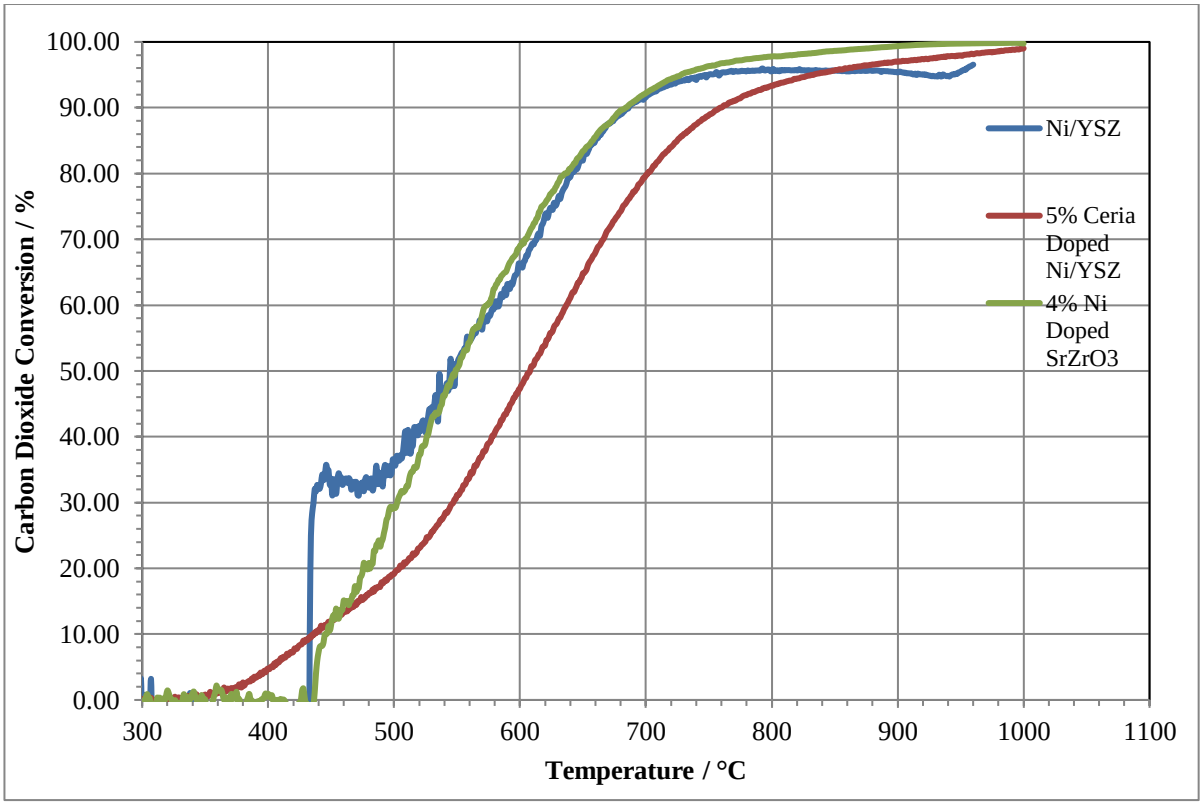

Figure 5-4 Carbon Dioxide for temperature programmed reaction of a 2:1 CH_4/CO_2 over Ni/YSZ, 5% ceria doped Ni/YSZ ad 4 mol% Ni doped $SrZrO_3$

5.3 Catalyst Behaviour towards Methane-Rich (Simulated Biogas) Reaction Mixtures

In this section the reforming activity of the three catalysts for a 2:1 CH_4:CO_2 reaction is evaluated using three hour reactions at temperatures between 600°C and 900 °C. The amount of carbon deposited on the catalyst surface is quantified.

In Section 5.2 the three catalysts were shown to be reasonably stable in the temperature range tested in that no loss of reforming activity was seen and synthesis gas products predominated rather than formation of total oxidation products. Figure 5-5 shows the reaction profiles for a 2:1 reaction of a CH_4:CO_2 mixture at 800 °C using Ni/YSZ, 5%

ceria doped Ni/YSZ and 4 mol% Ni doped $SrZrO_3$. Some excess consumption of methane is seen at the beginning of the reaction reflecting methane decomposition. This quickly subsides, and hydrogen and carbon monoxide is observed at an approximately 1:1 ratio, suggesting that an efficient dry reforming reaction is taking place over all three catalysts.

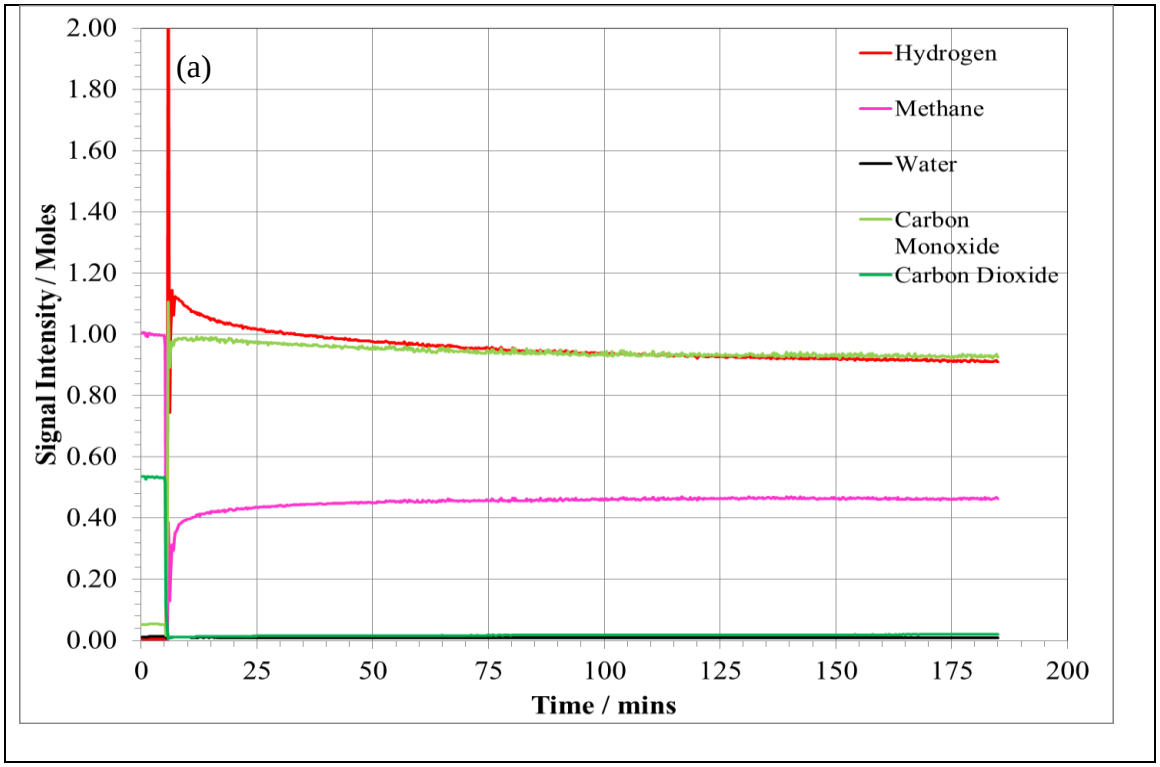

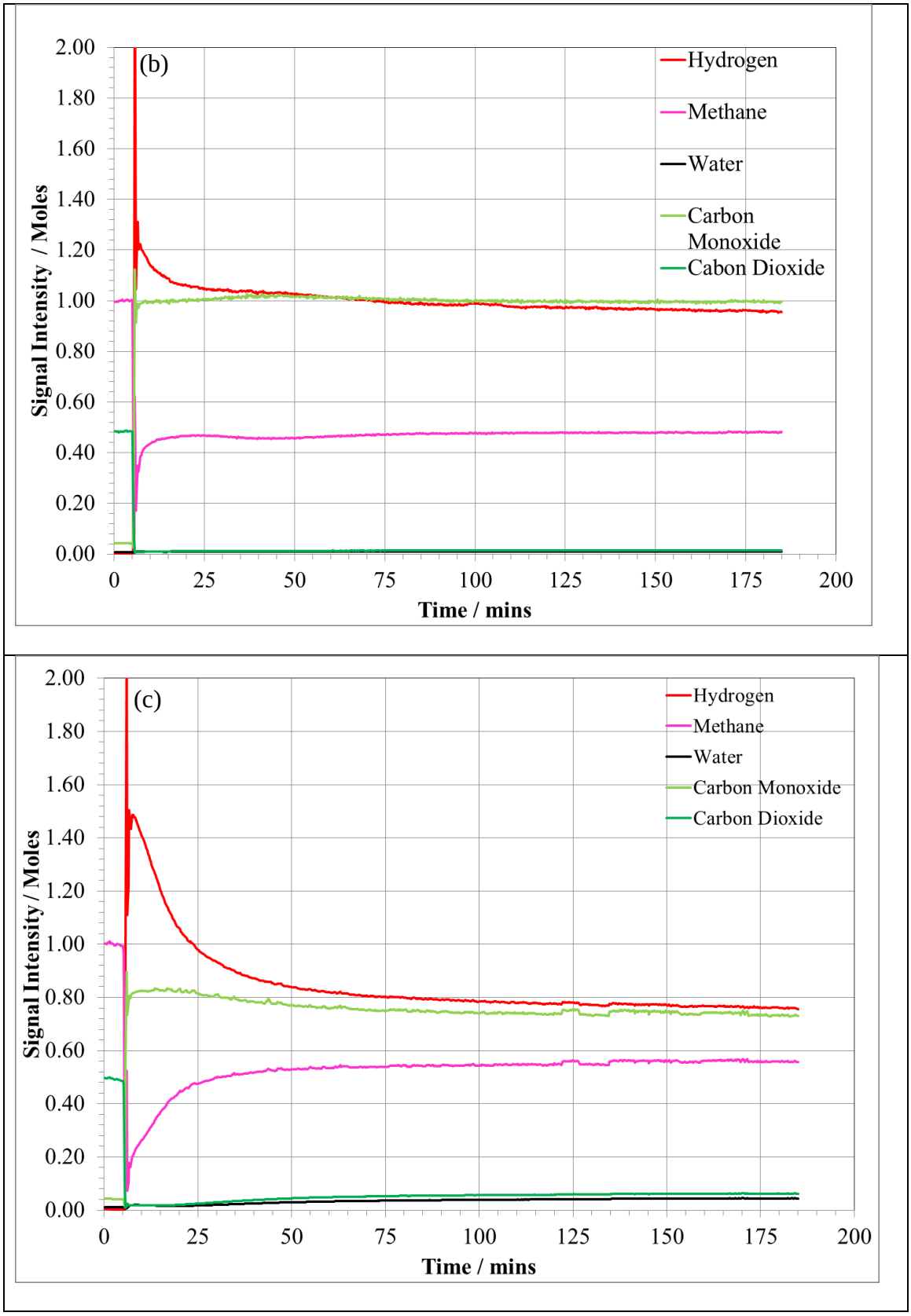

Figure 5-5 Reforming reaction profile of a 2:1 CH_4/CO_2 mixture over (a) Ni/YSZ, (b) 5% ceria doped Ni/YSZ and (c) 4 mol% Ni doped $SrZrO_3$ at 800 °C

Detailed analysis of product selectivity and reactant conversion is a good way to evaluate the key differences between what appear to be at first glance relatively similar reaction profiles between the three catalysts.

5.3.1.1 Methane and Carbon Dioxide Conversion

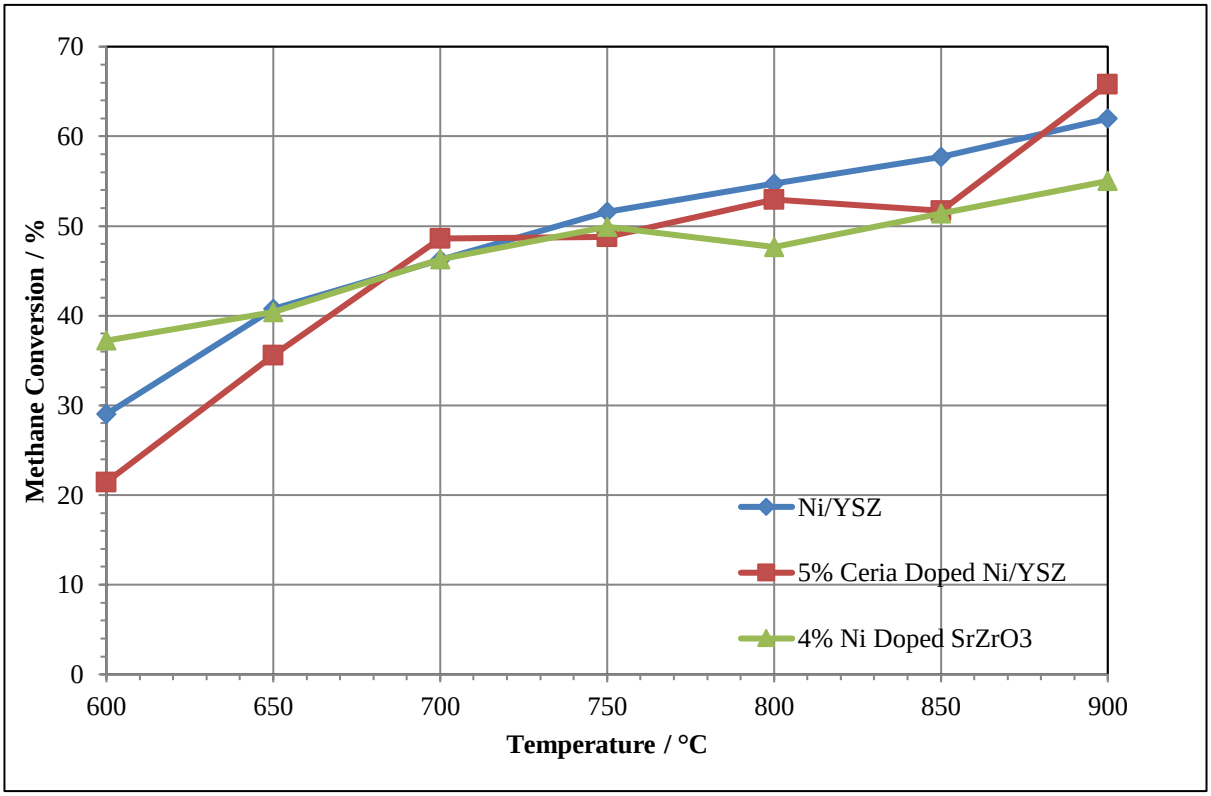

Figure 5-6 Average methane conversion over Ni/YSZ, 5% ceria doped Ni/YSZ and 4 mol% Ni doped $SrZrO_3$ for 2:1 methane to carbon dioxide dry reforming reaction at temperatures between 600 °C and 900 °C

A flatter profile for methane conversion with varying temperature was seen for 4 mol% Ni doped $SrZrO_3$ than was observed for the two cermet materials. This is caused by an increased activity at the lower temperatures compares to the cermets resulting in a higher conversion of methane. As the temperature is increased the perovskite material shows stoichiometric conversion of methane, resulting in ~50 % conversion. The nickel cermet materials show conversion of methane in excess of what could be achieved for stoichiometric DRM for a 2:1 CH_4:CO_2 reaction mixture. This is attributed to increased decomposition of excess methane once all the carbon dioxide had been consumed, which results in increased formation of solid carbon on the anode material. Between 600 °C and

700 ° the conversion of methane for the ceria doped material was lower than is observed for the undoped Ni/YSZ, this was caused by the slightly lower amount of nickel present in the sample as this was displaced for the ceria, or lower intrinsic reactivity of the ceria doped nickel cermet,

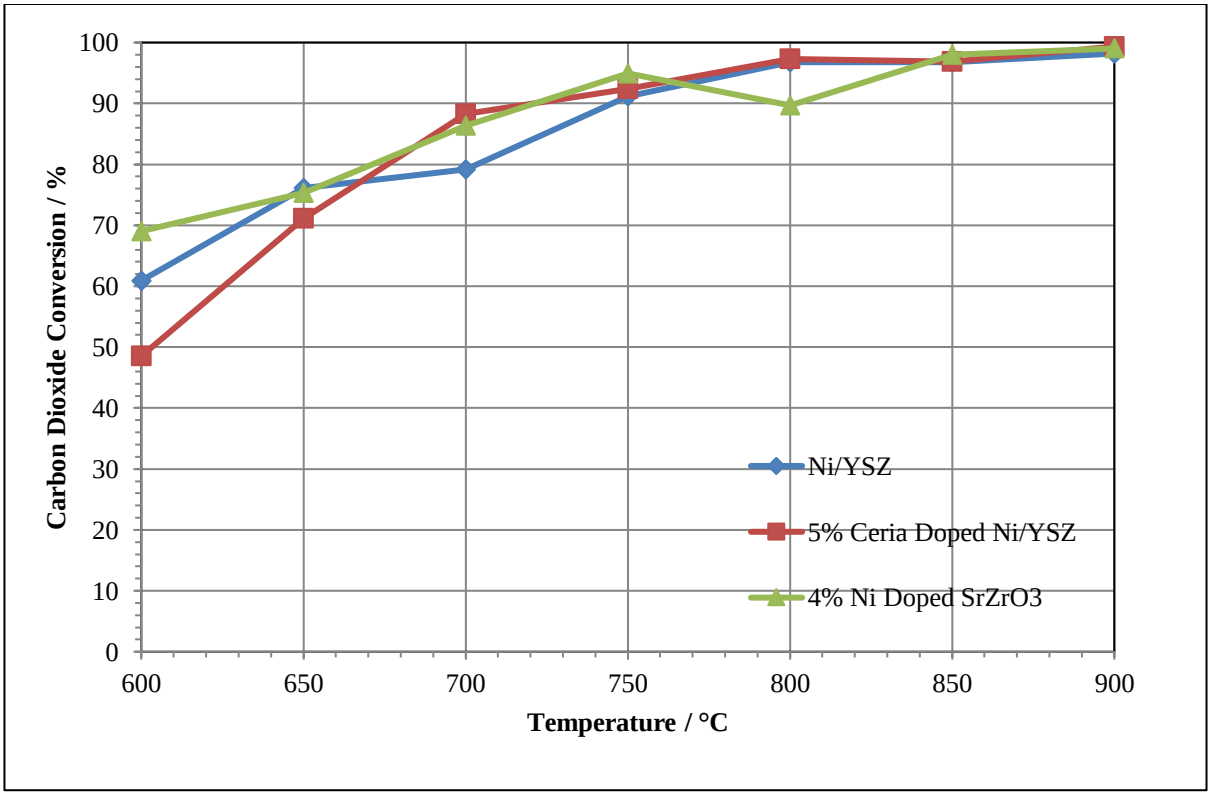

Figure 5-7 Average carbon dioxide conversion of Ni/YSZ, 5% ceria doped Ni/YSZ and 4 mol% Ni doped $SrZrO_3$ for 2:1 methane to carbon dioxide dry reforming reaction at temperatures between 600 °C and 900 °C

The imbalance between carbon dioxide and methane present in the reaction stream results in a conversion profile that is dissimilar for carbon dioxide compared to methane. All three materials had the same conversion by the highest temperatures due to full consumption of carbon dioxide. At 600 °C the 4 mol% Ni doped $SrZrO_3$ displays a carbon dioxide conversion that was higher than that of the two nickel cermets, and twice the

observed methane conversion at the same temperature as expected stoichiometrically. As was observed for methane conversion, at the lower temperatures the carbon dioxide conversion for 5 % ceria doped Ni/YSZ is less than that of the undoped sample. This difference decreased by 750 °C as the reaction kinetics become the limiting factor. The carbon dioxide conversion is above 98 % for all three catalysts by 850 °C and ~ 100 % by 900 °C.

5.3.1.2 Product Selectivity

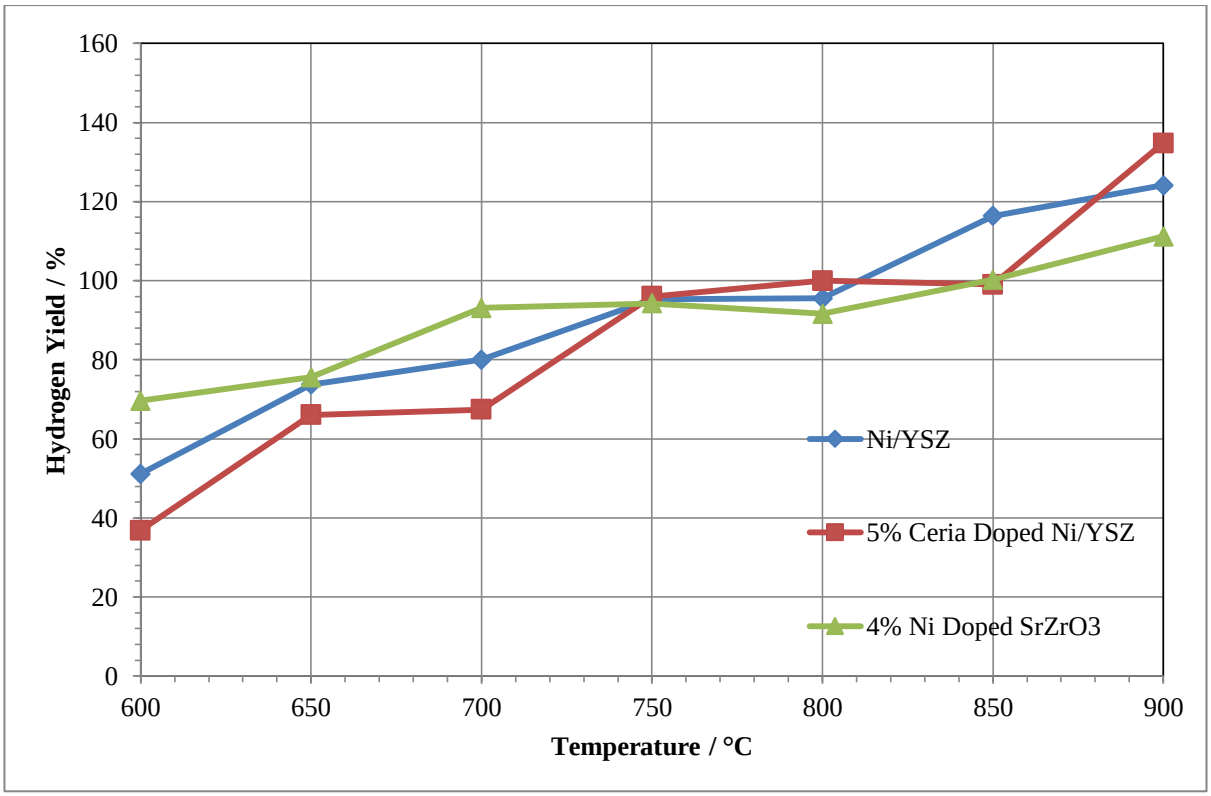

Figure 5-8 Average hydrogen yield of Ni/YSZ, 5% ceria doped Ni/YSZ and 4 mol% Ni doped SrZrO3 for 2:1 methane to carbon dioxide dry reforming reaction at temperatures between 600 °C and 900 °C

With all three catalysts displaying synthesis gas formation to some extent across the temperature range tested, analysis of product selectivity was an important tool for

distinguishing the differences in catalytic performance. Figure 5-8 shows the hydrogen yield as a factor of reaction temperature for all three catalysts. Between 600 °C and 800 °C the hydrogen yield for the perovskite catalyst either exceeds or equals the yield from the cermet materials; starting at a 70 % yield at 600 °C increasing to 95% by 700 °C which results from the increased conversion of methane that was seen in Figure 5-3. The hydrogen yield reaches 100 % by 850 °C. Above 850 °C the yield of hydrogen for the perovskite exceeds 100 % due to the formation of hydrogen *via* the decomposition of excess methane.

Both cermet materials give an initially lower yield of hydrogen due to their lower activity at the cooler reforming temperatures, below 750 °C. However at the higher reaction temperatures tested the cermet materials give a higher yield of hydrogen compared to 4 mol% Ni doped $SrZrO_{3,}$ as the consumption of methane continues to increase steadily despite the carbon dioxide being fully reformed, indicating that excess methane is being thermally decomposed[1,3,10–14]. 5 % ceria doped Ni/YSZ gave the highest yield of hydrogen at 900 °C, which is attributed to ceria also being active towards methane decomposition when in the 3+ oxidation state which ceria exists in under such harsh reducing conditions.

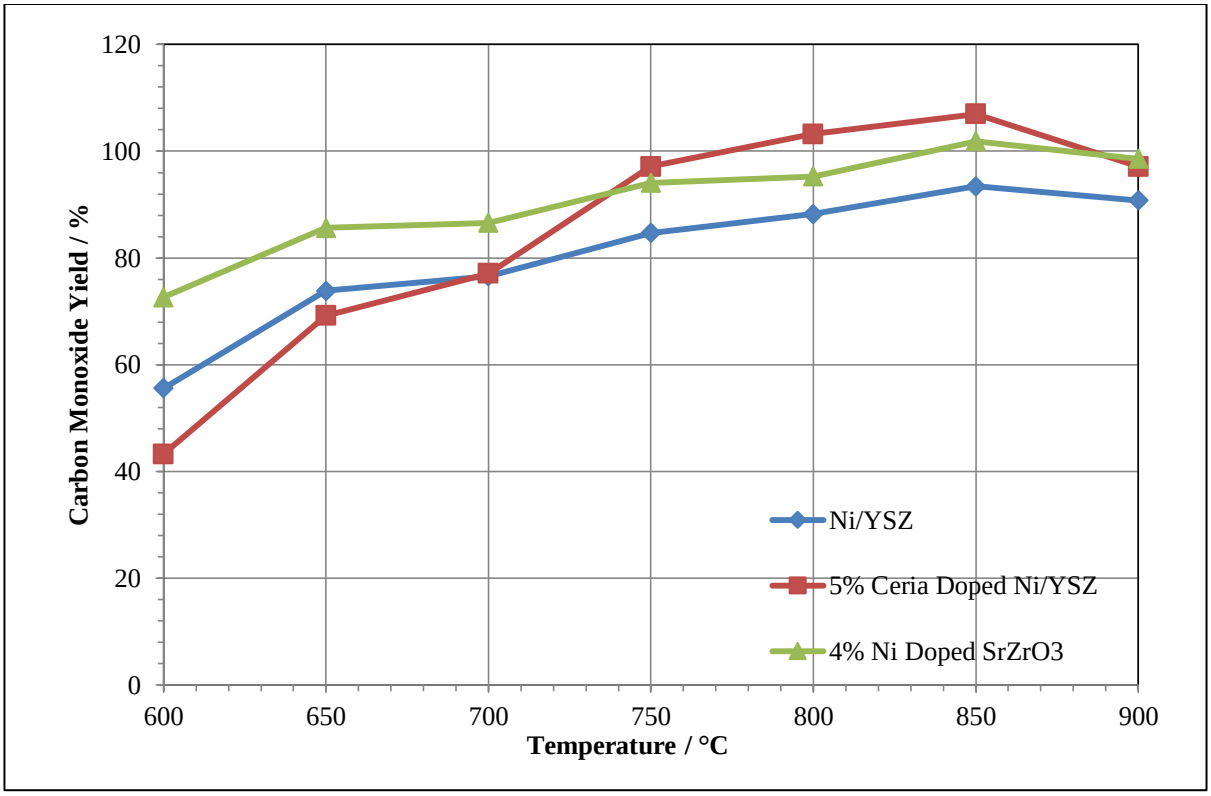

Figure 5-9 Average carbon monoxide yield of Ni/YSZ, 5% ceria doped Ni/YSZ and 4 mol% Ni doped SrZrO3 for 2:1 methane to carbon dioxide dry reforming reaction at temperatures between 600 °C and 900 °C

The 2:1 ratio of methane to carbon dioxide employed to simulate biogas means that the yield of carbon monoxide is closely linked to the partial pressure of carbon dioxide, as opposed to hydrogen yield is more closely linked to methane partial pressure. This is because when the carbon dioxide is fully consumed no more carbon monoxide can be produced. However, there is still potential for methane consumption and thus hydrogen production. As the carbon dioxide can be fully consumed by the DRM reaction the profile for carbon monoxide yield shown in Figure 5-9 is different to that of the hydrogen yield. For all three catalysts the carbon monoxide yield profile flattens as the carbon dioxide becomes fully consumed, as although carbon monoxide can be produced by side reactions

such as the reverse Boudouard or the reverse water gas shift reaction, this also requires some carbon dioxide to be available.

Similarly to Figure 5-8 the yield of carbon monoxide is initially higher for the nickel doped perovskite than for the two cermet materials. The reaction profiles show this is partly due to the perovskite producing less water *via* the water gas shift reaction suggesting this material is not as active towards the water gas shift reaction as nickel based cermets. As DRM becomes more thermodynamically favourable above 700 °C, the yield of carbon monoxide from the cermet materials became much higher with all three catalysts giving ~ 100% yield by 850 °C.

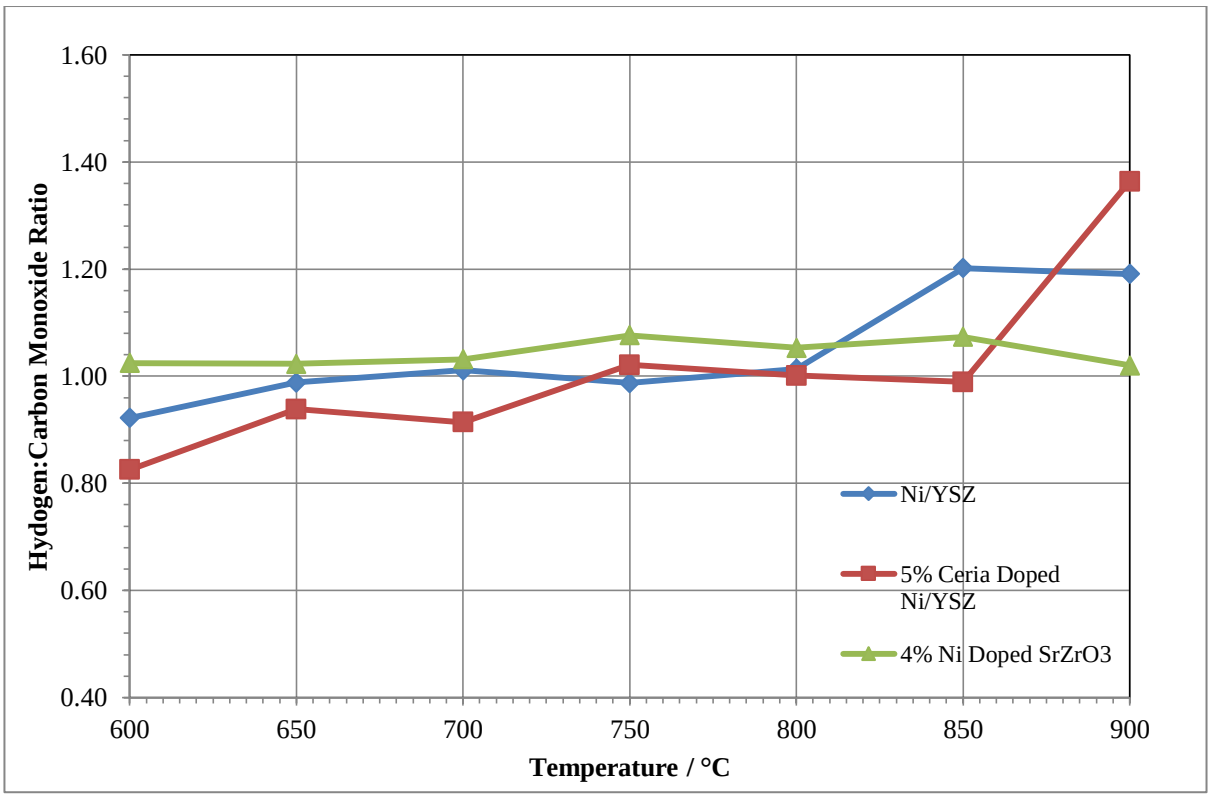

Figure 5-10 Hydrogen to carbon monoxide ratio of Ni/YSZ, 5% ceria doped Ni/YSZ and 4 mol% Ni doped SrZrO3 for 2:1 methane to carbon dioxide dry reforming reaction at temperatures between 600 °C and 900 °C

Figure 5-10 shows the H_2:CO ratio for Ni/YSZ, 5% ceria doped Ni/YSZ and 4 mol% Ni doped $SrZrO_3$ across the range of temperatures tested. Both the nickel cermet materials show a steady upward trend in the H_2:CO ratio with increasing temperature and then a large increase at 800 °C for Ni/YSZ and above 850 °C for 5 % ceria doped Ni/YSZ. The large increase was caused by the total consumption of carbon dioxide and methane decomposition. As the carbon dioxide becomes fully consumed the hydrogen consuming reverse water gas shift reaction is quenched and the hydrogen forming decomposition of methane reaction becomes more active. As a result of this both cermet materials have a H_2:CO ratio higher than 1 above 850 °C.

The nickel doped perovskite however has a H_2:CO of ~1 at 600 °C due to a suppressed formation of water *via* the reverse water gas shift reaction (Figure 5-11) compared to the cermets and also higher activity towards the DRM reaction. The H_2:CO ratio remains stable at ~1 across the full temperature range. This is due to the perovskite material being less active towards the undesirable decomposition of methane reaction so even at elevated reaction temperatures the production of hydrogen remains closer to the stoichiometrically predicted level for the DRM reaction compared to Ni/YSZ and 5% ceria doped Ni/YSZ. In the scope of the project aims and objective this is an important finding in relation to finding a catalyst that is active towards the DRM reaction and results in lower carbon deposition.

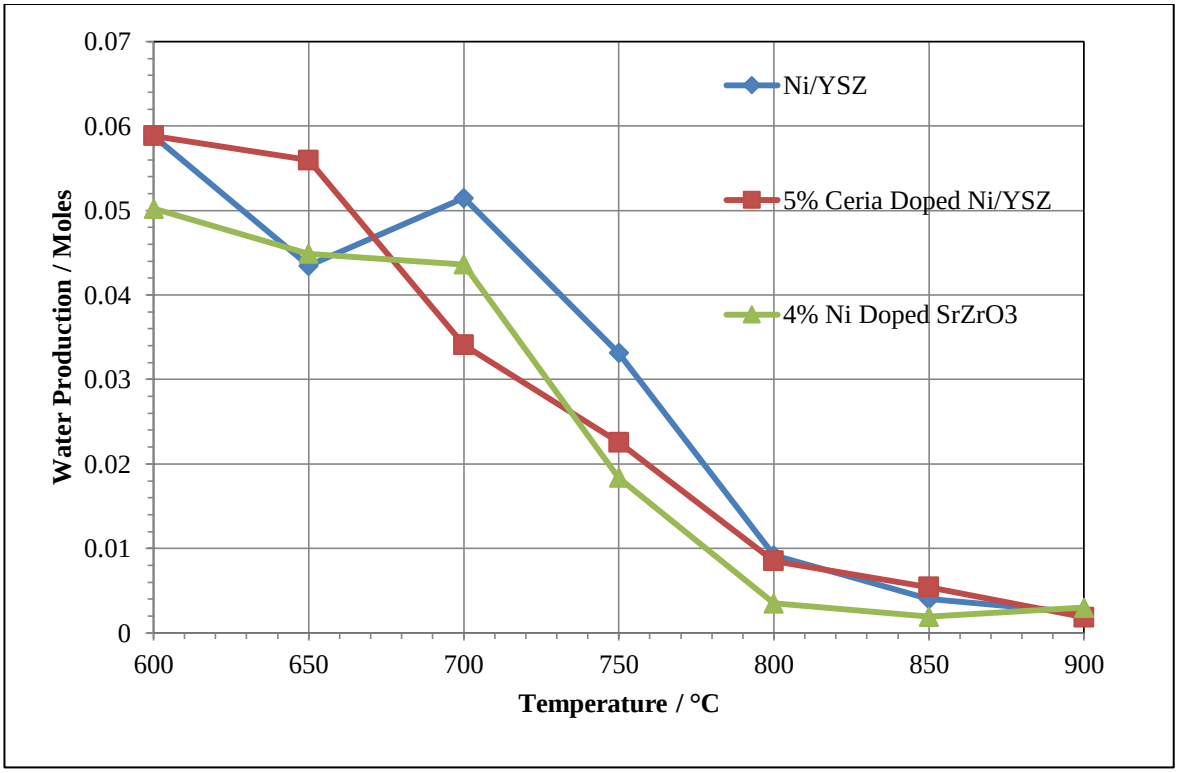

Figure 5-11 Water formation of Ni/YSZ, 5% ceria doped Ni/YSZ and 4 mol% Ni doped SrZrO3 for 2:1 methane to carbon dioxide dry reforming reaction at temperatures between 600 °C and 900 °C

Figure 5-11 shows that the formation of water across the range of temperatures tested is low for all three catalysts. There was a strong negative correlation between the reaction temperature and the formation of water due to decreased occurrence of the reverse WGS as the temperature increased. Both Ni/YSZ and 4 mol% Ni doped $SrZrO_3$ show a spike in water formation at 700 °C which may be caused by the reverse water gas shift reaction being more kinetically favoured as well as thermodynamically favourable at this temperature. However this was not seen for 5% ceria doped Ni/YSZ which suggests ceria doping has a suppressive effect on the reverse WGS under the reaction conditions used.

5.3.1.3 Carbon Deposition

Temperature programmed oxidation (TPO) of carbonaceous species from the catalyst samples post reforming provides both quantitative and qualitative data in that the temperature that the carbon species are removed at gives an indication of the nature of carbon that has been deposited.

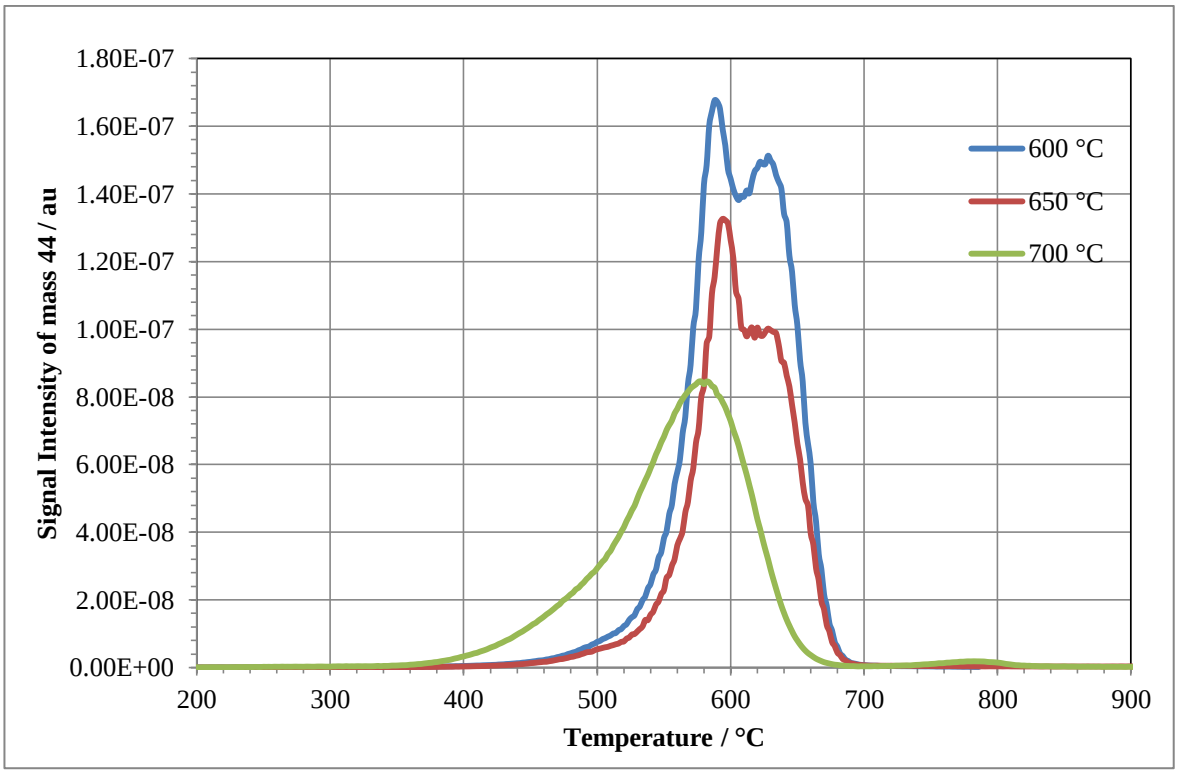

Figure 5-12 Post reaction TPO profile comparison for Ni/YSZ following reactions of a 2:1 methane to carbon dioxide dry mixture at 600 °C, 650 °C and 700 °C for 3 hours

Figure 5-12 shows the post reaction TPO profiles for a 2:1 methane to carbon dioxide mixture passed over Ni/YSZ at 600 °C, 650 °C and 700 °C. At 600 °C both the decomposition of methane and Boudouard reaction can take place over nickel based catalysts and this may be the cause of the formation of two distinct peaks on the TPO profile indicating that potentially at least two forms of carbon were present.

Increasing the temperature of reaction to 650 °C results in the suppression of the second peak, whilst the primary peak remains. By 700 °C only one peak is visible, suggesting that at 700 °C only one type of carbon was being formed. The higher temperature peak in the TPO profiles was associated with the formation of more ordered carbon in the form of nanotubes, filaments or whiskers as these types of carbon are formed by the Boudouard, reaction which is favoured at temperatures below 700 °C[1,4,15,16].

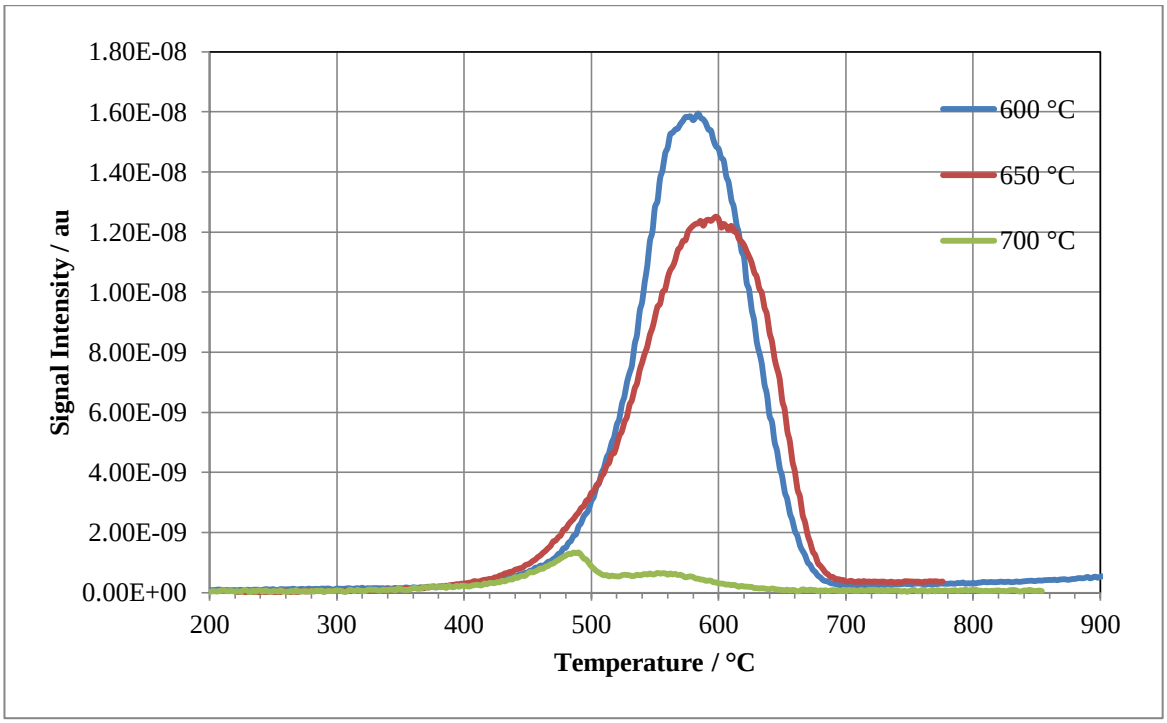

Figure 5-13 TPO profile comparison for 5% ceria doped Ni/YSZ following reactions of a 2:1 methane to carbon dioxide dry mixture at 600 °C, 650 °C and 700 °C for 3 hours

The addition of 5% ceria to Ni/YSZ has a significant effect on the TPO profiles as seen in Figure 5-13 following reactions at 600 °C and 650 °C, only one broader peak is observed, whilst following reaction at 700 °C where Ni/YSZ resulted in one peak, the ceria doped sample results in two carbon dioxide peaks. The single carbon dioxide peak for the reaction at 600 °C and 650 °C corresponded with the peak assigned to carbon deposited *via*

the Boudouard reaction in Figure 5-12, with no separate peak visible for decomposition of methane. At 700 °C a second carbon dioxide peak is observed whilst the peak assigned to carbon formed *via* the Boudouard reaction is still visible although suppressed. The lack of the second carbon dioxide peak for 5% ceria doped Ni/YSZ at 600 °C and 650 °C which has been attributed to graphitic and amorphous carbon could be due to the lower methane conversion compared to Ni/YSZ seen in Figure 5-7.

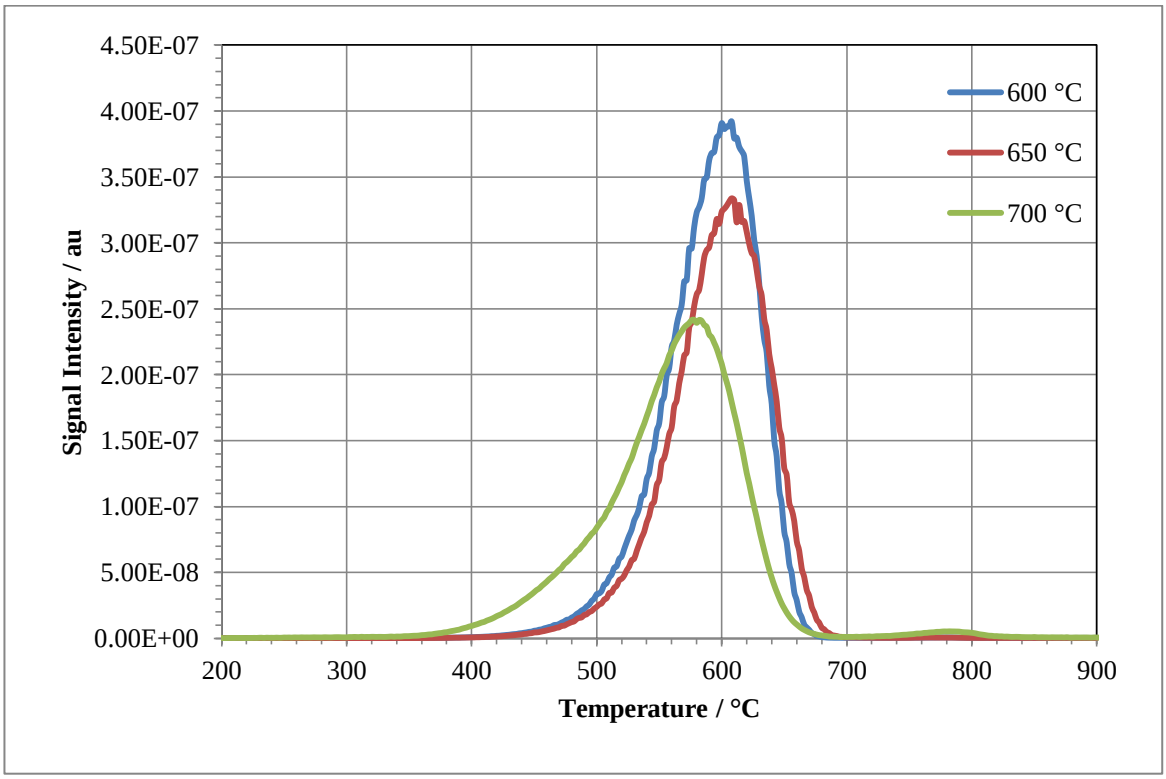

Figure 5-14 TPO profile comparison for 4 mol% Ni doped $SrZrO_3$ following reactions of a 2:1 methane to carbon dioxide dry mixture at 600 °C, 650 °C and 700 °C for 3 hours

Unlike the cermet materials the nickel doped perovskite displayed a single carbon dioxide peak in the post reaction TPO profiles as seen in Figure 5-14 following reaction at 600°C, 350 °C and 700 °C with a slight shift towards lower peak temperature seen at 700 °C. This could suggest that only one form of carbon is being formed over the nickel doped

perovskite catalyst and could link to the perovskite displaying lower propensity toward methane decomposition.

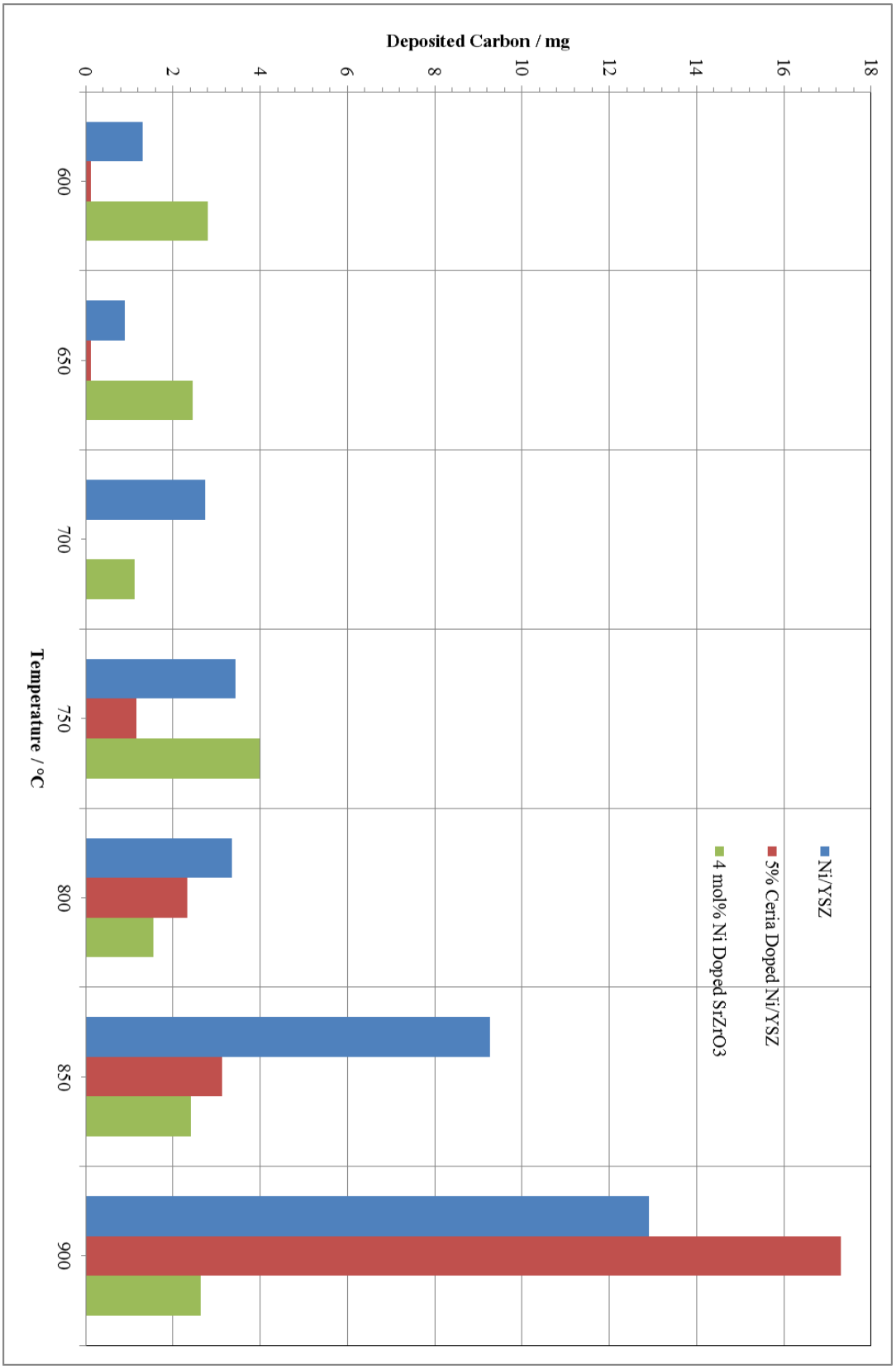

Figure 5-15 Comparison of carbon deposited on Ni/YSZ, 5% ceria doped Ni/YSZ and 4 mol% Ni doped $SrZrO_3$ at various temperatures

The comparison of the amount of carbon deposited on each catalyst after 3 hours of a reaction of a 2:1 methane to carbon dioxide mixture is compared in Figure 5-15. Ni/YSZ shows a trend of generally increased carbon deposition with increasing reaction temperature. This is in agreement with the data that was presented in Figure 5-6 and Figure 5-7 whereby the carbon deposition became high above 750 °C when the carbon dioxide is fully reformed. This is a result of decomposition of methane becoming more prevalent as the reaction becomes more rapid and there is insufficient carbon dioxide for the DRM reaction.

Doping with ceria proves to give the lowest level of carbon deposits of the three catalysts for all reaction temperatures up to 750 °C, due to ceria supressing the Boudouard reaction[17]. Up to 850 °C the carbon deposits on ceria doped Ni/YSZ remain lower than that deposited on the undoped sample. One of the reasons for ceria doping is the ability of ceria to store and release oxygen, and this is why the carbon deposits is suppressed for reaction temperatures up to 850 °C compared to Ni/YSZ[1,18,19]. Ce_2O_3 readily reacts with CO_2 to reform CeO_2 as long as CO_2 is available. At 900 °C the carbon dioxide is fully utilised and as a result cerium remains in the 3+ oxidation state. The cerium therefore has no available oxygen to release to oxidise deposited carbon. As the level of carbon is higher /than for the undoped Ni/YSZ sample at 900 °C the presence of Ce_2O_3 appears to have a negative effect on the amount of carbon deposited at elevated reaction temperatures, possibly due to promoting methane decomposition.

The 4 mol% Ni doped $SrZrO_3$ does not display the trend of increasing carbon deposition with increasing reaction temperature that is displayed by the nickel cermet materials. Instead the amount of carbon deposited remains relatively constant regardless of reaction temperature, with the largest amount of carbon deposited at 750 °C, a result of the perovskite promoting the Boudouard reaction to a far greater extent than the nickel cermets. The small amount of carbon deposited at reaction temperatures above 800 °C is caused by the suppression in methane decomposition compared to the cermet materials that was seen in Figure 5-6.

As the carbon is actually higher than Ni/YSZ and 5% ceria doped Ni/YSZ at lower reaction temperatures it could be inferred that the perovskite promotes the Boudouard reaction more than the cermets, and as a result at higher temperature when unreformed carbon dioxide is still available, promoted the reverse Boudouard reaction resulting in carbon removal. This can be seen in
Figure 5-15 following reaction at 800 °C, the highest temperature where carbon dioxide was still available where the deposited carbon was lowest.

5.4 Long Term Stability of 4 mol% Ni doped $SrZrO_3$ for Methane Rich (simulated biogas) dry reforming at 850 °C

Hydrothermally synthesised 4 mol% Ni doped $SrZrO_3$ was shown to be possess higher activity than Ni/YSZ at lower reaction temperatures and comparable activity to Ni/YSZ at higher reaction temperatures for DRM with methan rich reaction mixtures. This was observed whilst displaying lower deposits of solid carbon at standard SOFC operating temperatures above 700 °C due to suppressed methane decomposition as seen in

Figure 5-15. Although there was no discernible evidence of degradation during these reactions it is important to evaluate the long-term stability of the perovskite catalyst under reaction conditions, and in doing so establish the relationship between time on stream and quantity of carbon deposited.

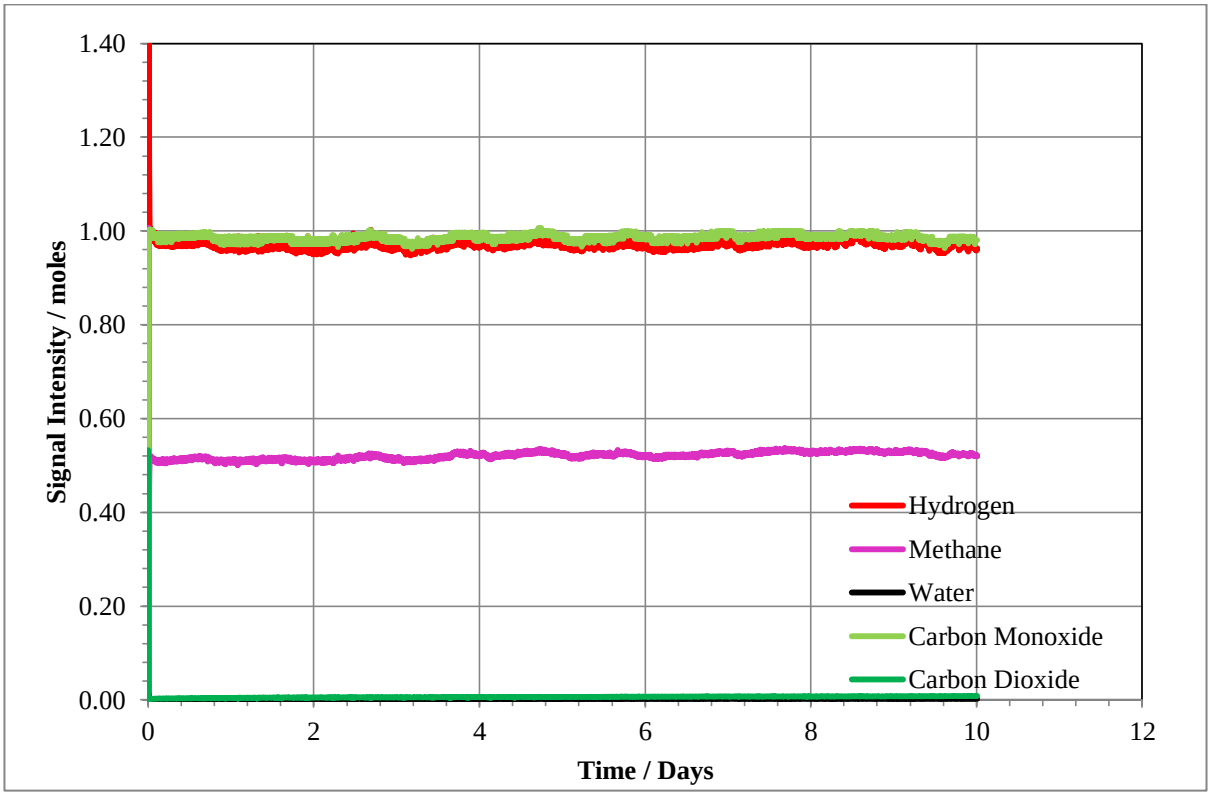

Figure 5-16 Reaction profile of a 2:1 CH_4/CO_2 mixture over 4 mol% Ni doped $SrZrO_3$ for 10 days at 850 °C

Several reactions were performed up to 10 days in length in a 2:1 methane to carbon dioxide reaction mixture in order to establish if there was any decrease in activity with time, and to obtain a carbon deposition with time profile. Figure 5-16 shows the longest of the experiments using the perovskite material with 10 days on stream at 850 °C. The consumption of carbon dioxide remains complete for the full 10 days of the reaction and the consumption of methane is maintained at ~50%. There is no observable formation of

water, and as the H_2:CO ratio is 1, which is stoichiometric for DRM it is assumed that if any side reactions are taking place they are insignificant.

5.4.1 Carbon Deposition

A comparison of the amount of carbon deposited on each catalyst with time of reaction for a 2:1 methane to carbon dioxide reaction mixture at 850 °C is shown in Figure 5-17. Ni/YSZ shows a relationship that is relatively linear with the amount of carbon deposited after 24 hours being more than double the mass of catalyst used at ~ 42 mg. The carbon formation is significantly suppressed by the addition of 5% ceria due to the oxygen storage capacity of ceria, releasing oxygen and as a result oxidising some surface carbon. However, despite this, a linear relationship is still seen between carbon formation and time. The perovskite material shows a carbon with time profile that is different to that of the cermet type materials in that the carbon deposited did not exhibit a clear relationship with time. Instead the amount of carbon remained constant regardless of the reaction time. The variation in mass seen may have been caused by the slight variation in catalyst mass, temperature of operation or flow rate fluctuations. This suggests that carbon formed on the perovskite catalyst may be transiently formed in the first moments of reaction, which coincides with the early consumption of methane observed which quickly subsides, as seen in Figure 5-5 or that a cycle of carbon deposition and carbon removal is occurs on the surface of the perovskite catalyst. This may partly explain why the amount of carbon on the perovskite did not increase with time.

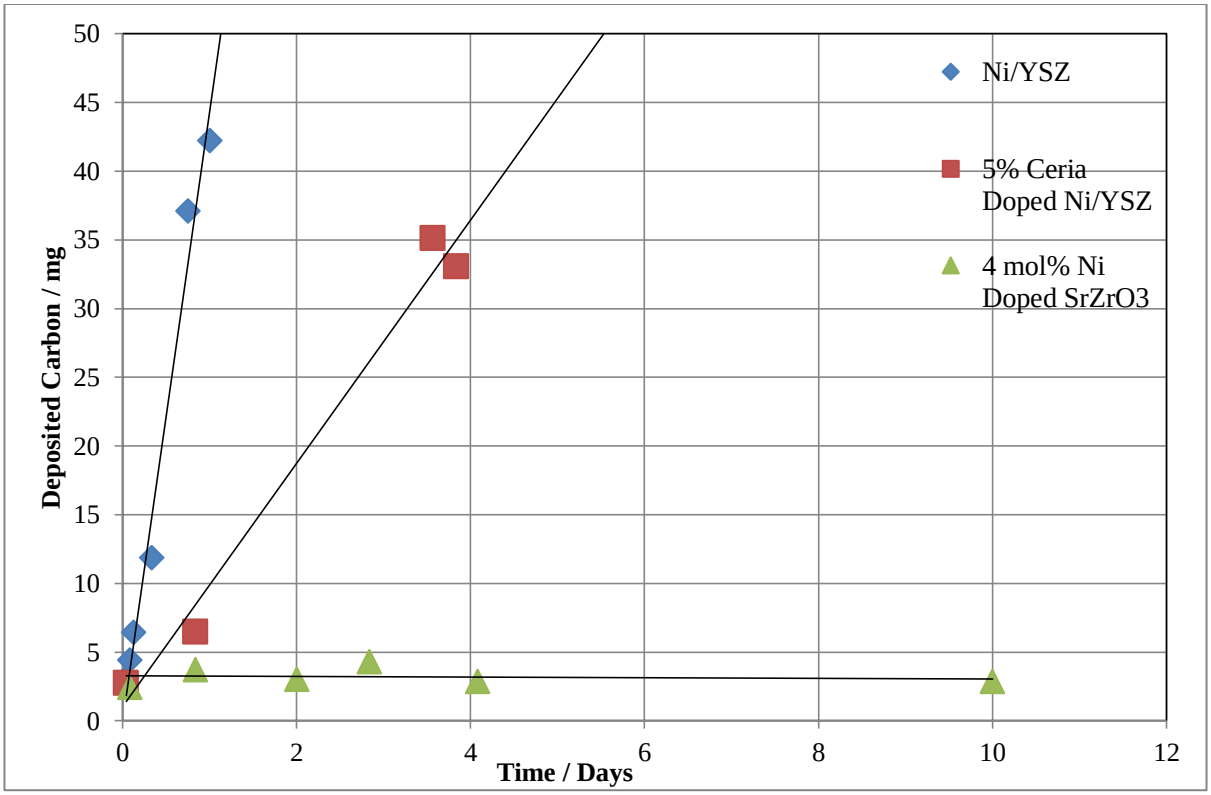

Figure 5-17 Comparison of amount of carbon deposition with reaction time for 2:1 CH_4 to CO_2 mixture over Ni/YSZ, 5% ceria doped Ni/YSZ and 4 mol% Ni doped $SrZrO_3$ at 850 °C

None of the materials showed loss of activity due to carbon deposition over the reaction times teste. However the cermet materials may show signs of physical degradation due to the sheer mass of carbon being formed blocking the flow of reactant gases, Figure 5-17 shows that carbon deposits would clearly continue to increase on the two nickel cermet samples with increasing reaction time.

5.5 Effect of varying the Methane to Carbon Dioxide Ratio

This work has thus far focused on methane rich simulated biogas with methane to carbon dioxide ratio of 2:1. In this section the dry reforming reaction characteristics were investigated when the ratio of methane to carbon dioxide was altered. One of the key reasons for investigating how the reaction chemistry changes with the changing ratio of carbon dioxide to methane is that biogas is highly variable in carbon dioxide and methane content depending on the conditions and biomass source[1,20–23]. The carbon dioxide to methane ratio was increased from 0.1 to 1.1, each reaction was carried out for 20 hours at 850 °C following the procedure outlined in Section 2.5

Figure 5-18 shows the reaction profiles for the different methane/carbon dioxide mixtures over Ni/YSZ at 850 °C. It is seen that whilst the reaction mixture remains methane rich, the synthesis gas formed was rich in hydrogen and the utilisation of methane is above stoichiometric for dry reforming indicative of methane decomposition and thus carbon deposition. Methane is thermally decomposed in all methane rich reactions, shown by the methane consumption and the hydrogen rich nature of the synthesis gas. When then reaction mixture was carbon dioxide rich, the consumption of carbon dioxide was still complete; this was caused by the reverse water gas shift reaction which results in a H_2:CO ratio of less than one and some formation of water. In this case the RWGS reaction is not desirable as it consumes a useful product in hydrogen, forming water.

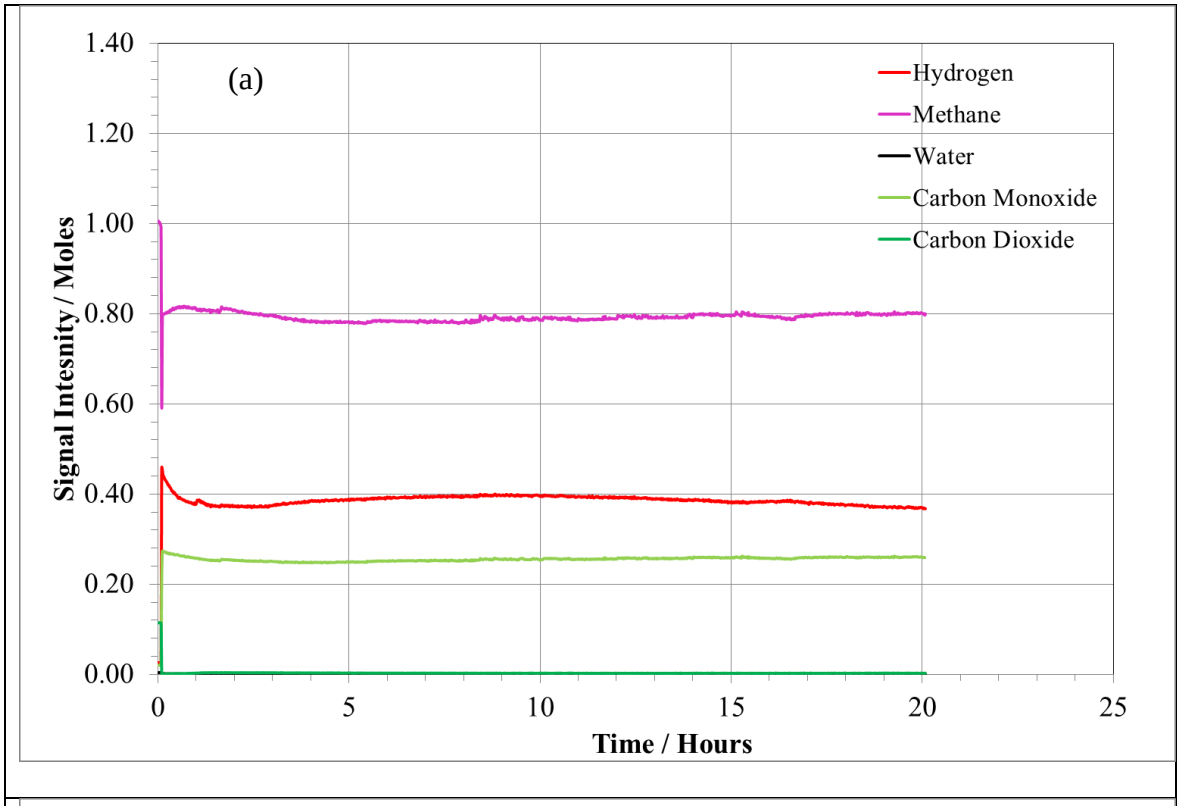
(a)
Signal Intesnity / Moles
1.40
1.20
1.00
0.80
0.60
0.40
0.20
0.00
0
5
10
15
20
25
Time / Hours
Hydrogen
Methane
Water
Carbon Monoxide
Carbon Dioxide

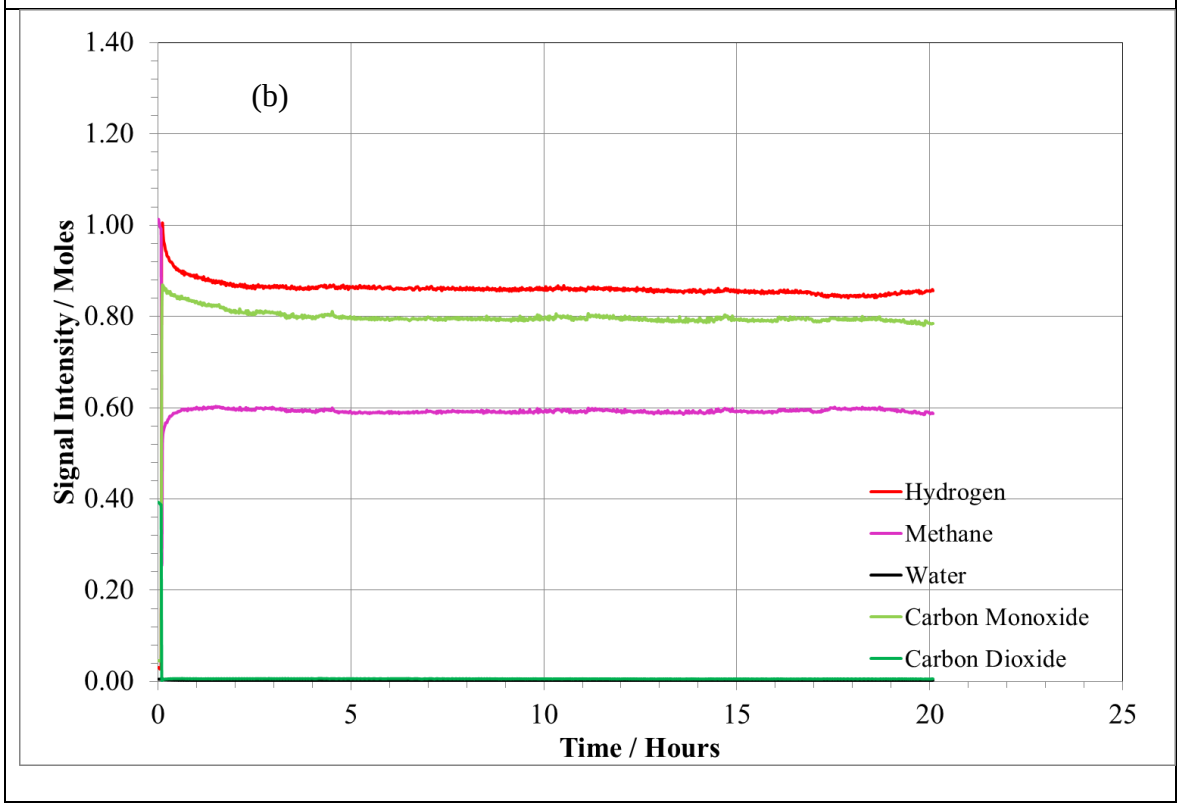
(b)
Signal Intensity / Moles
1.40
1.20
1.00
0.80
0.60
0.40
0.20
0.00
0
5
10
15
20
25
Time / Hours
Hydrogen
Methane
Water
Carbon Monoxide
Carbon Dioxide

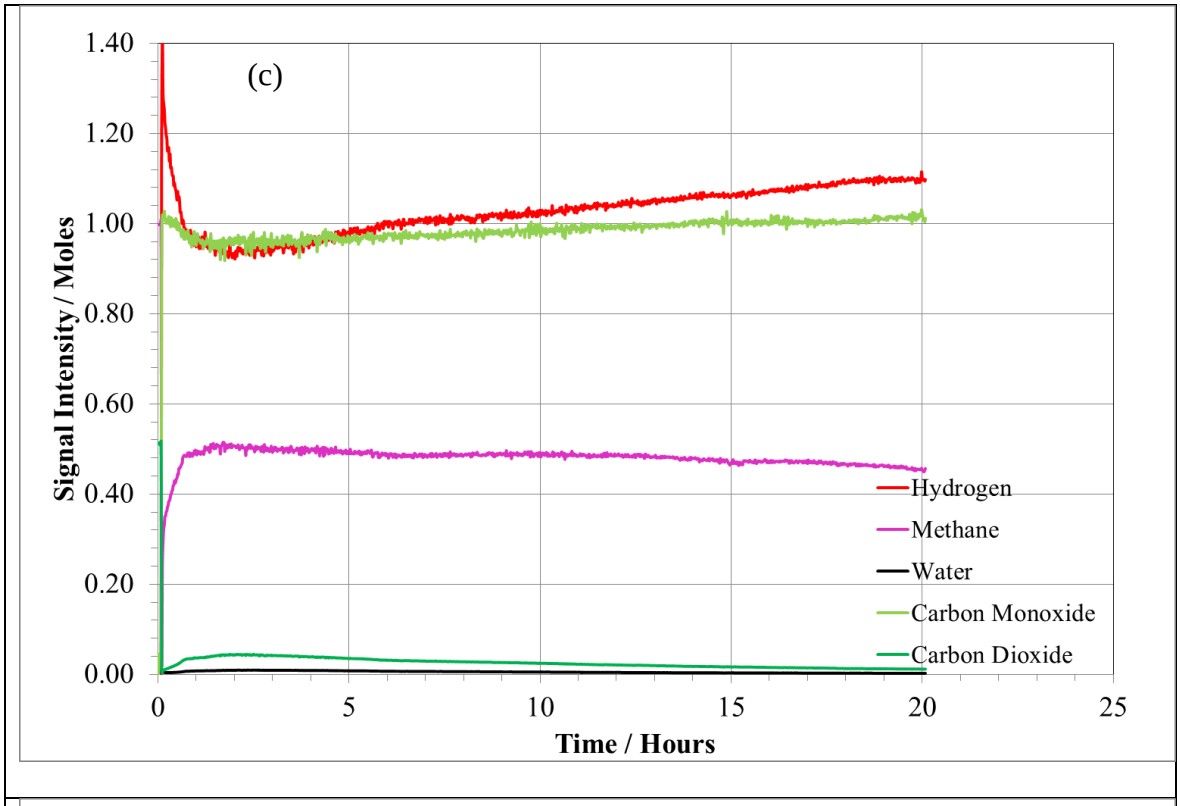
(c)
Signal Intensity / Moles
1.40
1.20
1.00
0.80
0.60
0.40
0.20
0.00
0
5
10
15
20
25
Time / Hours
Hydrogen
Methane
Water
Carbon Monoxide
Carbon Dioxide

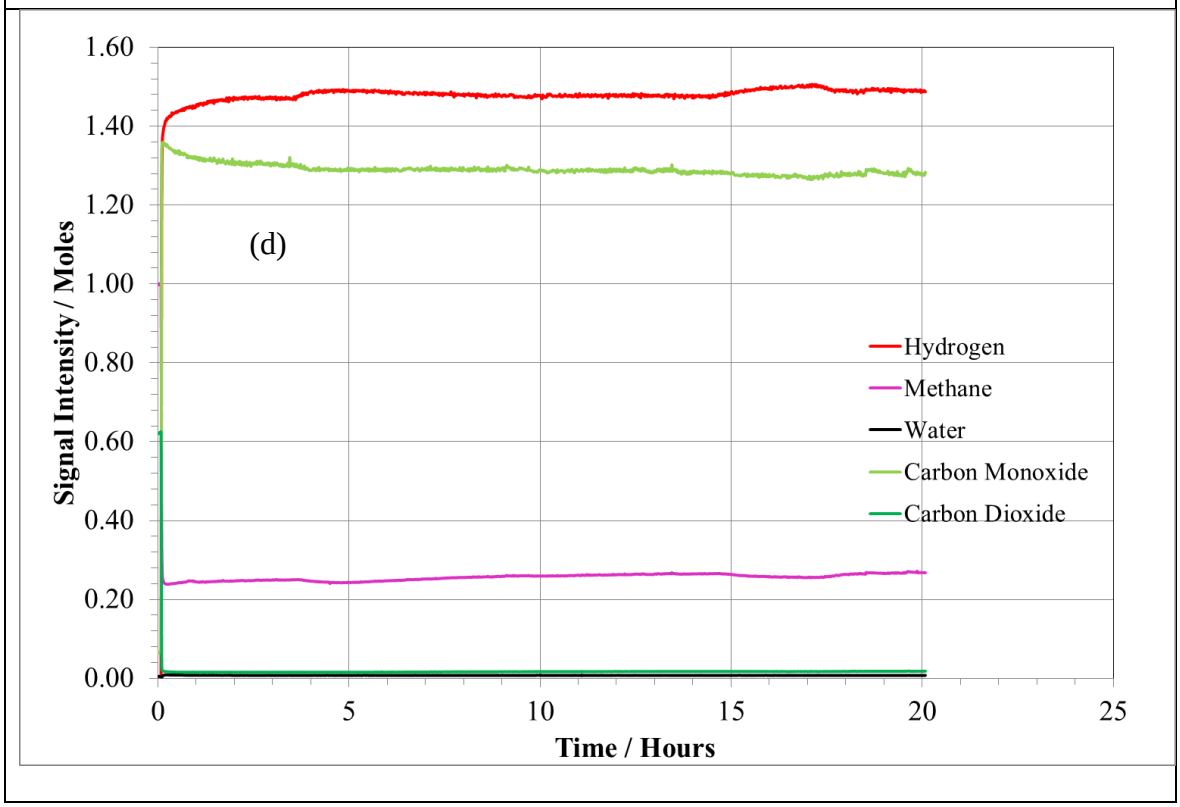
(d)
Signal Intensity / Moles
1.60
1.40
1.20
1.00
0.80
0.60
0.40
0.20
0.00
0
5
10
15
20
25
Time / Hours
Hydrogen
Methane
Water
Carbon Monoxide
Carbon Dioxide

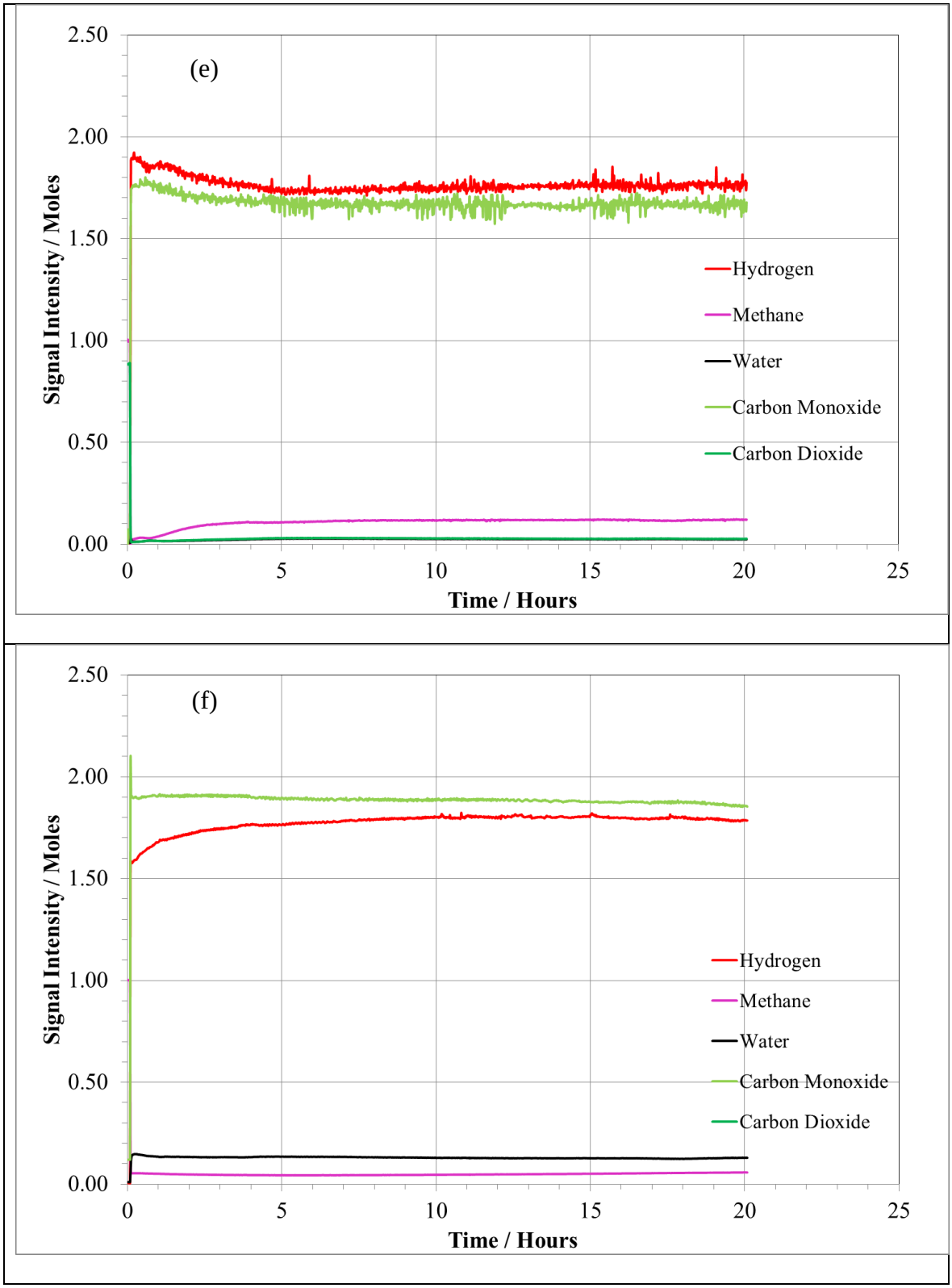

Figure 5-18 Reaction profiles following reaction of methane/carbon dioxide mixtures at 850 °C for 20 hours over Ni/YSZ with a methane to carbon dioxide ratios of : a) 0.1 b) 0.3 c) 0.5 d) 0.7 e) 0.9 f) 1.1

5.5.1 Methane Conversion

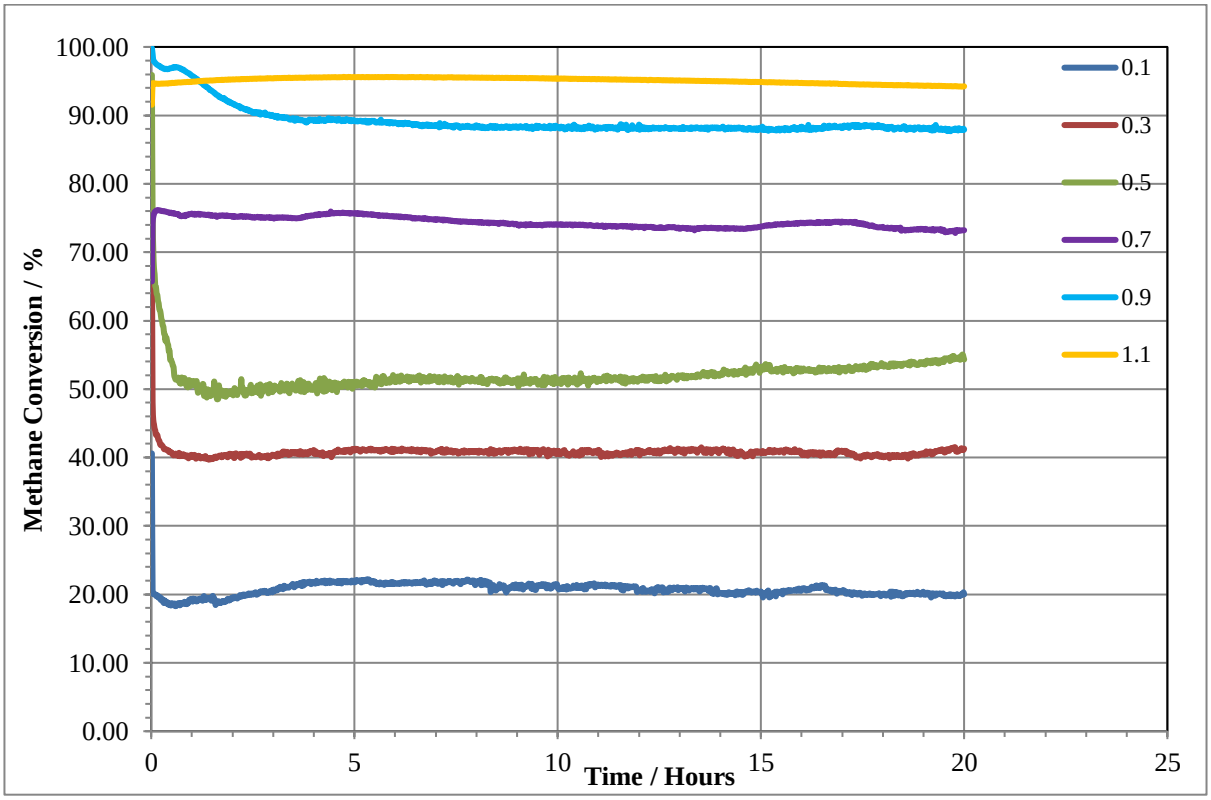

Figure 5-19 Methane conversion following reaction of methane/carbon dioxide mixtures at 850 °C for 20 hours over Ni/YSZ with a methane to carbon dioxide ratios of : a) 0.1 b) 0.3 c) 0.5 d) 0.7 e) 0.9 f) 1.1

Figure 5-19 shows the conversion of methane over Ni/YSZ at 850 °C with varying relative concentration of carbon dioxide to methane. The general trend that is observed is that at lower carbon dioxide concentrations the conversion of excess methane is higher than stoichiometric. As the concentration of carbon dioxide becomes closer to stoichiometric for the DRM reaction the amount of excess methane that is decomposed lessened. The reaction with excess carbon dioxide did not show 100 % methane conversion as might be expected, suggesting that there is another factor limiting the conversion of methane when the concentration of carbon dioxide is higher.

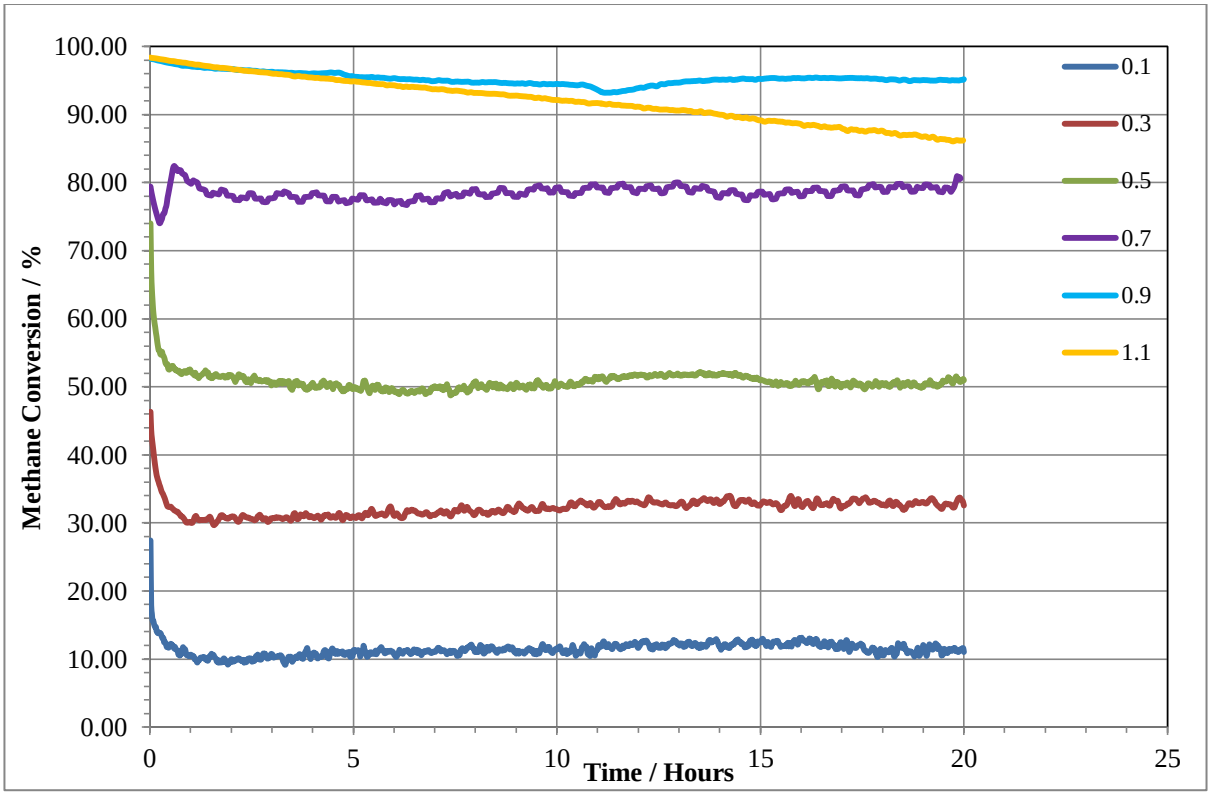

Figure 5-20 Methane conversion following reaction of methane/carbon dioxide mixtures at 850 °C for 20 hours over 5% ceria doped Ni/YSZ with a methane to carbon dioxide ratios of : a) 0.1 b) 0.3 c) 0.5 d) 0.7 e) 0.9 f) 1.1

Doping Ni/YSZ with 5 % ceria altered the methane conversion profiles significantly. At lower concentrations of carbon dioxide the methane conversion is closer to stoichiometrically predicted values than for Ni/YSZ showing that the conversion of excess methane is limited by ceria doping, however above the ratio of 2:1 the cracking of excess methane increased when compared to Ni/YSZ. When the reaction mixture becomes rich in carbon dioxide the methane conversion is seen to decrease with time. This is potentially due to sintering of the nickel particles and as a result loss of reactive area, but may also reflect blocking of active sites. As the carbon dioxide is in excess it is able to react with some hydrogen *via* the reverse water gas shift reaction and as a result water is formed.

Water has previously been shown to promote nickel coarsening when it remains unreacted in a reducing environment[24].

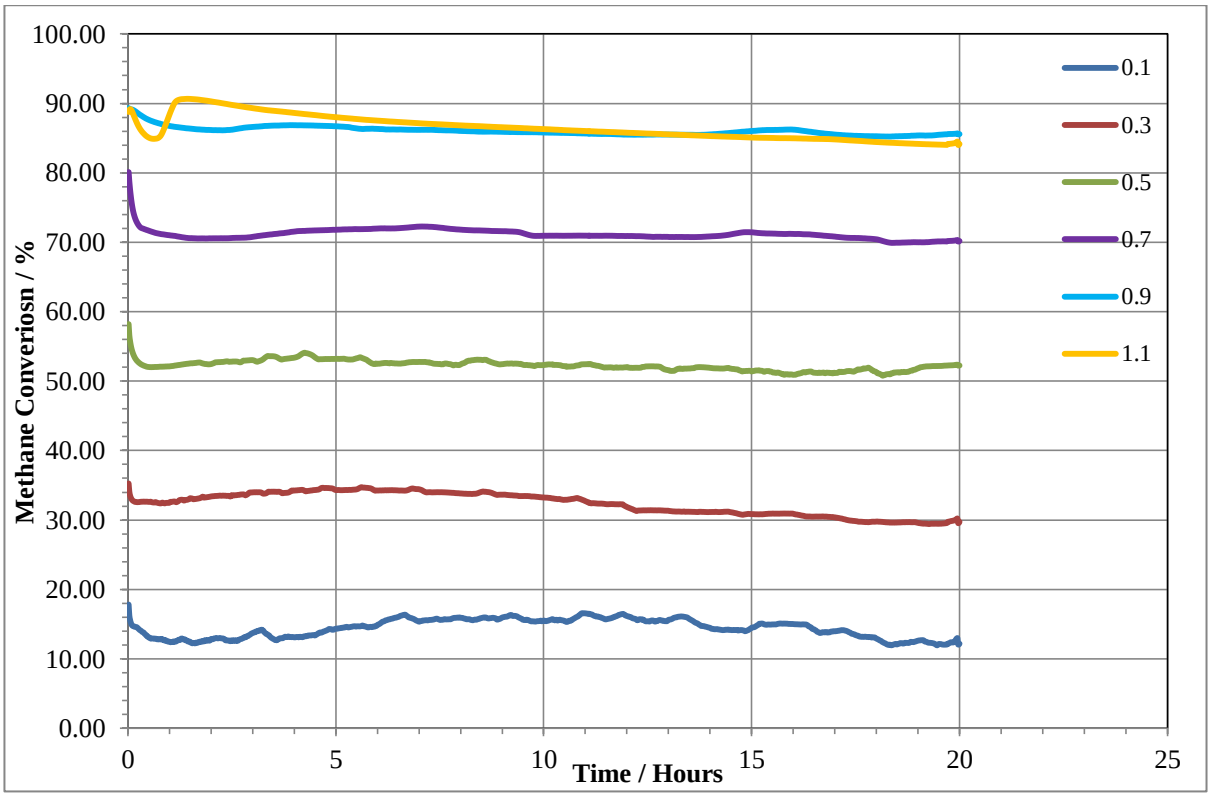

Figure 5-21 Methane conversion following reaction of methane/carbon dioxide mixtures at 850 °C for 20 hours over 4 mol% Ni doped $SrZrO_3$ with a methane to carbon dioxide ratios of: a) 0.1 b) 0.3 c) 0.5 d) 0.7 e) 0.9 f) 1.1

The perovskite catalyst displayed similar stability across the range of carbon dioxide concentrations to that of the cermet materials with no loss of activity seen for the concentration range between 0.1 - 0.9 moles of carbon dioxide relative to methane as seen in Figure 2-21. When the reaction mixture is carbon dioxide rich some loss of reforming activity is seen. However loss of activity is not as pronounced as that observed for 5% ceria doped Ni/YSZ. This loss of activity is possibly as a result of sintering caused by the increased amount of water in the exhaust feed.

5.5.2 Water Formation

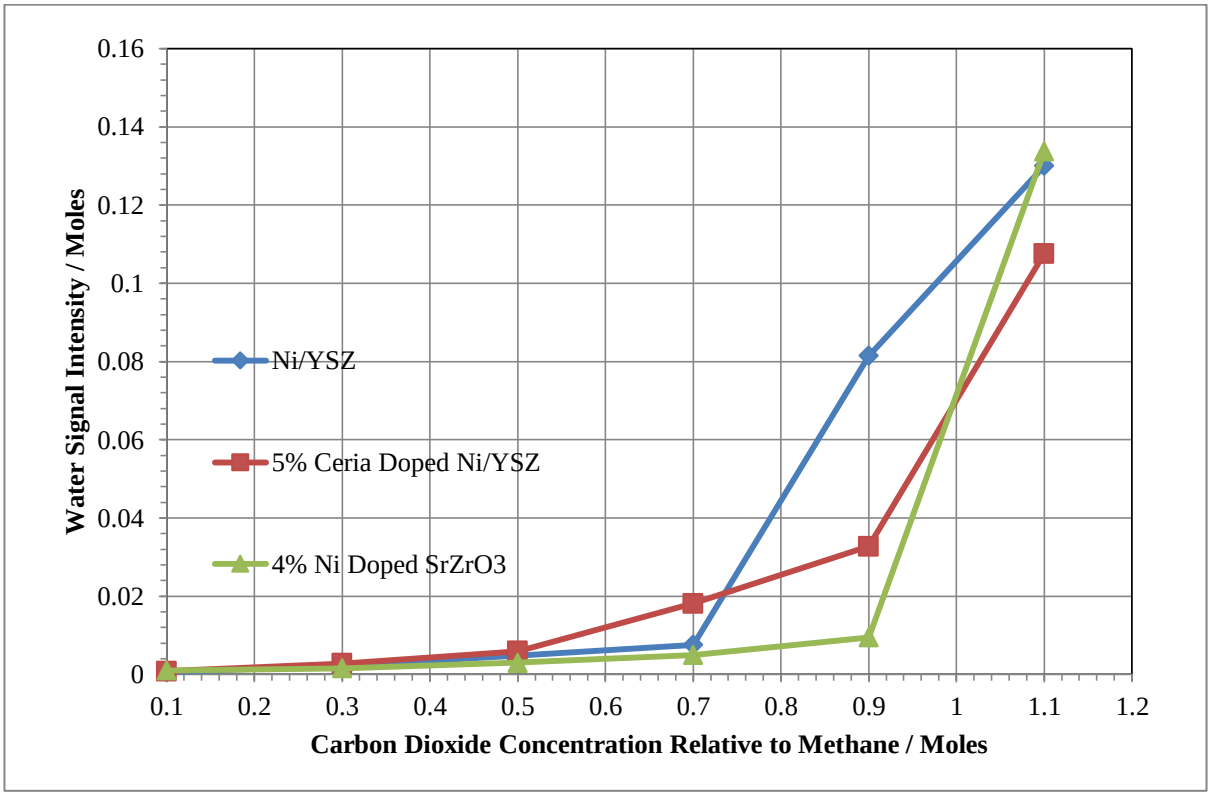

Figure 5-22 Water formation during reaction of methane/carbon dioxide mixtures over Ni/YSZ, 5% ceria doped Ni/YSZ and 4 mol% Ni doped $SrZrO_3$ at 850 °C with variable carbon dioxide concentration

Figure 5-22 shows how the formation of water changes with the carbon dioxide concentration over the three catalyst materials. When the carbon dioxide concentration is lower than 0.7 moles relative to methane, the water formation over all three catalyst materials is negligible. This is a result of the very high selectivity of all three catalysts towards the formation of synthesis gas rather than towards the formation of total oxidation products. After 0.7 moles relative to methane the formation of water for all three samples rose sharply due to the increased amount of carbon dioxide available for the reverse water gas shift reaction. The water formation for all three catalysts was highest when the reaction mixture was rich in carbon dioxide, as although the selectivity towards the formation of synthesis

gas had not lowered, some of the hydrogen being produced was being immediately consumed by reaction with excess carbon dioxide.

5.5.3 Carbon Deposition

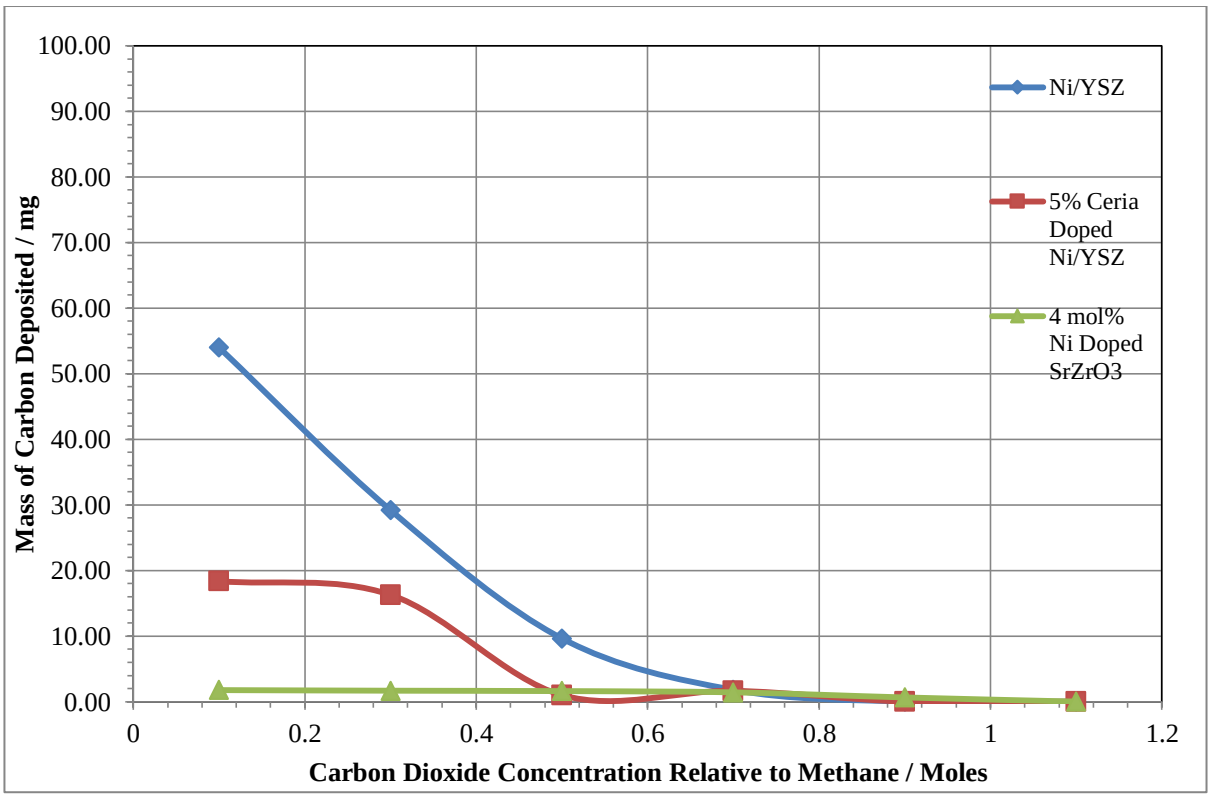

Figure 5-23 Amount of carbon formed following reaction of methane/carbon dioxide mixtures over Ni/YSZ, 5% ceria doped Ni/YSZ and 4 mol% Ni doped $SrZrO_3$ at 850 °C

The variation in the deposited carbon with varying relative concentration of carbon dioxide is shown in Figure 5-23. Ni/YSZ displayed a curve with carbon deposition decreasing as the amount of carbon dioxide available for reforming increased. At the highest ratio of methane to carbon dioxide the deposited carbon outweighed the amount of catalyst used by more than double. As the amount of carbon dioxide available approached the

stoichiometric 1:1 ratio for the DRM reaction the amount of carbon deposited after 20 hours is much less with ~ 1.5 mg deposited (per 20 mg of catalyst). Ceria doping suppressed carbon formation significantly at the higher methane to carbon dioxide concentrations; however the decrease seen in carbon formation was not as severe between 0.1 moles of carbon dioxide and 0.3 moles as was seen for Ni/YSZ.

The perovskite material did not display any real trend between the formation in carbon and the methane to carbon dioxide ratio used. The carbon deposited was low regardless of the composition of the reactant gases in regard to relative concentration of methane and carbon dioxide. This is attributed to a far lower propensity to thermally decompose excess methane in comparison to the cermet materials. The reaction temperature used (850 °C) is not thermodynamically favourable for the Boudouard reaction so this was thought to play a less than significant role in the change in carbon formation seen.

5.6 Conclusions

Detailed analysis of the reaction profiles has shown that the perovskite maintains a H_2:CO product ratio of ~1 even at higher reaction temperatures. This was because at higher reaction temperatures (> 800 °C), the perovskite catalyst was much less susceptible to decomposition of excess methane compared to Ni/YSZ or 5% ceria doped Ni/YSZ. This was reflected in the extent of carbon deposition which was significantly lower for 4% Ni doped $SrZrO_3$ at temperatures above 750 °C. Below 750 °C the perovskite gave rise to more carbon formation than the nickel cermet materials, which was attributed to promoting the Boudouard reaction to a greater extent than the cermet materials.

The long term performance and stability of the perovskite material was tested for up to ten days using methane rich simulated biogas (2.1 methane: carbon dioxide ratio) at 850 °C. A carbon deposition as a function of time on stream plot was constructed to compare the quantity of carbon deposition with that of Ni/YSZ and 5% ceria doped Ni/YSZ. The reaction was shown to be very stable over the perovskite material for the full ten days of reaction with no discernible loss in reforming activity. The deposition of carbon was found to be significantly less than Ni/YSZ and ceria doped Ni/YSZ and the deposition displayed no correlation with the time on stream. The cermet materials displayed a linear relationship between deposited carbon and time on stream. This difference was attributed to the perovskite having a far lower propensity towards decomposing excess methane, whereas the nickel cermets are active towards methane decomposition throughout the reaction lifetime.

The perovskite material was shown to be highly effective in forming synthesis gas *via* the dry reforming of methane reaction regardless of the methane to carbon dioxide ratio used. Importantly the amount of carbon formed on the perovskite catalyst was shown to remain very low, regardless of how much carbon dioxide was present in the reaction mixture. This trait is important if the material is to be used as a DRM catalyst for utilising biogas as the methane to carbon dioxide ratio can change significantly. Ni/YSZ and ceria doped Ni/YSZ were shown to form large deposits of carbon when the amount of carbon dioxide present was low.

The work in this chapter has shown that 4 mol% Ni doped $SrZrO_3$ is a very good catalyst for reforming simulated methane rich, sulphur free biogas. Although more work is

required the material has been shown to have promise as a reforming anode for use in SOFCs.

In order to fully establish suitability, more work is required, including sulphur contamination and with low levels of humidity to give a better biogas model. If the catalyst is shown to be stable and effective under these conditions it would then be of interest to attempt to use the material as either a reforming catalyst in conjunction with a Ni/YSZ anode, or as a direct replacement for Ni/YSZ, if the material is shown to possess the required conductivity and compatibility with existing electrolyte materials.

5.7 References

1 C. J. Laycock, J. Z. Staniforth and R. M. Ormerod, *Dalt. Trans.*, 2011, **40**, 5494.

2 S. P. Jiang and S. H. Chan, *J. Mater. Sci.*, 2004, **39**, 4405–4439.

3 N. P. Brandon and D. Thompsett, Eds., *Fuel Cells Compendium*, Elsevier, First Edit., 2005.

4 G. J. Offer, J. Mermelstein, E. Brightman and N. P. Brandon, *J. Am. Ceram. Soc.*, 2009, **92**, 763–780.

5 J. Myung, J.-J. Lee and S.-H. Hyun, *Electrochem. Solid-State Lett.*, 2010, **13**, B43.

6 D. J. Nixon, PhD Thesis, Keele University, 2013.

7 J. Jia, E. Tanabe, P. Wang, K. Ito, H. Morioka, Y. Wang and T. Shishido, *Catal. Letters*, 2001, **76**, 183–192.

8 C. Xu, J. W. Zondlo, M. Gong, F. Elizalde-Blancas, X. Liu and I. B. Celik, *J. Power Sources*, 2010, **195**, 4583–4592.

9 H. Arandiyan, J. Li, L. Ma, S. M. Hashemnejad, M. Z. Mirzaei, J. Chen, H. Chang, C. Liu, C. Wang and L. Chen, *J. Ind. Eng. Chem.*, 2012, **18**, 2103–2114.

10 S. C. Singhal and K. Kendall, *High Temperature Solid Oxide Fuel Cells: Fundamentals, Design and Applications*, Elsevier B.V., 2003.

11 A. S. A. Al-Fatesh and A. H. Fakeeha, *J. Saudi Chem. Soc.*, 2012, **16**, 55–61.

12 M. Yoshinaga, H. Kishimoto, K. Yamaji, Y. P. Xiong, M. E. Brito, T. Horita and H. Yokokawa, in *Solid State Ionics*, Elsevier B.V., 2011, vol. 192, pp. 571–575.

13 S. E. Evans, J. Z. Staniforth, R. J. Darton and R. M. Ormerod, *Green Chem.*, 2014, **16**, 4587–4594.

14 J. H. Edwards and A. M. Maitra, *Fuel Process. Technol.*, 1995, **42**, 269–289.

15 J. A. Moulijn, A. E. Van Diepen and F. Kapteijn, *Appl. Catal. A Gen.*, 2001, **212**, 3–16.

16 H. He and J. M. Hill, *Appl. Catal. A Gen.*, 2007, **317**, 284–292.

17 S. L. Suib, Ed., *New and Future Developments in Catalysis: Catalysis by Nanoparticles*, Elsevier, Oxford, 2013.

18 P. Fornasiero, M. Graziani and J. Kas, *Catal. Today*, 1999, **50**, 285–298.

19 V. M. Shinde and G. Madras, *RSC Adv.*, 2014, **4**, 4817.

20 D. Deublein and A. Steinhauser, *Biogas from Waste and Renewable Resources An Introduction*, Wiley-VCH, Weinheim, 2008.

21 J. Singh and S. Gu, *Renew. Sustain. Energy Rev.*, 2010, **14**, 1367–1378.

22 A. Lanzini and P. Leone, *Int. J. Hydrogen Energy*, 2010, **35**, 2463–2476.

23 S. S. Kapdi, V. K. Vijay, S. K. Rajesh and R. Prasad, *Renew. Energy*, 2005, **30**, 1195–1202.

24 W. Z. Zhu and S. C. Deevi, *Mater. Sci. Eng. A*, 2003, **362**, 228–239.

6 Humidified Simulated Biogas Reforming over Nickel Doped $SrZrO_3$, Ni/YSZ and Ceria Doped Ni/YSZ Cermet Materials

6.1 Introduction

Whilst a 2:1 methane to carbon dioxide mixture is a good, simple representation of biogas in the first instance, natural sources of biogas are always saturated with water[1–4]. The work in chapters four and five has used a dry source of simulated biogas. In this chapter, the simulated mixture used was humidified to more closely mimic biogas that would be attained naturally in landfill sites or from specially designed biogas digesters[2,4,5].

Supported nickel based catalysts including Ni/YSZ, have been previously shown to suffer degradation due to agglomeration of nickel particles and thus loss of reforming area when methane is reformed under 'wet' conditions[6,7]. It is not known whether this is the case for the perovskite based catalysts developed for this work under the same reforming conditions[8–11]. 'Sintering' or agglomeration has been shown to be correlated to reaction temperature and also to steam content, with an increase in either increasing sintering of supported nickel based supported catalysts[12]. It is important for supported nickel catalysts crystallite size to remain as small as possible as it has been previously shown that formation of carbon is inhibited on crystals below a critical size[13]. This may play a key role in the perovskite material maintaining a non-linear relationship between time on stream and carbon deposited as was seen in the previous chapter.

In order to create the low level of humidity observed in real biogas, once the gases were combined in the manifold they were then directed through a saturator containing water

maintained between 0 – 1 °C, in order to give a flow rate of 0.13 ml min^{-1} in a 20 ml min^{-1} total flow. The humidified gases were then sent to the reactor as described previously.

Ni/YSZ, 5% ceria doped Ni/YSZ and 4 mol% Ni doped $SrZrO_3$ were all tested initially on a temperature programme of 5 °C min^{-1} ramp up to 1000 °C before TPO analysis was performed. The temperature programme was analysed in order to identify the change in reaction profile changed with temperature and also has the addition of water effected the reactions taking place. Catalytic reactions were then subsequently carried out over each catalyst at 600 °C, 700 °C, 800 °C, 850 °C and 900 °C for 3 hours. Reactions of varying duration between 1 hour and 48 hours were utilised in order to elucidate a relationship between time on stream and deposition of solid carbon.

With the addition of 0.1 moles of water relative to methane in each reaction it is important to note that for pure combined steam and methane reforming the theoretical maximum methane conversion is 60%. Any conversion of methane above 60% cannot be solely attributed to a combination of dry reforming and steam reforming of methane.

6.2 Temperature Programmed Reaction Spectroscopy

Temperature programmed reaction profiles were used in order to identify what reactions were taking place, in addition to the reactions seen in the profiles without water. Figure 6-1 shows the humidified temperature programmed biogas reformation profile for Ni/YSZ, 5% ceria doped Ni/YSZ and 4 mol% Ni doped $SrZrO_3$. The dry reforming reaction starts at ~ 425 °C with some initial water consumption. This consumption is likely to be caused, at least in part, by the water gas shift reaction occurring due to the temperature being

relatively low for steam reforming. As the temperature increased to ~ 550 °C the water levels in the exhaust feed rose. This is because although the water gas shift reaction becomes faster with increasing temperature, the thermodynamics of the reaction start to favour reactants rather than products. This is seen in the hydrogen to carbon monoxide ratio which becomes closer to 1 by ~ 550 °C and also in that the consumption of carbon dioxide shows a small plateau. Above 600 °C the water levels again dropped and this is attributed to steam reforming of methane becoming more favoured. Above 700 °C methane consumption increased greatly such that all water and carbon dioxide is consumed by ~ 850 °C and by 1000 °C methane conversion was ~ 80 %. As both DRM and SRM are a ratio of 1:1 oxidant to methane reactions the theoretical conversion of methane if only these reactions were occurring should be ~ 60%. Thus a large amount of decomposition of excess methane is clearly occurring at elevated temperatures.

Doping with ceria resulted in a profile that is subtly different to the profile of undoped Ni/YSZ. The reforming reaction begins at a similar temperature to that of Ni/YSZ. However in the early reforming phase up to 700 °C, the H_2:CO ratio did not display a transient increase as was seen for Ni/YSZ. This suggests that ceria doping suppresses the waster gas shift reaction.

The temperature programmed reaction profile for 4 mol% Ni doped $SrZrO_3$ shows that this material began reforming at about the same temperature as the cermet materials. Unlike the nickel cermet materials the initial consumption of water is relatively low, and the DRM reaction is seen to proceed with the water appearing to initially act only as a spectator species. Up to 600 °C methane and carbon dioxide consumption increased linearly and the water consumption remained constant. There is no evidence of the water gas shift reaction

in this initial reaction period and this is reflected in the H_2:CO ratio being maintained at ~1. Between 600 °C and 800 °C an increase in hydrogen production and methane consumption is seen. This may be a result of a kinetic and thermodynamic balance being achieved making the Boudouard reaction prevalent. As the Boudouard reaction produces carbon dioxide, this is then consumed in turn by the DRM reaction resulting in almost complete methane consumption. As the temperature increases above 800 °C the Boudouard reaction becomes thermodynamically unfavourable despite the increase in kinetics and as a result methane consumption dropped, as did hydrogen formation. Although this gave a temperature range gave the greatest conversion of reactants and formation of products, it is also a regime where formation of carbon was high. By 800 °C water production is complete and this was seen in the hydrogen rich nature of the synthesis gas produced.

6.2.1 Water Conversion

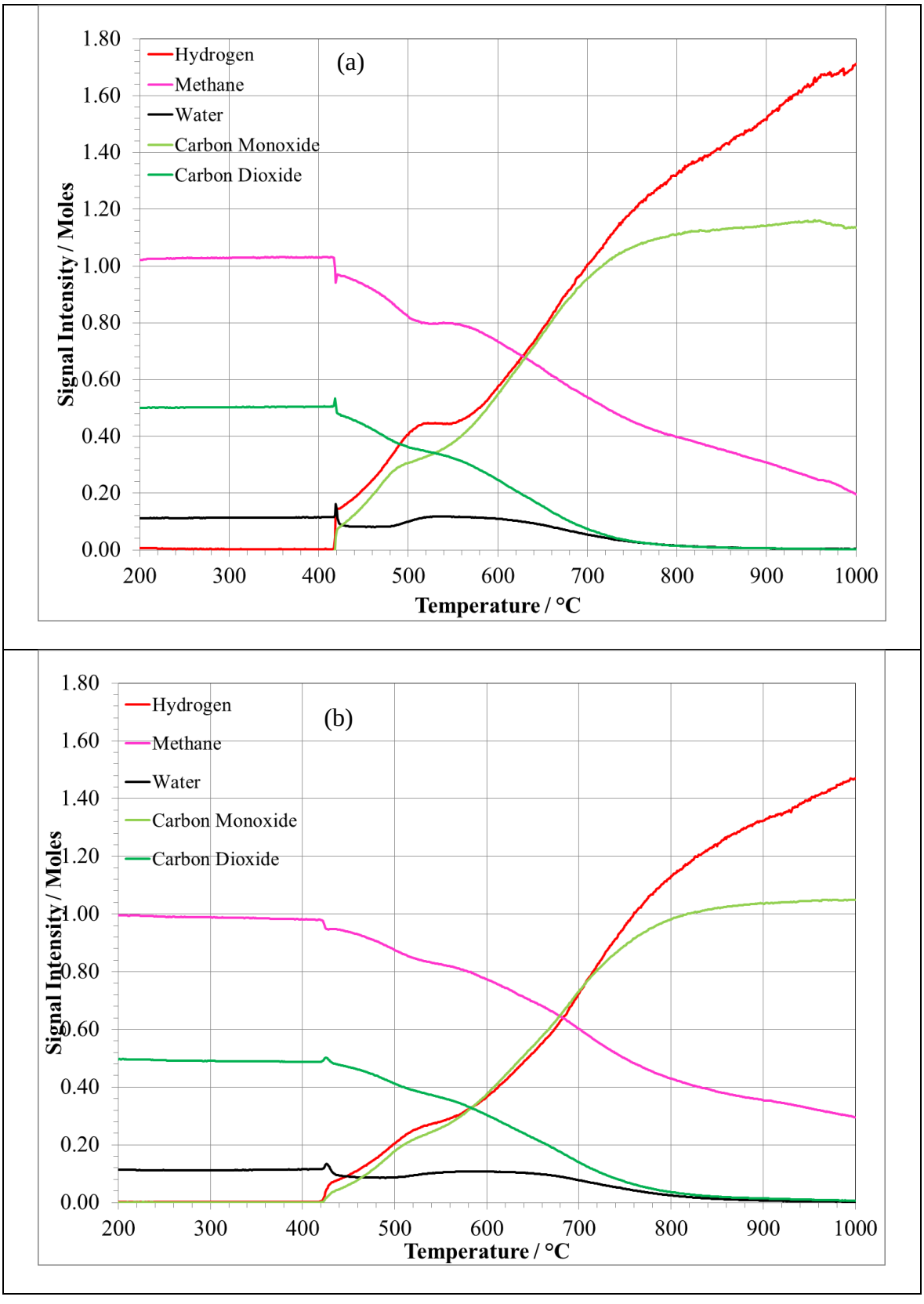

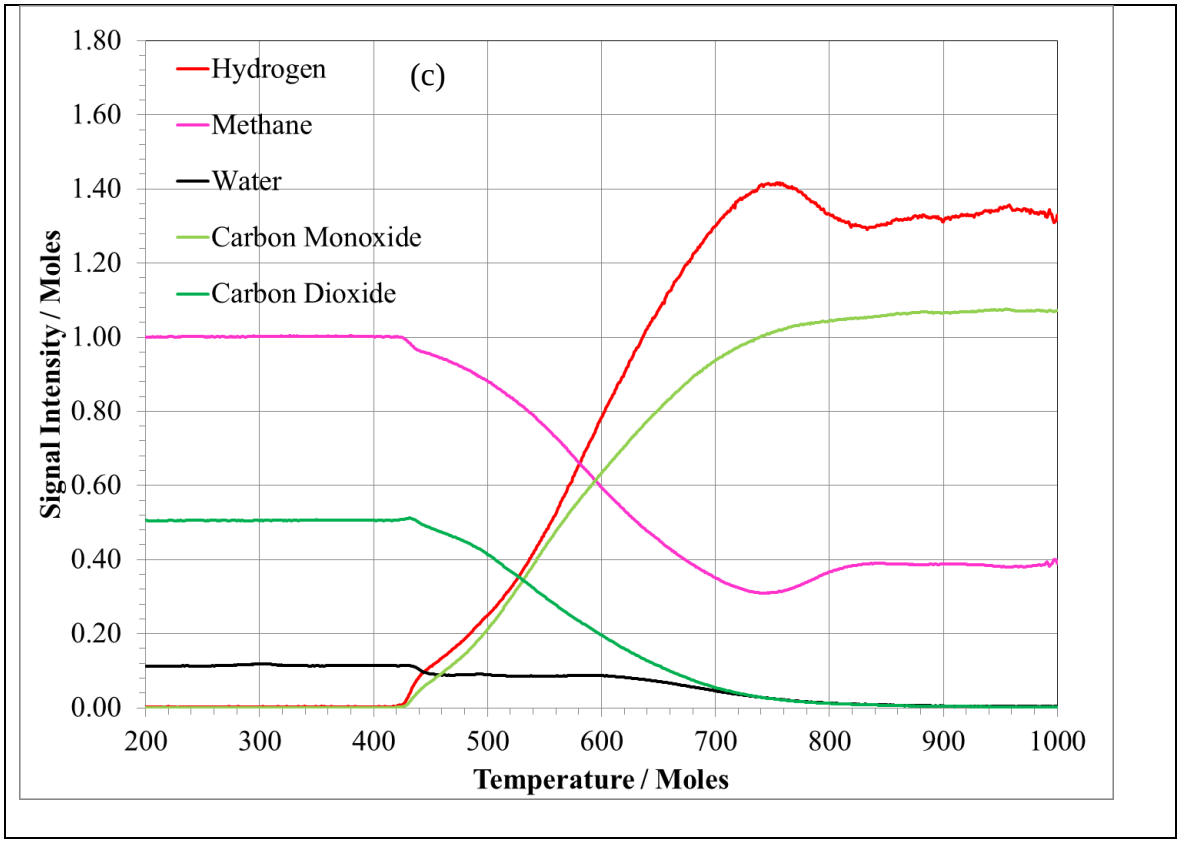

Figure 6-1 Temperature programmed reaction of humidified methane/ carbon dioxide mixture (methane: carbon dioxide = 2:1) over (a) Ni/YSZ (b) 5% ceria doped Ni/YSZ (c) 4 mol% Ni doped $SrZrO_3$

Figure 6-2 compares the water conversion for the three materials tested. All three materials convert around 25% of the water in the initial reaction phase which is attributed to the water gas shift reaction for the nickel cermet materials. This is substantiated by the occurrence of the reverse water gas shift reaction as the temperature increases as seen by the negative water conversion for both Ni/YSZ and the ceria doped sample between 400 °C and 600 °C. Although the perovskite shows a similar low temperature conversion of water, it does not display any evidence of the reverse water gas shift reaction. Instead water conversion remains fairly constant. Above 600 °C all three materials show linearly

increasing water conversion as the water is consumed by methane steam reforming, which plateaus as water conversion becomes almost complete by 1000 °C.

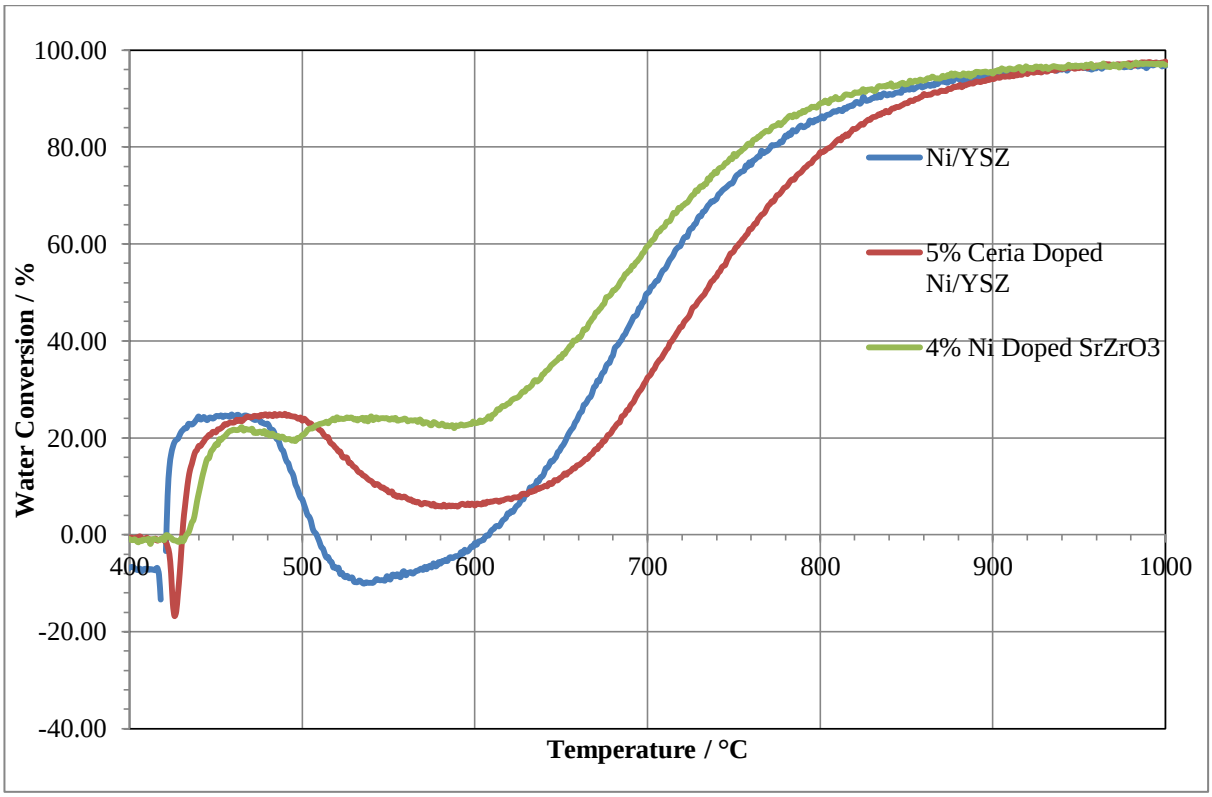

Figure 6-2 Water conversion for temperature programmed reaction of humidified methane/ carbon dioxide mixture (methane: carbon dioxide = 2:1) over Ni/YSZ, 5% ceria doped Ni/YSZ, 4 mol% Ni doped $SrZrO_3$

6.2.2 Methane Conversion

The methane conversion over the temperature programmed humidified biogas reforming reaction is shown in

Figure 6-3. It can be seen that the conversion of methane begins at ~ 425 °C for all three of the catalyst materials tested. The nickel cermet materials both follow a similar trend with the undoped material having a higher methane conversion at all reaction temperatures. Both cermet materials reach the theoretical maximum methane conversion for the reforming reaction at ~ 775 °C and then continue to consume methane *via* the pyrolysis of

methane. The perovskite material shows a much faster rate of conversion of methane than the two cermet materials, reaching the theoretical maximum methane conversion for the humidified DRM reaction by ~ 650 °C. Methane conversion continues to increase until ~ 700 °C, but then despite the continued temperature increase, the conversion of methane decreases as a result of a decrease in prevalence of the Boudouard reaction, limiting the amount of carbon dioxide available for the DRM reaction. By 1000 °C the methane conversion for the perovskite material fell to the theoretical maximum of 60 % for the humidified DRM reaction as no more carbon dioxide being created.

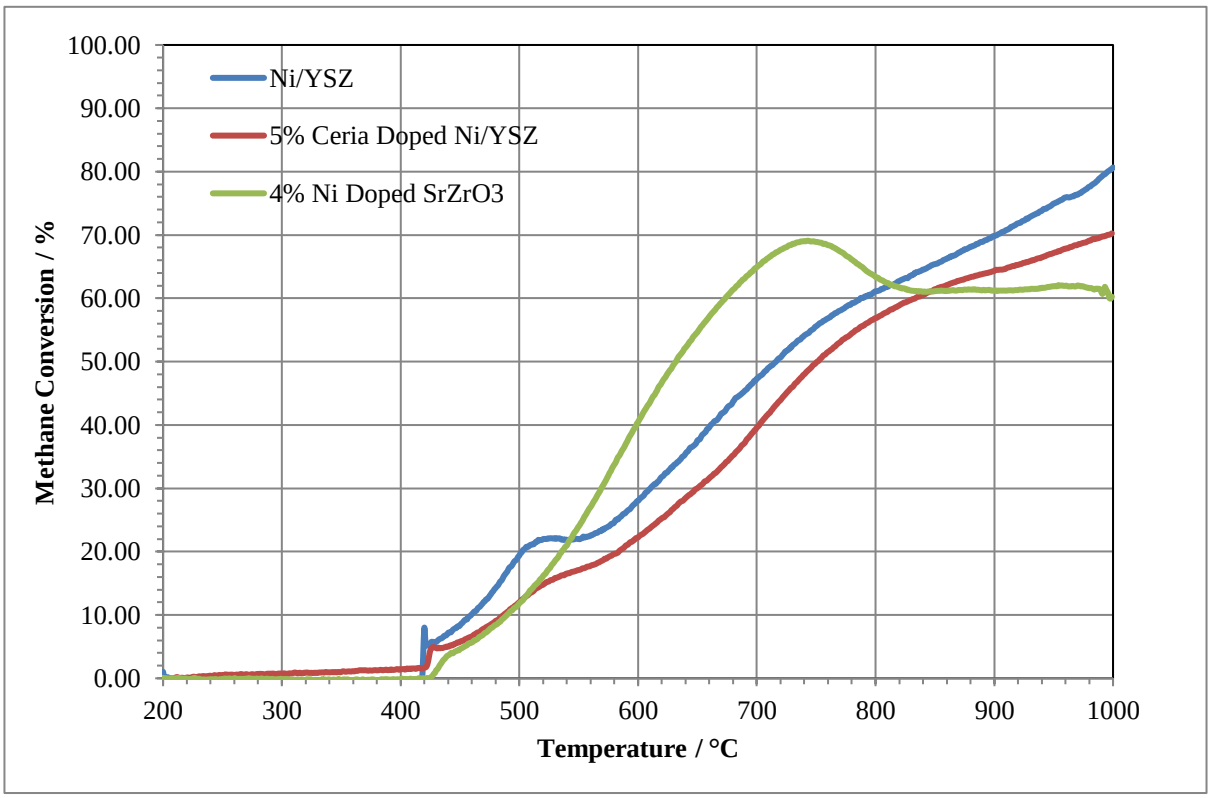

Figure 6-3 Methane conversion for temperature programmed reaction of humidified methane/ carbon dioxide mixture (methane: carbon dioxide = 2:1) over Ni/YSZ, 5% ceria doped Ni/YSZ, 4 mol% Ni doped $SrZrO_3$

6.2.3 Carbon Dioxide Conversion

From the carbon dioxide conversion in

Figure 6-4 it was possible to identify the presence of a period of the reverse water gas shift reaction occurring for the cermet materials between ~ 500 °C and ~ 550 °C. This is identified from the change in the gradient of the conversion curve caused by the formation of carbon dioxide by this reaction. This is not evident for the perovskite material which profile displays no evidence of a plateau. Despite having the highest onset temperature for the carbon dioxide conversion the perovskite is the first to fully utilise all of the available carbon dioxide (~ 920 °C). All three materials fully reform the available carbon dioxide by the end of the reaction. The conversion of carbon dioxide by the ceria doped sample follows the same profile of the undoped sample but with lower conversion in the same fashion as the methane conversion.

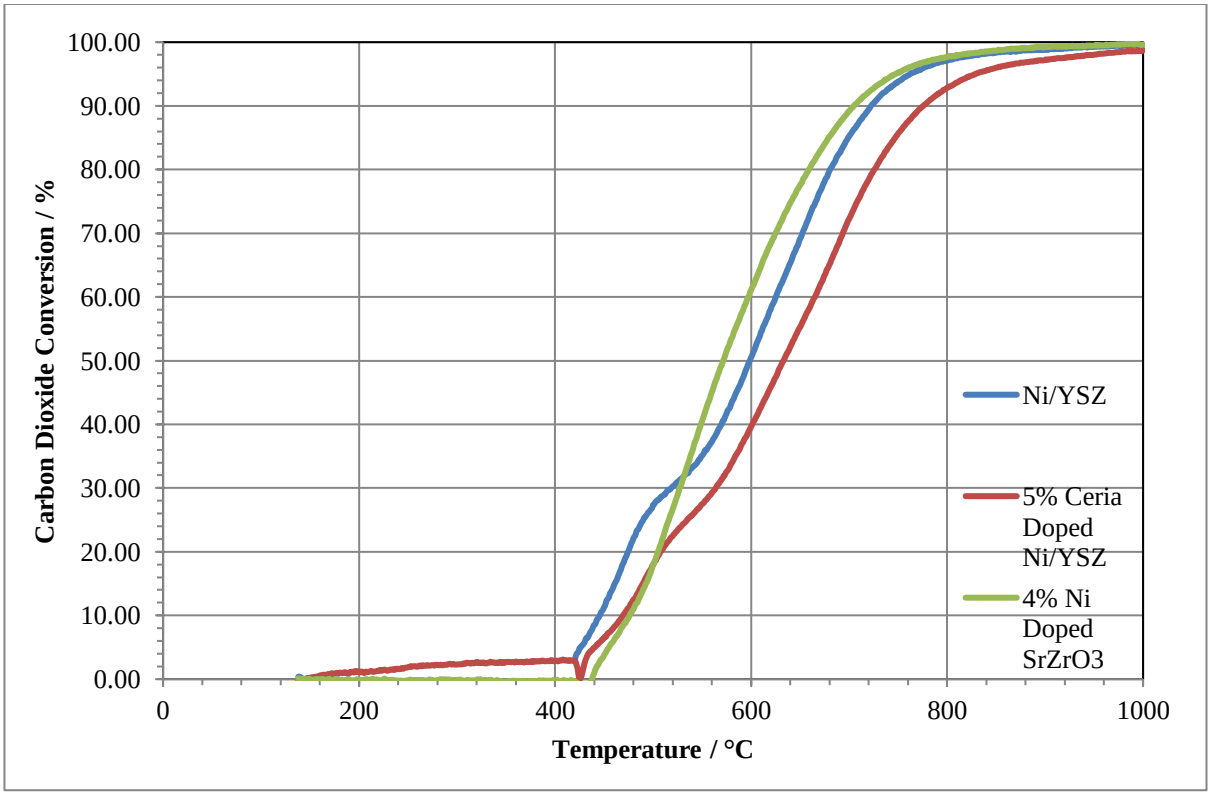

Figure 6-4 Carbon dioxide conversion for temperature programmed reaction of humidified methane/ carbon dioxide mixture (methane: carbon dioxide = 2:1) over Ni/YSZ, 5% ceria doped Ni/YSZ, 4 mol% Ni doped $SrZrO_3$

6.3 Comparison of humidified and non-humidified simulated biogas reforming over 4 mol% Ni Doped $SrZrO_3$.

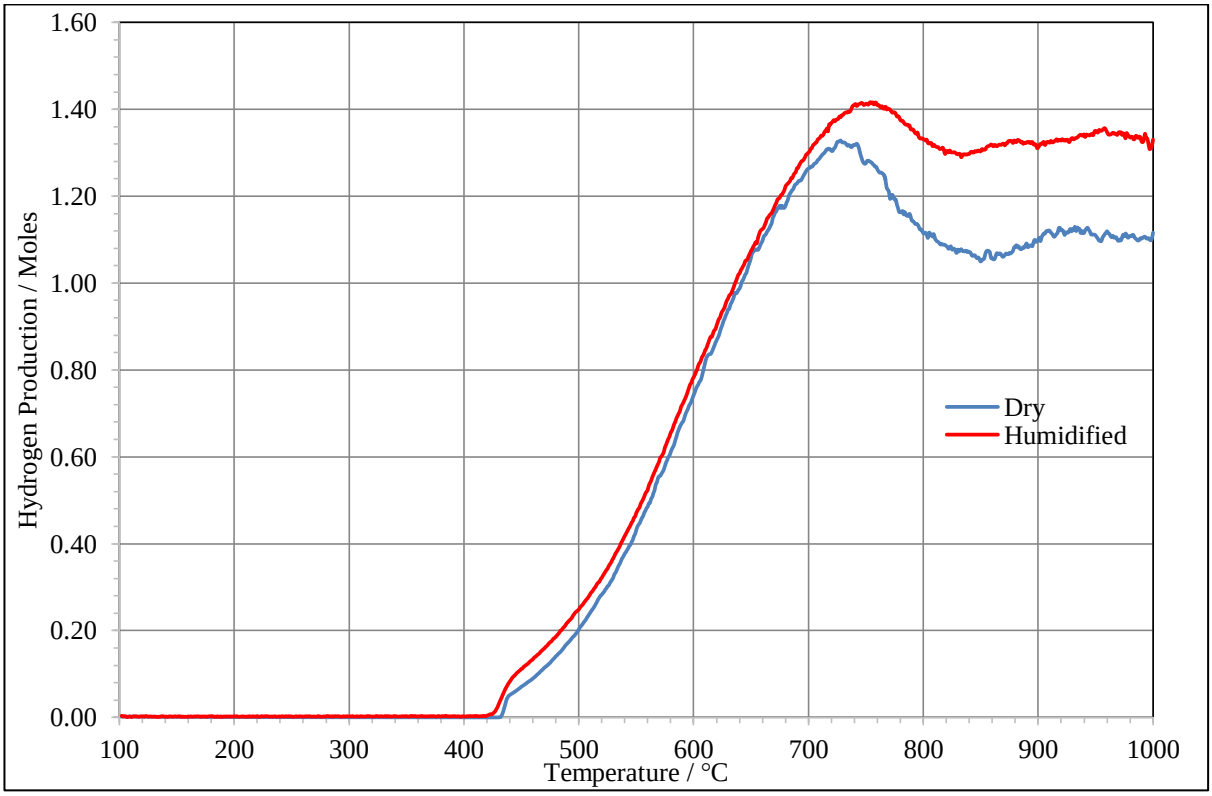

Figure 6-5 Hydrogen production for temperature programmed reaction of humidified methane/ carbon dioxide mixture (methane: carbon dioxide = 2:1) over 4 mol% Ni doped $SrZrO_3$.

The addition of 10% steam relative to methane content has little effect on the onset of the reaction over the perovskite material, as both the humidified and the non-humidified reaction start at ~ 425 °C as seen in Figure 6-5 and Figure 6-6. The hydrogen formation, as can be seen in Figure 6-5 was then almost identical for the two reaction mixtures up to 675

°C which suggest that the water plays little or no part in the initial phase of reaction. Above 675 °C the humidified reaction mixture gives a greater hydrogen yield. This is caused by the steam reforming of methane reaction consuming water and methane, which in turn produces extra hydrogen. The two reaction profiles suggest that the dry reforming of methane, and steam reforming of methane reaction occur in tandem at temperatures greater than 650 °C, and that the occurrence of the SRM reaction has no limiting effect on the DRM as seen by the shape of the reaction profile. The only difference seen at the higher temperatures is the increased of the formation of hydrogen and consumption of methane, as would be expected.

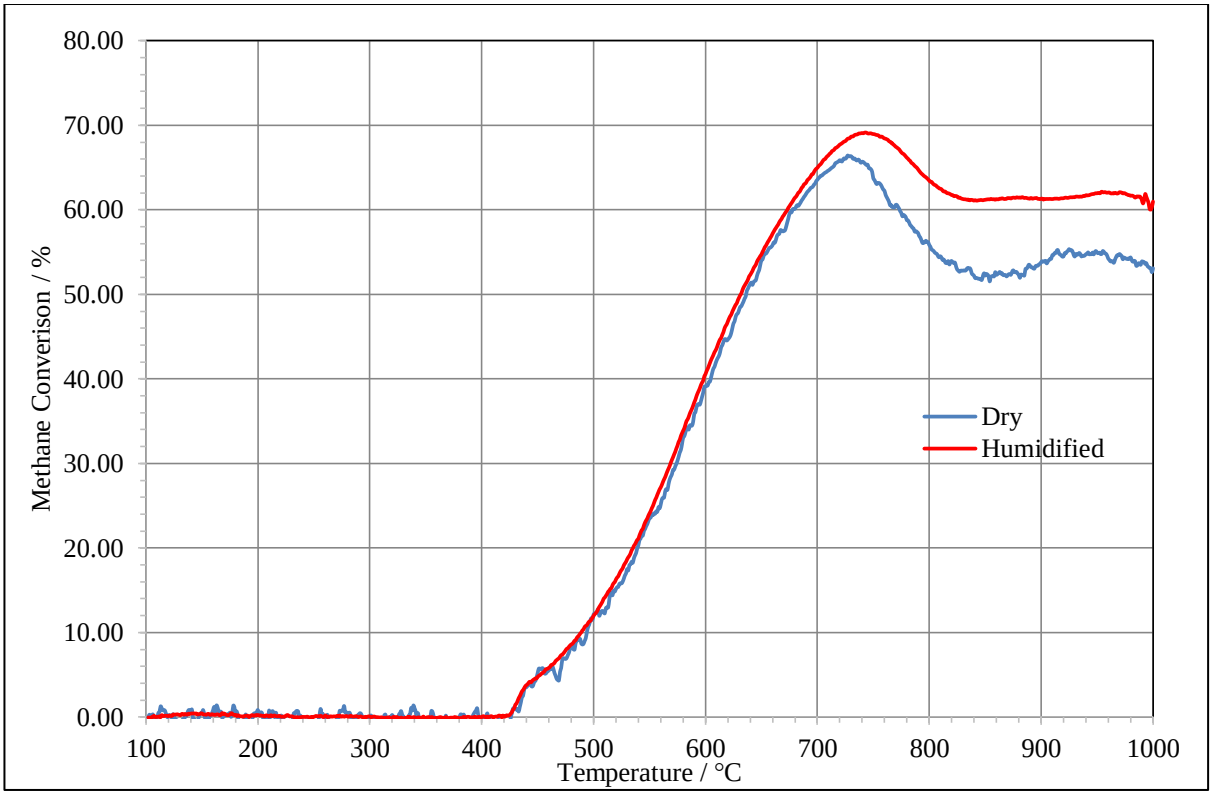

Figure 6-6 Methane conversion for temperature programmed reaction of humidified methane/ carbon dioxide mixture (methane: carbon dioxide = 2:1) over 4 mol% Ni doped $SrZrO_3$.

Figure 6-7 H_2:CO ratio for temperature programmed reaction of humidified methane/ carbon dioxide mixture (methane: carbon dioxide = 2:1) over 4 mol% Ni doped $SrZrO_3$.

The H_2/CO ratio for the humidified reaction shown in Figure 6-7 is consistently higher than for the dry reaction, which suggests that some carbon monoxide is being consumed by the reverse Boudouard reaction with the humidified mixture, which is not seen for the dry mixture. In line with a transient period of methane decomposition in the intermediate temperature phase of the reaction, the reaction profile for the humidified reaction mixture shows a peak in H_2/CO ratio, as is seen for the dry reaction. This shows that the addition of water has no effect on suppressing methane decomposition at these temperatures. By ~ 800 °C the H_2/CO ratio for both reactions stabilised, despite the increasing temperature which should in principle cause the methane decomposition reaction to increase, resulting in a hydrogen rich syn-gas mixture. The reaction profile for the humidified reaction

mixture stabilises at a higher H_2/CO ratio than for the dry reaction mixture as a result of the SRM reaction yielding more hydrogen than the DRM reaction.

6.4 Short Term Stability

In this section the reforming characteristics of the three catalyst materials for a 2:1 methane: carbon dioxide reaction mixture with 10% humidity relative to methane content is evaluated. The reaction temperatures used were 600 °C, 700 °C, 800 °C, 850 °C and 900 °C for three hours with the solid carbon deposits quantified using post reaction TPO analysis.

Figure 6-8 shows reaction profiles for humidified biogas reforming profiles for Ni/YSZ, 5% ceria doped Ni/YSZ and 4 mol% Ni doped $SrZrO_3$ at 800 °C. As for reaction of the non-humidified reaction mixture at the same temperature, Ni/YSZ fully consumes carbon dioxide present; the water from the reactant stream is also fully consumed. Methane conversion is expected to be at 60% for pure DRM and SRM reactions; however the total methane conversion is above 60%, indicating that methane decomposition must be occurring. The reaction appears to be stable over the reaction lifetime which suggests that no sintering of nickel particles occurs as a result of the water at this temperature over the 3 hours tested. The corresponding reaction over the ceria doped Ni/YSZ shows very similar reaction characteristics to the undoped catalyst. The conversion of water and carbon dioxide is complete immediately and remains this way for the extent of the reaction.

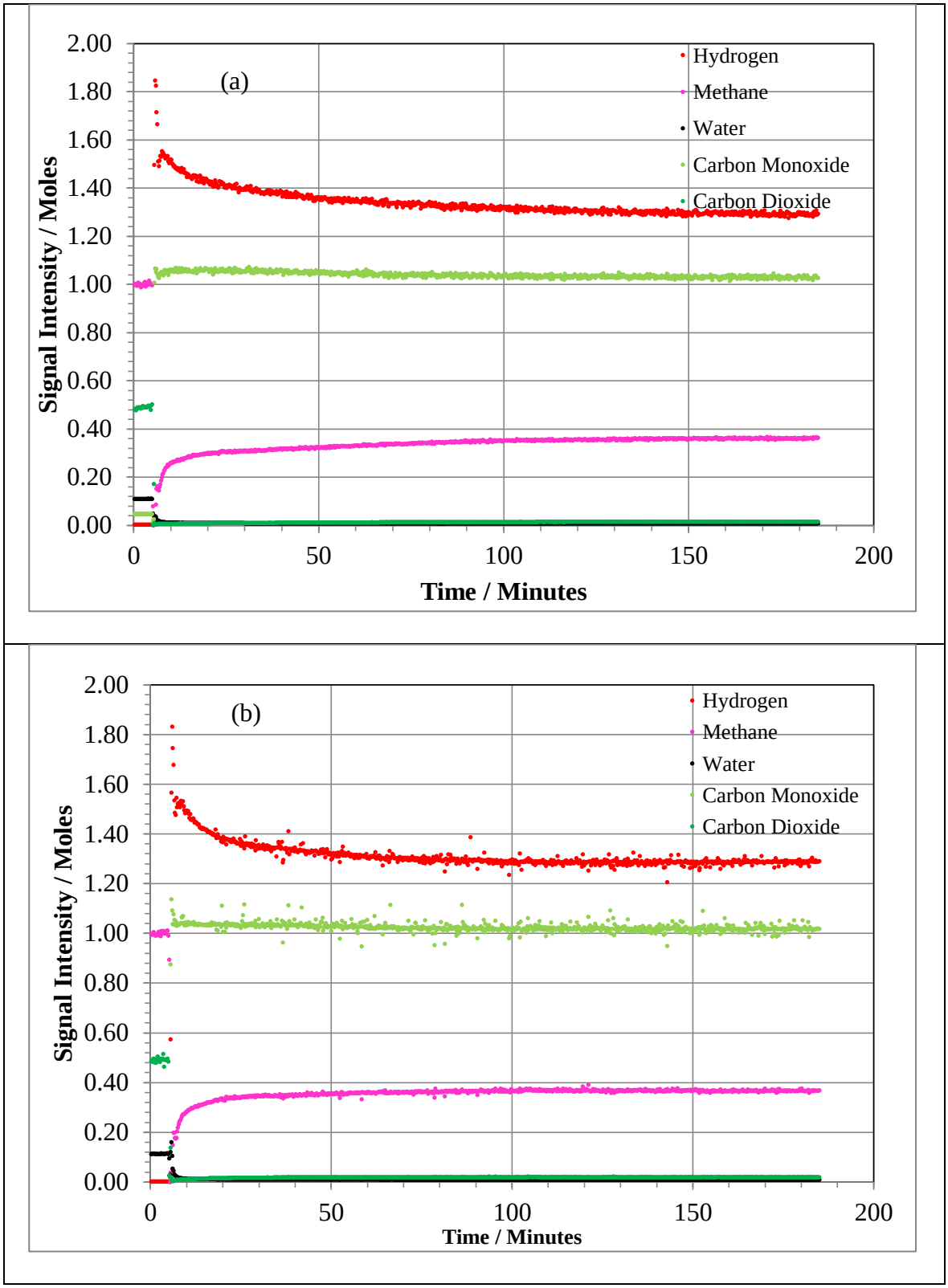
(a)
Hydrogen
Methane
Water
Carbon Monoxide
Carbon Dioxide
Signal Intensity / Moles
Time / Minutes
2.00
1.80
1.60
1.40
1.20
1.00
0.80
0.60
0.40
0.20
0.00
0
50
100
150
200
(b)
Hydrogen
Methane
Water
Carbon Monoxide
Carbon Dioxide
Signal Intensity / Moles
Time / Minutes

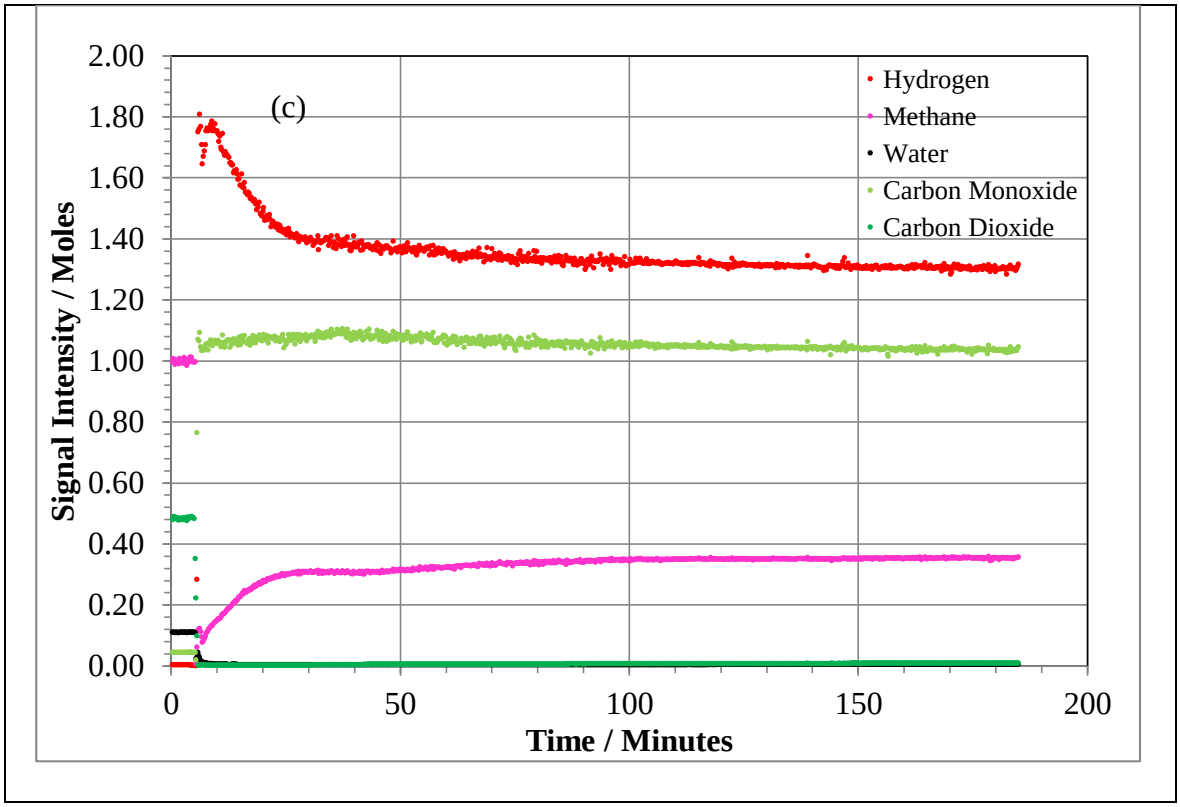

Figure 6-8 Reaction of humidified methane/ carbon dioxide mixture (methane: carbon dioxide = 2:1) over (a) Ni/YSZ (b) 5% ceria doped Ni/YSZ (c) 4 mol% Ni doped $SrZrO_3$

6.4.1 Reactant Conversion

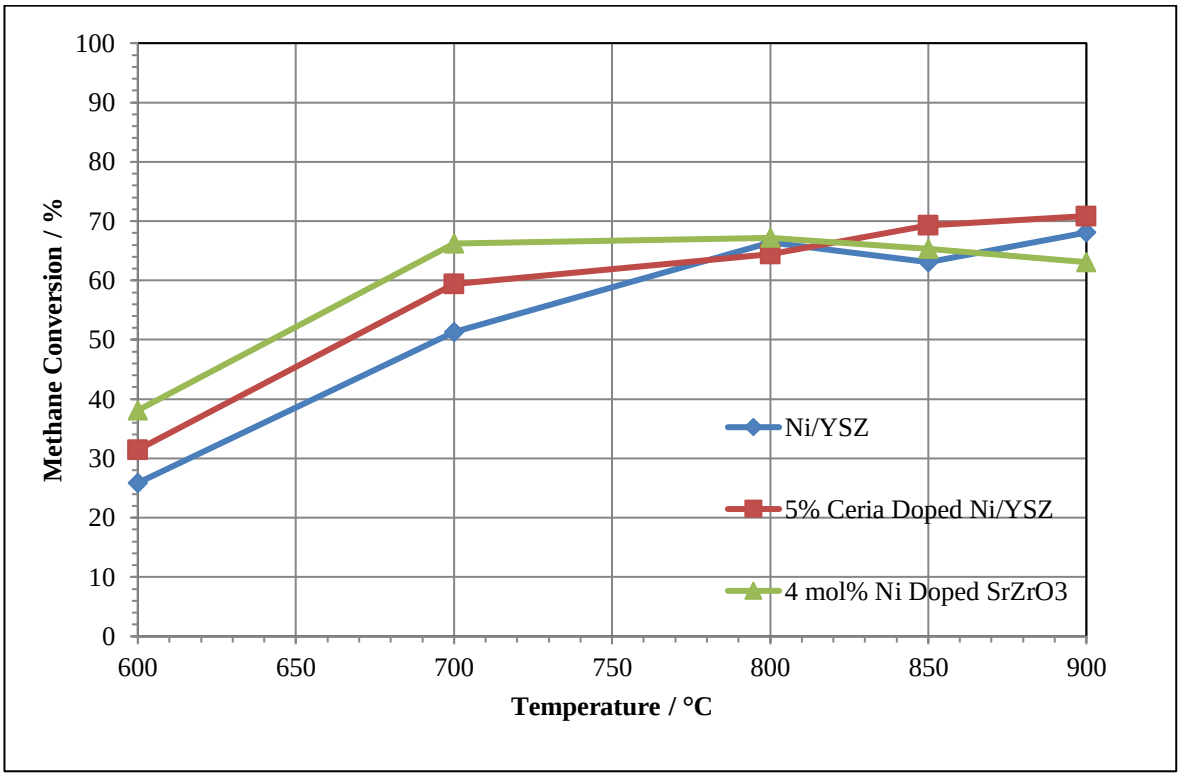

Figure 6-9 Methane Conversion of humidified methane/ carbon dioxide mixture (methane: carbon dioxide = 2:1) over Ni/YSZ, 5% ceria doped Ni/YSZ, 4 mol% Ni doped $SrZrO_3$

Between 600 °C and 700 °C the methane conversion is observed to be higher for the perovskite than for the nickel cermet materials, with methane conversion for all three materials increasing with temperature as seen in Figure 6-9. Methane conversion over the nickel cermet materials continues to increase with temperature resulting in a ~ 70 % methane conversion for both materials which indicates that at least 10% of the methane in the reactant stream is thermally decomposed in excess on the catalyst surface. In contrast to this the methane conversion is seen to drop for the perovskite material between 800 °C and 900 °C, to ~60%. This is indicative of pure dry and steam reforming with no undesirable decomposition of excess methane, due to the Boudouard reaction becoming thermodynamically unfavourable above 700 °C.

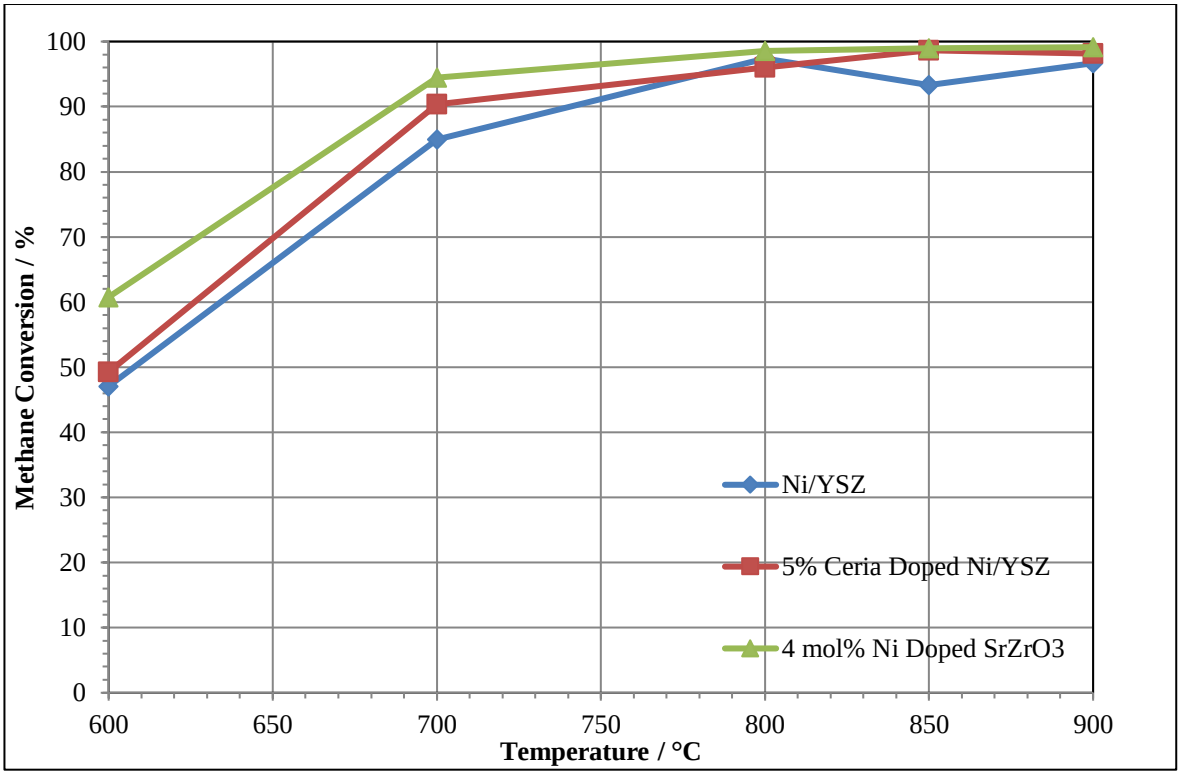

Figure 6-10 Carbon dioxide conversion of humidified methane/ carbon dioxide mixture (methane: carbon dioxide = 2:1) over Ni/YSZ, 5% ceria doped Ni/YSZ, 4 mol% Ni doped $SrZrO_3$

Figure 6-10 shows the carbon dioxide conversion as a factor of reaction temperature for the three materials tested. The perovskite maintains a greater carbon dioxide conversion than that of the nickel cermet materials indicating that the perovskite is a more active dry reforming catalyst. The difference in activity was particularly evident at the lower reaction temperatures tested (600 °C – 700 °C) where the perovskite converted about 10% more carbon dioxide than the nickel cermet materials. At higher reaction temperatures the difference is less discernible as the carbon dioxide conversion for all materials is greater than 95%.

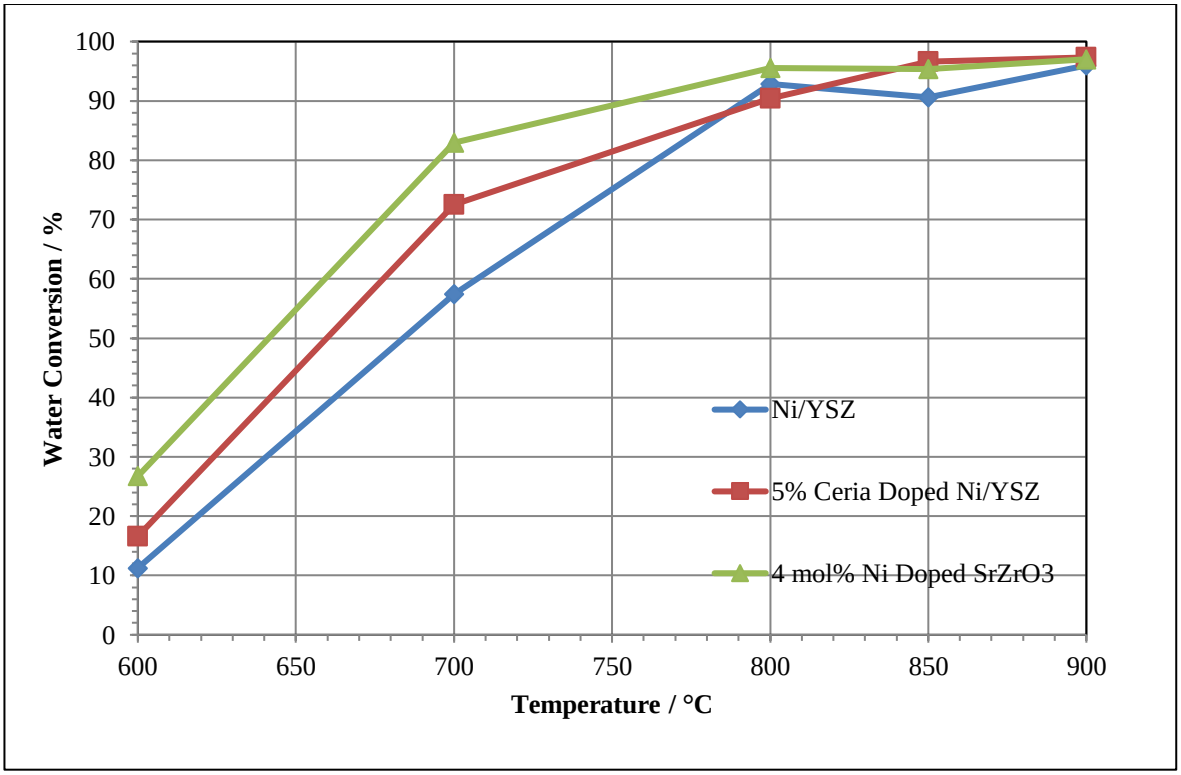

Figure 6-11 Water Conversion of humidified methane/ carbon dioxide mixture (methane: carbon dioxide = 2:1) over Ni/YSZ, 5% ceria doped Ni/YSZ, 4 mol% Ni doped $SrZrO_3$

A sharp increase in water conversion is seen in Figure 6-11 for all three materials between 600 °C and 650 °C. This is partly attributed to water formation *via* the reverse water gas shift reaction at 600 °C lowering the apparent conversion. Steam reforming of methane becomes more favourable as the temperature increases, the water consumption for all three materials rose to ~ 90 % by 800 °C. As with carbon dioxide conversion, the perovskite material shows a greater water conversion than the nickel cermet materials which indicates that the perovskite material is also more active towards the methane steam reforming reaction than the cermet materials, and has a lower tendency to favour the water gas shift reaction at lower temperatures.

6.4.2 Product Selectivity

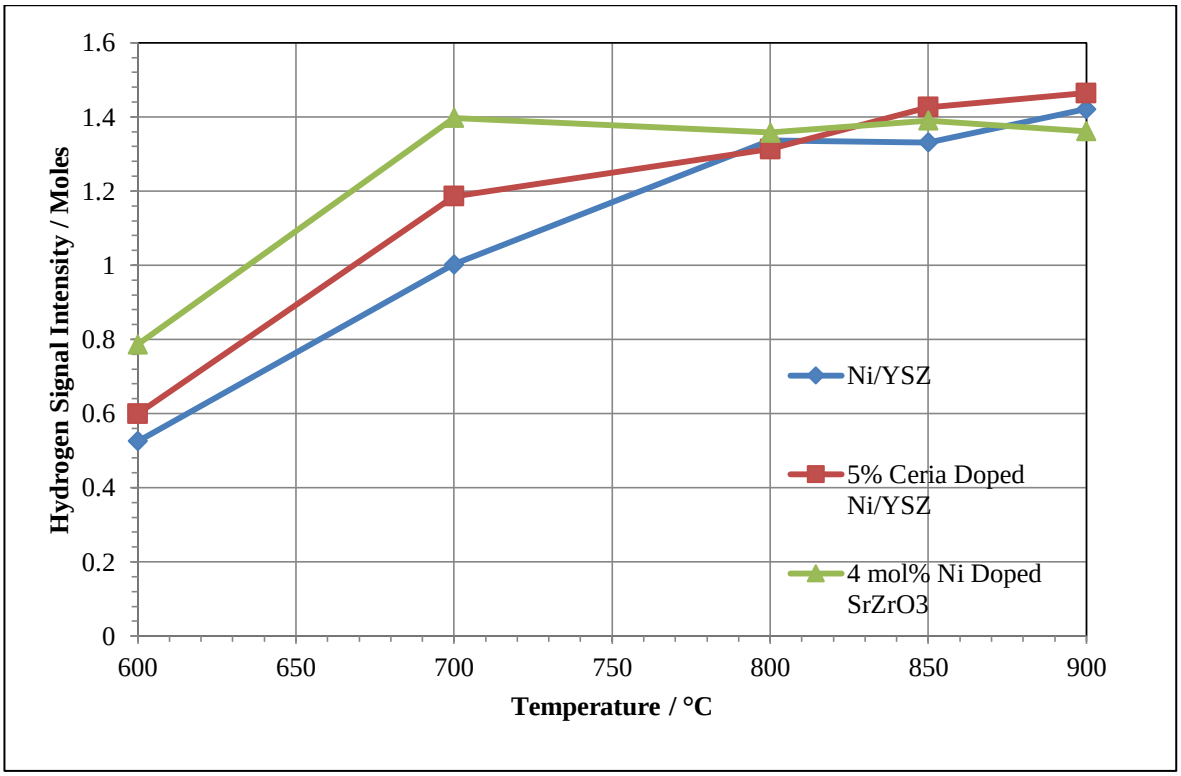

Figure 6-12 Hydrogen production of humidified methane/ carbon dioxide mixture (methane: carbon dioxide = 2:1) over Ni/YSZ, 5% ceria doped Ni/YSZ, 4 mol% Ni doped $SrZrO_3$

In Section 6.4.1 it was seen that the perovskite material gave a higher reactant conversion than the nickel cermet materials at lower reaction temperatures tested, and equivalent carbon dioxide and water conversions at the higher reaction temperatures. Analysis of the hydrogen production shows that this conversion is matched by high selectivity to synthesis gas as seen in Figure 6-12. The predicted hydrogen formation for complete consumption of carbon dioxide and water through reforming methane is 1.3 moles relative to methane. The perovskite material gives a hydrogen yield in excess of this at 700 °C, but equilibrated to this amount of hydrogen by 800 °C. The nickel cermet materials both display lower formation of hydrogen between 600 °C and 800 °C due to lowered activity towards both

dry and steam reforming of methane reactions. At 800 °C and above, the cermet materials exceed the predicted hydrogen formation for pure reforming due to thermal decomposition of some excess methane.

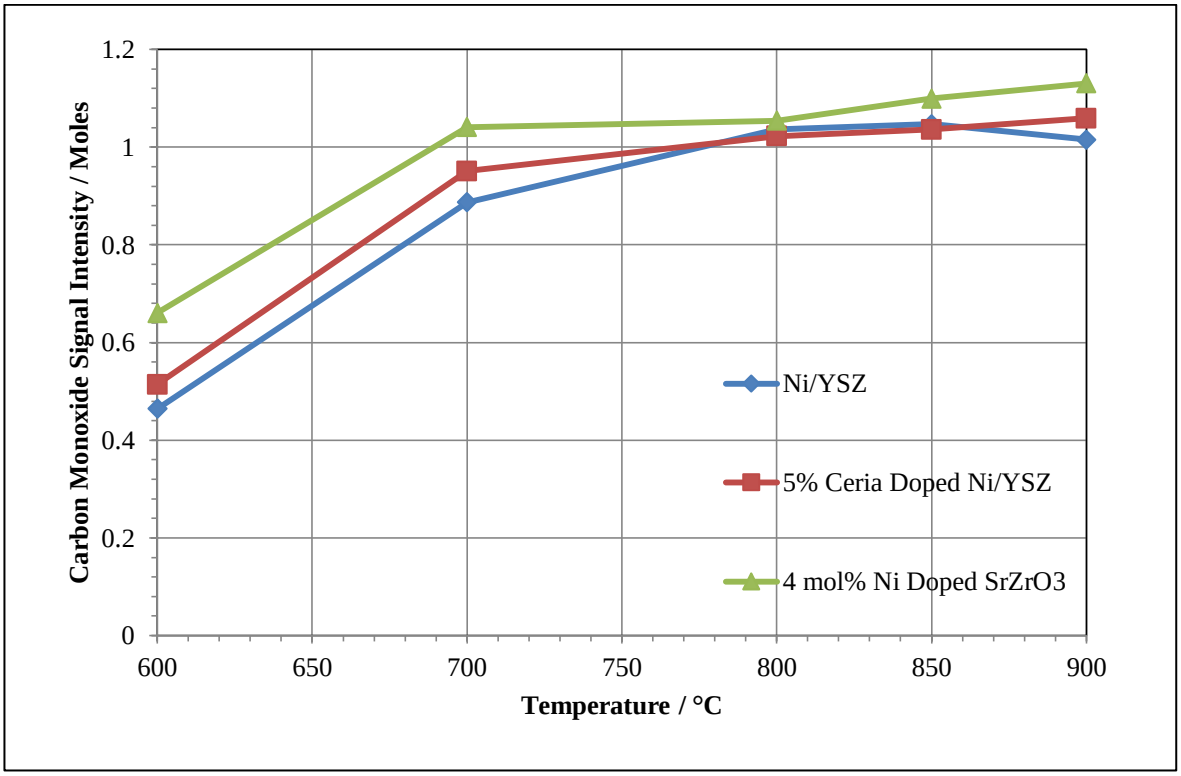

Figure 6-13 Carbon monoxide production of humidified methane/ carbon dioxide mixture (methane: carbon dioxide = 2:1) over Ni/YSZ, 5% ceria doped Ni/YSZ, 4 mol% Ni doped $SrZrO_3$

The carbon monoxide yield seen in Figure 6-13 for the perovskite material showed some differences to the hydrogen profile seen in Figure 6-12**.** At elevated temperatures the carbon monoxide formation increases until it reached the stoichiometric CO formation at 900 °C (1.1 moles). As the hydrogen production surpasses the stoichiometric production between 700 °C and 850 °C this suggests that the hydrogen was gained and carbon monoxide lost due to the reverse water gas shift reaction. The cermet materials display a plateau in carbon monoxide production as the oxidative reactants become close to fully consumed. Ceria doped Ni/YSZ gives higher production of both carbon monoxide and

hydrogen at lower reaction temperatures (600 – 700 °C) compared to Ni/YSZ, suggesting it has higher activity under humidified reaction conditions.

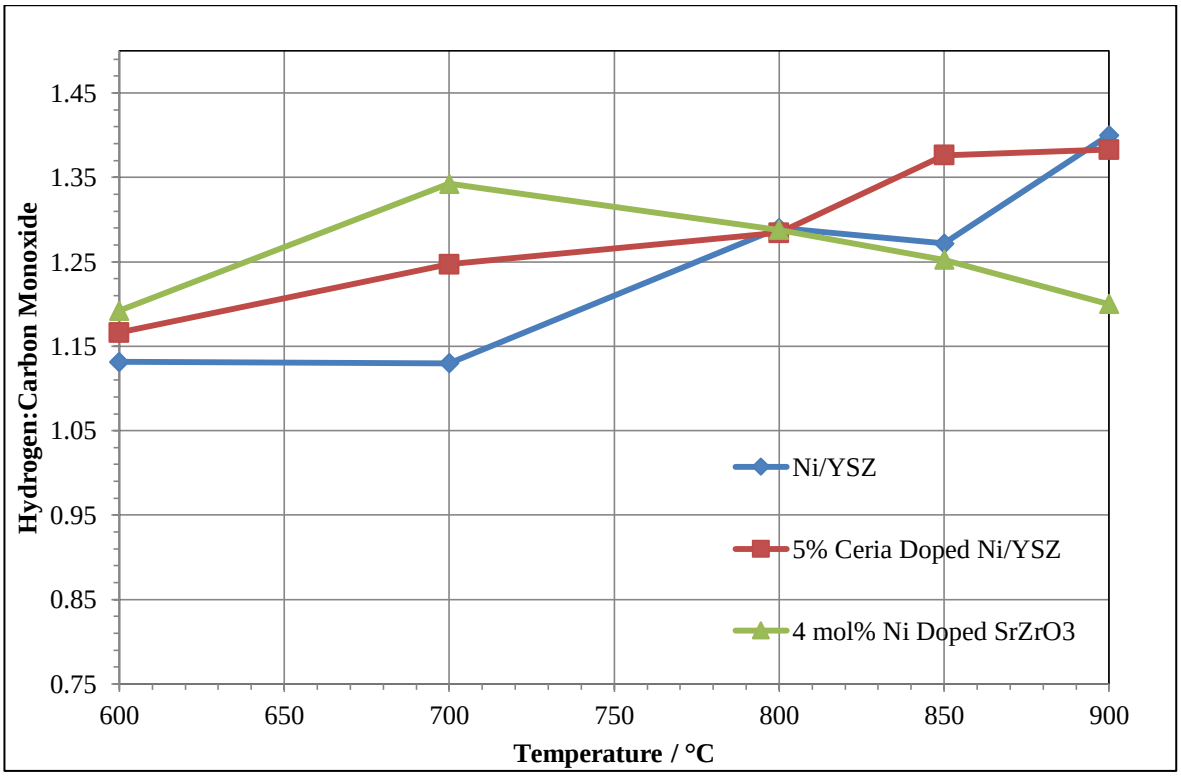

Figure 6-14 H_2:CO ratio of humidified methane/ carbon dioxide mixture (methane: carbon dioxide = 2:1) over Ni/YSZ, 5% ceria doped Ni/YSZ, 4 mol% Ni doped $SrZrO_3$

Figure 6-14 shows the H_2:CO ratio as a function of reaction temperature over all three materials. The decrease in the water gas shift reaction gives rise to a sharp decrease in H_2:CO ratio for the perovskite material above 700 °C as is seen in Figure 6-14. In contrast the cermet materials show a general trend of increasing H_2:CO ratio with ceria giving more hydrogen rich synthesis gas mixtures.

The predicted H_2:CO ratio for pure dry reforming and steam reforming of methane, with no methane dcomposition in a 1:0.5:0.1 configuration of CH_4:CO_2:H_2O is 1.18. This value exceeded by both 5% ceria doped Ni/YSZ and 4 mol% Ni doped $SrZrO_3$ at lower reaction

temperatures primarily due to less than stoichiometric formation of carbon monoxide, due to the Boudouard reaction. The ratio continues to increase for the cermet materials above 800 °C due to promotion of thermal decomposition of methane resulting in elevated hydrogen production.

6.4.3 Carbon Deposition

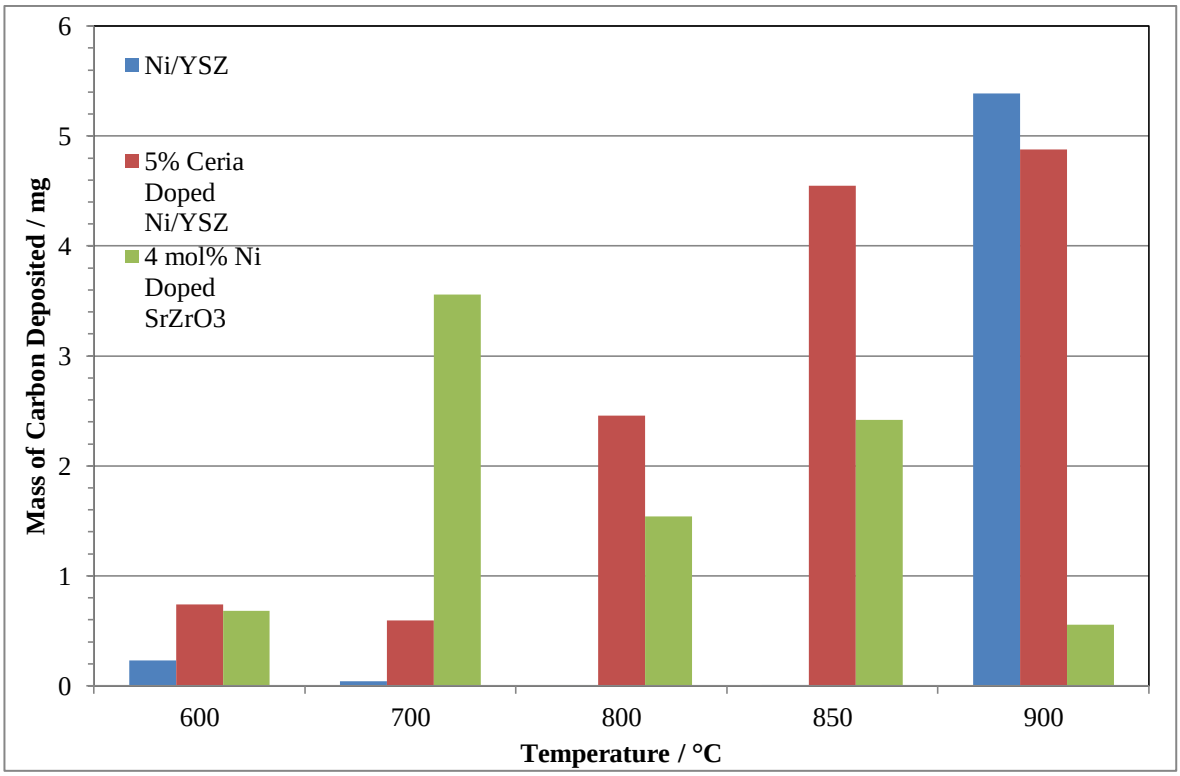

Figure 6-15 Carbon deposition of humidified methane/ carbon dioxide mixture (methane: carbon dioxide = 2:1) over Ni/YSZ, 5% ceria doped Ni/YSZ, 4 mol% Ni doped $SrZrO_3$

Ceria doping of Ni/YSZ has been shown to lower the carbon deposition during reaction of methane rich methane/ carbon dioxide mixtures compared to undoped Ni/YSZ both in this work (Chapter 5) and by Laycock *et al.*, however the effect of low levels of humidification has not been previously studied[14]. The inclusion of humidification to the reaction mixture

significantly suppressed carbon formation of Ni/YSZ at all reaction temperatures tested, with 900 °C being the only temperature where there is significant deposition of solid carbon, this is shown in Figure 6-15. The carbon deposited over the ceria doped catalyst is suppressed, however not to the extent as was seen for Ni/YSZ and this reflected the change in activity. A general trend of increasing carbon deposition with temperature is seen for the ceria doped catalysts material. In chapter 5 it was seen that Ni/YSZ consistently had a marginally higher activity which was attributed to slightly higher nickel content of the undoped catalyst. However the work in this chapter has shown that when humidity is added the ceria doped catalyst is the more active of the two. This suggests that ceria doping has a promoting effect on methane steam reforming, and also methane decomposition when humidity is present, leading to higher carbon deposits.

The level of carbon deposition over the perovskite material is more complex and no observable trend was seen. The highest level of carbon deposited is at 700 °C and this is reflected in a higher than stoichiometrically predicted conversion of methane, suggesting the carbon is formed *via* thermal decomposition of methane reaction despite this being less favourable than at higher temperatures.

6.5 Long Term Stability

In the previous chapter the long term stability of the perovskite material when reforming a methane rich methane/ carbon dioxide mixture was tested for up to 10 days and compared to the cermet materials, with no loss of activity observed. It was again important to test the catalyst for stability in reforming humidified simulated biogas for longer than the three hour reaction period used so far in this chapter. However the logistics of consistently

maintaining the saturator at 0 °C within a polyurethane container and also the limitations of the saturator volume meant that such long tests were not feasible. It was, however possible to maintain a stable flow of reactant gases for 48 hours and the results are presented in this section.

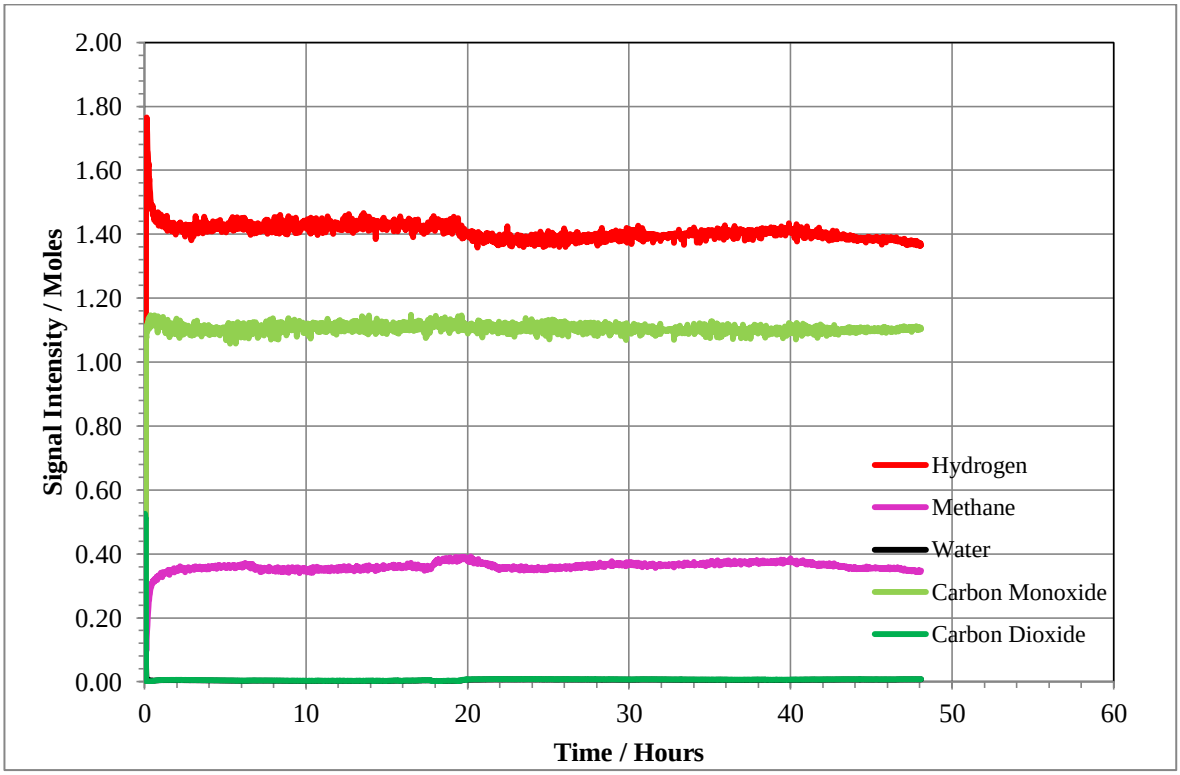

Figure 6-16 Reaction profile of humidified methane/ carbon dioxide mixture (methane: carbon dioxide = 2:1) over 4 mol% Ni doped $SrZrO_3$ at 850 °C

Figure 6-16 shows the longest reaction under humidified simulated biogas that was carried out using the perovskite based material which was for 48 hours. The reaction profile shows a stable reforming reaction with hydrogen rich synthesis gas formed and effectively complete consumption of carbon dioxide and water. Methane consumption remains at ~60% for the duration of the reaction which indicates minimal thermal decomposition of methane occurs. The profile does show some variances, particularly in the hydrogen signal, however this is attributed to saturator temperature variance and instability in the

QMS raw signals, and not in the performance of the catalyst material. This suggests that over two days of reaction, little or no noticeable sintering of the perovskite material or loss of reforming activity occurs.

6.5.1 Carbon Deposition

In stark comparison to the carbon deposition with time plot that was constructed using reactions devoid of humidity, the 5% ceria doped sample gave a profile which suggests the rate of deposition of carbon was greatest over this material. This is because the 5% ceria doped Ni/YSZ sample has a higher activity than undoped Ni/YSZ under these reaction conditions as seen in Figure 6-9 - Figure 6-13 resulting in a increased level of carbon decomposition from the methane pyrolysis reaction. The complete conversion of water and carbon dioxide at this temperature results in the ceria being unable to reoxidise into the 4+ CeO_2 state[14–16]. This is confirmed by the amount of carbon deposition being lower than the undoped Ni/YSZ for the shortest reaction time of one hour as the ceria is able to oxidise off some deposited carbon before all of the ceria switched to the Ce_2O_3 state.

The perovskite material shows a suppression in the carbon deposited by addition of water to the reaction feed, as was expected, and also maintains the previously seen nonlinear relationship between reaction time and carbon deposition in Figure 5-17.

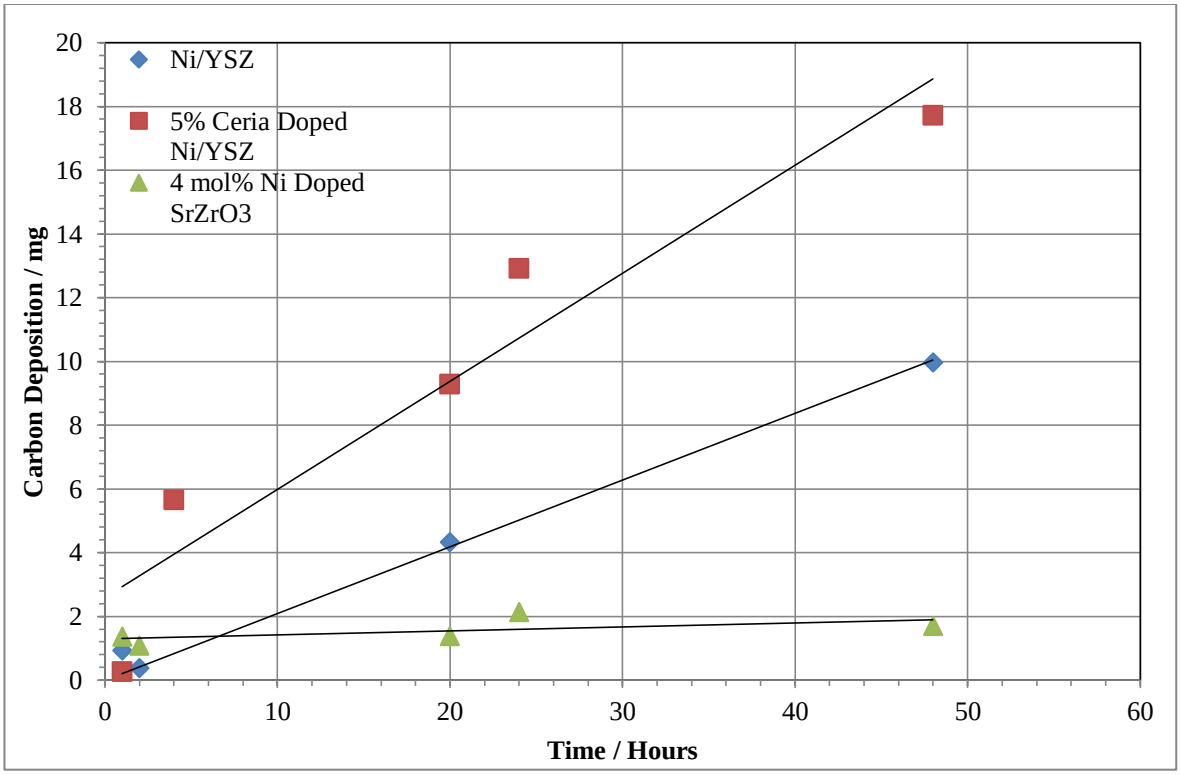

Figure 6-17 Comparison of Carbon deposition with time of humidified methane/ carbon dioxide mixture (methane: carbon dioxide = 2:1) over Ni/YSZ, 5% ceria doped Ni/YSZ, 4 mol% Ni doped $SrZrO_3$

6.6 Conclusions

Temperature programmed reactions were used to show how the dry reforming of methane reaction was altered by the addition of a low level of steam it the reactant feed to simulate the water that would naturally be present in biogas. The addition of water adds an oxidant potentially enabling steam and dry reforming of methane to take place simultaneously. At lower reaction temperatures it appears that the steam plays no role in reforming methane over the perovskite, with no water consumption observed. Above 600 °C water consumption begins indicating that steam reforming is occurring simultaneously to dry reforming.

In contrast to the supported nickel based catalysts tested the perovskite showed generally greater reforming activity indicated by higher reactant conversion. The 4 mol% Ni doped $SrZrO_3$ showed a similar fall in methane conversion to stoichiometric reforming levels at the higher temperatures as was seen for the corresponding reaction without water, which is in contrast to the cermet materials which thermally decompose more methane as the reaction temperature is increased.

Comparisons between the reactions with and without steam over the perovskite showed that in the initial phase of reaction the water content played no role in reforming, with almost identical methane conversion and hydrogen production observed. Above 650 °C the formation of hydrogen and conversion of methane increased for the humidified reaction which indicated simultaneous reformation of some methane with steam, resulting in hydrogen rich synthesis gas.

Short isothermal reaction tests confirm that the perovskite material possessed greater reforming activity than the existing SOFC anode materials at typical solid oxide fuel cell operation temperatures. The reactions also show that it would be feasible to run the perovskite material at lower temperatures than the cermet materials without sacrificing reforming activity.

Finally, experiments show that addition of water to the reactant feed did not cause observable loss of reforming activity within the experimental parameters used. This shows that the addition of steam to the reactant feed did not cause any agglomeration of the perovskite particles to an extent that resulted in observable visible loss of activity.

The deposition plot provides a less than clear relationship between temperature and the amount of carbon deposited as the number of possible reactions occurring increase due to the water addition. The carbon with time plot however, showed that the perovskite material, similarly to the reactions without added steam, did not show a relationship between time on stream and the amount of carbon deposited. This linear relationship was once again seen for the cermet materials with a suppression in solid carbon formation resulting from the water addition. Interestingly, the ceria doped catalyst gave a higher deposition of carbon than the undoped counterpart which was attributed to an increase in activity towards the reforming reactions caused by the addition of water.

The results in this chapter have shown that utilising sulphur free 'wet' biogas for formation of synthesis gas is feasible using 4 mol% Ni doped $SrZrO_3$. The material displays good reforming activity particularly when compared to standard nickel based SOFC anode materials, as well as resistance to particle agglomeration and fouling caused by deposits of solid carbon.

6.7 References

1 A. Lanzini and P. Leone, *Int. J. Hydrogen Energy*, 2010, **35**, 2463–2476.

2 D. Deublein and A. Steinhauser, *Biogas from Waste and Renewable Resources An Introduction*, Wiley-VCH, Weinheim, 2008.

3 A. Demirbas, *Energy Convers. Manag.*, 2008, **49**, 2106–2116.

4 P. Weiland, *Appl. Microbiol. Biotechnol.*, 2010, **85**, 849–60.

5 J. B. Tucker, *Environment*, 1982, **24**, 12–39.

6 B. Iwanschitz, L. Holzer, A. Mai and M. Schütze, *Solid State Ionics*, 2012, **211**, 69–73.

7 J. Sehested, *Catal. Today*, 2006, **111**, 103–110.

8 D. King, J. Strohm, X. Wang, H. Roh, C. Wang, Y. Chin, Y. Wang, Y. Lin, R. Rozmiarek and P. Singh, *J. Catal.*, 2008, **258**, 356–365.

9 N. F. P. Ribeiro, M. M. V. M. Souza, O. R. M. Neto, S. M. R. Vasconcelos and M. Schmal, *Appl. Catal. A Gen.*, 2009, **353**, 305–309.

10 E. Drożdż-Cieśla, J. Wyrwa, W. Pyda and M. Rękas, *J. Mater. Sci.*, 2011, 2807–2817.

11 Z. Jiao, N. Shikazono and N. Kasagi, *J. Power Sources*, 2011, **196**, 8366–8376.

12 J. Sehested, *J. Catal.*, 2004, **223**, 432–443.

13 K. O. Christensen, D. Chen, R. Lødeng and A. Holmen, *Appl. Catal. A Gen.*, 2006, **314**, 9–22.

14 C. J. Laycock, J. Z. Staniforth and R. M. Ormerod, *Dalt. Trans.*, 2011, **40**, 5494.

15 P. Fornasiero, M. Graziani and J. Kas, *Catal. Today*, 1999, **50**, 285–298.

16 M. Sugiura, *Catal. Surv. from Asia*, 2003, **7**, 77–87.

7 The Effect of adding Sulphur to Simulate Biogas on the Reforming Activity and Catalyst Performance

7.1 Introduction

Sulphur impurities naturally contained within biogas is one of two primary causes of loss of reforming activity when using a nickel based catalyst[1–6]. Sulphur poisoning of nickel occurs as a result of sulphur species blocking the adsorption of reactant gases. This can be *via* adsorption of sulphur to give a monolayer coverage, or by the formation of Ni_xS_y species is described in chapter 1[7–9]. Although it is possible to remove sulphur from biogas and other fuel sources it is a costly process and it is difficult to achieve 100% removal[4,9,10]. Despite the extensive literature on the interaction between sulphur species and nickel based anode materials, due to the relatively recent advancement in perovskite materials as catalysts, the behaviour when sulphur is introduced is unknown[1–4,10–16]. The chemically contained nickel in 4 mol% Ni doped $SrZrO_3$ as opposed to being oxide supported may completely alter the way in which this interaction occurs.

To evaluate the effect that sulphur containing gases within biogas had on the reforming characteristics, methane rich biogas was passed over the catalysts for 20 hours and several parameters were changed. The first parameter changed was the reaction temperature, which was varied between 700 °C and 1000 °C, with 10 ppm of H_2S added relative to the methane content. The second parameter changed was the sulphur concentration, with the reactor feed containing between 0 ppm and 10 ppm of H_2S relative to the methane content with the temperature set at 850 °C.

7.2 Effect of Sulphur Poisoning on the Catalytic Reaction

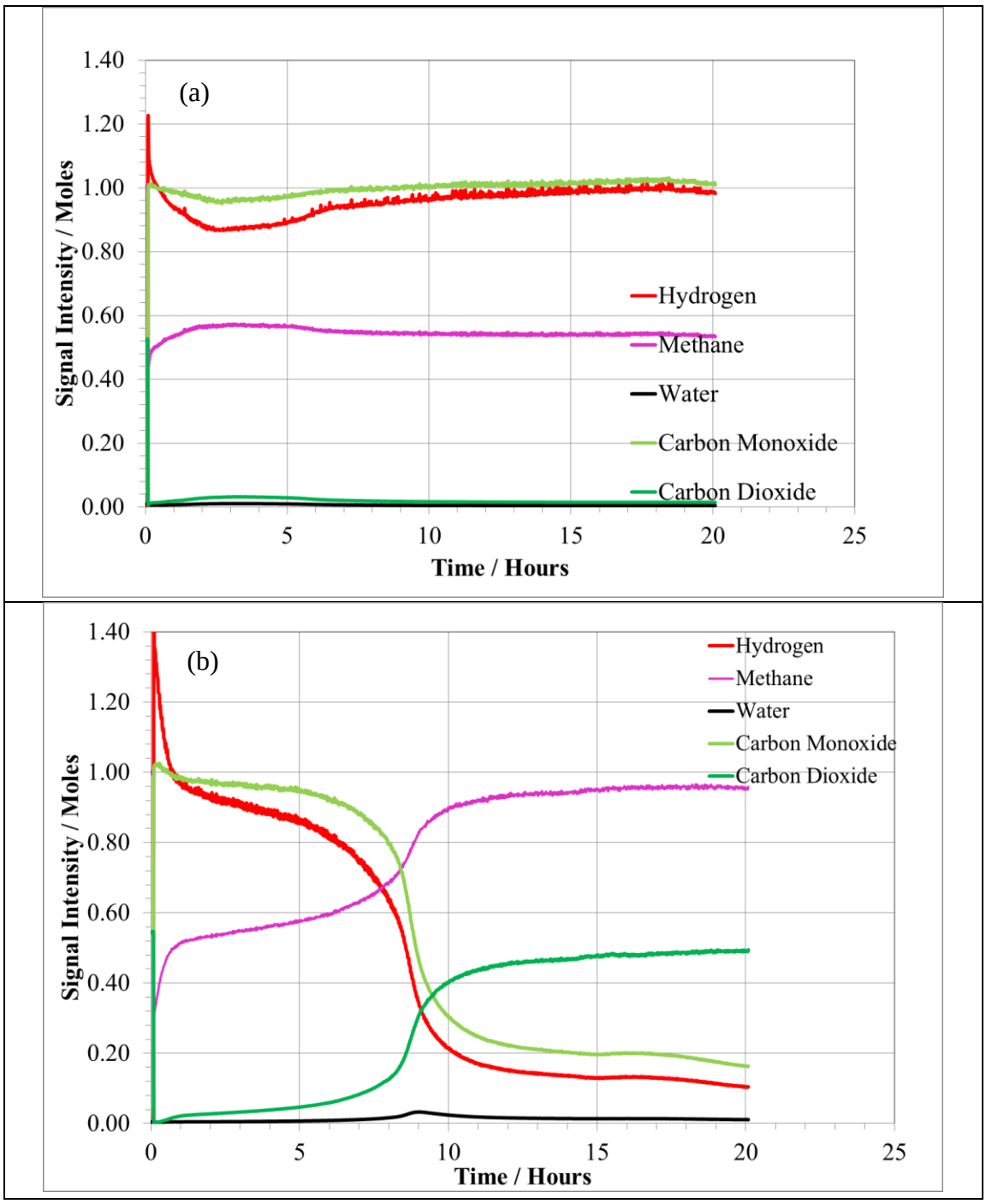

Figure 7-1 Reaction profile of 2:1 CH_4/CO_2 ratio passed over Ni/YSZ at 850 °C with (a) 0 ppm of H_2S and (b) 10 ppm of H_2S

Figure 7-1 show the difference in catalytic performance of the Ni/YSZ based anode material at 850 °C following addition of 10 ppm of H_2S in comparison to the simulated

biogas mixture. In the absence of sulphur an initial period of transient activity was followed by stable consumption of methane and carbon dioxide with equimolar formation of hydrogen and carbon monoxide, with no indication of loss of reforming activity as seen in Figure 7-1 (a). Addition of hydrogen sulphide to the reactant feed drastically changes the reaction profile as seen in Figure 7-2 (b), initially thermal decomposition of methane in excess becomes more favourable as seen by the higher methane consumption and production of hydrogen; however this quickly subsides as did the reforming reaction, as an initial steady phase of poisoning began. This is followed by a rapid phase of poisoning resulting in almost total loss of reforming activity after ~ 10 hours. Finally, although some low level reforming activity remains, this also decreases over the remaining 10 hours of reaction.

7.2.1 The Effect of Temperature

7.2.1.1 Methane Conversion

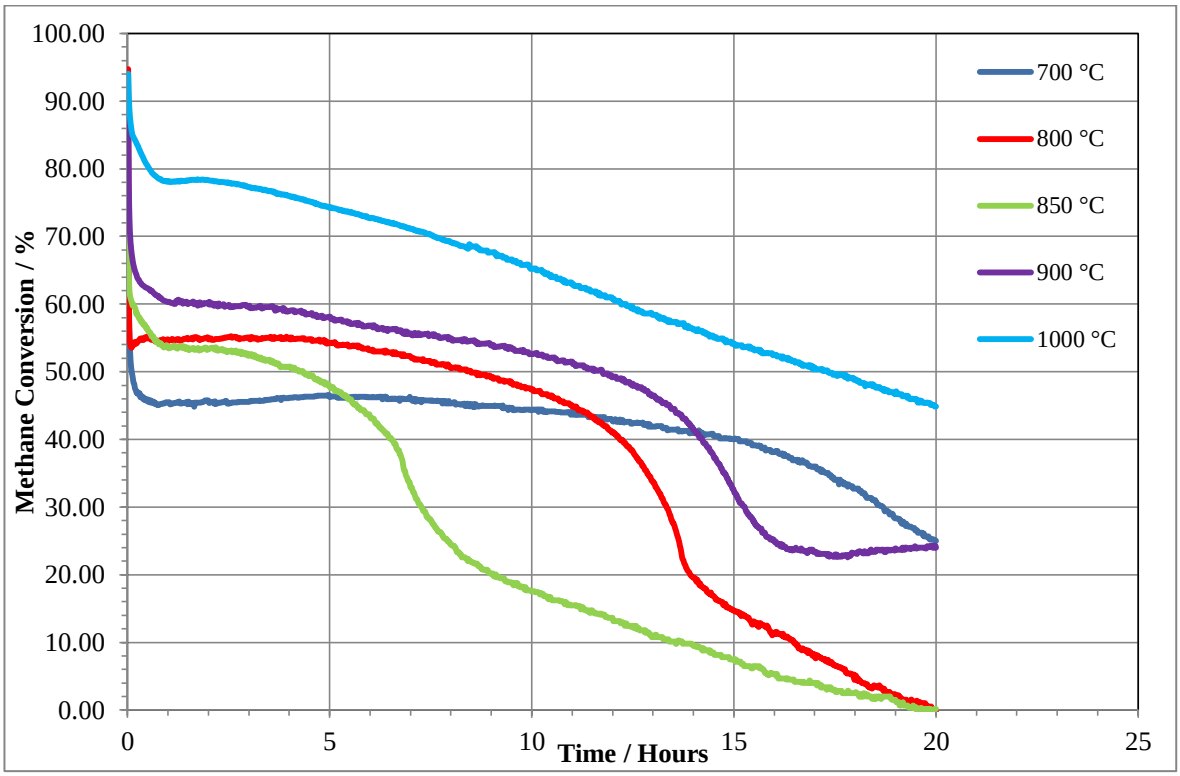

Figure 7-2 Methane conversion during reaction of a 2:1 CH_4:CO_2 mixture with 10 ppm of H_2S over Ni/YSZ at different reaction temperatures

At 1000 °C a relatively linear decrease in methane conversion is observed, from ~ 85% indicating a high percentage of methane is thermally decomposed down to the stoichiometric 50% by the end of the reaction. Decreasing the reaction temperature to 900 °C lowers the amount of methane that is decomposed and reduces the reaction lifetime, as would be expected, with sulphur adsorption being thermodynamically favoured at lower temperatures[17]. Recent modelling work by Appari and co-workers has proven that as the temperature is lowered the occupation of nickel atoms by sulphur may shift from one nickel atom at the highest temperatures to two nickel atoms as the temperature is decreased, which would further account for the increased rate of poisoning[18]. Lowering

the reaction temperature also introduced a secondary phase of poisoning, with a fast intermediate loss of activity between the two. The first phase has been linked to dissociative chemisorption of H_2S on active nickel sites[4]. As the reaction temperature is lowered from 900 °C to 850 °C the first phase of deactivation happens faster as the dissociative chemisorption becomes more favourable thermodynamically as the temperature is decreased. However, further decreasing the reaction temperature to 800 °C extended the first phase of deactivation. This is attributed to the kinetics of the reaction, with the formation of nickel sulphide although more favourable thermodynamically, happening at a slower rate. This is confirmed by the reaction at 700 °C having a first phase of deactivation of similar duration to the reaction at 900 °C. Interestingly much of the literature suggests a directly inverse relationship between sulphur poisoning of Ni/YSZ and reaction temperature[3,4].

The second phase of poisoning could be a direct result of the loss of excess sites, i.e in the first phase there was always an excess of sites for reforming to occur with extra sites available for thermal decomposition of methane. Once the number of sites left becomes less than required for reformation the drop in activity was steep. Alternatively, the second phase of degradation could be caused by formation of bulk nickel sulphide species. It has also been shown that nickel sulphide species can exist in different forms with different ratios if nickel to sulphur and that transitions from a high nickel to sulphur ratio (eg Ni_4S) to low nickel to sulphur ratios can exist eg Ni_6S_5 can occur and this may play some role[4,19–22].

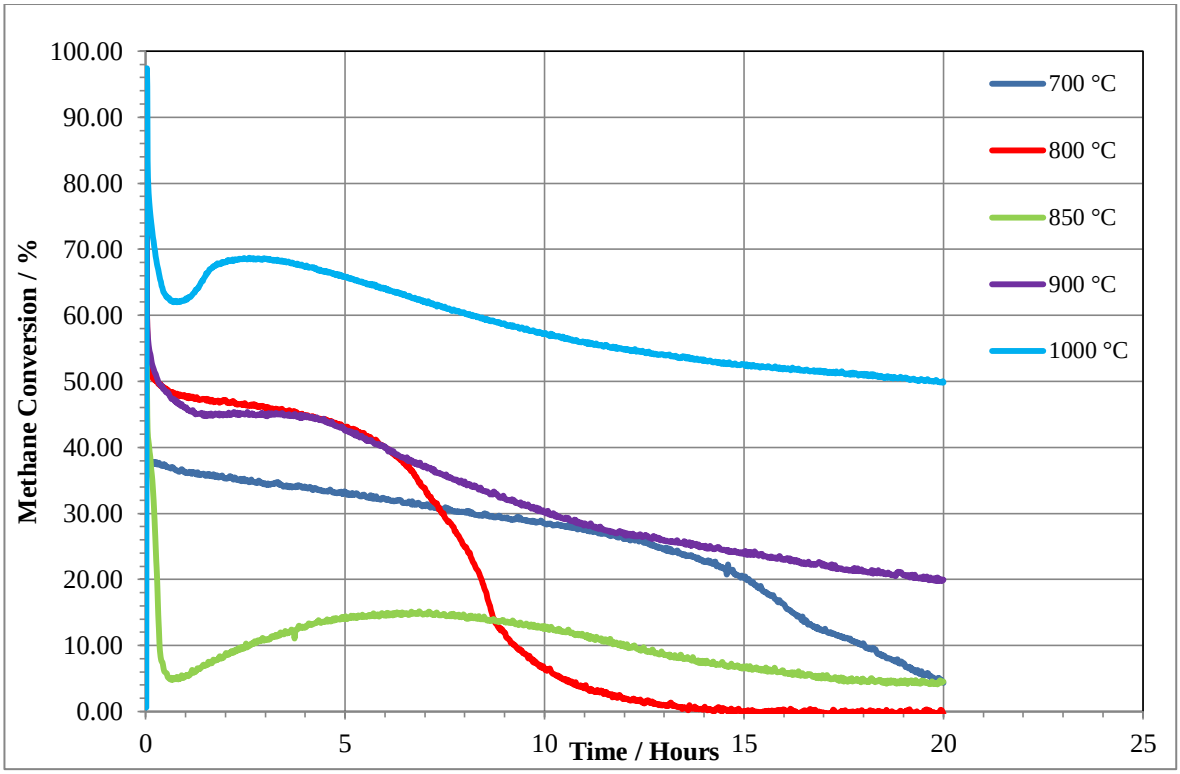

Figure 7-3 Methane conversion during reaction of a 2:1 CH_4:CO_2 mixture with 10 ppm of H_2S over 5% ceria doped Ni/YSZ at different reaction temperatures

Adding 5% ceria to the Ni/YSZ cermet very significantly changes the methane conversion profiles. At 1000 °C the extent of thermal decomposition of methane is suppressed when compared to Ni/YSZ although some does occur. The loss of activity is not as great, although this could also potentially be a consequence of less methane decomposition initially. At 900 °C a stable reaction occurs for the initial four hours of reaction. A single phase of poisoning then occurs resulting in a marginally lower final conversion of methane than was seen for Ni/YSZ. This initial stability may be as a result of the oxidative capacity of ceria, removing some of the chemisorbed sulphur from the catalyst surface in the form of SO_2. However as little oxidant is available to reoxidise the ceria to the oxidised +4 state, poisoning eventually occurs.

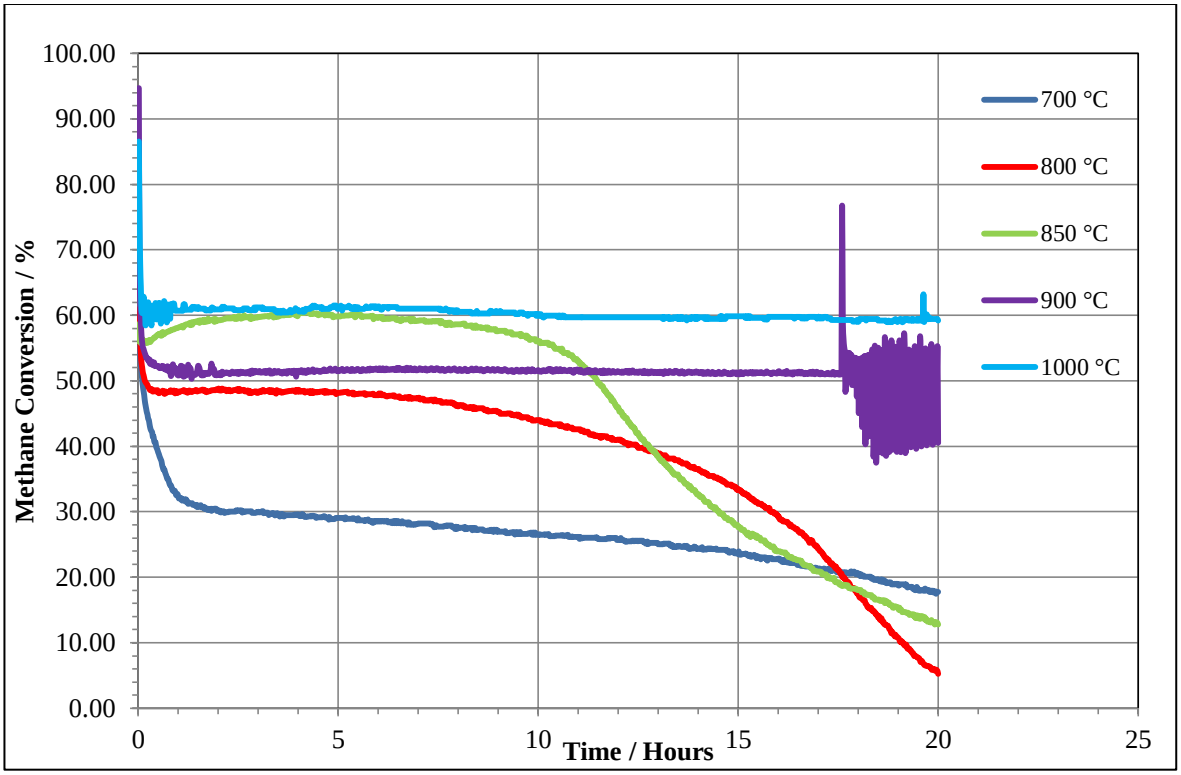

Figure 7-4 Methane conversion during reaction of a 2:1 CH_4:CO_2 mixture with 10 ppm of H_2S over 4 mol% Ni doped $SrZrO_3$ at different reaction temperatures

4 mol% Ni doped $SrZrO_3$ gives a very significantly sulphur different poisoning profile to that of the two cermet materials. At 1000 °C there is no indication that any loss of reforming activity occurs over duration of the reaction, although the methane conversion is significantly higher than is seen for the corresponding reaction under sulphur free reforming conditions, this increase in methane conversion suggests that although there is no obvious loss of reforming activity, the sulphur is playing a role and altering what happens at the catalyst surface. In the first two hours of reaction there is evidence of 'cycling'. Cycling is a phenomenon that has been previously identified and studied in catalysts containing ceria, with the phenomenon associated with continuous oxidation and reduction[22]. This results in phases of high activity and low activity with the duration of each phase generally being short, dependent on temperature and oxidant concentration.

Lowering the reaction temperature to 900 °C gave a relatively stable reaction for 18 hours with no observable loss of reforming activity. However, after this a period of fast cycling occurs until the end of the reaction. This suggests that throughout the lifetime of the reaction some dissociative chemisorption of sulphur is occurring, with the rate of desorption being slightly less than the rate of adsorption. At 850 °C no cycling occurs and a sharp loss of activity was seen after around 10 hours. This profile is replicated at 800 °C with the loss of overall activity being greater. Lowering the temperature to 700 °C shifts the initial sharp decline in reforming activity from 10 hours, indicating that the performance loss is more favourable at cooler reforming temperatures. Unlike the two cermet materials the perovskite does not completely lose reforming activity at any temperature.

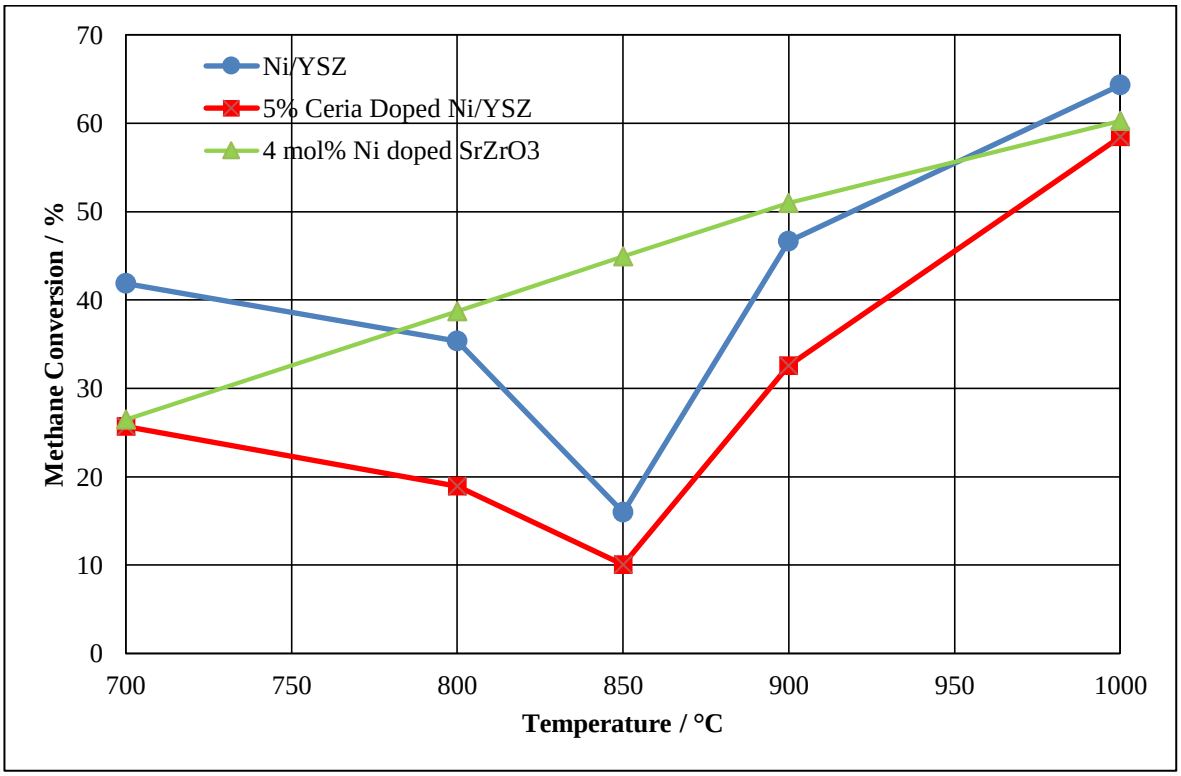

Figure 7-5 Average methane conversion during reaction of a 2:1 CH_4:CO_2 mixture with 10 ppm of H_2S over Ni/YSZ, 5% ceria doped Ni/YSZ and 4 mol% Ni doped $SrZrO_3$ at different temperatures

Figure 7-5 summarises the average methane conversion for the three materials with varying temperatures. The figure shows the thermodynamic and kinetic peak at 850 °C for the cermet materials in terms of loss of reforming activity with the methane conversion being lowest at this temperature. This peak is caused by a balance between the reaction happening quickly, and the reaction being favourable thermodynamically. As the temperature is increased past 850 °C despite the rate in which the poisoning reaction is occurring being faster, the reaction is less likely to occur. This is partly due to the relatively short reaction times used, as the reactions at 700 °C and 800 °C would have a lower methane conversion if the reaction time was longer due to the formation of nickel sulphide being thermodynamically favoured as temperature is decreased[23]. However as this happens faster at higher temperatures in this case the average methane conversion is lowest at 850 °C in this case. The perovskite material shows a different trend than the cermet materials and shows an almost linear relationship between methane conversion and temperature, suggesting that thermodynamics is the overriding effect for the perovskite, overwhelming the kinetic effects.

7.2.1.2 Carbon Dioxide Conversion

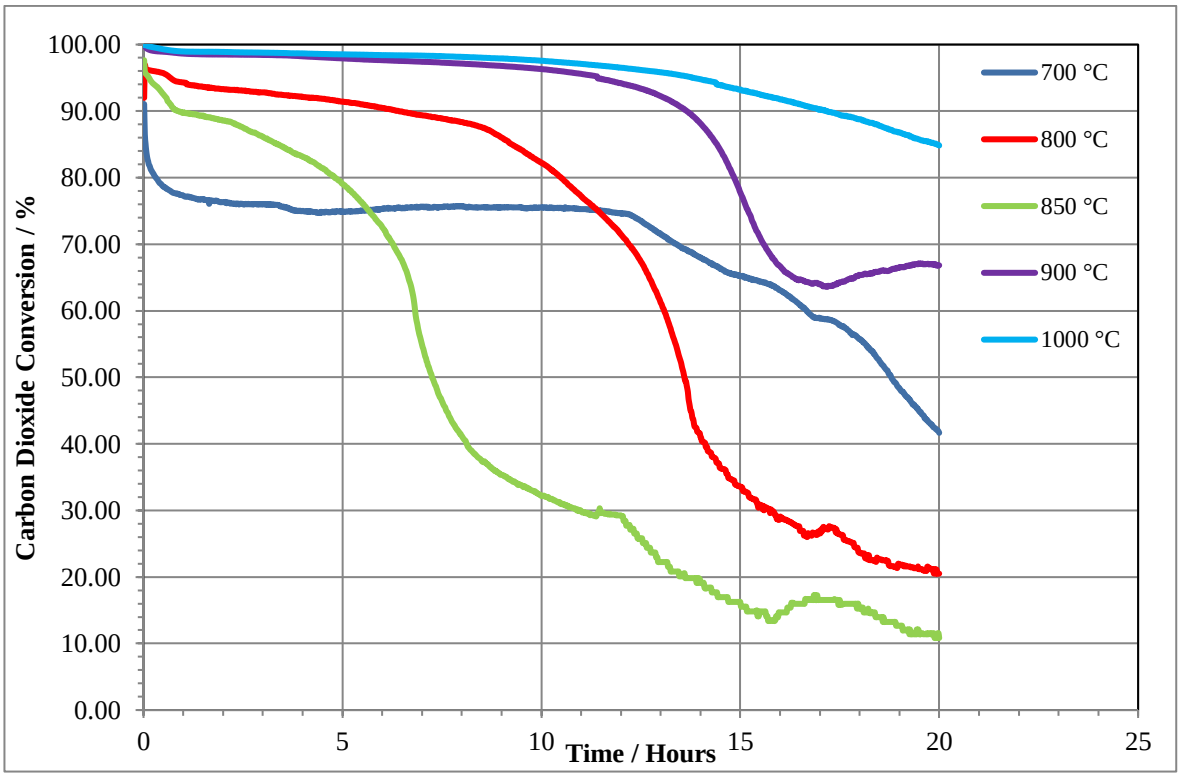

Figure 7-6 Carbon dioxide conversion during reaction of a 2:1 CH_4:CO_2 mixture with 10 ppm of H_2S over Ni/YSZ at different reaction temperatures

The profile for carbon dioxide conversion shows that at 1000 °C the loss of activity is mainly due to a sharp decrease in thermal decomposition of methane. In the first 10 hours of reaction methane conversion, as seen in Figure 7-2, falls by around 25% however the conversion of carbon dioxide only drops by ~ 2%, and this is similar for the reaction at 900 °C also. At 700 °C, 800 °C and 850 °C the carbon dioxide conversion is much more similar to that of methane conversion seen in Figure 7-6 indicating that the dry reforming reaction is the primary reaction taking place. At 700 °C between 5 and 10 hours on stream there appears to be a period of equilibrium as the carbon dioxide conversion does not fall. However in this period the conversion of methane is seen to drop. This is attributed to promotion of the water gas shift reaction at this temperature, as at this stage of the reaction both water and carbon monoxide are available, and due to the water gas shift reaction

being mildly exothermic the reaction conditions are favourable. This result suggest that the reaction pathway for the dry reforming of methane over Ni/YSZ may occur in two separate stages, the first being the thermal decomposition of methane followed by the reverse Boudouard reaction.

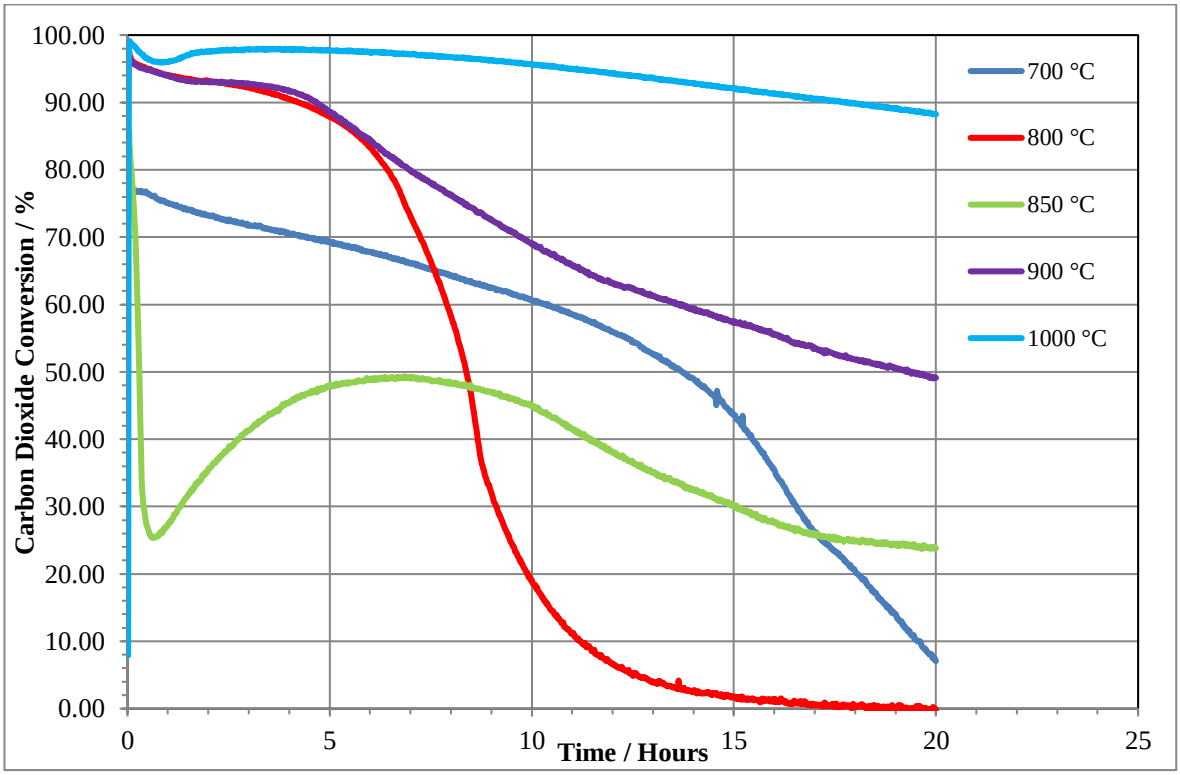

Figure 7-7 Carbon dioxide conversion during reaction of a 2:1 CH_4:CO_2 mixture with 10 ppm of H_2S over 5% Ceria doped Ni/YSZ at different temperatures

The extent of the recovery of the carbon dioxide signal for ceria doped Ni/YSZ at 850 °C shown in Figure 7-7, and the subsequent sharp increase in consumption suggest that the catalyst becomes oxidised or that pre reaction reduction is incomplete, and that the initial recovery is caused by the catalyst being reduced under the methane flow. The remaining reactions show similar behaviour to Ni/YSZ in that at 1000 °C the drop in carbon dioxide conversion is not as severe as the methane conversion, due to a decrease in methane decomposition, but also the elevated temperature decreases the extent of loss of DRM

activity compared to cooler reaction temperatures. Again the carbon dioxide conversion profiles at 700 °C, 800 °C and 850 °C, as would be expected, closely follow that of the methane conversion profile as the extent of side reactions occurring is lower. The reaction at 700 °C does show some variance to the methane conversion profile in that the carbon dioxide conversion falls at a much faster rate in the final five hours of reaction. This is thought to be a result of the Boudouard reaction which is favoured in this temperature regime over nickel based catalysts[24]. This is also reflected in an increased deposition of carbon as seen in Figure 7-10. This effect is not seen for the undoped material, resulting in the inference that under the specific reaction conditions the inclusion of ceria promotes the Boudouard reaction.

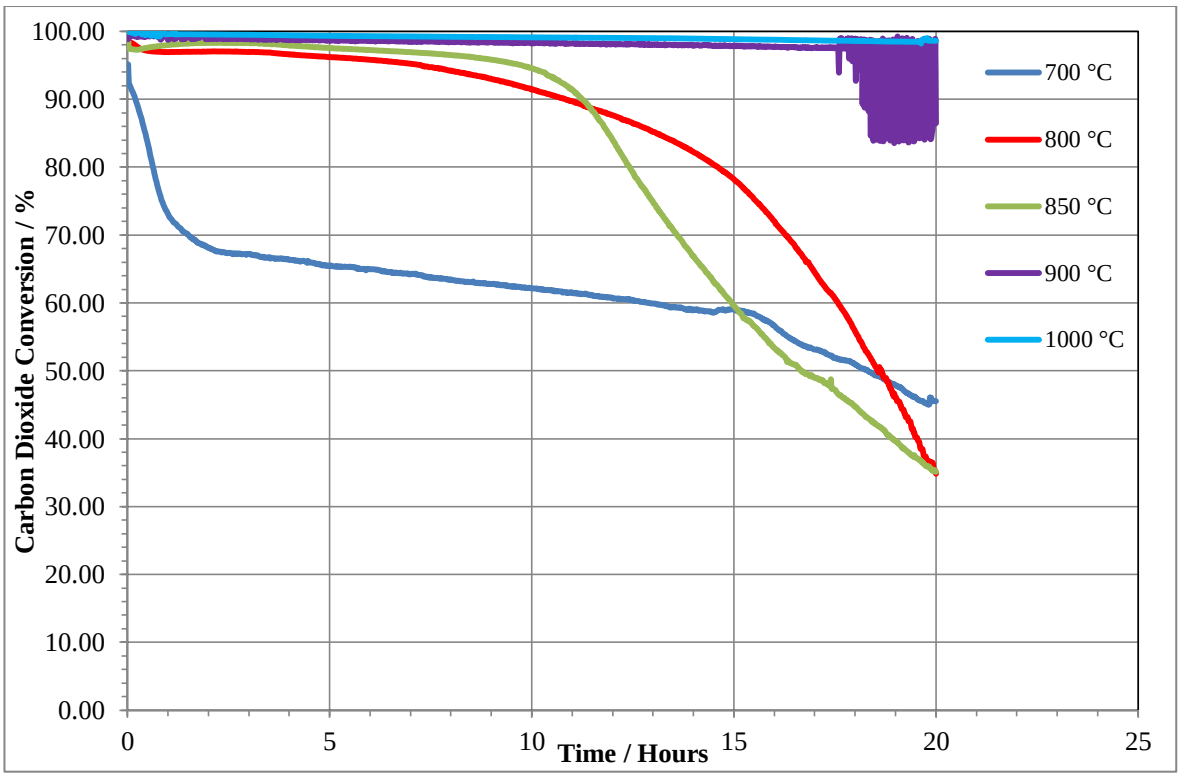

Figure 7-8 Carbon dioxide conversion during reaction of a 2:1 CH_4:CO_2 mixture with 10 ppm of H_2S over 4 mol% Ni doped $SrZrO_3$ at different reaction temperatures

The carbon dioxide conversion for the perovskite as seen in Figure 7-9 has very similar profiles to the methane conversion profiles. There are minor differences, for instance at

850 °C there is a recovery in the conversion of methane in the first five hours of reaction which is not seen in the carbon dioxide profile, indicating that this was solely caused by increased thermal decomposition of methane. This is confirmed by the carbon dioxide conversion in the period of reaction remaining stable and being completely consumed

7.2.1.3 Carbon Deposition

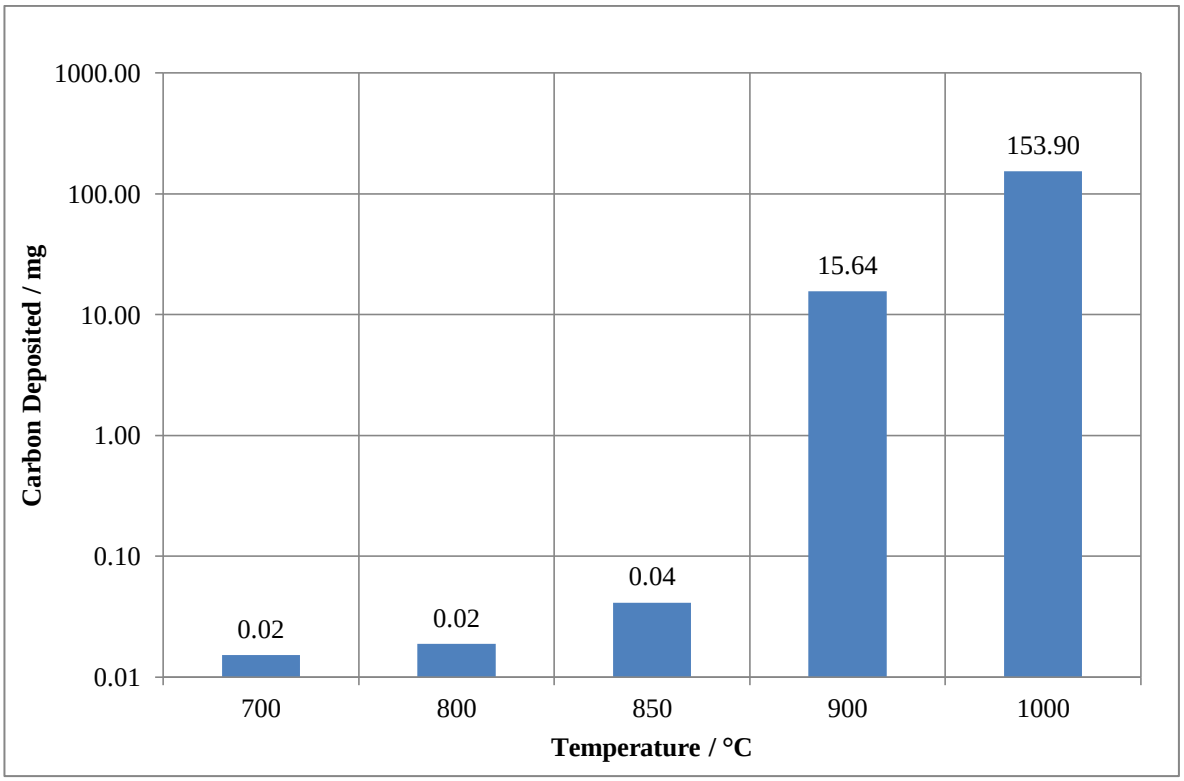

Figure 7-9 Carbon deposition following reaction at various temperatures for a 2:1 CH_4:CO_2 reforming reaction over Ni/YSZ with 10 ppm of H_2S

The variation in the amount of carbon deposition for Ni/YSZ with reaction temperature is shown below in Figure 7-9 and a clear trend between temperature and carbon deposition is seen. At 900 °C and 1000 °C the amount of carbon deposited is extremely high due to promotion of methane decomposition at elevated temperature as well as a promoting effect caused by the sulphur in the reactant stream. Carbon deposition at lower reaction

temperatures is negligible, which is in part a result of the loss of activity as a result of sulphur poisoning, all three reactions converted below 900 °C less than the stoichiometrically predicted 50% of methane for the majority of the reaction and this falls quickly with time.

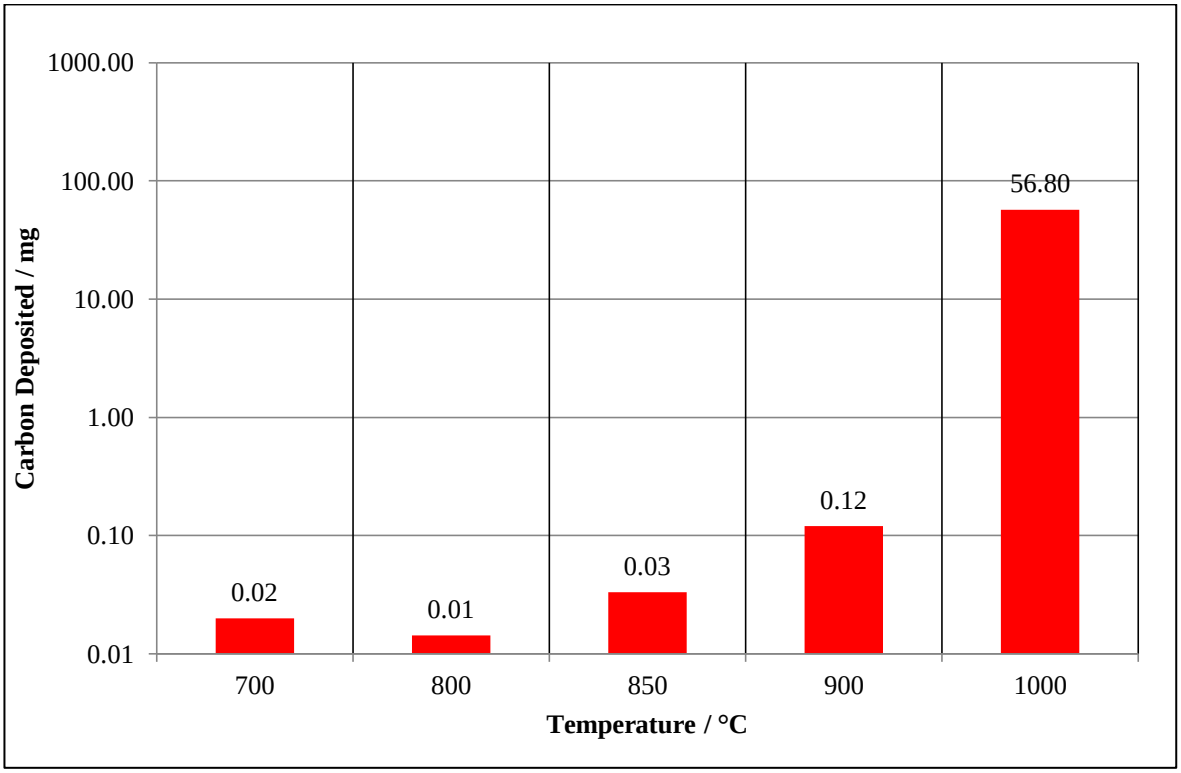

Figure 7-10 Carbon deposition following reaction at various temperatures for a 2:1 CH_4:CO_2 reforming reaction over 5% Ceria doped Ni/YSZ with 10 ppm of H_2S

Addition of ceria suppresses the amount of carbon deposition significantly at higher reaction temperatures. This can be explained by the oxygen storage capacity (OSC) of ceria and the availability of oxidant in the form of carbon dioxide and some water. Despite the elevated temperatures at 900 °C and 1000 °C, due to the presence of H_2S, the carbon dioxide in the reactant stream is not fully reformed during the reaction. As a result of this the simultaneous removal of carbon by ceria which is then in turn oxidised by carbon dioxide occurs. At the lower reforming temperatures (700 °C – 850 °C), the difference in

carbon deposition between the two cermet materials is insignificant due to both materials being significantly deactivated quickly by sulphur poisoning as predicted thermodynamically[25].

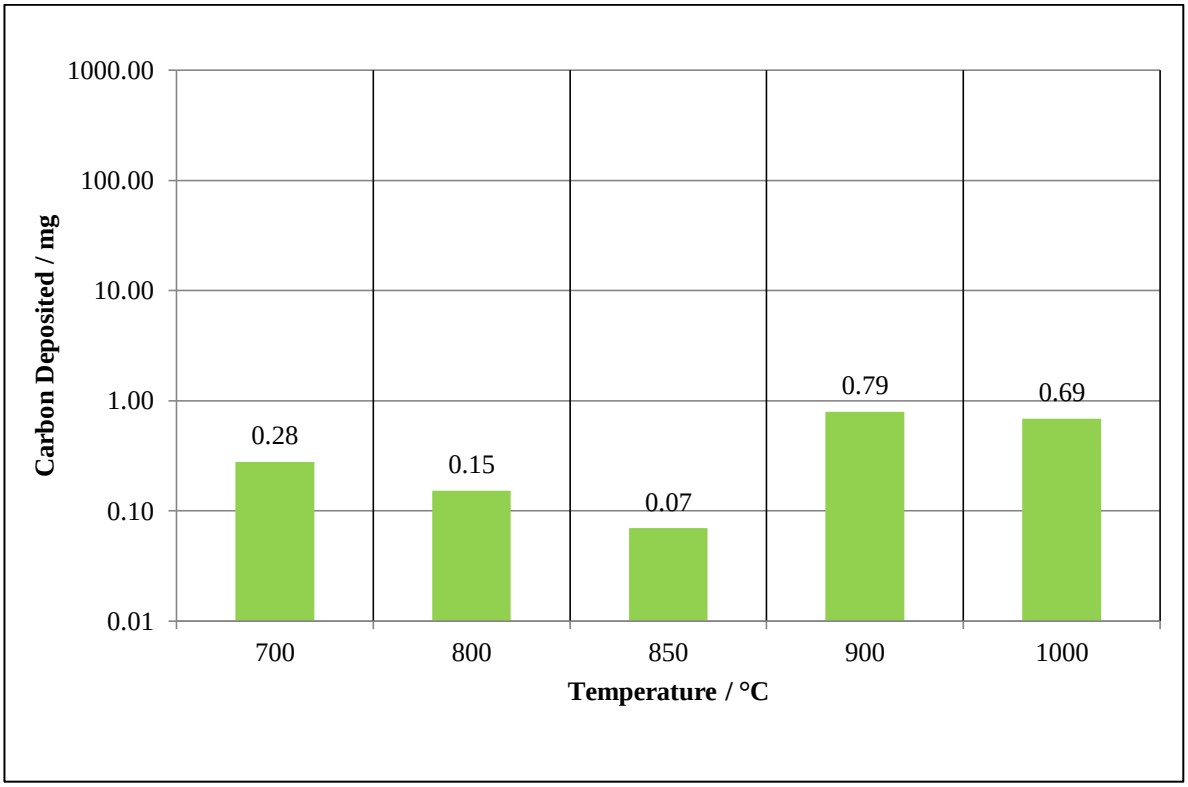

Figure 7-11 Carbon deposition from reactions at various temperature for a 2:1 CH_4:CO_2 reforming reaction over 4 mol% Ni doped $SrZrO_3$ with 10 ppm of H_2S

The perovskite material has been shown in chapters 5-7 to promote the Boudouard reaction, particularly at 700 °C. This is the case with the addition of sulphur with a trend of falling carbon deposition between 700 °C and 850 °C despite the activity increasing between these temperatures. At 1000 °C the perovskite consistently converts more than 50% of the methane in the reactant stream, indicating that thermal decomposition of methane must be occurring. Despite this the carbon deposition is extremely low. This could be a result of three things. Firstly, as the perovskite material promotes the Boudouard reaction, at higher reaction temperatures it is possible that the reverse

Boudouard reaction occurs. However, the amount of carbon dioxide available for this is low, making this unlikely. A second explanation could be attributed to the structure of the perovskite material, with each nickel atom being isolated from the next nickel atom. It is possible that the formation of C-C bonds is difficult due to the lack of proximity and as a result carbon is removed. The final explanation could be that the presence of sulphur on the surface of the perovskite causes coupling of methane and resulted in the formation of ethane, ethene or ethyne. This would cause an increase in the conversion of methane and a decrease in the amount of carbon deposited relative to the same conversion of methane by the pyrolysis reaction.

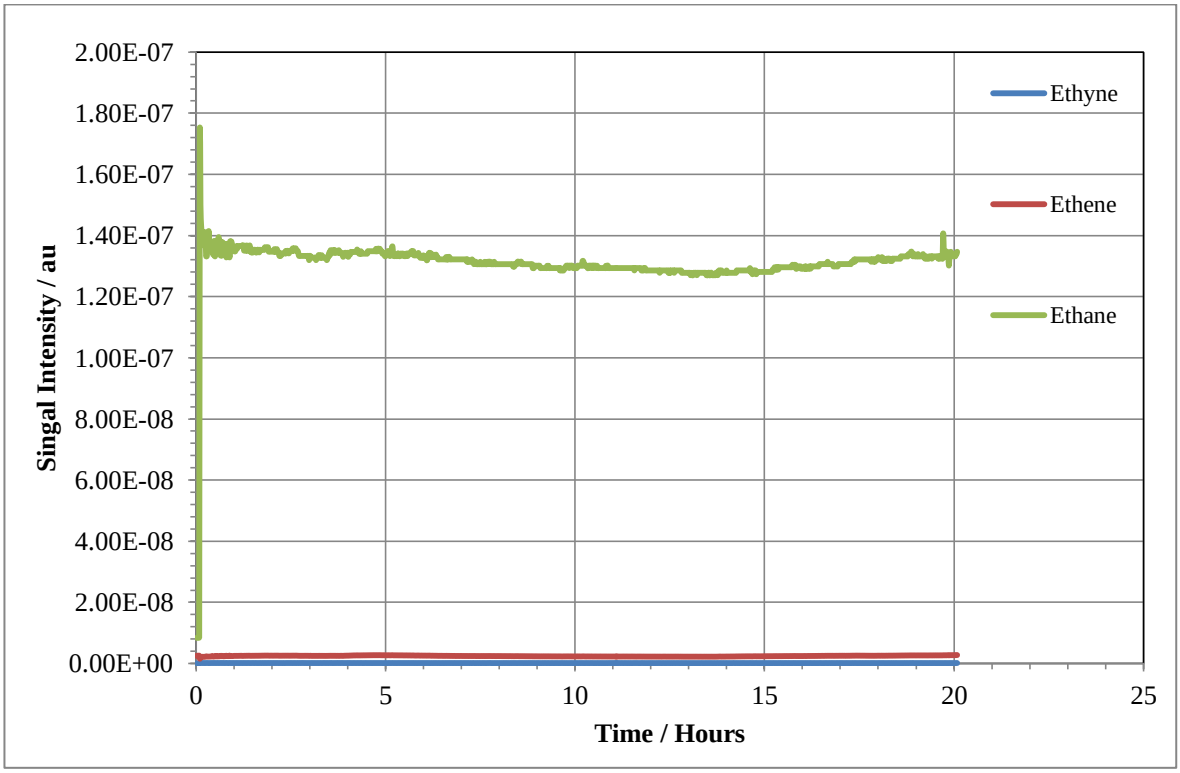

Figure 7-12 Comparison of ethane, ethene and ethyne coupling fragments for a 2:1 CH_4:CO_2 reaction mixture over 4 mol% Ni doped $SrZrO_3$ with 10 ppm of H_2S

In order to further explore the possibility that the addition of hydrogen sulphide to the reactant stream promoted coupling of methane, three (uncalibrated) fragments were plotted

for the reaction over the perovskite at 1000 °C; 25 for ethyne, 27 for ethene and 29 for ethane. The results are presented in Figure 7-12. Although it is difficult to precisely quantify the amount of ethane, ethene and ethyne in the reactant stream as calibrations for these masses are not available, Figure 7-12 shows that some coupling does occur and this results in the formation of ethane. The quantification of the ethane signal is further complicated by electronic interference from neighbouring signals, particularly signal 28 used for carbon monoxide. This made any further analysis or evaluation problematic.

7.2.2 Effect of Sulphur Concentration

7.2.2.1 Methane Conversion

To compare the effect that sulphur concentration had on the reaction profile, reactions were carried out at 850 °C with the hydrogen sulphide concentration within the reactor feed ranging from 0 ppm to 10 ppm. As would be expected, increasing the concentration of sulphur in the reactant stream increases the extent of poisoning of Ni/YSZ. This is seen in Figure 7-13 Methane conversion during reaction of a 2:1 CH_4:CO_2 mixture over Ni/YSZ at 850 °C with different concentrations of hydrogen sulphide as seen by the methane conversion at the end of reaction.

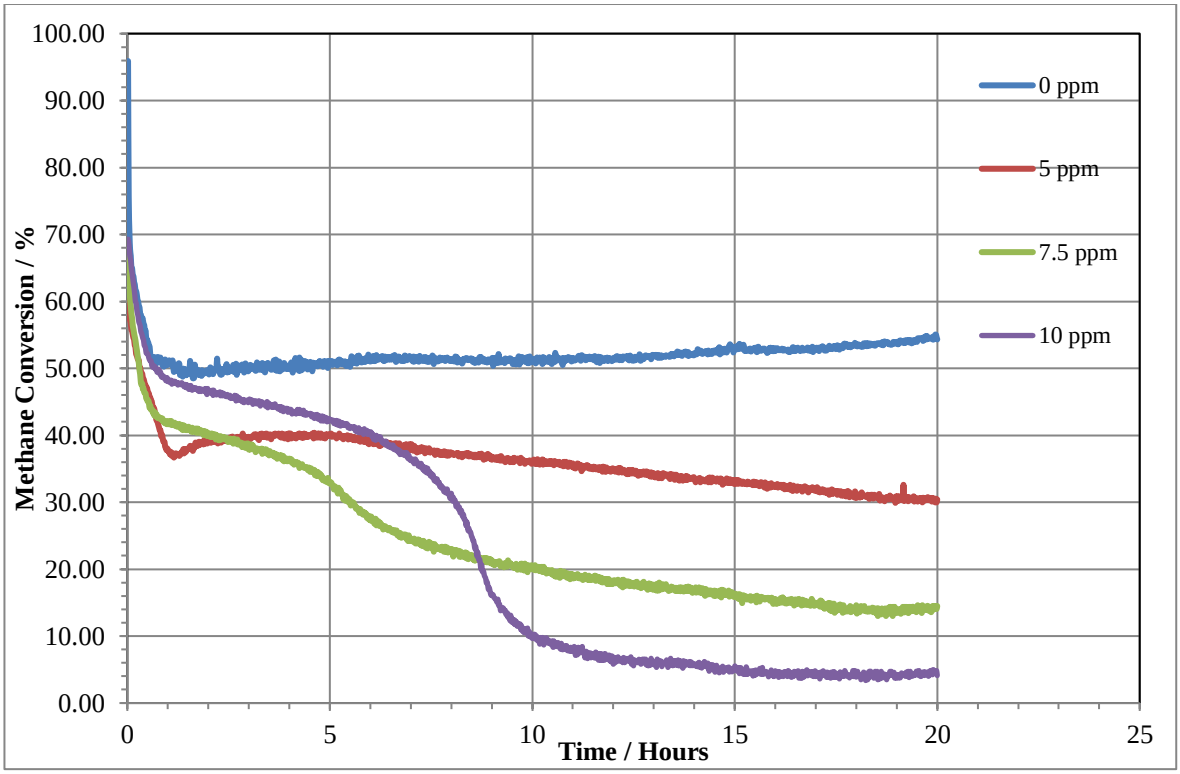

Figure 7-13 Methane conversion during reaction of a 2:1 CH_4:CO_2 mixture over Ni/YSZ at 850 °C with different concentrations of hydrogen sulphide

The methane conversion in the absence of sulphur is stable for the extent of the reaction, although slightly above 50% caused by the reaction mixture being marginally carbon dioxide richer than intended. When 5 ppm of H_2S is added to the reactant stream the first five hours of reaction exhibit a relatively similar profile. However, after five hours a fairly linear decrease in the methane conversion is seen as a result of sulphur poisoning. This suggests that a fairly linear loss of nickel sites occurs between five hours and 20 hours, although loss of reforming activity was not complete. Increasing the sulphur concentration to 7.5 ppm changes the poisoning profile with evidence of a second faster poisoning phase. Increasing the concentration to 10 ppm increases the rate of this second phase.

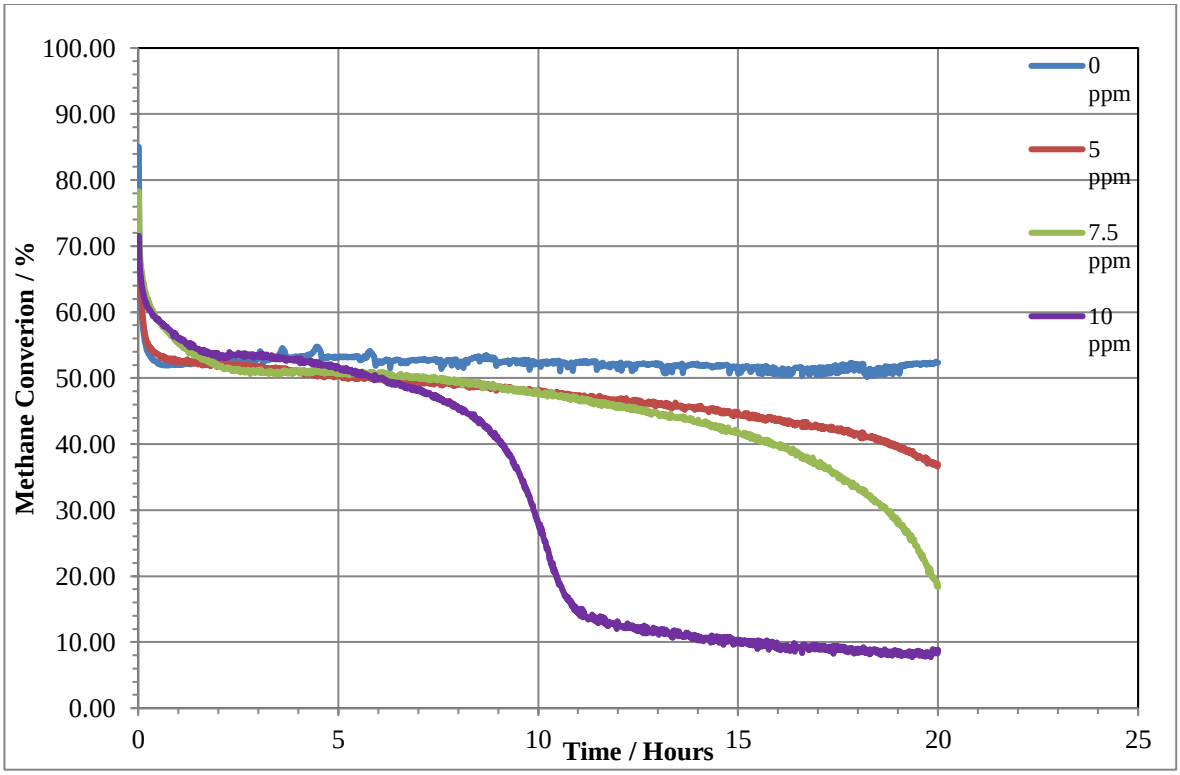

Figure 7-14 Methane conversion during reaction of a 2:1 CH_4:CO_2 mixture 5% Ceria doped Ni/YSZ at 850 °C with different concentrations of hydrogen sulphide

The addition of ceria in the Ni/YSZ cermet extends the time it took for poisoning to begin. All four reactions for Ni/YSZ show immediate signs of loss of activity, however the reactions for 5% ceria doped Ni/YSZ all show stability in methane conversion for the initial five hours of reaction. This suggests that addition of ceria increases the rate of desorption of sulphur species from the surface of the catalyst. The reactions for reaction mixtures containing 5 ppm and 7.5 ppm of sulphur both only display a single phase of deactivation. However as the rate of poisoning was slow it is likely that the second phase of reaction would eventually begin if the reaction time was longer. At 10 ppm a two phase loss of activity is seen with the addition of ceria making little difference to the conversion of methane by the end of reaction.

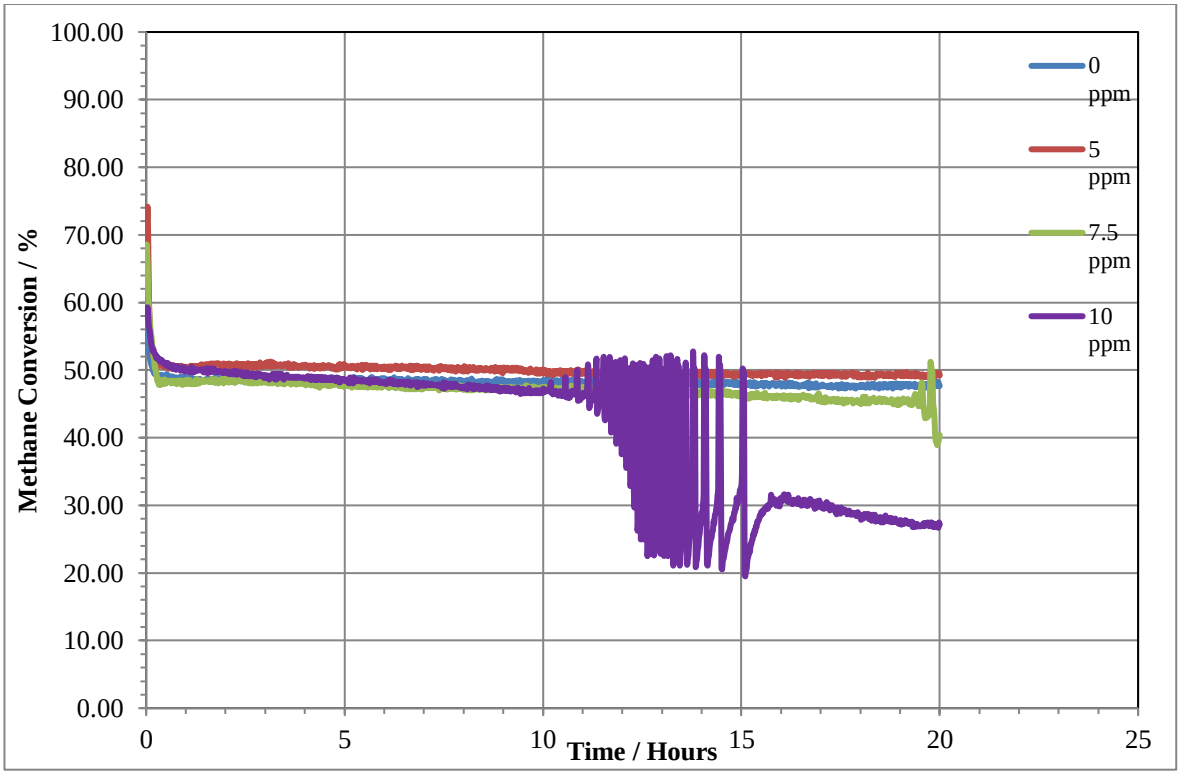

Figure 7-15 Methane conversion for 2:1 CH_4:CO_2 reforming reactions over 4 mol% Ni doped $SrZrO_3$ at 850 °C with variable concentrations of hydrogen sulphide

Figure 7-15 shows that the perovskite catalyst shows a greater resistance to sulphur poisoning at the lower sulphur concentrations tested. At 5 ppm of sulphur no loss of reforming activity over the 20 hour period tested whereas both cermet materials show significant performance losses over the same length of time. Ni/YSZ and 5% ceria doped Ni/YSZ both only have methane conversions between 10% and 20% after 20 hours of the reaction with 7.5 ppm of H_2S in the reactant stream. However, the perovskite material displays little loss of reforming activity until the very end of the 20 hour reaction when some low level cycling was observed. Similarly the reaction in the presence of 10 ppm of hydrogen sulphide was also relatively stable for the first 10 hours of reaction before a period of large product cycling occurs. However in this case the cycling decreases and a more linear loss of activity was seen in the final phase of reaction.

These results show that the perovskite does show more resistance to sulphur poisoning, particularly when compared to the cermet materials. The results suggest that the rate of adsorption of sulphur on the perovskite surface could be slower than over Ni/YSZ based materials, resulting in a slower rate of poisoning. The structure of the perovskite results in the nickel being enclosed with oxygen making it difficult for the relatively large sulphur to come into proximity with the nickel. As a result of this is it likely the rate of adsorption is slow due to steric hindrance considerations. A further consideration that was made is that it is theorised that initially one sulphur can occupy several nickel sites in supported nickel catalysts[3,19]. In the perovskite structure the distance between the nickel ions means that this is not possible, and this results in a slower rate of poisoning.

7.2.2.2 Carbon Dioxide Conversion

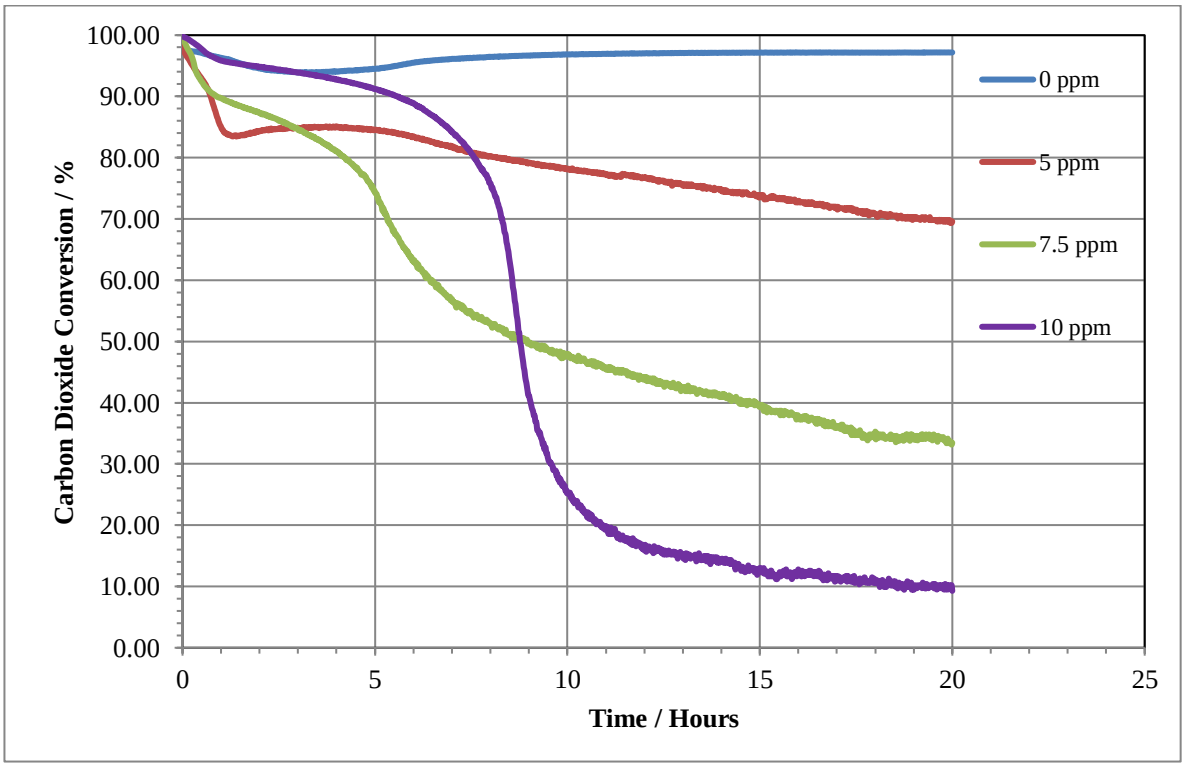

Figure 7-16 Carbon dioxide conversion during reaction of a 2:1 CH_4:CO_2 mixture over Ni/YSZ at 850 °C with different concentrations of hydrogen sulphide

Using the conversion of carbon dioxide, little extra insight was gained into the extent and the mechanism of poisoning over all three materials, as seen in Figure 7-16 - Figure 7-18. The relatively high reaction temperature prevents the water gas shift reaction from occurring, however the temperature is also low enough that thermal decomposition of methane is not great.

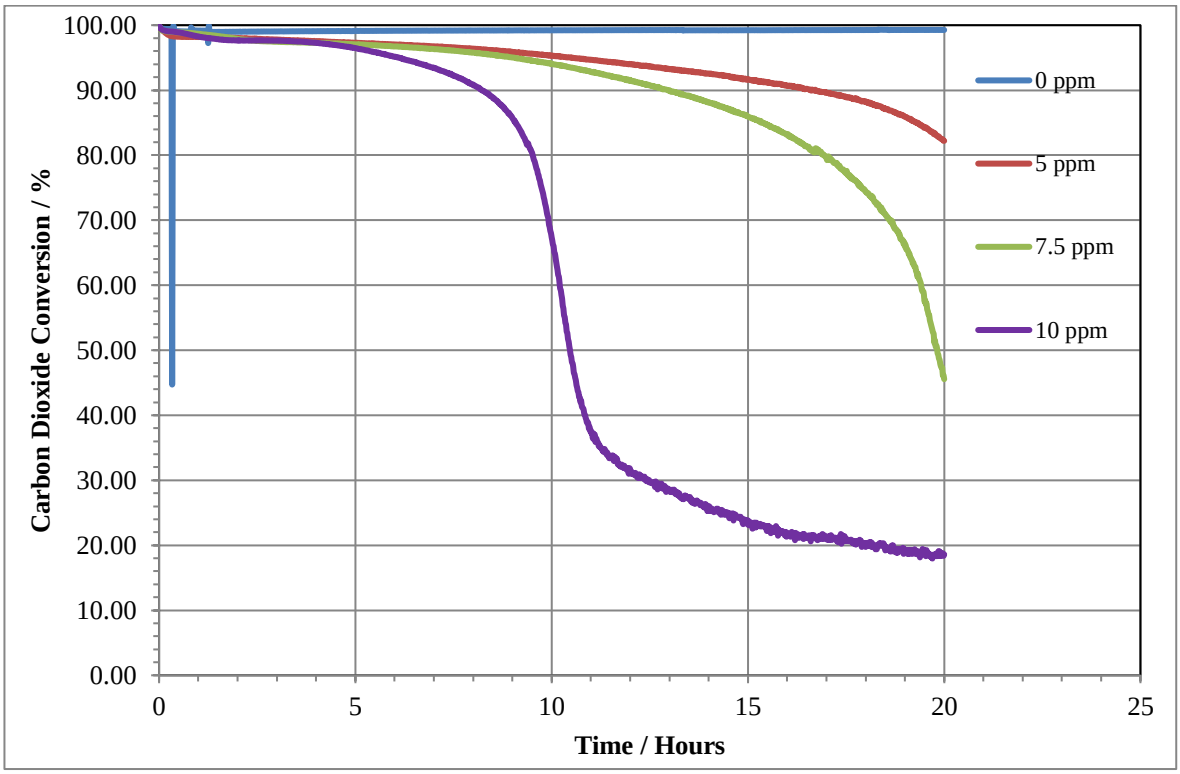

Figure 7-17 Carbon dioxide conversion during reaction of a 2:1 CH_4:CO_2 mixture over 5% ceria doped Ni/YSZ at 850 °C with different concentrations of hydrogen sulphide

The resistance to sulphur caused by the addition of ceria to the cermet material is highlighted in Figure 7-17, as all three sulphur containing reactions show little performance loss in the first five hours of reaction. The reaction containing 10 ppm of hydrogen sulphide in the reaction feed, for both Ni/YSZ and 5% ceria doped Ni/YSZ displays the two phase activity loss that is observed in Section 7.2.1.1 which suggests that the increased sulphur concentration has an effect on the type of poisoning that occurs.

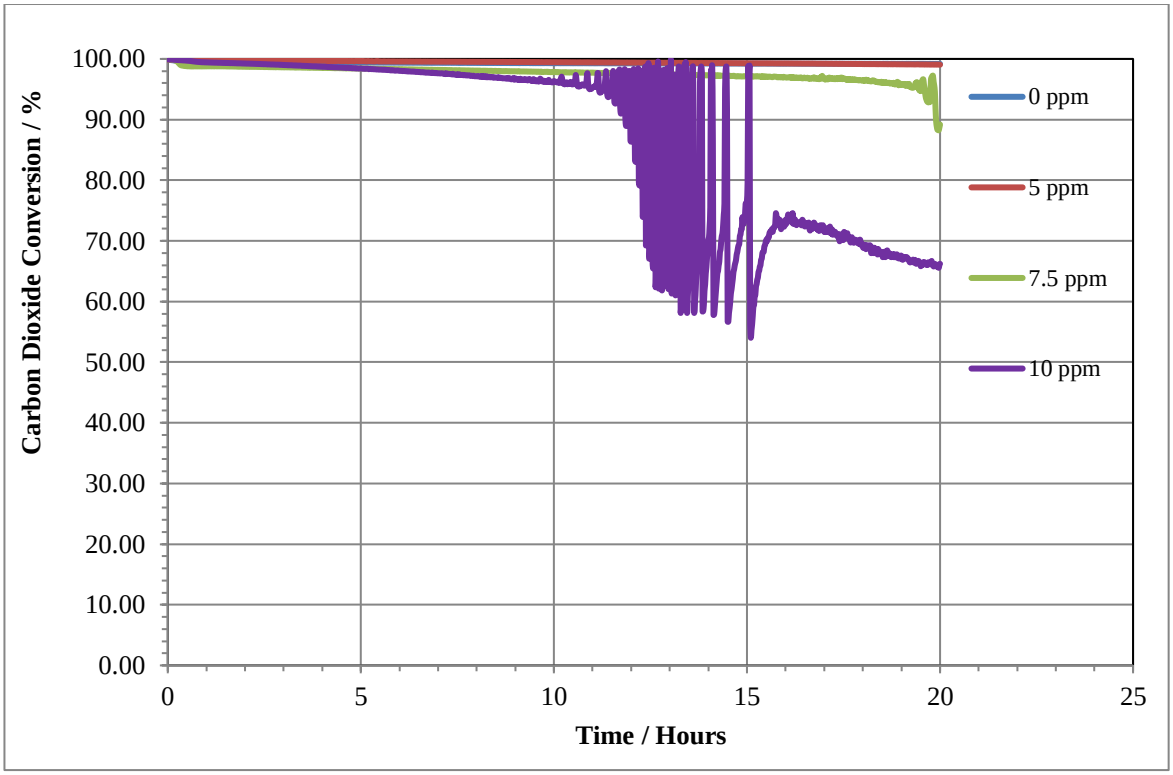

Figure 7-18 Carbon dioxide conversion during reaction of a 2:1 CH_4:CO_2 mixture over 4 mol% Ni doped $SrZrO_3$ at 850 °C with different concentrations of hydrogen sulphide

The data for the carbon dioxide conversion over the perovskite seen in Figure 7-18 shows no discernible difference to the methane conversion due to the conversions being so high for much of the reaction. The carbon dioxide conversion does however correlate to the methane conversion in the period of cycling for the reaction with 10 ppm of H_2S, which shows that the DRM is peaking and troughing rather than methane decomposition or another side reaction.

7.2.2.3 Carbon Deposition

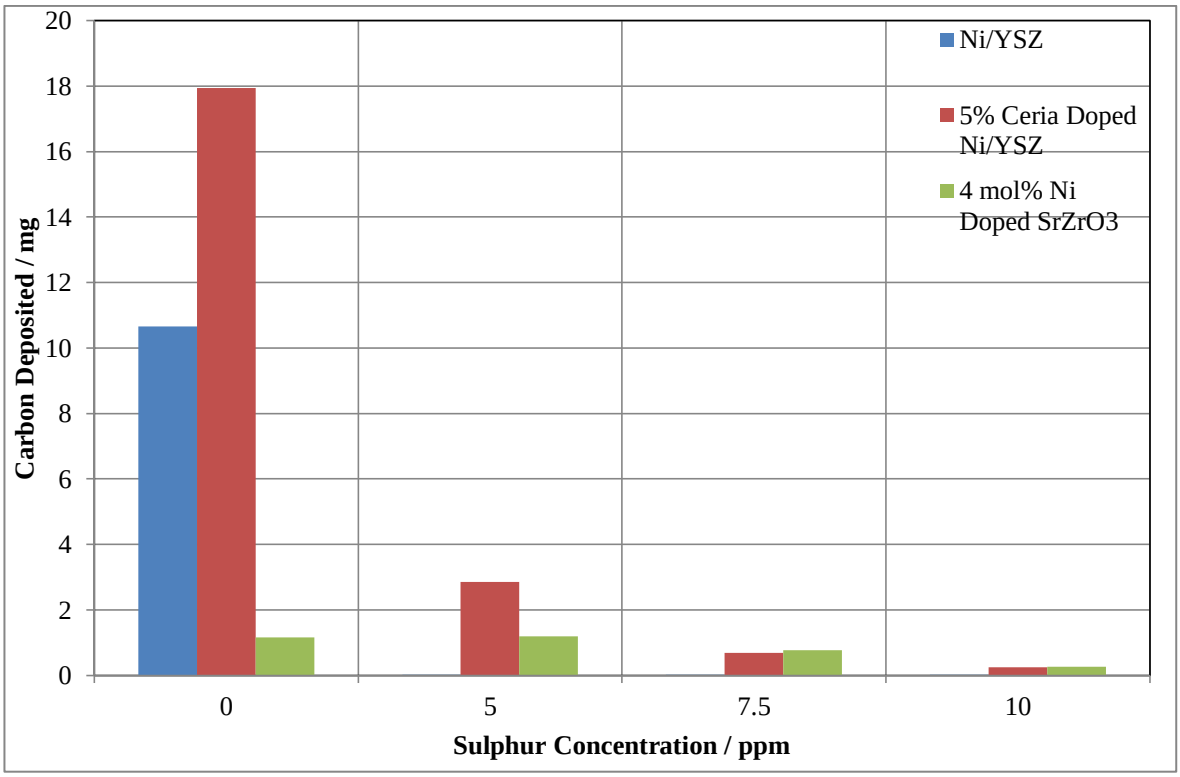

Figure 7-19 Carbon deposition after reaction of reaction of a 2:1 CH_4:CO_2 mixture over Ni/YSZ, 5% ceria doped Ni/YSZ and 4 mol% Ni doped $SrZrO_3$ at 850 °C with different concentrations of hydrogen sulphide

In the absence of sulphur in the reactant gas feed, the amount of carbon deposited over both cermet materials is relatively high (Figure 7-19), with the ceria doped Ni/YSZ giving the highest deposition due to the promotion of methane decomposition and lack of oxidant available to utilise the OSC of ceria. The perovskite material gives very low carbon deposition in sulphur free reforming conditions. The addition of 5 ppm of H_2S makes no noticeable difference to the carbon deposition on the perovskite material, as the activity remained the same for the lifetime of the reaction. However, for both Ni/YSZ and 5% ceria doped Ni/YSZ the carbon deposition is suppressed due to the loss of reforming activity seen This suppression is relative to the extent of the loss in that Ni/YSZ suffered the greatest performance loss, has the lowest deposition of carbon. Similarly at a level 7.5

ppm of sulphur in the reactant feed there is little difference in the amount of carbon deposition over the 4 mol% Ni doped $SrZrO_3$ sample due to the maintained reforming activity. No detectable carbon is deposited over Ni/YSZ as the activity is so low for the majority of the reaction. The resistance seen for the ceria doped Ni/YSZ sample again gives an elevated deposition of carbon compared to the undoped counterpart. The drop in activity at 10 ppm H_2S did result in a lowering of the deposition of carbon over the perovskite, as is seen for the cermet materials.

7.3 Conclusions

Sulphur poisoning of Ni/YSZ under methane rich biogas reforming conditions displayed a characteristic two phase loss of reforming activity as has been reported previously in the literature, whereby the first phase is caused by formation of surface nickel sulphide caused by dissociative chemisorption of H_2S[2,26]. Between 700 °C and 850 °C the rate of formation of the first phase was accelerated by increasing temperature, indicating that at these reaction temperatures the rate of the first phase was governed with the reaction kinetics. The second phase of activity loss was consistent with the thermodynamics of sulphur poisoning, which is favoured at lower reaction temperatures tested. As a result this second phase was formed more quickly at the lower reaction temperatures. This can be linked to the formation of bulk nickel sulphide species.

4 mol% Ni doped $SrZrO_3$ showed significantly increased resistance to sulphur poisoning under the range of temperatures showing little or no loss of reforming activity at 1000 °C, although some cycling occurred at 900 °C. At the lower reaction temperatures tested the nickel doped perovskite maintained better reforming activity when compared to the nickel

cermet materials and over twenty hours reaction did not fully lose reforming activity. Much of the increased resistance to sulphur poisoning of the perovskite wass attributed to the structure of the material and steric considerations in relation to sulphur being able to come into close proximity with nickel within the structure.

Analysis of deposited carbon showed a trend for both nickel cermet materials of increasing carbon deposition with temperature, with high levels of carbon deposition resulting from methane decomposition at higher reaction temperatures, and low levels of carbon as a result of low reforming activity at the lower reaction temperatures. The oxygen storage capacity of ceria resulted in lower deposits of carbon on the ceria doped Ni/YSZ sample despite some of the reactions displaying a better activity. The perovskite material did not show the same trend as observed for the nickel cermet materials, with similar levels of deposition at all reaction temperatures. This was despite showing an increased conversion of methane at 1000 °C, which would usually result in an elevated deposition of carbon. Further analysis of this reaction showed that the excessive conversion may have been caused by a carbon coupling reaction that was promoted by the inclusion of sulphur in the reactant stream.

Increasing the concentration of H_2S in the reactant stream increased the level of sulphur poisoning for all three materials, consistent with other studies[1,3,11,27]. The cermet materials both showed significant loss of reforming activity at the lowest concentration in the reactant stream. Increasing the sulphur concentration introduced a two-phase loss of reforming activity for the cermet materials and the extent of the poisoning observed. The perovskite displayed a strong resistance to 5 ppm and 7.5 ppm for the 20 hours tested. At

10 ppm of sulphur in the biogas reaction mixture, in the initial 10 hours of reaction the rate of desorption of sulphur from the perovskite surface was significant.

The analysis of carbon deposition from these reactions gave some insight, however many of the reactions gave carbon deposition that is extremely low. Generally there was a correlation between activity and level of carbon deposited for the nickel cermet materials and little or no correlation for the nickel doped perovskite.

The work in this chapter highlights that several experiments had not reached equilibrium so longer experiment times would be useful. It would also be interesting to alter the amount of oxidant present and to monitor how this altered the poisoning profile and lifetime of the materials. Finally as it is possible to have different levels of nickel within the perovskite structure, so identifying a relationship between this and the lifetime would have been of interest.

7.4 References

1 E. Brightman, D. G. Ivey, D. J. L. Brett and N. P. Brandon, *J. Power Sources*, 2011, **196**, 7182–7187.

2 C. J. Laycock, J. Z. Staniforth and R. M. Ormerod, *Electrochem. Soc. Trans.*, 2009, **16**, 177–188.

3 L. Deleebeeck, M. Shishkin, P. Addo, S. Paulson, H. Molero, T. Ziegler and V. I. Birss, *Phys. Chem. Chem. Phys.*, 2014, **16**, 9383–9393.

4 G. J. Offer, J. Mermelstein, E. Brightman and N. P. Brandon, *J. Am. Ceram. Soc.*, 2009, **92**, 763–780.

5 T. R. Smith, A. Wood and V. I. Birss, *Appl. Catal. A Gen.*, 2009, **354**, 1–7.

6 C. S. Lau, A. Tsolakis and M. L. Wyszynski, *Int. J. Hydrogen Energy*, 2010, **36**, 397–404.

7 V. I. Birss, L. Deleebeeck, S. Paulson and T. Smith, in *Electrochemical Society Transactions*, 2011, vol. 35, pp. 1445–1454.

8 Z. Cheng and M. Liu, *ECS Trans.*, 2013, **58**, 217–229.

9 M. Gong, X. Liu, J. Trembly and C. Johnson, *J. Power Sources*, 2007, **168**, 289–298.

10 S. C. Singhal and K. Kendall, *High Temperature Solid Oxide Fuel Cells: Fundamentals, Design and Applications*, Elsevier B.V., 2003.

11 J. Hepola and P. Simell, *Appl. Catal. B Environ.*, 1997, **14**, 305–321.

12 J. Sehested, *Catal. Today*, 2006, **111**, 103–110.

13 J. A. Anderson and M. F. Garcia, Eds., *Supported Metals in Catalysis*, Imperial

College Press, 5th edn.

14 J. A. Moulijn, a. E. Van Diepen and F. Kapteijn, *Appl. Catal. A Gen.*, 2001, **212**, 3–16.

15 P. Lohsoontorn, D. J. L. Brett and N. P. Brandon, *J. Power Sources*, 2008, **183**, 232–239.

16 K. Kendall, *Int. Mater. Rev.*, 2005, **50**, 257–264.

17 I. A. Proctor, A. L. Hopkin and R. M. Ormerod, *Ionics (Kiel).*, 2003, **9**, 242–247.

18 S. Appari, V. M. Janardhanan, R. Bauri, S. Jayanti and O. Deutschmann, *Appl. Catal. A Gen.*, 2014, **471**, 118–125.

19 O. B. J. Fraser, *Trans. Electrochem. Soc.*, 1937, **71**, 425.

20 Z. Cheng, S. Zha and M. Liu, *J. Electrochem. Soc.*, 2006, **153**, A1302.

21 C. H. Bartholomew, *Appl. Catal. A Gen.*, 2001, **212**, 17–60.

22 D. J. Nixon, PhD Thesis, Keele University, 2013.

23 T. S. Li and W. G. Wang, *J. Power Sources*, 2011, **196**, 2066–2069.

24 S. Wang, G. Q. M. Lu and G. J. Millar, *Energy Environ. Sci.*, 1996, **10**, 896–904.

25 J. F. B. Rasmussen and A. Hagen, *J. Power Sources*, 2009, **191**, 534–541.

26 C. J. Laycock, J. Z. Staniforth and R. M. Ormerod, *Dalt. Trans.*, 2011, **40**, 5494.

27 R. J. Gorte and J. M. Vohs, *Curr. Opin. Colloid Interface Sci.*, 2009, **14**, 236–244.

8 Catalyst recovery from sulphur poisoning following biogas reforming

8.1 Introduction

The initial reactions focussing on sulphur poisoning during biogas reforming determined the effect that operating temperature and sulphur concentration had on the rate and also the extent of sulphur poisoning of Ni/YSZ, 5% ceria doped Ni/YSZ and 4 mol% Ni doped $SrZrO_3$. This was evaluated for Ni/YSZ and 5% ceria doped Ni/YSZ for which some limited literature exists[1–15]. This was then used as a baseline for 4 mol% Ni doped $SrZrO_3$ for which there is no reported literature on sulphur tolerance under catalytic biogas reforming conditions. The work in this chapter has implications for the use of this catalyst material as a biogas reforming catalyst or in SOFCs, as regeneration from sulphur poisoning is an important issue. This could be achieved by switching the reactant gas source to a feed that is free of sulphur contamination[4,16,17]. Other ways to achieve catalyst regeneration involve 'shut-down'; oxidation and re-reduction of the catalyst.

As discussed in chapter 7, sulphur poisoning can occur *via* chemisorbed sulphur, from dissociative chemisorption of H_2S on the surface of a nickel based catalyst. This is a reversible reaction under the right reaction parameters, including temperature[4,17], reaction time[18] and concentration of sulphur in the reactant stream[19]. Regeneration from sulphur poisoning can occur under sulphur free reaction conditions by adsorbed sulphur desorbing into the gas phase in the form of SO_2, CS_2 or H_2S resulting in the recovery of the nickel surface[20–22]. Although well documented for the supported nickel catalysts the interaction and recovery of perovskites with sulphur contamination is largely unknown, and also likely to be dependent on the specific perovskite formulation utilised as a catalyst.

8.2 Experimental Methodology

Catalyst deactivation was achieved using a 2:1 ratio of methane to carbon dioxide (1 ml min^{-1} and 0.5 ml min^{-1} respectively, typical of biogas) with the total flow maintained at 20 ml min^{-1} with different levels of H_2S and helium as a carrier, with a reaction temperature of 800 °C with the recovery monitored using QMS. In each reaction at the end of the poisoning phase the H_2S was removed from the reactant stream, and helium added in order to maintain a constant total flow throughout the reaction. The reaction temperature was also simultaneously altered.

Two types of catalyst recovery were investigated; 1) the initial concentration of hydrogen sulphide was varied, with H_2S levels of 10 ppm, 15 ppm and 20 ppm, 2) the temperature of the recovery phase was investigated at 700 °C, 800 °C and 900 °C. Due to logistical difficulties, the time of both the poisoning phase and recovery phase was fixed 24 hours for each phase with sulphur concentration as the variable, and 22 hours for each phase where temperature was the variable.

8.3 Catalyst Recovery from Sulphur Poisoning: Changing the Concentration of Sulphur

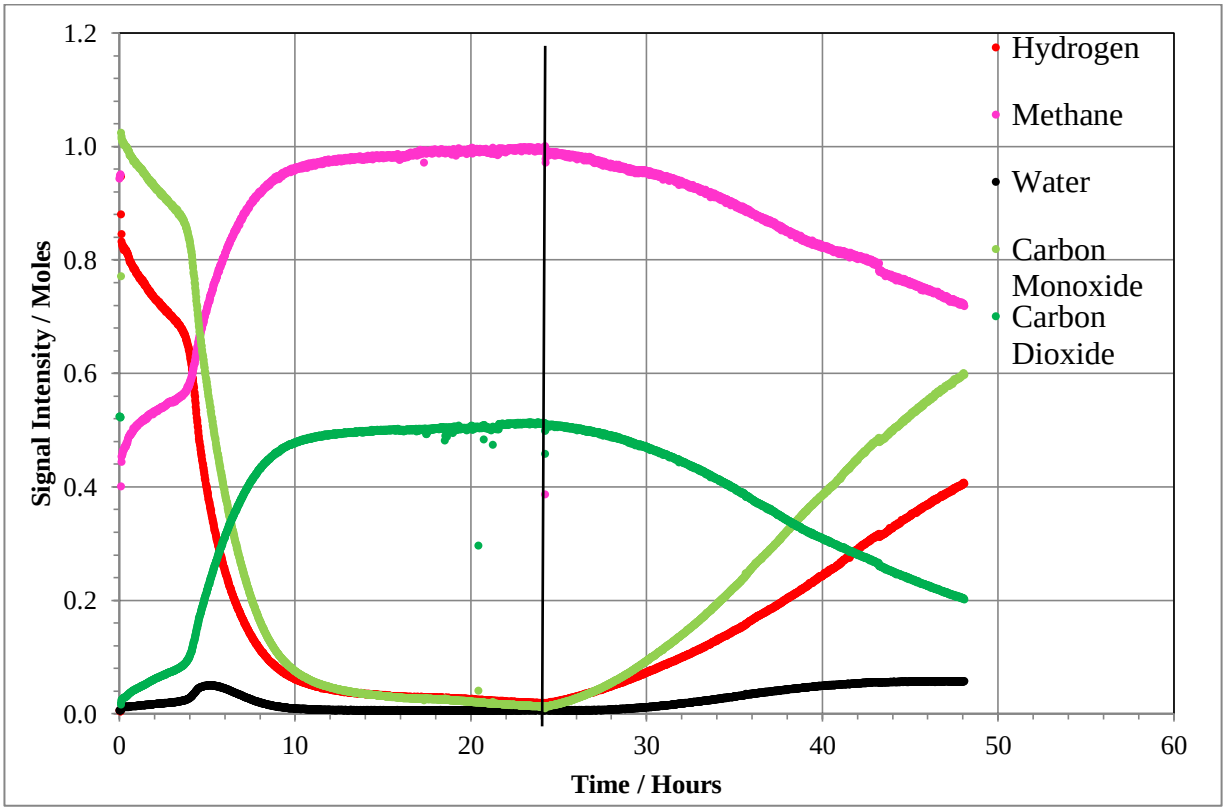

Figure 8-1 Sulphur poisoning and recovery from sulphur poisoning experiment using a 2:1 CH_4/CO_2 ratio with 10 ppm of H_2S and H_2S removed from the reactant feed after 24 hours, passed over Ni/YSZ at 800 °C

Figure 8-1 shows an example of a recovery experiment over Ni/YSZ with both the poisoning and recovery phase displayed. In this experiment a reaction mixture containing a 2:1 ratio of methane to carbon dioxide and 10 ppm of sulphur relative to methane was used to poison the catalyst for 24 hours at 800 °C. The catalyst is fully poisoned after this time as seen by detection of only methane and carbon dioxide *via* QMS, with no product formation. At this point the H_2S source is removed and the gas flow topped up with helium to maintain a consistent total flow. Upon removal of H_2S the methane and carbon dioxide conversion increases quickly at first. This is because the surface coverage of

sulphur is high, resulting in the desorption being favourable energetically. As the reaction continues the rate of recovery possibly slows marginally as the sulphur surface coverage decreased. Within the reaction time used, complete recovery of the catalyst material is not seen. However, the reaction had not plateaued and thus full recovery may eventually occur. In two stages of the reaction where the reaction mixture is hydrogen and carbon dioxide rich (between 0-10 hours and 28- 48 hours), the reverse water gas shift reaction is seen to occur resulting in the formation of both water and carbon monoxide, in both the poisoning and recovery stage of the reaction. This meant that the H_2:CO ratio is consistently low.

8.3.1 Methane Conversion

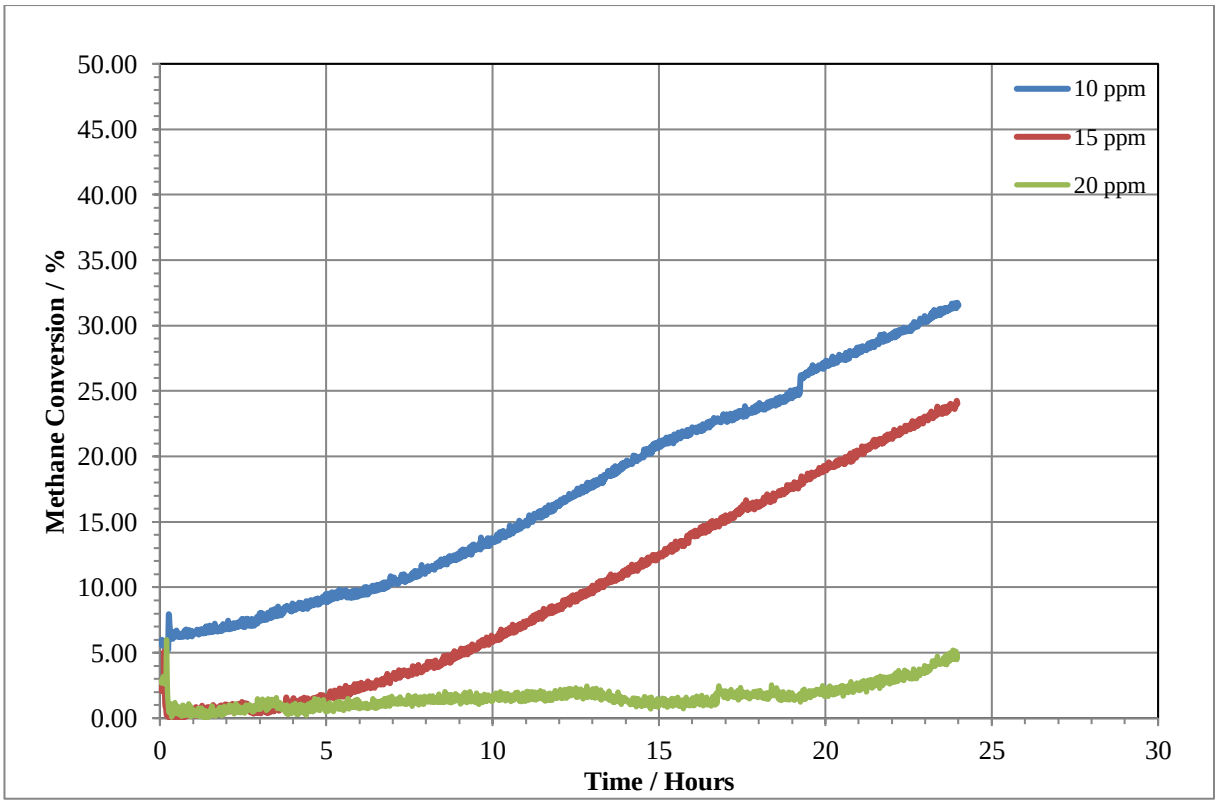

Figure 8-2 Comparison of methane conversion in the recovery from sulphur poisoning using a 2:1 CH_4/CO_2 reaction mixture passed over Ni/YSZ at 800 °C with varying H_2S concentration with recovery at 800 °C

The difference in the recovery stage of reaction when the concentration of sulphur is altered for Ni/YSZ is shown in Figure 8-2. All three reactions are seen to be fully poisoned in that methane and carbon dioxide are the only species detectable by QMS at the point at which the H_2S source was turned off. Despite the fact that all three catalysts appear to be at the same state of poisoning, the recovery profiles are very different and show a clear trend in that the time in which it took for recovery to begin is significantly longer when the concentration of sulphur is greater. Despite this, the rate at which recovery occurs once it starts appears to be very similar in each case this gave, which gives some insight into the mechanism of both poisoning and recovery. With the onset of recovery starting at different times this suggests that although the apparent activity is the same under each set of reaction conditions, the amount of sulphur that had adsorbed was greater when a greater concentration of H_2S is passed over the material and as a result sulphur adsorbs to areas which did not possess catalytic activity for this reaction. Once the sulphur source is removed the rate of sulphur desorption exceeds the rate of adsorption resulting in recovery. The starting point for recovery is different as some sulphur that desorbs is able to adsorb again, and as there is a greater availability of sulphur when the concentration is higher this results in longer time to recovery. Once recovery commences the ratio of rate of adsorption to rate of desorption is the same, as evident by the rate of recovery shown in *Table 8-1*.

Table 8-1 Rate of recovery of methane conversion after sulphur removed from reactant feed ($\%H^{-1}$)

	Ni/YSZ	**5% Ceria Doped Ni/YSZ**	**4 mol% Ni Doped $SrZrO_3$**
10 ppm	1.11	1.38	1.18
15 ppm	0.99	0.86	0.82
20 ppm	0.20	0.66	0.90

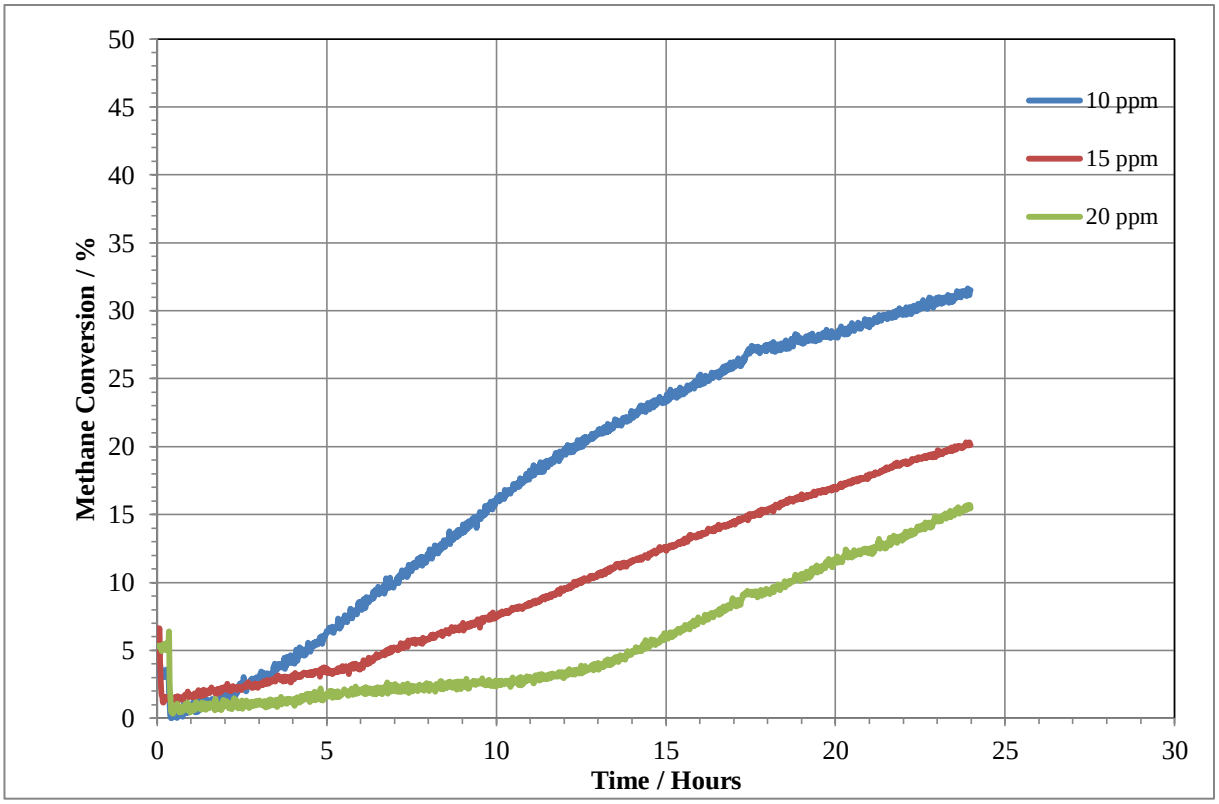

Figure 8-3 Comparison of methane conversion in the recovery from sulphur poisoning using a 2:1 CH_4/CO_2 reaction mixture passed over 5% ceria doped Ni/YSZ at 800 °C with varying H_2S concentration with recovery at 800 °C

For the ceria doped Ni/YSZ, the oxygen storage capacity of ceria gives a twofold improvement in the recovery from sulphur poisoning under the reaction conditions tested (Figure 8-3). Firstly, for all three sulphur concentrations tested, methane consumption

begins after a shorter period of time when compared to the undoped Ni/YSZ, with the biggest difference seen at the highest H_2S concentration (20 ppm). The second difference observed for 10 ppm and 20 ppm of H_2S (see Table 8-1) is that the rate of recovery is quicker. The trend seen for Ni/YSZ and the OSC of ceria suggest that the result for 15 ppm using the ceria based catalyst is anomalous. Ceria inclusion increases the rate of desorption of sulphur once the source is removed, in the form of SO_2[23]. This causes the earlier and faster recovery. This is a result of carbon dioxide as an oxidant source, so that the ceria in the catalyst could switch between the reduced and oxidised state, releasing oxygen as a result.

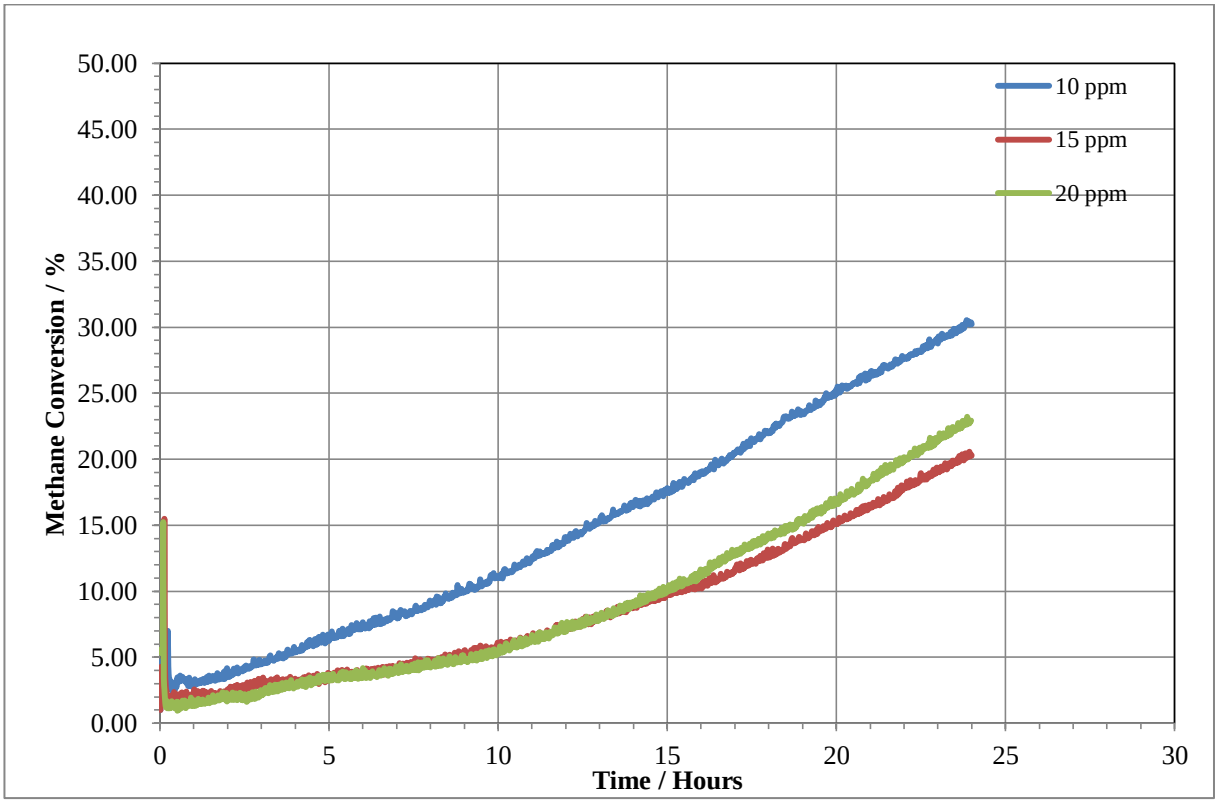

Figure 8-4 Comparison of methane conversion in the recovery from sulphur poisoning using a 2:1 CH_4/CO_2 reaction mixture passed over 4 mol% Ni doped $SrZrO_3$ at 800 °C with varying H_2S concentration with recovery at 800 °C

It is not known whether the perovskite would recover from complete poisoning by hydrogen sulphide given the absence of relevant literature on sulphur poisoning of perovskite materials. It is seen that regardless of sulphur concentration recovery did occur (Figure 8-4). Unlike the nickel cermet materials recovery starts as soon as the hydrogen sulphide is removed from the reactant stream for all three reactions. Once recovery begins the rate and also extent is seen to be highest for the reaction poisoned at 10 pm of H_2S. For the reactions at 15 ppm and 20 ppm the rate (see Table 8-1) extent and shape of the recovery profile is very similar. This coupled with the fact that recovery starts immediately indicates that unlike the cermet materials that have excess sites that can be poisoned but do not affect catalysis, the perovskite material contains active sites that are all poisoned and once sulphur is removed and recovery begins, all are then available for reaction. Despite recovery beginning immediately the rate of recovery at all three concentrations is slowest for the perovskite compared to the cermet materials once recovery begins, although the profile shows evidence that the recovery accelerates for the perovskite, and remains fairly linear for the nickel cermets.

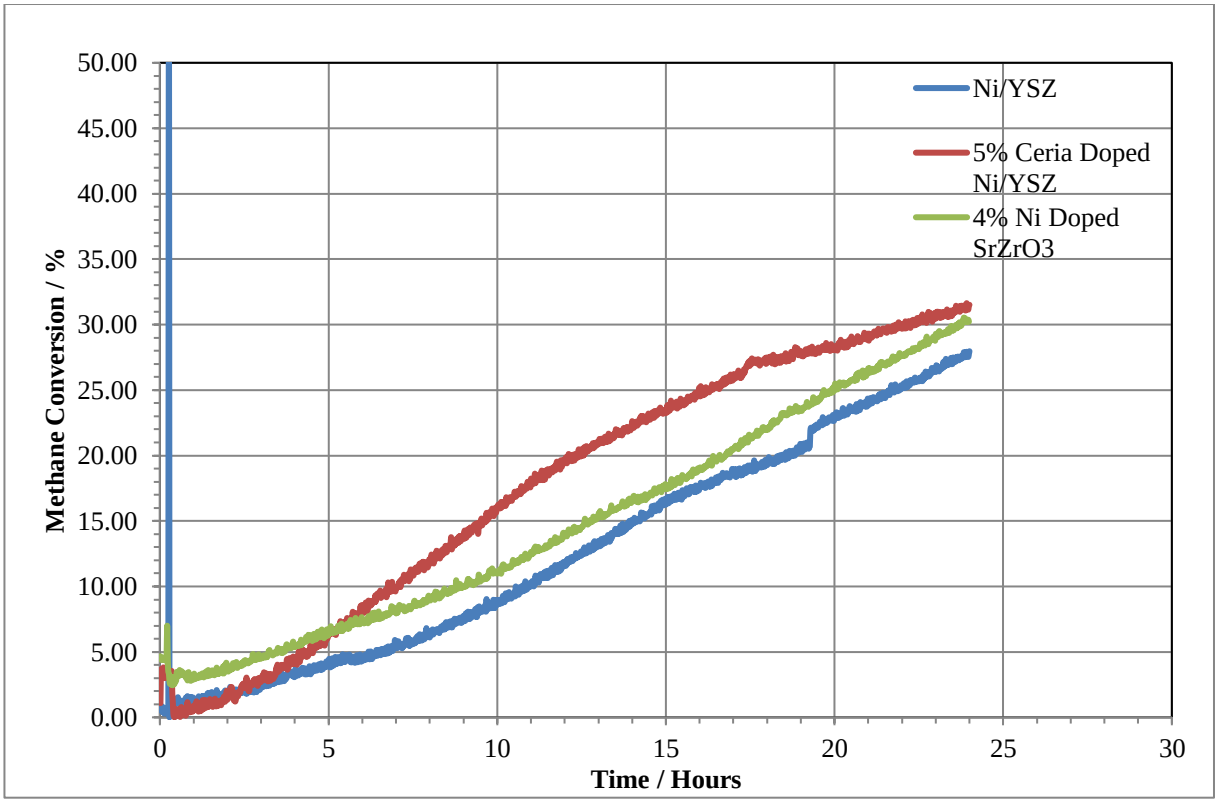

Figure 8-5 Comparison of methane conversion in the recovery from sulphur poisoning using a 2:1 CH_4/CO_2 reaction mixture passed over Ni/YSZ, 5% ceria doped Ni/YSZ and 4 mol% Ni doped $SrZrO_3$ at 800 °C with 10 ppm of H_2S with recovery at 800 °C

Comparing the three materials when poisoned, for example 10 ppm of H_2S (Figure 8-5) it is clear to see that the perovskite started to recover earlier than the cermets but at a similar rate. The final methane conversions for the three materials have a separation of ~8%. None of the reactions reach equilibrium and it is unclear whether recovery would have been full (50% methane conversion) for all three of the materials or if there is some permanent loss of catalytic activity.

8.3.2 Carbon Dioxide Conversion

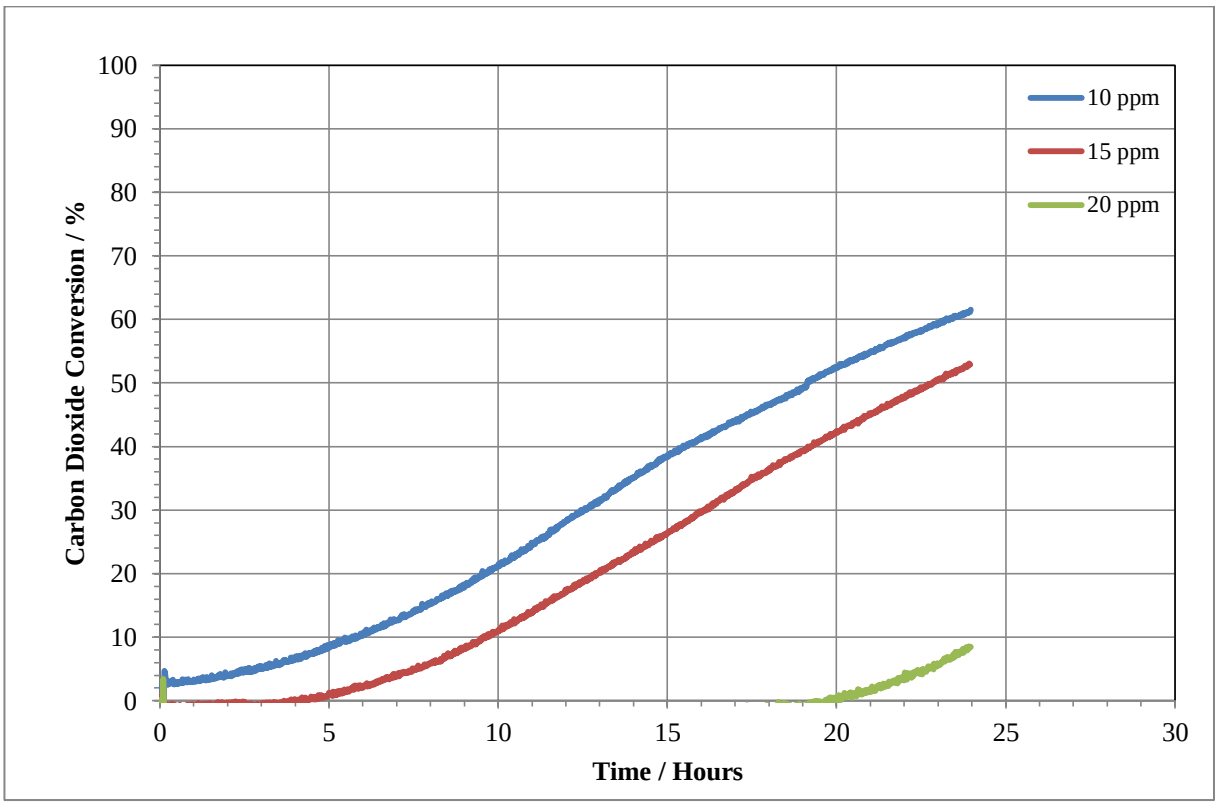

Figure 8-6 Comparison of carbon dioxide conversion in the recovery from sulphur poisoning using a 2:1 CH_4/CO_2 reaction mixture passed over Ni/YSZ at 800 °C with varying H_2S concentration with recovery at 800 °C

The profile for the carbon dioxide conversion during the recovery phase (Figure 8-6) for the Ni/YSZ catalyst is very similar to the methane profile (Figure 8-2). This indicates that the recovery reflected dry reforming and not decomposition of methane. The conversion of carbon dioxide is approximately double the conversion of methane for the extent of the reaction as is expected and the recovery of carbon dioxide conversion begins at the same time as the recovery of methane begins. .

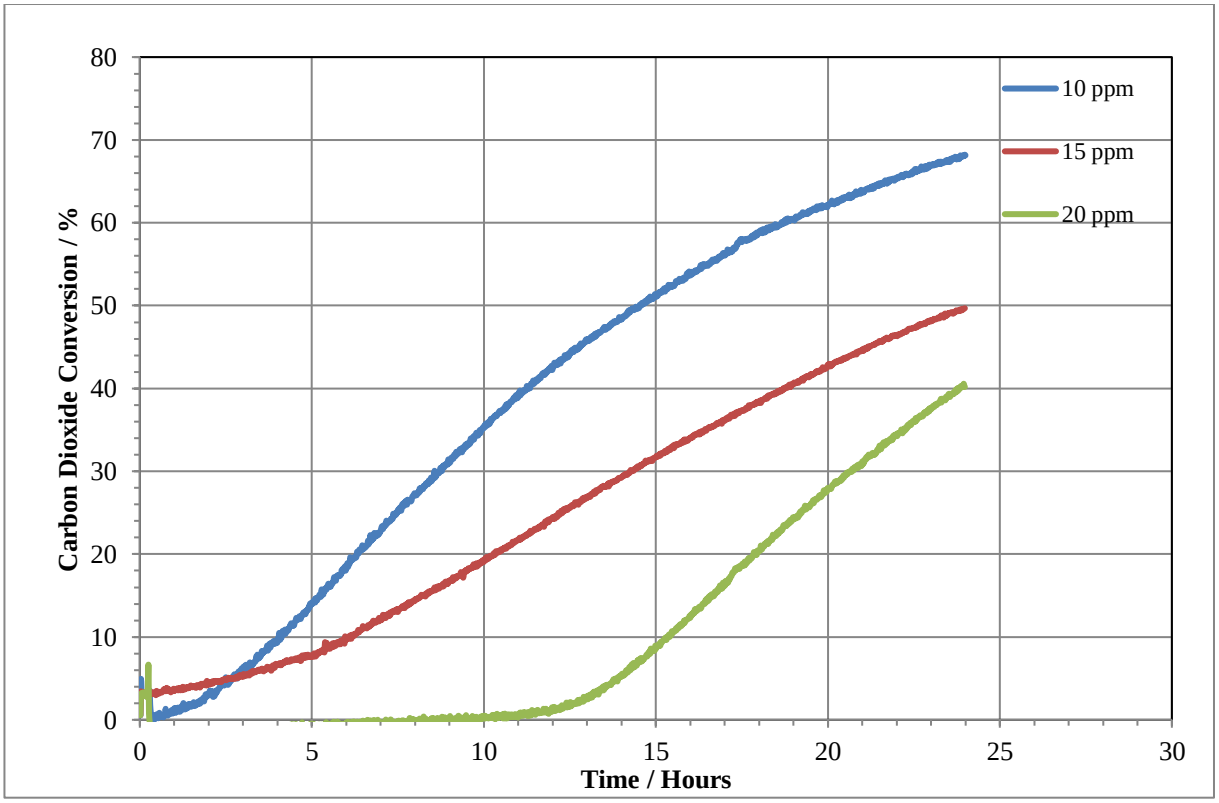

Figure 8-7 Comparison of carbon dioxide conversion in the recovery from sulphur poisoning using a 2:1 CH_4/CO_2 reaction mixture passed over 5% ceria doped Ni/YSZ at 800 °C with varying H_2S concentration with recovery at 800 °C

As for Ni/YSZ, for 5% ceria doped Ni/YSZ (Figure 8-7) the profile for carbon dioxide conversion during recovery is remarkably similar to that of methane conversion and offers little insight into occurrence of side reactions. The nickel doped perovskite material also shows the same behaviour as can be seen in Figure 8-8.

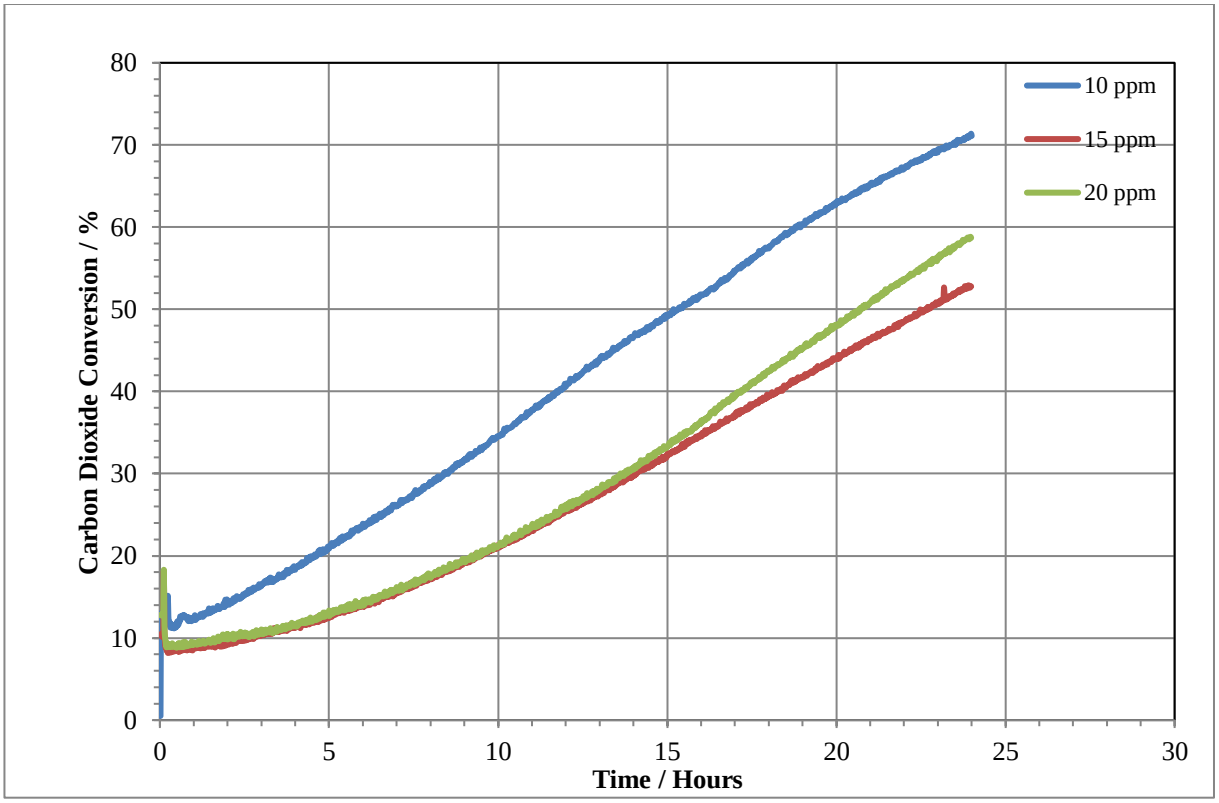

Figure 8-8 Comparison of carbon dioxide conversion in the recovery from sulphur poisoning using a 2:1 CH_4/CO_2 reaction mixture passed over 4 mol% Ni doped $SrZrO_3$ at 800 °C with varying H_2S concentration with recovery at 800 °C

8.3.3 H_2:CO Ratio

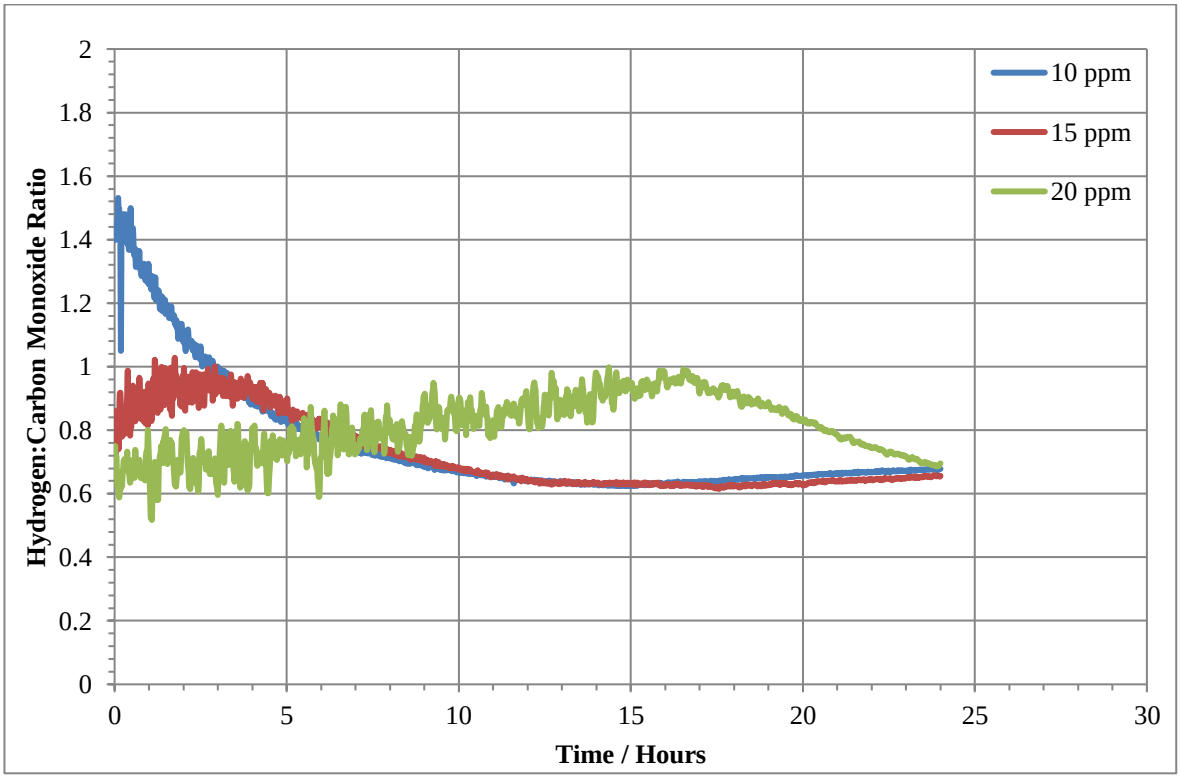

Figure 8-9 Comparison of hydrogen: carbon monoxide ratio in recovery stage from experiments using a 2:1 CH_4/CO_2 ratio passed over Ni/YSZ at 800 °C with varying sulphur concentration and recovered at 800 °C

Plotting the variation of the hydrogen to carbon monoxide ratio with time on stream for Ni/YSZ (Figure 8-9) shows that early in the recovery process, as the conversion of methane begins to increase, the ratio of hydrogen to carbon monoxide decreased. This is a result of the concentration of carbon dioxide in the gaseous mixture still being high, and as a result conversion of hydrogen and carbon dioxide to carbon monoxide and water was occurring *via* the reverse water gas shift reaction. As the reaction progresses this reaches equilibrium and then as the consumption of carbon dioxide *via* the DRM increases, the

hydrogen to carbon monoxide ratio begins to increase towards a ratio of 1, indicating an efficient dry reforming of methane reaction. The recovery profiles following reactions with 10 ppm and 15 ppm of H_2S give profiles that are very similar, once the recovery progress begins. At 20 ppm as the recovery did not begin until ~18 hours, much of the hydrogen to carbon monoxide ratio data is useless due to the value for each signal being almost nil. Once the recovery begins the ratio falls in the same fashion as the reactions at 10 ppm and 15 ppm, indicating the presence of the reverse water gas shift reaction. As the reactions do not equilibrate, it is unclear if the inclusion of sulphur in the reactant stream causs a permanent change in the distribution of the product gases when recovery is complete.

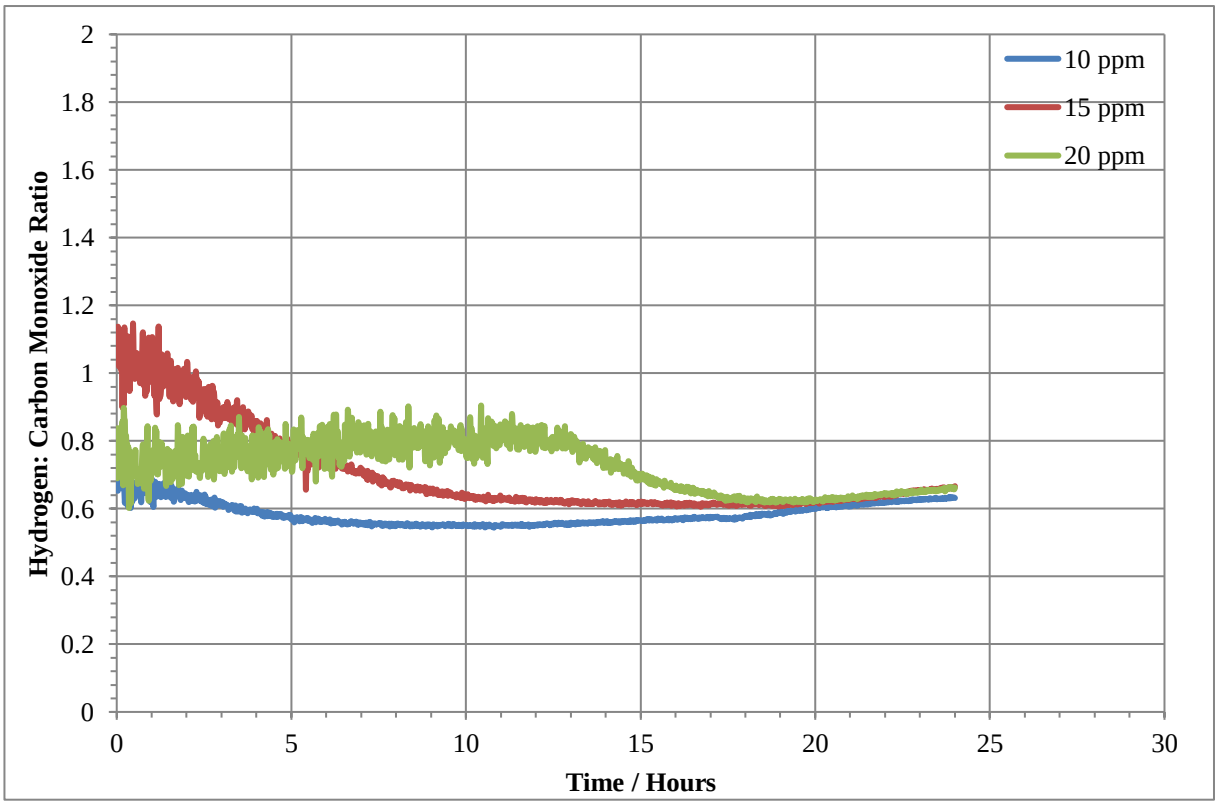

Figure 8-10 Comparison of hydrogen: carbon monoxide ratio in recovery stage from experiments using a 2:1 CH_4/CO_2 ratio passed over 5% ceria doped Ni/YSZ at 800 °C with varying sulphur concentration and recovered at 800 °C

Plotting the same data for 5% ceria doped Ni/YSZ gives very similar profiles for H_2:CO ratios. A trend of decreasing ratio as hydrogen formation begins, which in turn reacts with carbon dioxide to form water and carbon monoxide, as is seen for Ni/YSZ.

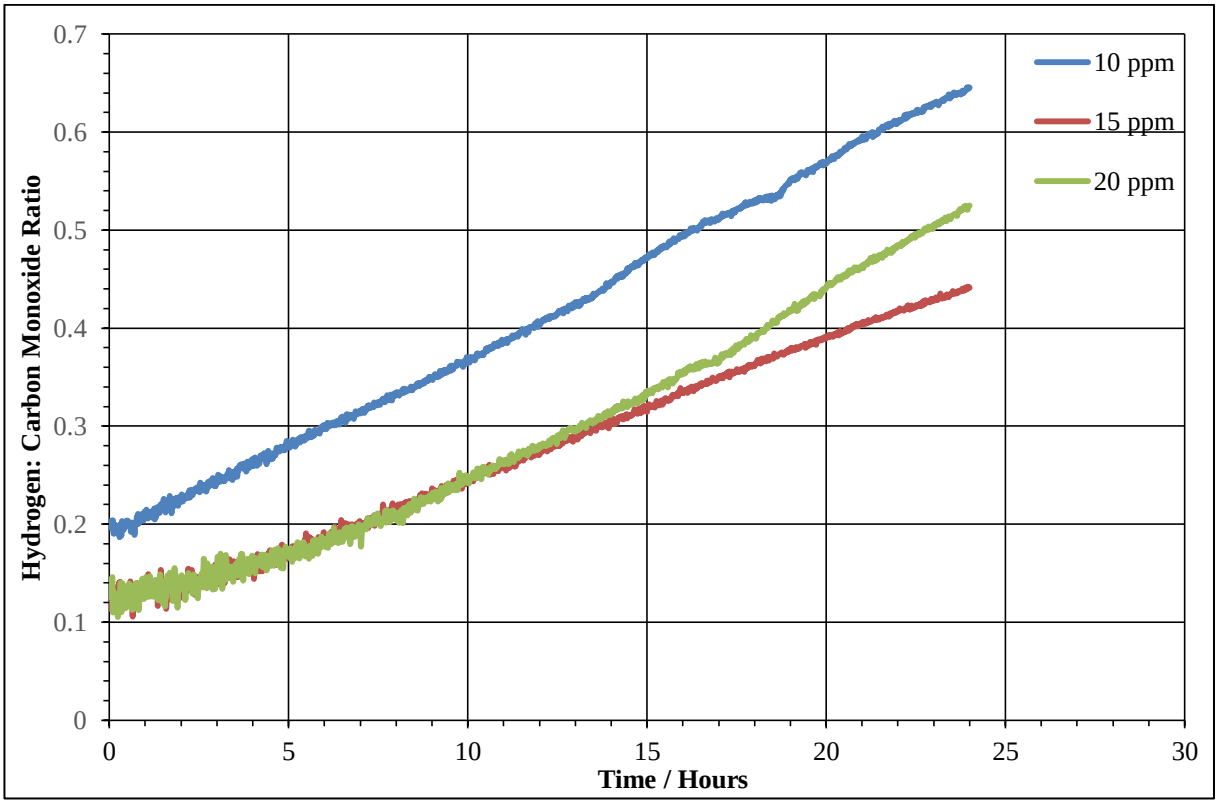

Figure 8-11 Comparison of hydrogen: carbon monoxide ratio in recovery stage from experiments using a 2:1 CH_4/CO_2 ratio passed over 4 mol% Ni doped $SrZrO_3$ at 800 °C with varying sulphur concentration and recovered at 800 °C

The increased propensity for 4 mol% Ni doped $SrZrO_3$ towards the reverse water gas shift reaction in comparison to the cermet materials gives a profile that differs significantly. The increased formation of water and carbon monoxide *via* the reverse water gas shift (RWGS) reaction lowers the H_2:CO ratio in the early stages of the recovery with a H_2:CO ratio as low as 0.1, meaning that there is ten times more carbon monoxide than hydrogen in the exhaust gas. All three profiles (10 ppm, 15 ppm and 20 ppm) then show a broadly linear relationship between the H_2:CO ratio and time in the recovery phase of reaction.

This results from a linear increase in the consumption of carbon dioxide with time, meaning less carbon dioxide was available for the RWGS.

8.4 Catalyst Recovery: Changing the Temperature of the Recovery Phase

8.4.1 Methane Conversion

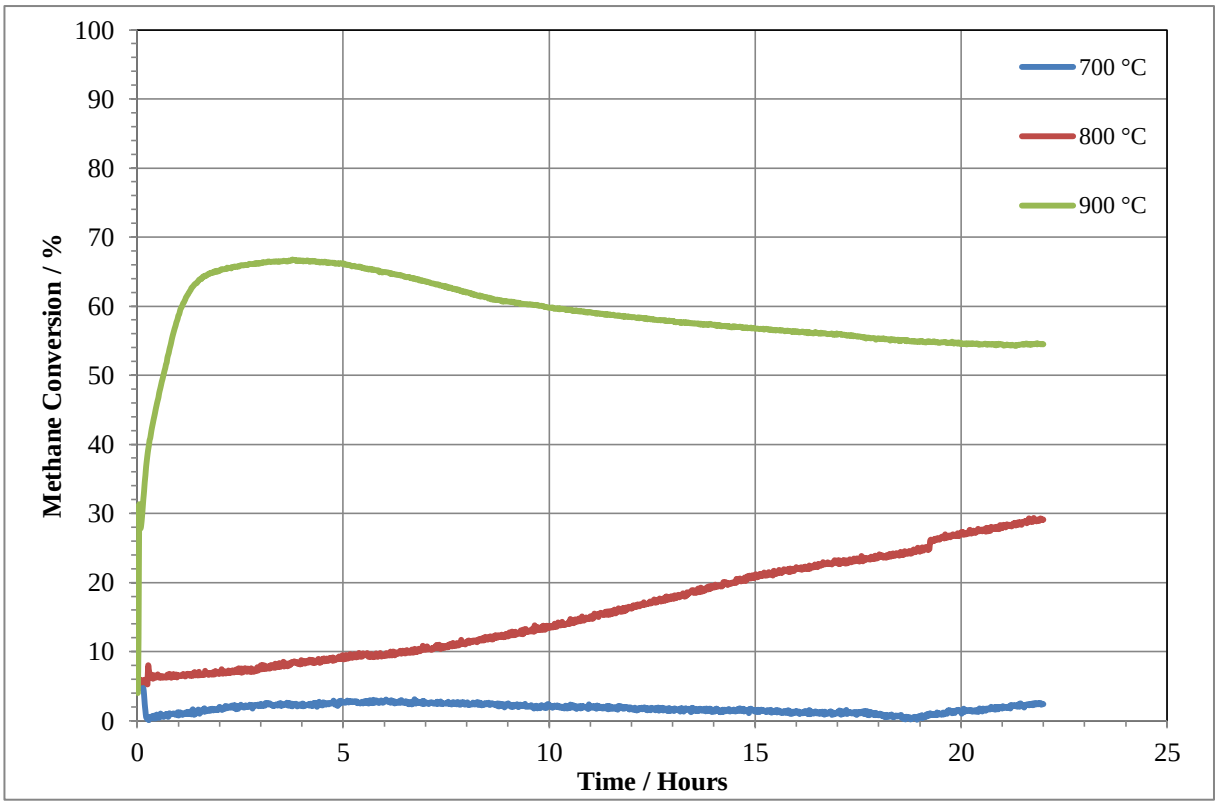

Figure 8-12 Comparison of methane conversion in the recovery from sulphur poisoning using a 2:1 CH_4/CO_2 reaction mixture passed over Ni/YSZ at 800 °C with 10 ppm of H_2S and recovered at different temperatures

When the temperature of the sulphur free recovery phase is varied, there is a stark difference in the recovery profile for Ni/YSZ when poisoned with 10 ppm of hydrogen sulphide in the biogas at 800 °C. This is due to the exothermic nature of sulphur adsorption (Figure 8-12). 700 °C is the temperature where the formation of nickel sulphide

species is the most favoured thermodynamically [17,20]. This results in the rate of desorption of sulphur being the slowest of the three temperatures studied. This is seen by the rate of recovery of methane conversion being negative after an initial slight increase until after 19 hours of recovery when a slight indication of recovery beginning is seen. As the reaction is halted soon after this phase begins, the extent of recovery is unknown.

Increasing the temperature to 800 °C in the recovery phase makes a significant difference to both the rate and the extent of recovery. The formation of nickel sulphide species becomes less favourable due to the temperature increase and so as a result desorption of sulphur becomes more favourable. Increasing the temperature also causes an increase in the rate of dissociation due to kinetic considerations. After 22 hours of recovery the methane conversion reached ~30%, more than half of the stoichiometrically predicted conversion for full recovery. Similarly to the recovery reaction at 700 °C the reaction has not reached a point of equilibrium so the full extent of recovery is not known. At 900 °C recovery starts immediately with recovery of methane conversion complete within one hour, some conversion of excess methane is also seen. As the reaction progresses the excess methane conversion decreases with time. The methane conversion remains above 50% for the extent of the reaction suggesting continuing methane decomposition.

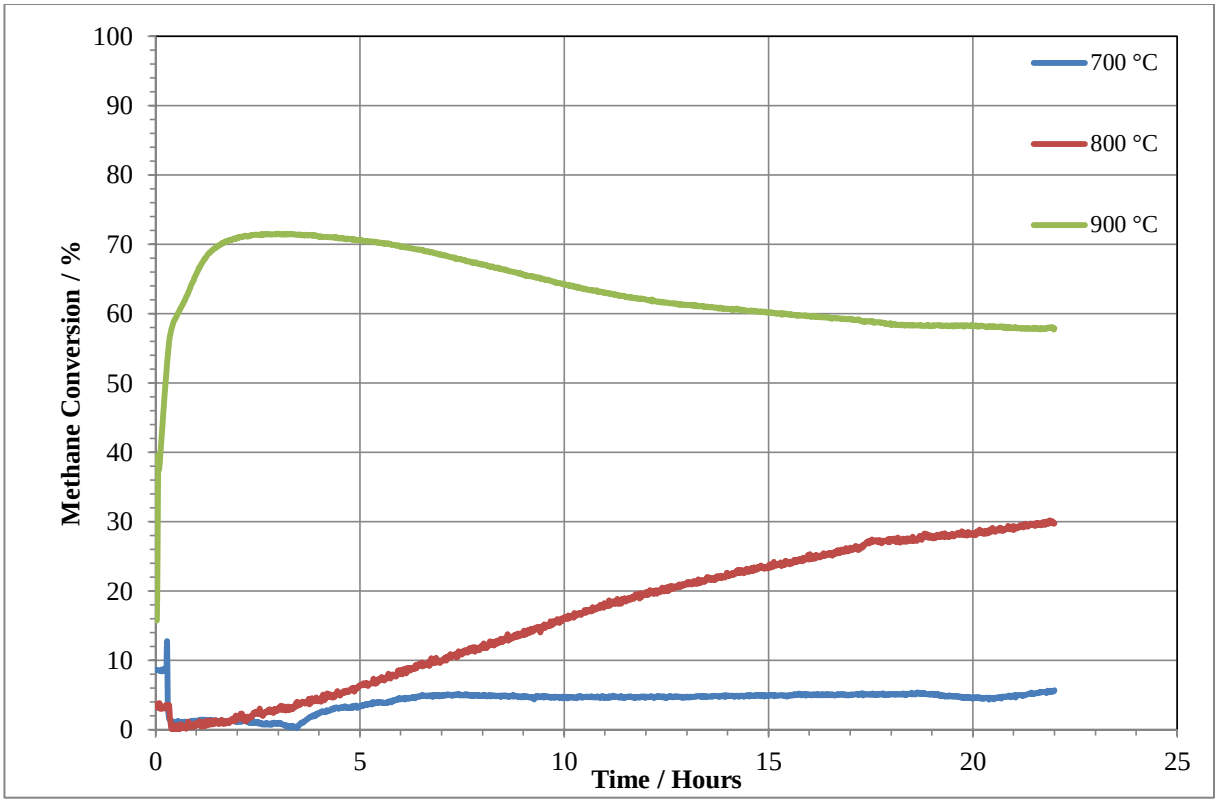

Figure 8-13 Comparison of methane conversion in the recovery from sulphur poisoning using a 2:1 CH_4/CO_2 reaction mixture passed over 5% ceria doped Ni/YSZ at 800 °C with 10 ppm of H_2S and recovered at different temperatures

For 5% ceria doped Ni/YSZ (Figure 8-13), the basic profile shape of recovery at various temperatures is similar to Ni/YSZ. However perhaps surprisingly, the recovery in general at the lower reaction temperatures is not as good. At 700 °C Ni/YSZ showed little recovery until a significant passage of time where an indication of some recovery is seen. The ceria doped sample initially shows a good recovery with activity beginning after 4 hours to ~ 5% methane conversion, however the recovery levels out after this and shows little evidence of further recovery despite the inclusion of ceria being shown to increase the rate in which sulphur is oxidised from the surface of ceria doped nickel catalyst[12,24]. At 800 °C the rate of recovery is the most similar to Ni/YSZ, with the final recovery over ceria doped Ni/YSZ being almost identical to that of the Ni/YSZ catalyst. At 900 °C the

behaviour is very similar to that of Ni/YSZ, with rapid recovery of reforming activity, due to the nickel sulphide species being thermodynamically unstable at the reaction temperature. The ceria doped sample promotes further thermal decomposition of methane in the initial phase of reaction compared to Ni/YSZ, and similarly to Ni/YSZ this drops over time towards the stoichiometrically predicted 50% conversion, although remains above 50% for the extent of the reaction.

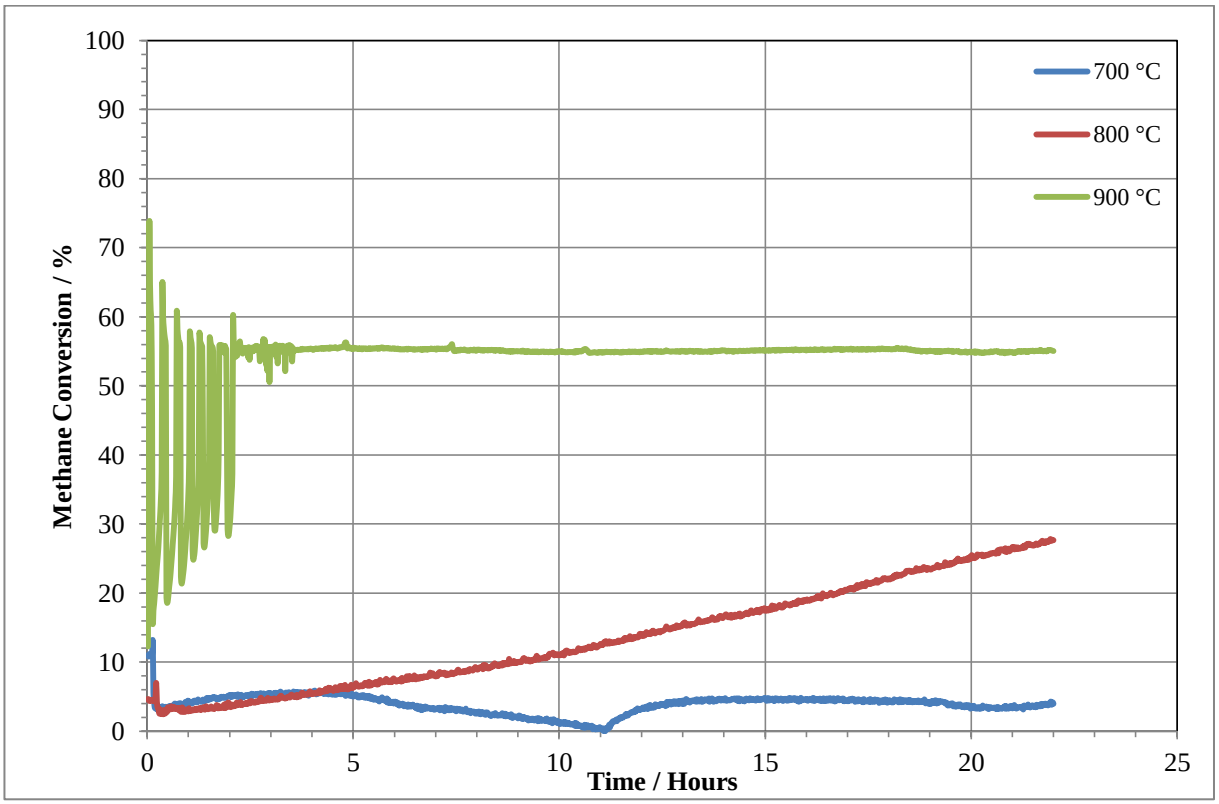

Figure 8-14 Comparison of methane conversion in the recovery from sulphur poisoning using a 2:1 CH_4/CO_2 reaction mixture passed over 4 mol% Ni doped $SrZrO_3$ at 800 °C with 10 ppm of H_2S and recovered at different temperatures

At 700 °C and 800 °C the recovery profile for the perovskite material (Figure 8-14) is very similar to the nickel cermet materials. This suggests that thermodynamics overrides any advantages associated with structure, particularly at 700 °C where the recovery is poor with only a 4% recovery in methane conversion by the end of the reaction. It is possible

that sulphur is being individually bonded to a nickel atom in the perovskite structure due to steric considerations. Increasing the temperature to 800 °C gives a more linear recovery profile as the desorption of sulphur into the gaseous phase becomes more favourable as well as occurring faster due to kinetics. Equilibrium is not reached by the end of the reaction and thus the extent of recovery is unknown. At 900 °C there is a unique recovery profile that begins with a phase of cycling that decreases in magnitude over the first four hours of recovery. Methane conversion in this initial period is as high as 73% which suggests that this temperature, adsorbed sulphur species play a role in the extent of thermal decomposition that is occurring. As the reaction progresses and the amount of sulphur adsorbed to the perovskite decreases, so does the extent of the thermal decomposition of methane, with methane conversion lowering with every cycle. After the cycling stops a stable conversion of methane continues for the remaining reaction time with 5% methane decomposed in excess.

8.4.2 Carbon Dioxide Conversion

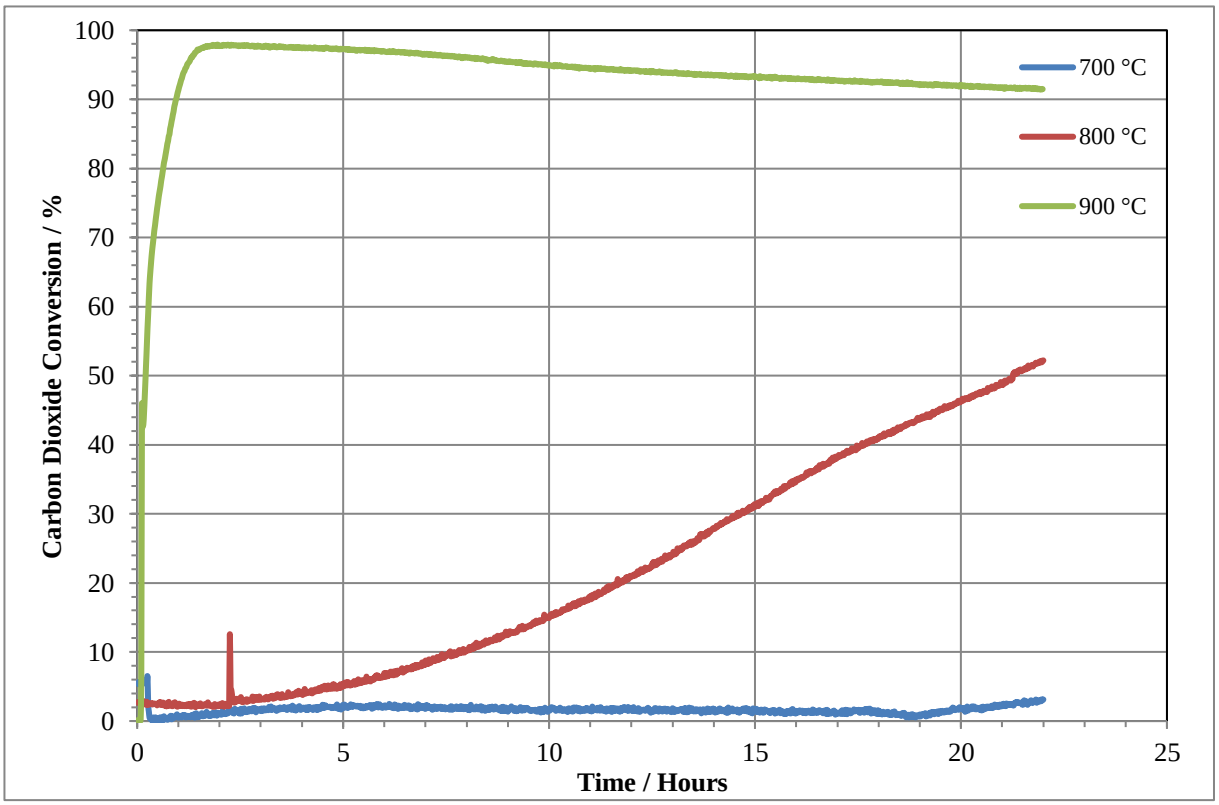

Figure 8-15 Comparison of carbon dioxide conversion in the recovery from sulphur poisoning using a 2:1 CH_4/CO_2 reaction mixture passed over Ni/YSZ at 800 °C with 10 ppm of H_2S and recovered at different temperatures

Analysing the conversion of carbon dioxide gives some insight into the mechanism of recovery that may not be deduced from the methane conversion profile alone, due to formation and consumption of carbon dioxide by side reactions, in particular the reverse water gas shift reaction. Figure 8-12 indicates that the recovery of the DRM reaction at 900 °C was complete and that the fall in methane conversion was caused by a decrease in the thermal decomposition of methane reaction. However Figure 8-15 shows that the conversion of carbon dioxide fall in the same period. This indicates that the recovery from

poisoning by sulphur is in fact incomplete and the initial complete recovery is not indicative of the final state of the catalyst material. In the initial hours of reaction surface sulphur is liberated from the catalyst surface quickly and this results in the initial quick recovery in performance. This result suggests that some sulphur remains within the Ni/YSZ structure and as the reaction proceeds sulphur segregates from the bulk to the catalyst surface. At 800 °C the conversion of carbon dioxide in the early stages of reaction differs from the conversion of methane, and this results in the formation of carbon monoxide *via* the reverse water gas shift reaction, as a result of the lower reaction temperature and also higher availability of carbon dioxide than the equivalent reaction at 900 °C. At 700 °C as there is such low recovery in performance, it is difficult to deduce any differences between the carbon dioxide profile and methane recovery.

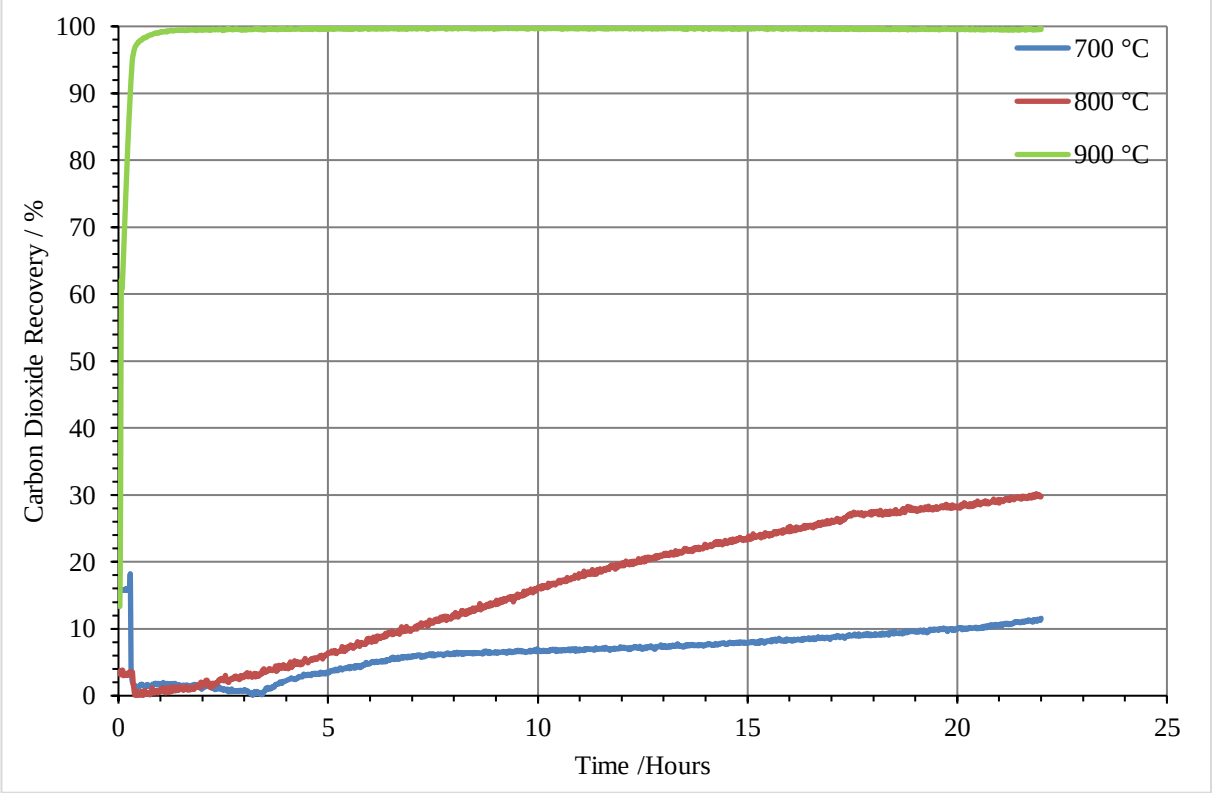

Figure 8-16 Comparison of carbon dioxide conversion in the recovery from sulphur poisoning using a 2:1 CH_4/CO_2 reaction mixture passed over 5% ceria doped Ni/YSZ at 800 °C with 10 ppm of H_2S and recovered at different temperatures

The ceria containing Ni/YSZ catalyst gives a different profile for the recovery in carbon dioxide conversion after being poisoned with sulphur at various temperatures. At 900 °C Ni/YSZ recovers quickly, with the conversion of carbon dioxide then falling with time. When ceria is added to the cermet material, the recovery in the carbon dioxide was almost instant and then remains complete for the entirety of the reaction. This suggests that the ceria aids the removal of all sulphur from the cermet material, and causes no observable change to the material, in relation to the conversion of carbon dioxide. Decreasing the reaction temperature to 800 °C has a considerable effect on the recovery of ceria doped Ni/YSZ from sulphur poisoning. At 800 °C the recovery is not instantaneous as the kinetics and thermodynamics of sulphur removal become slower and less favourable

respectively. Conversely recovery from sulphur poisoning did begin as soon as the source of sulphur is removed from the reactant gas stream. At 700 °C the thermodynamics of sulphur removal are not favourable and the cooler reaction temperature results in a slower rate of reaction and this is reflected in the recovery of carbon dioxide which begin ~3.5 hours after the sulphur source is removed from the reactant stream. This is much faster than the corresponding reaction over Ni/YSZ which took ~ 19 hours for carbon dioxide conversion to begin, and the maximum conversion only reaching~3%. In contrast, 5% ceria doped Ni/YSZ a carbon dioxide conversion of ~11% was reached after 22 hours of recovery, a significant improvement.

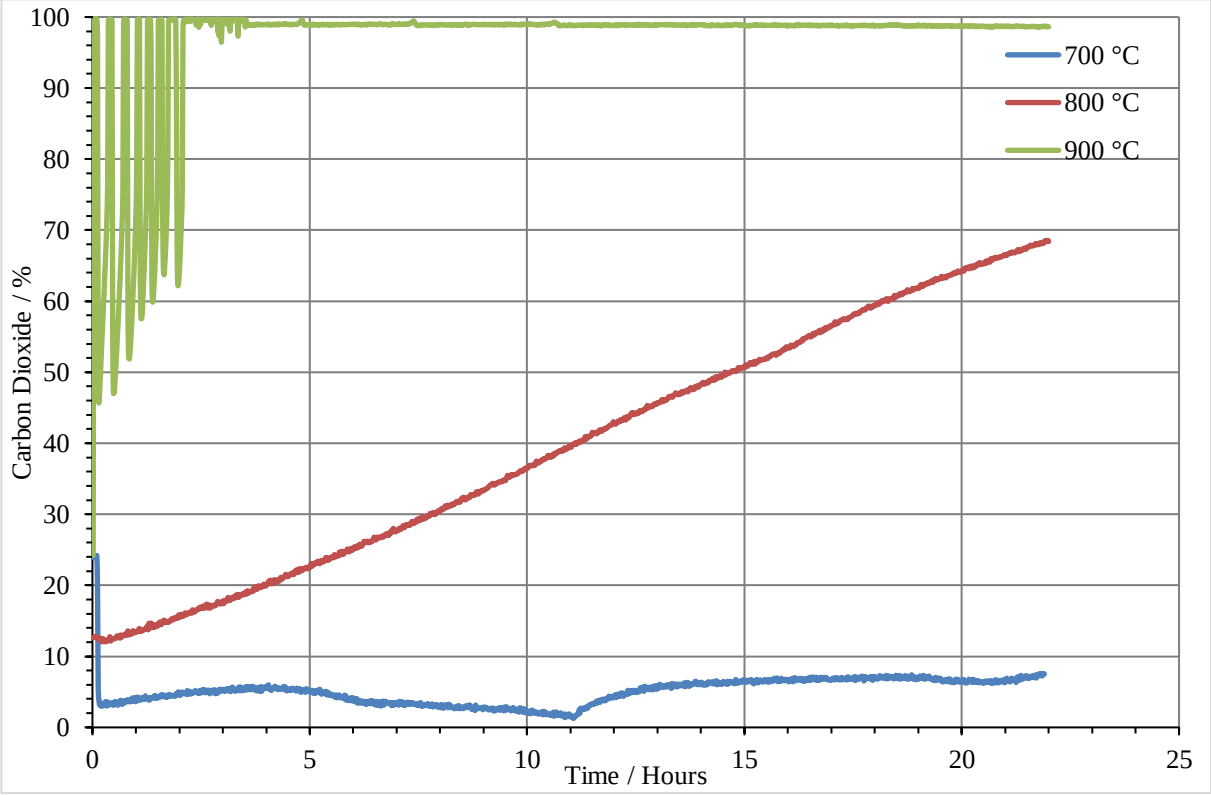

Figure 8-17 Comparison of carbon dioxide conversion in the recovery from sulphur poisoning using a 2:1 CH_4/CO_2 reaction mixture passed over 4 mol% Ni doped $SrZrO_3$ at 800 °C with 10 ppm of H_2S and recovered at different temperatures

For the perovskite material at 900 °C, as is seen with the conversion of methane in the recovery phase, a four hour period of cycling occurs for the recovery of carbon dioxide conversion (Figure 8-17). The extent of the cycling decreases with time which suggests that sulphur is being removed from the catalyst surface during this time. After four hours, other than a few minor bumps in the profile, the conversion of carbon dioxide remains constant at very close to 100% conversion, which indicates that sulphur removal is complete and under the specified reaction and recovery conditions no permanent loss of reforming activity occurs. Lowering the temperature of the recovery period to 800 °C gives a completely different recovery profile to that at 900 °C. A relatively linear recovery is seen at 800 °C consistent with the observed recovery of methane (Figure 8-14). This indicates that a direct relationship between removal of sulphur and time is being observed. The final extent of recovery is unknown. The removal of sulphur from a nickel based species is thermodynamically unfavourable as the temperature is decreased and this is seen for the reaction at 700 °C. There are some fluctuations in the detected levels of carbon dioxide, and the conversion as a result. The profile gives no clear indication that true recovery is occuring, or would occur. It is possible that some recovery could be seen over a much longer period if the rate is very low.

8.4.3 H_2:CO Ratio

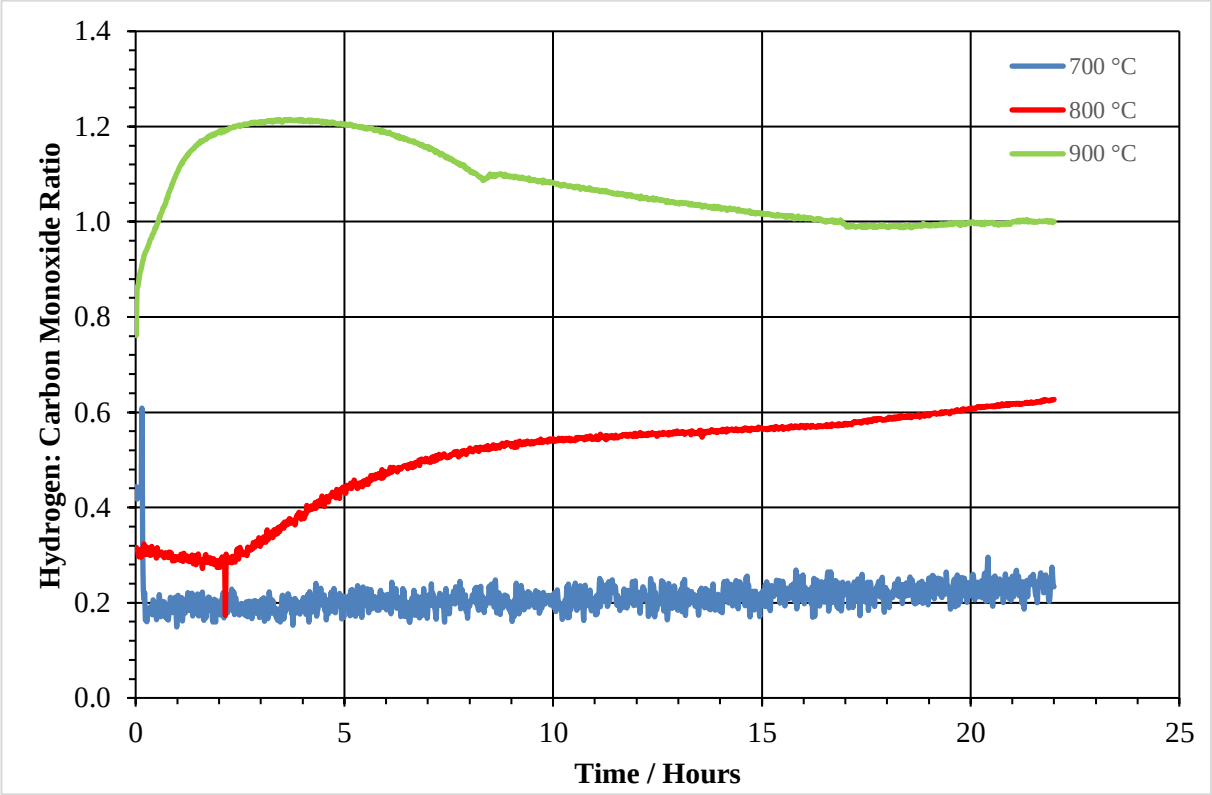

Figure 8-18 Comparison of H_2:CO ratio in the recovery from sulphur poisoning using a 2:1 CH_4/CO_2 reaction mixture passed over Ni/YSZ at 800 °C with 10 ppm of H_2S and recovered at different temperatures

Comparing the hydrogen to carbon monoxide ratio in the recovery phase of reaction over Ni/YSZ shows a clear pattern between reaction temperature and the temperature of the recovery phase (Figure 8-18). At 700 °C the H_2:CO ratio is ~ 0.2 at the start of the recovery phase and changes very little over the course of the reaction. This is due to the recovery from sulphur poisoning being extremely slow in this instance. When the temperature of the recovery phase is increased to 800 °C the rate of recovery also increases. The increase in the H_2:CO ratio follows this recovery as the removal of carbon dioxide from the reactant stream *via* the dry reforming of methane reaction decreases the

consumption of hydrogen *via* the reverse water gas shift reaction. This shift is also seen at 900 °C and the increase in temperature causes this to occur much faster as the formation of gaseous sulphur species becomes more favourable thermodynamically, and also as the reaction kinetics dictated.

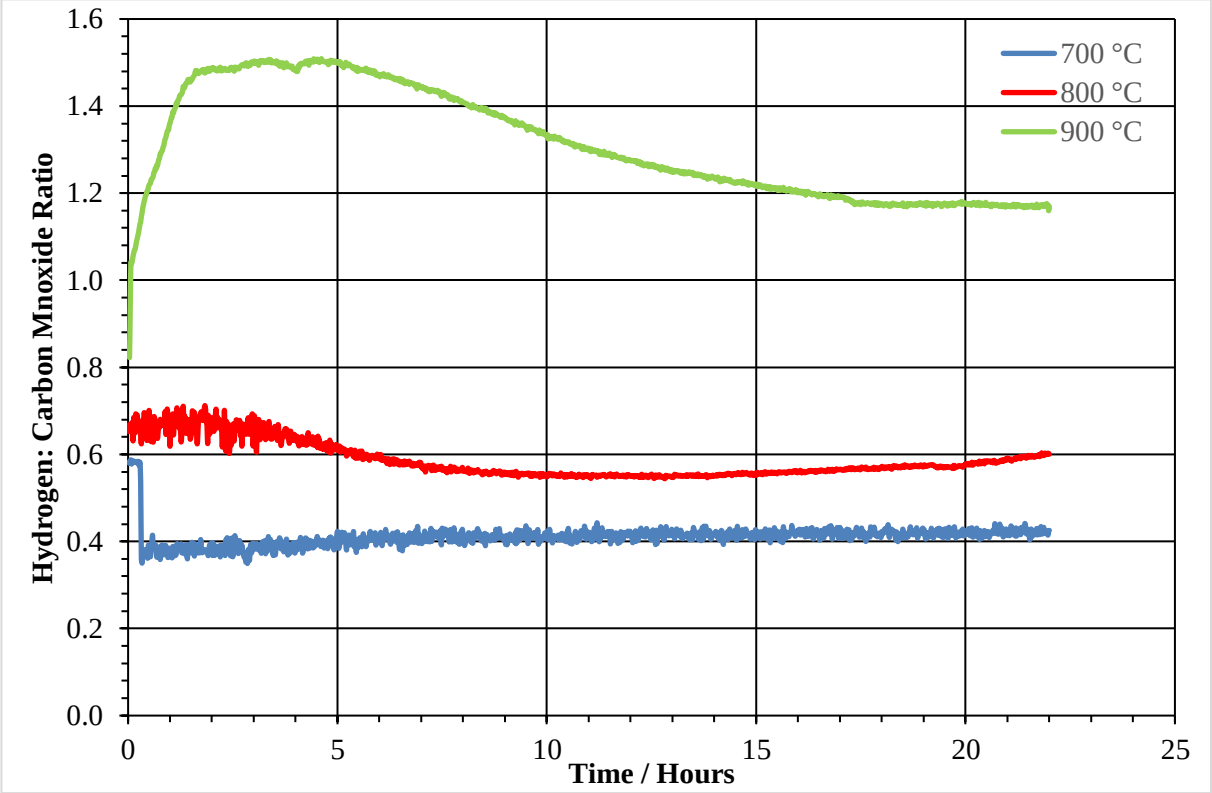

Figure 8-19 Comparison of H_2:CO ratio in the recovery from sulphur poisoning using a 2:1 CH_4/CO_2 reaction mixture passed over 5% ceria doped Ni/YSZ at 800 °C with 10 ppm of H_2S and recovered at different temperatures

At 700 °C the H_2:CO profile for 5% ceria doped Ni/YSZ (Figure 8-19) appears very similar to that of the corresponding Ni/YSZ profile. Conversely, the initial H_2:CO ratio is higher, which is a result of the recovery from sulphur poisoning being greater when ceria is added to Ni/YSZ. The ceria appears to initially oxidise some sulphur from the surface, seen by an increase in products and the H_2:CO ratio. However it does not increase the subsequent rate of recovery at this temperature. Increasing the temperature to 800 °C,

unexpectedly, does not show an increase in the rate of recovery when compared to Ni/YSZ either. At 800 °C there is some evidence of a lull in what is expected to be an increasing H_2:CO ratio. Upon further inspection this is caused by a burst in water formation *via* the RWGS reaction that quickly subsides as the recovery progresses. Increasing the temperature to 900 °C is enough to quickly remove sulphur from the cermet material with a sharp recovery seen, exaggerated by excessive formation of hydrogen *via* the thermal decomposition of methane. The increased activity resulting from the addition of ceria maintains an environment where excess methane is decomposed throughout the recovery phase. This excessive consumption of methane is in line with what was seen under the sulphur free reaction conditions in chapter 5.

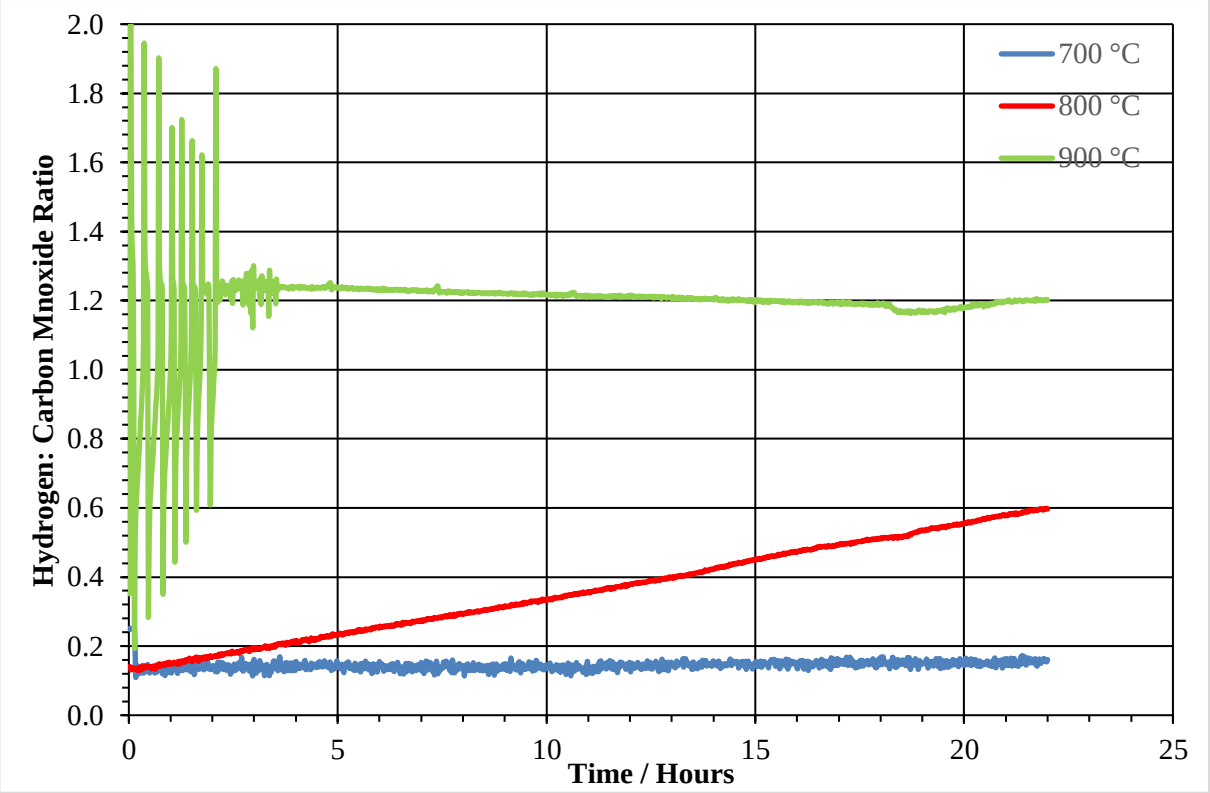

Figure 8-20 Comparison of H_2:CO ratio in the recovery from sulphur poisoning using a 2:1 CH_4/CO_2 reaction mixture passed over 4 mol% Ni doped $SrZrO_3$ at 800 °C with 10 ppm of H_2S and recovered at different temperatures

The Ni doped $SrZrO_3$ perovskite (Figure 8-20) displays reaction profiles that are different to those of the cermet materials. At 700 °C the production of synthesis gas is low, and the H_2:CO ratio reflects the consumption of hydrogen resulting in water formation. The ratio is seen to be lower than for both of the cermet materials tested under the same reaction conditions, with the increase in H_2:CO ratio with time being negligible. This suggests that at 700 °C the bonds formed between the sulphur and the active sites on the perovskite are strong, and the breaking of these bonds was not thermodynamically favourable. This result is in stark contrast to what is seen at 800 °C, where recovery begins immediately after the source of sulphur is removed from the reactant gas stream, and the H_2:CO ratio increases linearly with time. This results from a linear increase in the formation of synthesis gas, which indicates that the removal of sulphur from the perovskite under the specified conditions was zero order in respect to rate. As is seen for the conversion of methane (Figure 8-14) at 900 °C the H_2:CO ratio shows a 'cycling' behaviour. As the consumption of methane, and thus production of synthesis gas displays cycling properties this is unsurprising and perhaps offers little extra additional insight other than further evidence that the cycling is related directly to the DRM and decomposition of methane reaction, identifiable by the higher than predicted H_2:CO ratio for DRM alone. Once the cycling subsided the H_2:CO ratio falls with time, caused by a lower tendency to thermally decompose methane as the reaction progressed and stabilised.

8.5 Conclusions

This chapter has focused on the ability of Ni/YSZ and 5% ceria doped Ni/YSZ to recover from poisoning caused by sulphur impurities in a simulated biogas mixture. These results were then used to benchmark the performance of 4 mol% Ni doped $SrZrO_3$ under identical

reaction conditions in order to assess the potential to use of 4 mol% Ni doped $SrZrO_3$ to reform such reaction mixtures to form synthesis gas with the overall aim of using the material as the anode in a SOFC or as a biogas reforming catalyst.

The first major variable in this test was the concentration of sulphur that was used to poison the materials. Under the reaction conditions tested all the materials displayed a relationship between the concentration of sulphur in the biogas mixture and the time at which they recovered when the sulphur was removed from the reactant stream. As the amount of sulphur in the biogas mixture was increased, the time in which they recovered from the poisoning effects increased, despite the fact that all three materials displayed no activity at the start of the recovery phase. This suggested that sulphur was able to adsorb to both active sites, and also inactive sites on the materials, and as the recovery progressed sulphur was able to desorb and re-adsorb between the two types of site.

At lower concentrations of sulphur in the reaction feed, the difference between the cermet materials and the nickel doped perovskite in terms of recovery was negligible. However at 20 ppm, the highest concentration tested, the nickel doped perovskite recovered much faster than the two nickel cermets and there was little difference between 15 ppm and 20 ppm of H_2S in the reactant feed. This indicates that unlike the cermet materials the perovskite does not have excess sites that could adsorb sulphur that were not involved in catalysis, and thus when a sulphur is removed from a site, the site is available for reforming for catalysis.

The second experimental procedure was altering the temperature of the recovery phase. For Ni/YSZ and ceria doped Ni/YSZ the trend between temperature and recovery of

reforming catalysis was clear. At 700 °C, recovery in both cases was negligible, resulting from the dissociation of sulphur from nickel sulphide species at this temperature being less thermodynamically favourable than at higher temperatures. Due to the low reaction temperature the rate in which the dissociation occurred was also slow resulting from the reaction kinetics. Increasing the temperature to 800 °C resulted in a relatively linear recovery in the methane conversion profile, as the thermodynamics became more favourable and the rate faster due to kinetics of the sulphur dissociation. Although a steady recovery was seen, neither reaction reached equilibrium, thus the final extent of the recovery remained unknown.

At 900 °C rapid catalytic regeneration *via* the recovery of active nickel sites was observed. Increasing the temperature caused the formation of nickel-sulphur bonds to be unstable, and the elevated reaction temperature caused methane to be thermally decomposed in excess on active sites which resulted in greater than stoichiometric methane conversion for much of the recovery lifetime. The recovery of the perovskite reflected the cermets at the lower two reaction temperatures with little recovery seen at 700 °C and linear recovery of catalytic performance at 800 °C. The main difference was seen at 900 °C where the perovskite recovered instantaneously upon removal of the sulphur source, however the conversion of methane and carbon dioxide cycled for a sustained period. The magnitude of the cycles decreased with time until a flat methane and carbon dioxide conversion profile was seen. After this time a steady formation of synthesis gas was observed.

The results of this chapter showed that 4 mol% Ni doped $SrZrO_3$ recovered reforming activity slightly faster than the nickel cermet counterparts. This is positive in terms of the potential use of the nickel doped perovskite catalyst material as an alternative to Ni/YSZ

for reforming biogas that contains minor sulphur impurities. The full recovery of the catalytic activity of the perovskite material under the right conditions in sulphur free biogas mixtures was particularly encouraging as this indicated that the material may not need to be replaced, simply periodically regenerated. At lower reaction temperatures the extent of recovery would be crucial in using any of the catalysts post regeneration. If this was possible at cooler reaction temperatures over a longer time period the benefit of sulphur tolerance and regeneration of reforming catalysis would be further enhanced.

8.6 References

1 V. I. Birss, L. Deleebeeck, S. Paulson and T. Smith, in *Electrochemical Society Transactions*, 2011, vol. 35, pp. 1445–1454.

2 K. Sasaki, S. Adachi, K. Haga and M. Uchikawa, *Electrochem. Soc. Trans.*, 2007, **7**, 1675–1683.

3 P. Lohsoontorn, D. J. L. Brett and N. P. Brandon, *J. Power Sources*, 2008, **183**, 232–239.

4 V. I. Birss, L. Deleebeeck, S. Paulson and T. Smith, in *ECS Trans*, 2011, vol. 35, pp. 1445–1454.

5 Z. Cheng and M. Liu, *Solid State Ionics*, 2007, **178**, 925–935.

6 Z. Cheng, S. Zha and M. Liu, *J. Electrochem. Soc.*, 2006, **153**, A1302.

7 Y. M. Choi, C. Compson, M. C. Lin and M. Liu, *Chem. Phys. Lett.*, 2006, **421**, 179–183.

8 M. Gong, X. Liu, J. Trembly and C. Johnson, *J. Power Sources*, 2007, **168**, 289–298.

9 A. Hagen, J. F. B. Rasmussen and K. Thyd??n, in *Journal of Power Sources*, Elsevier B.V., 2011, vol. 196, pp. 7271–7276.

10 S. P. Jiang and S. H. Chan, *J. Mater. Sci.*, 2004, **39**, 4405–4439.

11 J. N. Kuhn, N. Lakshminarayanan and U. S. Ozkan, *J. Mol. Catal. A Chem.*, 2008, **282**, 9–21.

12 C. J. Laycock, J. Z. Staniforth and R. M. Ormerod, *Electrochem. Soc. Trans.*, 2009, **16**, 177–188.

13 T. S. Li and W. G. Wang, *J. Power Sources*, 2011, **196**, 2066–2069.

14 A. Lussier, S. Sofie, J. Dvorak and Y. U. Idzerda, *Int. J. Hydrogen Energy*, 2008, **33**, 3945–3951.

15 J. F. B. Rasmussen and A. Hagen, *J. Power Sources*, 2009, **191**, 534–541.

16 Y. Shiratori, T. Oshima and K. Sasaki, *Int. J. Hydrogen Energy*, 2008, **33**, 6316–6321.

17 T. R. Smith, A. Wood and V. I. Birss, *Appl. Catal. A Gen.*, 2009, **354**, 1–7.

18 D. J. Nixon, PhD Thesis, Keele University, 2013.

19 S. Zha, Z. Cheng and M. Liu, *J. Electrochem. Soc.*, 2007, **154**, B201–B206.

20 G. J. Offer, J. Mermelstein, E. Brightman and N. P. Brandon, *J. Am. Ceram. Soc.*, 2009, **92**, 763–780.

21 Y. Matsuzaki, *Solid State Ionics*, 2000, **132**, 261–269.

22 E. Brightman, D. G. Ivey, D. J. L. Brett and N. P. Brandon, *J. Power Sources*, 2011, **196**, 7182–7187.

23 J. Hepola and P. Simell, *Appl. Catal. B Environ.*, 1997, **14**, 305–321.

24 A. Fuerte, R. X. Valenzuela, M. J. Escudero and L. Daza, *Int. J. Hydrogen Energy*, 2014, **39**, 4060–4066.

9 Conclusions and Future Work

9.1 Summary

The primary aim of this work was to carry out a detailed analysis of a new nickel doped perovskite material synthesised by hydrothermal synthesis. This material was to be used as a biogas reforming catalyst and for use as an alternative SOFC anode material, particularly for the utilisation of biogas as a fuel. Within this aim improving the longevity of catalytic reforming of biogas compared to Ni/YSZ and 5% ceria doped Ni/YSZ anode materials, with focus on carbon deposition and resistance to sulphur poisoning.

A strontium zirconate material was identified as a suitable 'host' perovskite structure and it was found that doping with the strontium zirconate with nickel using hydrothermal synthesis provided very good catalytic activity towards the reforming of a methane rich biogas mixture into synthesis gas with minimal carbon deposition. Experiments were conducted in order to identify an optimum nickel loading which gave good catalysis as well as a low propensity to form carbon. On the basis of these results, and also structural characterisation using x-ray diffraction, Brunauer, Emmett and Teller theory and temperature programme reduction, 4 mol% nickel doped strontium zirconate $Sr_{0.8}Ni_{0.2}SrZrO_3$ was identified the candidate for further detailed studies.

Further detailed analysis into the dry reforming characteristics of 4 mol% Ni doped $SrZrO_3$ showed that the perovskite material decomposed a smaller proportion of excess methane at temperatures above 800 °C compared to the two chosen nickel cermet materials, Ni/YSZ and 5% ceria doped Ni/YSZ. However, it was also seen that at lower reaction temperatures carbon was formed *via* the Boudouard reaction. The nickel doped perovskite

material was seen to maintain very good resistance to carbon formation and good reforming ability when the methane to carbon dioxide ratio was altered, an important characteristic for the utilisation of biogas which is inherently variable in composition.

On the basis of this work it was then important to attempt to characterise the long term performance of the perovskite material towards carbon dioxide reforming of methane. The experiment showed that within the parameters of the experiment, 4 mol% Ni doped $SrZrO_3$ was capable of reforming methane and carbon dioxide into synthesis gas for extended periods of time, with no increase in the amount of carbon deposits after an initial deposit in the very early stages of reaction. This was a significant finding when compared to Ni/YSZ and ceria doped Ni/YSZ materials which both show a linear dependence between carbon deposited and time on stream, and thus will eventually degrade through extensive carbon deposition.

To more closely mimic biogas which contains water due to the process in which it is formed. Temperature programmed reactions were used to identify the role that water played in the reforming reaction and this showed that as reforming began, initially water acted as a spectator species. When the temperature reached 600 °C steam reforming of methane began in conjunction with the dry reforming reaction, thus increasing the methane consumption and formation of useful products in the form of synthesis gas. The nickel doped perovskite was shown to possess superior reforming activity at lower reaction temperatures than Ni/YSZ and 5% ceria doped Ni/YSZ, an important property if the widespread utilisation of SOFCs is to become a reality. Reactions were again used to show the longevity and stability of the perovskite material. The nature of the experimental set up meant that these experiments were limited to 48 hours, but over this time no loss of

reforming activity was seen. Carbon deposition over the perovskite material did not increase with time.

Sulphur impurities present in hydrocarbon fuels are a major poison for nickel based catalyst materials utilised for SOFCs. This was also shown for 4 mol% Ni doped $SrZrO_3$ which suffered from loss of reforming activity, particularly at higher concentrations of sulphur in the fuel. However the nickel doped perovskite did show greater resistance to sulphur poisoning than the nickel cermet materials tested, both at the highest and lowest temperatures, and at lower concentrations of H_2S in the biogas in particular. Experiments where the concentration of sulphur in the biogas was altered suggested that the rate of sulphur removal from the perovskite through desorption was higher than for the cermet materials under the same reaction conditions, providing some insight into why the perovskite material provided greater resistance to sulphur poisoning. This increased resistance was attributed to the structure of the perovskite and the difficulty in the sulphur ~~ions~~ getting within the correct proximity and orientation to bond to the nickel ions within the perovskite.

Upon addition of sulphur, the perovskite continued to show little or no relationship between the amount of carbon formed and the time on stream. This was not the case for the nickel cermet materials, which displayed lower deposits of carbon, but still displayed a correlation between the time on stream and the amount of carbon deposited, as long as activity was maintained.

In addition to the poisoning effect of sulphur impurities, the reaction characteristics once these impurities were removed was also investigated in order to identify if the perovskite

material could be recovered and reused post poisoning. The perovskite was shown to display good recovery from sulphur poisoning over relatively short periods of time, particularly at lower concentrations of sulphur, or at higher recovery temperatures. This was promising in respect to the use of the perovskite material with sulphur contaminated fuels, as it suggested that activity could be recovered and regenerated if the fuel is switched to a sulphur free source, saving on the expense that would be caused by cells being replaced. Both Ni/YSZ and the ceria doped derivative also showed similar recovery characteristics over similar time frames under the same reaction conditions.

9.2 Closing Remarks

In this thesis a nickel doped perovskite catalyst was designed and manufactured to act as either a reforming catalyst or as an anode component within a solid oxide fuel cell. The material was tested under a number of conditions for the dry reforming of methane reaction with particular focus on synthesis gas production, resistance to carbon formation and resistance to loss of activity caused by sulphur impurities.

The perovskite has been shown to be comparable or superior to Ni/YSZ and ceria doped Ni/YSZ in terms of activity and resistance to deleterious carbon deposition. The 4 mol% Ni doped $SrZrO_3$ has also been shown to display resistance to sulphur poisoning and good recovery characteristics from sulphur poisoning.

The catalytic properties for biogas reforming have been thoroughly investigated and found the perovskite to be a promising material for SOFC applications. However there are a number of aspects that still needed to be explored.

9.3 Future Work

In terms of future work, it would be clearly useful to perform sulphur recovery experiments with longer recovery times in order to really evaluate the full extent of recovery. Secondly, extending the study to use real biogas from a landfill site would be of interest due to the variability in concentration of methane and carbon dioxide and the presence of other contaminants naturally present n biogas.

With the catalytic performance of the perovskite material evaluated, the next logical step would be to test the electrical and ionic conductivity of the material, either individually or in situ. Formation of a button type perovskite cell by sintering would provide a basis to test the electrical and ionic conductivity of the material. Some initial work not included in this thesis has been carried out by the author. The requirements for the anode layer of a SOFC dictate the material must be electrically conductive. If hydrothermally synthesised 4 mol% Ni doped $SrZrO_3$ meets the requirements then full cell testing as an anode or an anodic functional layer would be an area of particular interest.

More detailed characterisation and spectroscopic analysis in order to understand the material and the structure more comprehensively would be another area of interest. This work has shown that the nickel doped perovskites can be synthesised and are suitable candidates for the formation of synthesis gas from methane and carbon dioxide, and with

the numerous combinations of ions and ratio of ions possible within a lattice structure, further perovskite materials should be synthesised as potential candidates for other hydrocarbon reforming reactions, such as steam reforming and partial oxidation.

Several reactions series were limited by the available time, and if this work were continued extending these reactions would be of interest. Reactions that were saturated with water were limited by the size of the saturator used. Increasing the size of the saturator, or using a steam generator instead, would mean the extent of these reaction could be longer. This would offer greater insight into how the water present in biogas changed the reaction profile. It would also give more distribution to the points on the carbon deposited with time plot. The second set of reactions that required longer reaction times was the sulphur recovery reactions. Several reactions in this set were continuing to recover when the reaction was switched off and resulted into little insight into the full extent of the recovery from sulphur poisoning being gained.

The work in this study goes some way towards justifying the potential use of perovskites as catalysts for biogas reforming. It is also the first major step in using 4 mol% Ni doped $SrZrO_3$ or a similar perovskite type structure as the material in a solid oxide fuel cell.

10. Appendix

10.1. Calibration of Mass Flow Controllers

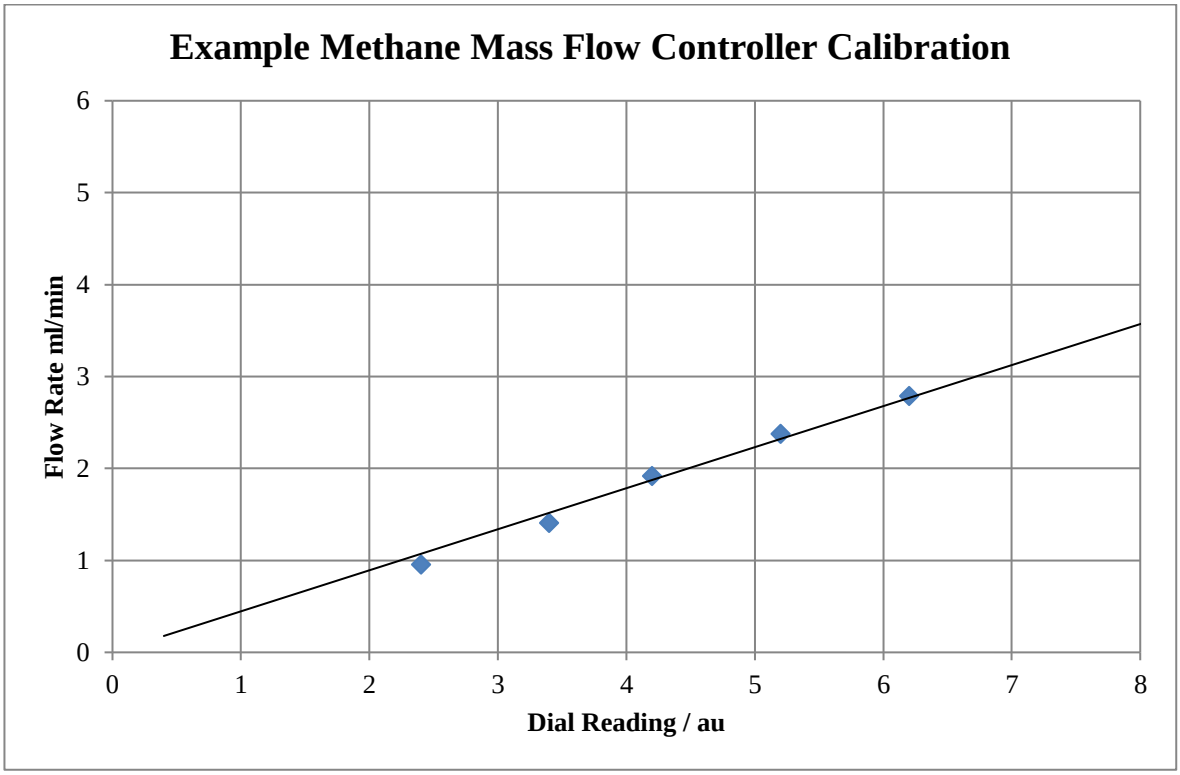

To relate dial number on the mass flow controller to flow rate provided at room temperature a calibration was created for each mass flow controller used. To attain the data a value was set on the mass flow controller and the gas diverted away from the reactor to a bubble flow meter. The time for a bubble to move a set distance on the bubble flow meter was recorded and the repeated so that a total of three values were recorded. The three values were then averaged and converted to give a flow rate. For example, if it took 60 seconds on average for the bubble to move from 0 ml to 20 ml on the bubble flow meter the flow rate recorded would be 20 – 0 = 20 ml. 60 / 60 = 1 minute. 20 / 1 = 20 ml min^{-1}.

These values would be used to initially set the dial value, however as each flow rate fluctuates with temperature, for every experiment the dial value would be used as a starting point. The gases would be remeasured and altered until the flow rate recorded was the desired flow rate for each individual experiment.

10.2. Calibration for Quantification of Carbon Deposited on Catalyst Surface

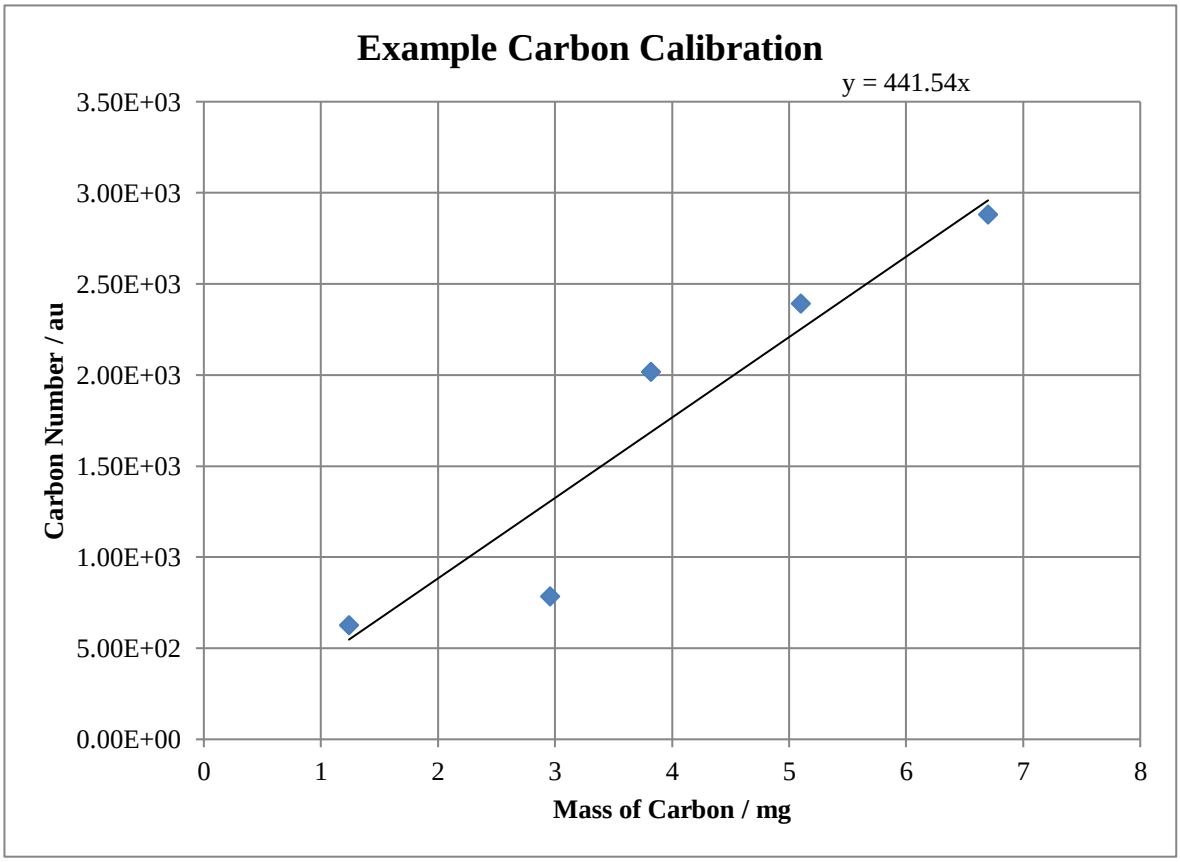

To quantify the amount of carbon deposited on the catalyst surface during each experiment, a series of calibration experiments were performed. This creates a straight line

with the mass of carbon deposited on the x-axis and a arbitrary carbon number on the y-axis. Each calibration experiment used 2 ml min^{-1} of oxygen in 18 ml min^{-1} of helium and a known mass of carbon placed within the reactor. The carbon was oxidised using a temperature programme of 2 °C min^{-1} from room temperature to 900 °C. This programme produces a carbon dioxide curve. The sum of the carbon dioxide signals was calculated and used to create a carbon dioxide number. This was repeated for several masses of carbon which is used to produce a straight line.

10.3. Sample of Gas Relative Ionisation

Sample of sensitivity values calculated for various mass fragments using method shown in section 2.13.

Hydrogen	0.81
Methane	1.30
Water	1.33
Carbon Monoxide	1.70
Oxygen	1.00
Carbon Dioxide	1.26
Helium	0.22

10.4. Bibliographic details of Publications

S. E. Evans, O. J. Good, J. Z. Staniforth, R. M. Ormerod and R. J. Darton, RSC Adv., 2014, 4, 30816.

S. E. Evans, J. Z. Staniforth, R. J. Darton and R. M. Ormerod, Green Chem., 2014, 16, 4587–4594.

J. Z. Staniforth, S. E. Evans, O. J. Good, R. J. Darton and R. M. Ormerod, Dalton Trans., 2014, 43, 15022-15027